Imperial College London
Department of Aeronautics

Vortex dynamics, non-normality and small-scale statistics in a separated flow around a finite wing

Juan Carlos Bilbao-Ludena

November 2023

Submitted in part fulfilment of the requirements for the degree of Doctor of Philosophy in Aeronautics of Imperial College London and the Diploma of Imperial College London.

Declaration

I declare that this thesis has been composed solely by myself and that it has not been submitted, in whole or in part, in any previous application for a degree. Except where states otherwise by reference or acknowledgment, the work presented is entirely my own.

The copyright of this thesis rests with the author. Unless otherwise indicated, its contents are licensed under a Creative Commons Attribution-Non Commercial 4.0 International Licence (CC BY-NC). Under this licence, you may copy and redistribute the material in any medium or format. You may also create and distribute modified versions of the work. This is on the condition that: you credit the author and do not use it, or any derivative works, for a commercial purpose. When reusing or sharing this work, ensure you make the licence terms clear to others by naming the licence and linking to the licence text. Where a work has been adapted, you should indicate that the work has been changed and describe those changes. Please seek permission from the copyright holder for uses of this work that are not included in this licence or permitted under UK Copyright Law.

Juan Carlos Bilbao-Ludena

To the Señor de los Milagros, my dear parents and sister.

Acknowledgements

I would like to first thank my supervisor Dr. George Papadakis for his invaluable guidance and expertise throughout my journey. His openness to listen to my ideas, attention to detail and focus on what truly matters in research have been very important in achieving significant milestones and executing the present work.

I am grateful to my examiners, Dr. Chris Keylock and Dr. Sylvain Laizet for their insightful comments and contributions in the review of this thesis. I would like to extend my appreciation to Clodagh Li and Lisa Kelly for their prompt and reliable support. I am also grateful to my friends and colleagues from my research group for their technical assistance during my first year as well as to all my friends in CAGB 141 and throughout the department.

I am grateful to the ARCHER2 UK National Supercomputing Service with I had access via the UK Turbulence Consortium (EPSRC Grant No. EP/R029326/1). Additional computational resources were provided by the UK Materials and Molecular Modelling Hub, which is partially funded by EPSRC (EP/P020194/1, EP/W032260/1 and EP/T022213/1) and Imperial College London. This work also used the Isambard 2 UK National Tier-2 HPC Service operated by GW4 and the UK Met Office and funded by EPSRC (EP/T022078/1). I would like to extend my thanks to all the people behind the helpdesks who provided me with the HPC technical support.

I would like to thank for the financial support by the National Program of Scholarships and Educational Credit (PRONABEC) of Peru as part of the Beca Generación Bicentenario Ph.D. scholarship which has made it possible for me to pursue my doctoral studies in the United Kingdom.

Finally, I extend my gratitude to my parents and sister and I want to especially acknowledge my dear mother, whose continuous support and encouragement have been a source of strength since the beginning of my journey.

Abstract

This thesis focuses on the analysis of vorticity and small-scale dynamics in a three-dimensional separated shear flow. The effect of large scale (time-average) motion as well as the non-normality of the small-scale statistics are examined. Direct numerical simulations (DNS) were employed to investigate the transitional flow around a finite NACA 0018 wing at a 10° angle of attack. We first analyse how each of the identified large-scale streamwise vortices forms and sustains or loses its strength in some of the most inhomogeneous regions around the tip and the near wake. This region is highly convoluted, strongly three-dimensional, multi-scale and far from being self-similar. We show how the main wingtip vortex emerges from the amalgamation and interaction of the different vortices in the near wake. The wall-normal term $-2\langle u_2 u_2 \rangle \frac{\partial \langle U_2 \rangle}{\partial x_2}$ was responsible for maintaining $\langle u_2 u_2 \rangle$ primarily in the spiral wakes in the near field. Subsequently, we study the small-scale dynamics along the transitional region and across the recirculating bubble under the influence of the mean strain-rate field. The non-normality of the Velocity Gradient Tensor (VGT) is analysed using the Schur decomposition which separates the local, eigenvalue-based dynamics from non-local effects. We uncover new features along the transitional flow and across the recirculation zone and departures from Homogeneous Isotropic Turbulence (HIT) are quantified. We extend the Schur decomposition to mean fields for the first time. Finally, we study the Lamb vector which is the source of non-linearities in the Navier-Stokes equations (NSE). The effect of the potential component of the Lamb vector is quantified. As the flow transitions, the presence of the potential part decreases but stagnates rapidly after the flow becomes fully turbulent. This suggests that the potential part becomes less crucial as the flow is less dependent on the mean shear.

Contents

Acknowledgements **7**

Abstract **9**

Contents **10**

List of Figures **17**

List of Tables **24**

1 Introduction **25**
1.1 Motivation . . . 25
1.2 Streamwise vortices in finite wings . . . 27
1.3 Separated shear flows and recirculating bubbles over wings . . . 29
1.4 Anisotropic and inhomogeneous turbulence . . . 30
1.4.1 K41 and the scales of turbulence . . . 31
1.4.2 Small-scale dynamics . . . 35
1.4.3 Studies on small-scale dynamics . . . 40
1.4.4 Schur decomposition of the VGT . . . 41
1.5 Decompositions of the Velocity Gradient Tensor . . . 42
1.5.1 Transport equations for the invariants of A . . . 46
1.6 The Lamb vector . . . 48
1.6.1 Properties and physical importance . . . 49
1.6.2 Studies on the Lamb vector . . . 52
1.7 Aims and objectives of the thesis . . . 54
1.8 Journal papers, conferences, seminars and competitions . . . 58

2 Numerical methodology and validation **60**
2.1 Solver . . . 60
2.1.1 Fractional step method . . . 62
2.1.2 Hardware and parallelization strategy . . . 64
2.2 Computational setup and validation . . . 64
2.3 Computational details for the simulation of the finite wing for $Re_c = 10000$ . . . 66
2.4 Computational details for the simulation of the finite wing for $Re_c = 5000$ . . . 70

3 Structure of vorticity and turbulence fields in a separated flow around a finite wing **73**
3.1 Main features of the near wake velocity field . . . 73

3.2 Origins of streamwise vortical structures and their evolution due to vortex stretching/tilting mechanisms . . . 77
3.2.1 Generation of streamwise structures . . . 77
3.2.2 The role of vortex stretching and tilting on the evolution of vortical structures - early stage . . . 81
3.2.3 Emergence of the wake tip vortices V1 and V2 - Late stage . . . 92
3.3 Turbulence structure of the separated wake . . . 95
3.3.1 Production mechanisms for normal Reynolds stresses . . . 98
3.4 Summary . . . 102

4 Non-normality and small-scale statistics in a separated shear flow 105
4.1 Flow characteristics . . . 105
4.2 Eigencontributions to turbulence production . . . 109
4.3 Analysis of enstrophy and total strain . . . 112
4.4 Dynamics of vortex stretching due to small-scale strain . . . 120
4.5 Dynamics of vortex stretching due to the mean flow strain . . . 122
4.6 On the intermittent nature of vorticity and strain-self amplification . . . 124
4.7 Analysis of the non-normality of the velocity gradient tensor . . . 135
4.8 Non-normality in interaction terms between mean flow and fluctuations . . . 144
4.9 Summary . . . 147

5 The structure of the Lamb vector in a separated three-dimensional turbulent flow 149
5.1 The Lamb vector of the mean flow . . . 149
5.2 The Lamb vector of the turbulent fluctuations . . . 155
5.3 Lamb vector and mean flow enstrophy . . . 159
5.4 Alignments between velocity and vorticity . . . 164
5.5 Interaction of the fluctuating, mixed and mean flow quantities in the Lamb vector and its potential component . . . 166
5.6 Summary . . . 175

6 Conclusions and future work 179
6.1 Summary of main findings . . . 179
6.1.1 A further discussion on the physical and technical findings . . . 183
6.2 Discussion and future work . . . 185

Bibliography 190

A Derivation of transport equation of $\langle s_{ij}s_{ij}\rangle$ from the NSE 202

B Schur decomposition in complex form 207

C Proof that $\|S_C\|^2 = \|\Omega_C\|^2$ 210

D Proof that the traces of matrices involving triple products of the form of $S_BS_BS_C$ and $\Omega_B\Omega_BS_C$ are zero 212

E Derivation of the Schur decomposition of enstrophy production by mean strain-rate fields 214

F Proof that all the terms of the fluctuating-mean combination are not identically zero **215**

G Norm of the Lamb vector and its potential term including mean, fluctuating and mixed terms **217**

Nomenclature

List of Abbreviations

CFD	Computational Fluid Dynamics
CFL	Courant-Friedrichs-Lewy number
DNS	Direct Numerical Simulation
FVM	Finite Volume Method
HIT	Homogeneous Isotropic Turbulence
HPC	High Performance Computing
KH	Kelvin-Helmholtz
LES	Large Eddy Simulation
MPI	Message Passing Interface
NACA	National Advisory Committee for Aeronautics
PDF	Probability Density Function
PETSC	Portable, Extensible Toolkit for Scientific Computation
RANS	Reynolds-Averaged Navier-Stokes
SGS	subgrid-scale
TKE	Turbulent Kinetic Energy
VGT	Velocity Gradient Tensor

Greek Symbols

α	Bernoulli function, angle of attrack
β	Component of the solenoidal vector $\nabla \times \beta$
Δ	Discriminant of the characteristic equation of the VGT of fluctuating velocity field
Δ_A^M	Discriminant of the characteristic equation of the VGT of time-average velocity field

Δ_A	Discriminant of the characteristics equation of matrix A
Δ_{SGS}	Filtered length with respect to the subgrid scale model
$\Delta^{'}_{SGS}$	Filtered test length with respect to the subgrid scale model
ϵ	Dissipation rate
η	Kolmogorov length scale
κ	Wavenumber
Λ_i^M	Eigenvalues of the mean strain-rate tensor
λ_i^s	Eigenvalues of the fluctuating strain-rate tensor
$\langle\Gamma_x^{V1}\rangle$, $\langle\Gamma_x^{V2}\rangle$	Mean streamwise circulation of vortex V1 and V2 respectively
$\langle\Omega\rangle$	Mean vorticity vector
$\langle\Omega_i\rangle$	Mean vorticity in the i-th direction
ν	Dynamic viscosity
Ω	Instantaneous vorticity vector
Ω_i	Instantaneous vorticity in the i-th direction
Ω_A	Fluctuating rotation tensor
Ω_B	Normal fluctuating rotation tensor
Ω_C	Non-normal fluctuating rotation tensor
Ω_{ij}	Instantaneous rotation tensor in index notation
τ	Time length scale
ζ_i	Taylor microscale in the i-th direction
l	Integral length scale

Roman Letters

k_{BC}	Non-normality index
$\langle C_f\rangle$	Mean skin friction coefficient
$\langle C_p\rangle$	Mean pressure coefficient
$\langle P\rangle$	Mean pressure
$\langle S_{ij}\rangle$	Strain-rate tensor of the mean flow
$\langle U\rangle$	Mean velocity vector
$\langle U_i\rangle$	Mean velocity in the i-th direction

ω	Fluctuating vorticity vector
ω_i	Fluctuating vorticity in the i-th direction
A	Velocity Gradient Tensor of the fluctuations
A^M	Velocity Gradient Tensor of the mean flow
A_{ij}	Velocity Gradient Tensor of the fluctuations in index notation
B	Normal matrix
C	Non-normal matrix
C_k	Kolmogorov constant
C_s	Smagorisnky constant
E	Energy spectrum
e_i^M	Eigenvectors of the mean strain-rate tensor
e_i^s	Eigenvectors of the fluctuating strain-rate tensor
H_{ij}	Pressure Hessian
H_{ij}^{dev}	Deviatoric part of the pressure Hessian tensor
L	Instantaneous Lamb vector $L = \Omega \times U$
P	Instantaneous pressure, first invariant of the characteristic equation of A_{ij}
p	Fluctuating pressure
P_A^M	First invariant of the characteristic equation of A^M
P_A	First invariant of the characteristic equation of A
Q	Second invariant of the characteristic equation of A_{ij}
Q_A^M	Second invariant of the characteristic equation of A^M
Q_A	Second invariant of the characteristic equation of A
R	Third invariant of the characteristic equation of A_{ij}
R_A^M	Third invariant of the characteristic equation of A^M
R_A	Third invariant of the characteristic equation of A
r_c	Radial location of the maximum azimuthal velocity
Re_{ζ_i}	Taylor based Reynolds number
Re_c	Chord-based Reynolds number
S_B^M	Strain-rate tensor of the mean flow

S_C^M	Strain-rate tensor of the mean flow
S_A	Fluctuating strain-rate tensor
S_B	Normal fluctuating strain-rate tensor
S_C	Non-normal fluctuating strain-rate tensor
S_{ij}	Instantaneous strain-rate tensor in index notation
s_{ij}	Fluctuating strain-rate tensor in index notation
U	Instantaneous velocity vector
u	Fluctuating velocity vector
U_∞	Inlet velocity
U_i	Instantaneous velocity in the i-th direction
u_i	Fluctuating velocity in the i-th direction
V	Cell volume
W_{ij}	Fluctuating rotation tensor in index notation

List of Figures

1.1 (a) Visualization of wingtip vortices during flight (image obtained from USCG [2012]) and (b) Illustration of future UAM infrastructure (image obtained from NASA [2018]). 26
1.2 Sketch of energy spectrum and different regions. 33
1.3 Illustration of the interaction between the strain self-amplification and vortex stretching process (adapted from Sagaut and Cambon [2008]). 37
1.4 (a) Example of a joint pdf of Q_A and R_A invariants in the form of a teardrop [Galanti and Tsinober, 2004, Tsinober, 2009] and (b) three-dimensional topologies in the $Q_A R_A$ plane obtained from Soria et al. [1994], Perry and Chong [1994]. 39

2.1 Comparison of time- and spanwise-averaged (a) streamwise velocity profiles at equally spaced intervals $x/C = 0.1, 0.2, \ldots, 1.0$. ($b$) $\langle C_p \rangle$ distribution and (c) $\langle C_f \rangle$ distribution. Present results are compared with those of Zhang and Samtaney [2015]. 66
2.2 Computational domain (front and top views) and mesh layout for the finite wing simulation. The trailing edge is located at $x/C = 1$, $y/C = 0$ and extends in the spanwise direction $z/C = -1 \ldots 0$. Only half of the wing is simulated (and shown). The dotted orange curve demarcates the region of the mesh inside which a constant cell thickness growth rate (equal to 1.01) is employed. Around the airfoil, this curve is located at a distance $0.25C$ in the wall-normal direction). . . 68
2.3 Plots of the grid size to Kolmogorov length scale ratio, $V^{1/3}/\eta$. (a) Contours in the $y - z$ plane at $x/C = 1.1$. The white curve represents the $Q = 5$ isoline, the red dotted line marks the location of the wingtip plane, and the green dot the trailing edge tip corner. (b) Variation of $V^{1/3}/\eta$ along the dashed blue line shown in (a) at $y/C = 0.04$. (c) Contours of $V^{1/3}/\eta$ at $x-y$ plane at $z/C = -0.5$ (quarter-span). 69
2.4 Comparison of distribution of $\langle U_1 \rangle$ velocity obtained using different mesh sizes along the (a) spanwise and (b) streamwise directions, along the dashed lines placed at $x/C = 0.5$ and $y/C = 0.12$ for (a), and $y/C = 0.2$ and $z/C = -0.5$ for (b). 70
2.5 Contours of $V^{1/3}/\eta$ in the $x - y$ plane at $z/C = -0.2$. The white dotted line A goes through the recirculating zone and B through the transition. 71
2.6 Variation of grid size to Kolmogorov length scale ratio, $V^{1/3}/\eta$ along (a) line A and (b) line B. The vertical dashed lines in (a) denote the boundaries of the recirculation zone. 71

3.1 Contours of the mean axial velocity $\langle U_1 \rangle$ at equally spaced planes $x/C = 0.2, \ldots 1.3$. The purple-coloured contour line represents $\langle U_1 \rangle = 0$. 74

3.2 (a) Instantaneous isosurface of $Q = 5$. The wing is shown in green colour in the background. (b) Contours of the time-average $\langle Q \rangle$ at equally spaced planes $x/C = 0.1, 0.2, ..., 1.3$. with designated vortical structures. (c) Visualization and designation of vortical structures using the iso-surface $\langle Q \rangle = 5$. (d) Organization of the vortex structure topology at $x/C = 0.75$. 75
3.3 Contours of time-averaged streamwise vorticity (top row) and pressure coefficient (bottom row) at different x planes, highlighting the early formation of vortical structures RV, LV and V0. 78
3.4 Contours of $\langle C_p \rangle$ over the wing (a) superimposed with the $\langle U_1 \rangle = 0$ isosurface, (b) zoomed-in view around the leading edge. The white dashed line marks the stagnation line across the span. The three white triangles indicate the streamwise locations $x/C = 0.05$, 0.1, and 0.2. 79
3.5 Contour plots of time-averaged vorticity components (streamwise at top row; wall-normal at middle row; spanwise at bottom row) at different x/C planes. The isoline $\langle Q \rangle = 7$ is indicated in white colour. 80
3.6 (a) Axial elongation rate (filled purple contours) superposed with streamwise vorticity (blue/red) line contours, (b) Convection term (filled contours) and (c) budgets of the vorticity transport equation along the horizontal yellow dashed line shown in panels (a) and (b). The white isoline depicts $\langle Q \rangle = 5$. The vertical solid black line in (c) demarcates the boundary between the shear layer and vortex core regions. Vertical dashed lines are placed in the same spanwise location in (a) and (b). Results at plane $x/C = 0.6$. 83
3.7 Isosurface of vorticity convection $-U_j \frac{\partial \langle \Omega_1 \rangle}{\partial x_j} = 78$ (orange colour). Vortex V0 is visualised by $\langle Q \rangle$ criterion (same values as in figure 3.2(b)) at equally spaced planes $x/C = 0.4 - 1.2$. The pink isosurface represents $\langle U_1 \rangle = 0$ and encloses the two separated flow regions (one that starts in the leading edge, and the other in the trailing edge, around the tip). The vorticity convection isosurface value corresponds to $\approx 52\%$ of the positive maximum value found within the core of V0 at the $z - y$ plane located at $x/C = 0.6$. 84
3.8 Isosurfaces of (a) vorticity stretching rate $\langle \Omega_x \rangle \langle S_{xx} \rangle = 14$ (in green colour) (b) vorticity compression rate $\langle \Omega_x \rangle \langle S_{xx} \rangle = -30$ (in yellow colour). The pink isosurface represents $\langle U_1 \rangle = 0$. Results are shown at equally spaced planes $x/C = 0.2 - 1.2$. The isosurface values of the vortex stretching/compression rate correspond to $(a) \approx 32\%$ of the positive maximum value found within V1 at $x/C = 1.2$ and $(b) \approx 44\%$ of the minimum negative value within the core of V0 at the z-y plane located at $x/C = 0.85$. the reach self-similarity 85
3.9 Coloured (filled) contours of elongation rate superposed with coloured (line) contours of $\langle \Omega_x \rangle$ at two planes $x/C = 0.85$ (left) and $x/C = 0.99$ (right). The white isoline depicts $\langle Q \rangle = 5$. 86
3.10 Coloured contours of (a) $\langle \Omega_i \rangle \langle \Omega_j \rangle \langle S_{ij} \rangle$ $\langle \Omega_x \rangle$ and (b) $\langle S_{ij} \rangle \langle S_{jk} \rangle \langle S_{ki} \rangle$ at $x/C = 0.85$. The white isoline depicts $\langle Q \rangle = 10$. 87
3.11 Coloured contours of (a) $\langle Q \rangle$ and (b) $\langle R \rangle$ at $x/C = 0.85$. The white isoline depicts $\langle Q \rangle = 10$. 88
3.12 Isosurface of vorticity stretching rate $\langle S_{xx} \rangle = 14$ in the tip (green colour). Vortex LV is visualised by plotting the $\langle Q \rangle$ criterion (same values as in figure 3.2(b)) at equally spaced planes $x/C = 0.1 - 1.1$. The pink isosurface represents $\langle U_1 \rangle = 0$. The isosurface $\langle S_{xx} \rangle$ value corresponds to $\approx 11\%$ of the positive maximum value found within the core of LV at the $z - y$ plane located at $x/C = 0.3$. 89

3.13 Contour plots of axial vorticity generation term (a) stretching only and (b) stretching and tilting, for vortex LV at $x/C = 0.35$. The solid white isoline depicts $\langle Q \rangle = 5$. Spanwise distribution of the budget terms of the vorticity transport equation along (c) the core and (d) the feeding shear of LV. The exact locations are marked as white dashed lines in panels (a) and (b). 90
3.14 Contours of vortex stretching rate $\langle \Omega_x \rangle \langle S_{xx} \rangle$ at planes (a) $x/C = 0.85$ and (b) $y/C = 0.1$. (c) Balance of the vorticity transport equation along the dashed yellow line shown in panel (a) that crosses RV. The solid white isolines in (a) and (b) depict $\langle Q \rangle = 5$. 91
3.15 Emergence of the wake tip vortices V1 and V2. Contours (filled) of streamwise strain rate $\langle S_{xx} \rangle$ superposed to coloured isolines of positive $\langle \Omega_x \rangle$ at different x/C planes. The solid white line indicates $\langle Q \rangle = 5$. 91
3.16 Isosurfaces of vortex intensification terms, stretching and/or tilting, superimposed on $\langle Q \rangle = 5$. (a) Stretching term $\langle \Omega_x \rangle \langle S_{xx} \rangle = 14$, (b) Tilting terms $\langle \Omega_y \rangle \langle S_{xy} \rangle + \langle \Omega_z \rangle \langle S_{xz} \rangle = 14$, (c) Sum of all terms, $\langle \Omega_j \rangle \langle S_{xj} \rangle = 12$. (d) $\langle \Omega_x \rangle = 8$. The isosurface values correspond to $(a) \approx 32\%$, $(b) \approx 67\%$, $(c) \approx 54\%$ and $(d) \approx 72\%$ of their corresponding positive maximum values within V1 in the z-y planes located at $x/C = 1.2$ (at $x/C = 1.3$ for (b)). 93
3.17 Isosurface of the vorticity intensification term $\langle \Omega_j \rangle \langle S_{xj} \rangle = 12$ (purple colour) superimposed on $\langle Q \rangle = 5$ (top). Normalised azimuthal velocity profile inside V1 at two positions $x/C = 2$ and 5, and comparison with self-similar profiles from the literature (bottom). The distances in the figure inset are measured downstream of the trailing edge. 94
3.18 Contours of k plotted at equally spaced planes $x/C = 0.5 - 1.3$. The black contour line represents $\langle U_1 \rangle = 0$. 96
3.19 Contour plots of TKE production $P = -\langle u_i u_j \rangle \langle S_{ij} \rangle$ at equally spaced planes $x/C = 0.5 - 1.3$. The black contour line represents $\langle U_1 \rangle = 0$. 97
3.20 Isosurfaces of (a) k, (b) $\langle u_1 u_1 \rangle$, (c) $\langle u_2 u_2 \rangle$ and (d) $\langle u_3 u_3 \rangle$ with values 0.05, 0.05, 0.04 and 0.02 respectively. These values correspond to $(a) \approx 45\%$, $(b) \approx 55\%$, $(c) \approx 49\%$, and $(d) \approx 29\%$ of the maximum value of the corresponding quantities at the $z-y$ plane located at x/C=1.2. (e) Isosurfaces of k with value 0.5 (blue) and turbulence production with value 0.2 (red). The isosurface values correspond to $\approx 55\%$ and $\approx 31\%$ of the maximum value of k and $\mathcal{P}$ respectively in the $z - y$ plane located at $x/C = 1.2$. (f) Turbulence production $\mathcal{P}$ colored by k. The isosurface $\langle Q \rangle = 5$ is superimposed in all plots to visualise the vortical structures. 98
3.21 Production terms of $\langle u_1 u_1 \rangle$ (a) The magenta isosurface represents $-2[\langle u_1 u_1 \rangle \frac{\partial \langle U_1 \rangle}{\partial x_1}] = 0.4$ with pink lines representing the contours of $\langle u_1 u_1 \rangle = 0.03$ and blue line representing compression $\frac{\partial \langle U_1 \rangle}{\partial x_1} = -2$. (b) The purple isosurface represents $-2[\langle u_1 u_2 \rangle \frac{\partial \langle U_1 \rangle}{\partial x_2}] = 0.5$, blue lines represent the contours of shear strain coming from the top wing surface with $\frac{\partial \langle U_1 \rangle}{\partial x_2} = -7$ and orange lines $\langle u_1 u_2 \rangle = 0.01$, the red line represents shear from the bottom wing surface with $\frac{\partial \langle U_1 \rangle}{\partial x_2} = 7$ and the corresponding orange line $\langle u_1 u_2 \rangle = -0.01$ and (c) total production of $\langle u_1 u_1 \rangle$: iso-surface $\mathcal{P}_{11}^{R-s} = 0.3$ colored by $\langle u_1 u_1 \rangle$. The isosurface values are equal to $(a) \approx 45\%$, $(b) \approx 36\%$ and $(c) \approx 27\%$ of the positive maximum value of the corresponding quantities in the $z - y$ plane located at $x/C = 1.2$ (at $x/C = 0.9$ for (a)). The isosurface $\langle Q \rangle = 5$ is superimposed in all plots to visualise the vortical structures. 99

3.22 Production terms of $\langle u_2u_2\rangle$ (a) Isosurface of $-2\langle u_2u_2\rangle\frac{\partial\langle U_2\rangle}{\partial x_2} = 0.3$, blue lines represent contours $\frac{\partial\langle U_2\rangle}{\partial x_2} = -3, -4$ and the pink line represents $\langle u_2u_2\rangle = 0.04$ (b) Isosurface of $\mathcal{P}_{22}^{R-s} = 0.3$ colored by $\langle u_1u_1\rangle$. The contour values correspond to $(a) \approx 61\%$ and $(b) \approx 64\%$ of their respective positive maximum value in the $z-y$ plane located at $x/C = 1.2$. The isosurface $\langle Q\rangle = 5$ is superimposed in all plots to visualise the vortical structures. 100
3.23 (a) Contours of $-2[\langle u_1u_2\rangle\frac{\partial\langle U_1\rangle}{\partial x_2}]$ (b) $-2[\langle u_2u_2\rangle\frac{\partial\langle U_2\rangle}{\partial x_2}]$ superimposed with the integration area S_z at $x/C = 1.2$. (c) Streamwise locations of the integration planes (that capture the spatial evolution of vortex V1) superimposed on $\langle Q\rangle = 5$ isosurface. 101
3.24 Streamwise evolution of quantities related to (a) the vorticity field and (b) the production of Reynolds stresses. The quantities shown are integrated over the surface S_z marked in panels (a) and (b) of figure 3.23. The vertical dashed line indicates the streamwise location where $\langle U_1\rangle = 0$. 102

4.1 Contours of (a) $\langle U_1\rangle$, (b) turbulent kinetic energy (TKE) k and (c) its production term $-\langle u_iu_j\rangle\langle S_{ij}\rangle$ in the $x-y$ plane at $z/C = -0.2$. 107
4.2 Distribution of $\langle U_1\rangle$ (blue line) and k (black line) for (a) along line A and (b) along the transition line B. The dashed vertical lines in (a) indicate the boundaries of the recirculation zone. 107
4.3 Reynolds stresses (a) along line A and (b) along line B. 108
4.4 Taylor microscales ζ_i and Kolmogorov scale along (a) line A and (b) line B. The dashed lines indicate the region upstream of transition. 109
4.5 Reynolds number based on the Taylor microscale (a) along line A and (b) along line B. Dashed lines indicate the region upstream of transition. 109
4.6 Eigendecomposition of turbulent production (left axis) and eigenvalues of the mean strain rate tensor (right axis) (a) along line A and (b) along line B. 110
4.7 Time-average alignment of u and the principal components of the mean-strain rate fields (a) along line A and (b) along line B. 111
4.8 Pdf's of the absolute alignments between u and the principal direction of mean strain rate for (a) transitional flow between $x/C = 1.32 - 1.43$ and (b) $x/C = 2.74 - 3.36$. 112
4.9 Contours of (a) $0.5\langle\omega_i\omega_i\rangle$ and (b) $\langle s_{ij}s_{ij}\rangle$ in the $x-y$ plane at $z/C = -0.2$. . . 113
4.10 $0.5\langle\omega_i\omega_i\rangle$ (blue line) and $\langle s_{ij}s_{ij}\rangle$ (black line) distribution (a) along line A and (b) along line B. 113
4.11 Sequence of instantaneous contours of $0.5\omega_i\omega_i$ ((a) $t = 194$, (c) $t = 194.2$, (e) $t = 194.4$) and $s_{ij}s_{ij}$ ((b) $t = 194$, (d) $t = 194.2$, (e) $t = 194.4$). The light green line represents the instantaneous vortical structures with $Q = 2$. The white line represents the recirculation zone boundary. 115
4.12 Main components of enstrophy and $\langle\omega_1\omega_2\rangle$ in (a) along line A and (b) along line B. 115
4.13 Isosurfaces of enstrophy production due to vortex stretching by the mean flow $\mathcal{EM}_\omega$ and fluctuations $\mathcal{EF}_\omega$ (light green and pink colour with a value of 300 respectively). Vortical structures are represented by the Q-criterion value of 2. 117
4.14 Budgets of the transport equation of $0.5\langle\omega_i\omega_i\rangle$ for (a) along line A and (b) along line B. Spanwise averaging over a distance $0.08C$ centered around $z/C = -0.2$ was performed to increase the sample size. 118

4.15 Budgets of the transport equation of $\langle s_{ij}s_{ij}\rangle$ for (a) along line A and (b) along line B. Spanwise averaging over a distance $0.08C$ centered around $z/C = -0.2$ was performed to increase the sample size. 119
4.16 Eigencontributions to enstrophy production due to vortex stretching $\langle\omega_i\omega_j s_{ij}\rangle$ (left axis) and averaged eigenvalues of the fluctuating strain rate tensor (right axis) (a) along line A and (b) along line B. 120
4.17 Average alignments between fluctuating vorticity and the eigenvectors of the fluctuating strain rate tensor (a) along line A and (b) along line B. Horizontal lines represent the average values for HIT $Re_{\zeta i} = 107$, data taken from Schumacher et al. [2007], Hamlington et al. [2008]. 121
4.18 Pdf's of the alignments between vorticity and the principal directions of strain rate tensor in the transitional regions in different sections: (a) "growth" ($x/C = 1.2 - 1.3$), (b) "peak" ($x/C = 1.4 - 1.6$) and (c) "decay" ($x/C = 2.5 - 3.5$). Dashed lines indicate pdf's of HIT ($Re_{\zeta i} = 107$) data taken from Schumacher et al. [2007], Hamlington et al. [2008]. 122
4.19 Eigencontribution of enstrophy production by mean strain rate $\langle\omega_i\omega_j\rangle\langle S_{ij}\rangle$ (left axis) and eigenvalues of the mean strain rate tensor (right axis) (a) along line A and (b) along line B. 123
4.20 Alignment of fluctuating vorticity and the principal directions of the mean strain rate tensor (a) along line A and (b) along line B. Horizontal lines represent the values for HIT ($Re_{\zeta i} = 107$) [Schumacher et al., 2007, Hamlington et al., 2008]. 123
4.21 Pdf's of the absolute value of the cosine of the angle between fluctuating vorticity and the eigenvector of mean strain rate for (a) recirculating flow between $y/C = 0.87 - 0.155$ and (b) transitional flow between $x/C = 1.325 - 1.371$. Dashed lines represent values from HIT ($Re_{\zeta i} = 107$) , data from Schumacher et al. [2007], Hamlington et al. [2008] are superimposed. 124
4.22 Contours of (a) Δ and (b) regions of the QR space based on fluctuations in the $x - y$ plane at $z/C = -0.2$. The light green isoline (a) represents $Q = 2$. 126
4.23 Joint pdf showing the QR regions for the transitional flow in the "decay" section ($x/C = 2.46 - 3.43$). The grey dashed line is the locus of points where $\Delta = 0$. . 127
4.24 Occupancy fractions of QR regions (1)-(6) for the (a) along line A and (b) along line B. The dotted lines correspond to HIT values ($Re_{\zeta i} = 433$) obtained from Keylock [2018], see table 4.1. 128
4.25 Contribution of different QR regions to $\langle\omega_i\omega_j s_{ij}\rangle$ (a) along line A and (b) along line B. 128
4.26 Contribution of different QR regions to $-\langle s_{ij}s_{jk}s_{ki}\rangle$ (a) along line A and (b) along line B. 129
4.27 Pdf of $\omega_i\omega_j s_{ij}$ (top row) and $-s_{ij}s_{jk}s_{ki}$ (bottom row) at different locations. Recirculating flow sample locations (a), (c): "recirculation" ($y/C = 0.15 - 0.17$), "right peak" ($y/C = 0.21 - 0.25$). Transitional flow sample locations (b), (d): "growth" ($x/C = 1.2 - 1.3$), "peak" ($x/C = 1.4 - 1.63$) and decay ($x/C = 2.46 - 3.43$). . 130
4.28 Isosurfaces of instantaneous enstrophy $0.5\omega_i\omega_i$ (cyan) and vortex stretching $\omega_i\omega_j s_{ij}$ (purple). (a) values of 100 and 300 respectively and (b) large events in the form of spiky bursts with values 1000 and 3000 (10 times higher). Vortical structures in the background are visualised in grey colour (value of Q-criterion equal to 2). 130
4.29 Contribution of events with values equal or larger than 10 times the time-average (large events) to the mean value (orange for $\omega_i\omega_j s_{ij}$ and yellow for $-s_{ij}s_{jk}s_{ki}$) (a) along line A and (b) along line B. 132

4.30 Frequency of events large events (a) along line A and (b) along line B (green line for $\omega_i\omega_j s_{ij}$ and blue line for $-s_{ij}s_{jk}s_{ki}$) and number of standards deviations σ_{std} between the time-average and the fix value of ten times the mean (c) along line A and (d) along line B. 133
4.31 Occupancy fractions of QR regions for values of vortex stretching and strain-self amplification larger than 10 times the mean. Colours of different regions as in figure 4.24. 134
4.32 Contribution of each QR region to the mean at different locations within the recirculation zone. Measurement points at $y/C = 0.14$, 1.9 and 0.27. Colours of different regions as in figure 4.24. 134
4.33 Contribution of each QR regions on the mean at different locations within the transitional region. Measurement points are $x/C = 1.23$, 1.63, 2.18 and 3.22. Colours of different regions as in figure 4.24. 135
4.34 Variation of non-normality index k_{BC} conditioned on QR regions for the (a) recirculating and (b) transitional flow sections. Occupancy fractions of different QR regions at each measurement point where the non-normality index is $k_{BC} < 0$ (c) recirculating and (d) transitional flow. The dotted pink line corresponds to HIT values ($Re_{\zeta i} = 433$), data obtained from Keylock [2018]. 136
4.35 Contours of instantaneous (a) $\|\Omega_B\|^2$, (b) $\|S_B\|^2$, (c) $\|\Omega_C\|^2$ (note $\|\Omega_C\|^2 = \|S_C\|^2$) in the $x-y$ plane. Light green line represents the instantaneous vortical structures represented by the Q-criterion value of 2. 137
4.36 Distribution of the different components of $\langle\|S_A\|^2\rangle$ and $\langle\|\Omega_A\|^2\rangle$ for (a) and (c) along line A and (b), and (d) along line B. 138
4.37 Distribution of $\langle\|\Omega_A\|^2|^{QR=1,2,6}\rangle$ for (a), (c), (e) along line A and (b), (d), (f) along line B. 139
4.38 Distribution of $\langle\|S_A\|^2|^{QR=1,2,6}\rangle$ accross all regions for (a), (c) along line A and (b), (d) along line B. 140
4.39 Distribution of $-\langle\det(S_A)\rangle$ (top row) and $-\langle\det(S_A)|^{QR=6}\rangle$ (bottom row) for (a), (c) along line A and (b), (d) along line B. 141
4.40 Distribution of $\langle\mathrm{Tr}(\Omega_A^2 S_A)\rangle$ (top rows) and $\langle\mathrm{Tr}(\Omega_A^2 S_A)|^{QR=1,2}\rangle$ (mid and bottom rows) for (a), (c), (e) along line A and (b), (d), (f) along line B. 143
4.41 Contours of (a) $\|S_B^M\|^2$ and (b) $\|S_C^M\|^2$ in the $x-y$ plane at $z/C = -0.2$. . . . 145
4.42 Contours of (a) Δ_A^M and (b) regions of the Q_A^M-R_A^M space based on the mean flow in the $x-y$ plane at $z/C = -0.2$. 146
4.43 Distribution of the components of $\mathrm{Tr}(\langle\Omega_A^2\rangle S_A^M)$ where S_A^M, S_B^M and S_C^M are the mean strain rate fields. 146

5.1 Contours of the three components of $\langle\Omega\rangle\times\langle U\rangle$ (a) x-component (b) y-component (c) z-component. The white dotted line A goes through the recirculating flow and B through the transition. 150
5.2 Variation of the three components of $\langle\Omega\rangle \times \langle U\rangle$ (a) along line A and (b) along line B. 151
5.3 Contours of (a) $\nabla\cdot(\langle\Omega\rangle\times\langle U\rangle)$ and its components (b) $\frac{1}{2}\langle\Omega\rangle\cdot\langle\Omega\rangle$ and (c) $\frac{1}{2}\nabla^2(\langle U\rangle\cdot\langle U\rangle)$ in the $x-y$ plane at $z/C = -0.2$. The light blue isoline represents $\langle S\rangle$: $\langle S\rangle = 250$. 153
5.4 The components of $\nabla\cdot(\langle\Omega\rangle\times\langle U\rangle)$ (a) along line A and (b) along line B. 153
5.5 Contours of $\cos(\langle U\rangle, \langle\Omega\rangle)$ in the $x-y$ plane at $z/C = -0.2$. 154
5.6 Variation of $\cos(\langle U\rangle, \langle\Omega\rangle)$ (a) along line A and (b) along line B. 155

5.7 Plot of components of $\nabla \cdot \langle \omega \times u \rangle$ (equation 5.5) (a) along line A and (b) along line B. 156
5.8 Contours of $\nabla \cdot \langle \omega \times u \rangle$ and its components in the $x - y$ plane (left column); instantaneous snapshots are shown in the right column. Vortical structures are represented by the Q-criterion value of 2. 157
5.9 Contours of (a) $\mathcal{CM}_\Omega$ and (b) $\mathcal{EM}_\Omega$ in the $x - z$ at $y/C = 0.26$ (vertical position of line B). 161
5.10 Contours of(a) $\mathcal{DM}_\Omega$ and (b) $\mathcal{PM}_\Omega$ in the $x - z$ plane at $y/C = 0.26$ (vertical position of line B). 162
5.11 Vertical evolution ($y/C = 0.2 - 0.34$) of the budgets of the transport equation of $0.5\langle\Omega_i\rangle\langle\Omega_i\rangle$ measured at (a) $x/C = 0.2$, (b) $x/C = 0.5$ and (c) $x/C = 0.9$. Dashed lines correspond to components containing fluctuations. 164
5.12 Vertical evolution ($y/C = 0.2 - 0.34$) of the budgets of the transport equation of $0.5\langle\Omega_i\rangle\langle\Omega_i\rangle$ measured at (a) $x/C = 1.1$, (b) $x/C = 1.2$ and (c) $x/C = 1.3$. Dashed lines correspond to components containing fluctuations. 165
5.13 Contours of instantaneous absolute values of (a) $|u \times \omega|$, (b) $|\langle U \rangle \times \omega|$, and (c) $|u \times \langle\Omega\rangle|$ are shown, along with their alignments (b) $|\cos(u, \omega)|$, (d) $|\cos(\langle U \rangle, \omega)|$, and (f) $|\cos(u, \langle\Omega\rangle)|$. 166
5.14 Contours of (a) $\langle U \rangle \cdot u$ and (b)$|\cos(\langle U \rangle, u)|$. 167
5.15 Contours of $|\nabla \times (\langle\Omega\rangle \times \langle U \rangle)|$. The light blue isoline in (b) represents $\frac{1}{2}\langle\Omega\rangle \cdot \langle\Omega\rangle = 250$. 168
5.16 Streamwise evolution of $\langle L \cdot L \rangle$ and $\langle \nabla\alpha \cdot \nabla\alpha \rangle$ along line B. 169
5.17 Streamwise evolution of $\langle \nabla\alpha \cdot \nabla\alpha \rangle / \langle L \cdot L \rangle$ along line B. 170
5.18 Contours of (a) $\langle \nabla\alpha \cdot \nabla\alpha \rangle / \langle L \cdot L \rangle$, (b) $\langle \nabla\alpha \cdot \nabla\alpha \rangle$ and (c) $\langle L \cdot L \rangle - \langle \nabla\alpha \cdot \nabla\alpha \rangle$ in the $x - y$ plane at $z/C = -0.2$. The light blue isoline represents $\frac{1}{2}\langle\Omega \cdot \Omega\rangle = 250$. 171
5.19 Streamwise evolution (along line B) of components of $\langle L \cdot L \rangle$. 172
5.20 Streamwise evolution (along line B) of components of $\langle \nabla\alpha \cdot \nabla\alpha \rangle$. 173
5.21 Vertical evolution of terms comprising the Lamb vector $\langle L \cdot L \rangle$ and Potential term $\langle \nabla\alpha \cdot \nabla\alpha \rangle$ measured at different downstream locations: (a) $x/C = 1.2$, (b) $x/C = 1.3$, (c) $x/C = 1.4$ and (d) $x/C = 1.5$. 174
5.22 Vertical evolution of $\langle \nabla\alpha \cdot \nabla\alpha \rangle / \langle L \cdot L \rangle$ measured at different locations: (a) $x/C = 1.2$, (b) $x/C = 1.3$, (c) $x/C = 1.4$ and (d) $x/C = 1.5$. 174
5.23 Vertical evolution of components of $\langle L \cdot L \rangle$ measured at different locations: (a) $x/C = 1.2$, (b) $x/C = 1.3$, (c) $x/C = 1.4$ and (d) $x/C = 1.5$. 176
5.24 Vertical evolution of components of $\langle \nabla\alpha \cdot \nabla\alpha \rangle$ measured at different locations: (a) $x/C = 1.2$, (b) $x/C = 1.3$, (c) $x/C = 1.4$ and (d) $x/C = 1.5$. 177

List of Tables

1.1 Summary of the types of flow conditions. 51

4.1 Occupancy fractions F(I) of the 6 QR regions for $Re_{\zeta i} = 433$ (data obtained from Li et al. [2008] as cited by Keylock [2018]). 125

Chapter 1

Introduction

1.1 Motivation

Fully developed turbulence is characterised by chaotic motion in space and time and involves a wide range of scales. Within this chaotic motion however, turbulence exhibits elements of order. This order as quoted by She et al. [1991] emerges through the organization by local self-interaction. In engineering applications, the larger scales, which are comparable to the size of the flow domain, play a crucial role. For instance, in the case of turbulent flow over an aircraft wing, the larger scales of turbulence have a significant impact on the overall aerodynamic performance of the wing. These larger scales are responsible for carrying most mass, momentum, and heat, making them essential in the design and operation of various devices like gas or wind turbines, heat exchangers, etc. On the other hand, the smaller scales of turbulence, such as the inertial and dissipative scales, receive energy from the large scales and are of great interest from a fundamental perspective. These scales can exhibit universal properties regardless of the specific flow configuration or forcing mechanism. One of the assumptions of the Kolmogorov universal equilibrium [Hunt et al., 1991, Pope, 2000] is the wide separation of scales for large Reynolds numbers. Given that these small-scale motions have small time scales (high-frequency motions), it can be assumed that they are statistically uncorrelated to the slower and larger-scale motions, as well as the time-averaged flow.

Few practically relevant flows are free from recirculation zones. Recirculation is often very extensive, encompassing a major proportion of the domain and determines the operational characteristics of devices, such as the lift and drag of an aerofoil. Understanding the intricacies of separated flows is essential for optimizing aircraft performance at high angles of attack. Finite

(a) (b)



Figure 1.1: (a) Visualization of wingtip vortices during flight (image obtained from USCG [2012]) and (b) Illustration of future UAM infrastructure (image obtained from NASA [2018]).

wings, which have specific span sizes, often face intricate aerodynamic characteristics resulting from the interaction of different vortical and flow patterns. Given its technological significance, numerous research efforts in the areas of flow control, aircraft design, and optimization have been dedicated to separated aerodynamic flows. To fully comprehend the flow characteristics in the separated regions, particularly during the transition process of the leading edge shear layer and the complex system of streamwise vortices at the tip (refer to figure 1.1 (a) for a visual representation), better analysis of the evolution of flow patterns is needed.

In the coming years, Urban Air Mobility (UAM) aims to alleviate traffic congestion, reduce travel time, and provide a direct and convenient mode of transportation in urban environments. This innovative transport will serve as a modern network operating within urban and nearby areas. It will use small electric vertical takeoff and landing (eVTOL) vehicles, commonly known as air taxis or flying cars, to facilitate a more efficient and sustainable transport of people and goods within cities (refer to Figure 1.1 (b) for an illustrative example). The high volume of these vehicles operating in close proximity could result in heightened congestion in the airspace which brings an additional level of complexity to airspace management [Wu and Zhang, 2021]. The potential hazards that could lead to a loss of control and compromise safety such as heightened congestion, interactions with vehicle wake vortices and the complexity of airspace management [Young et al., 2020], emphasize the need for a more detailled and comprehensive understanding of separated flows with particular focus on their spatial development.

The purpose of this thesis is to gain insights into the vortical and shear flow patterns that develop in separated aerodynamic flows. By utilizing High Performance Computing (HPC) to achieve the necessary level of accuracy in small-scale resolution, it is envisaged that the findings from this research will improve our understanding of turbulence modelling, especially in complex geometric environments, and contribute to the acceleration of industrial processes as well as to the overall improvement of energy efficiency by enabling improved active control techniques.

1.2 Streamwise vortices in finite wings

Lifting surfaces with finite aspect ratio produce persistent, stable and coherent tip vortices [Spalart, 1998]. These vortices are ubiquitous in transport and power generation applications, for example aircraft wings, maritime propellers, helicopter rotors, wind turbines, compressor and turbine blades etc. It is well known that wingtip vortices reduce the lift capabilities and increase drag [Milne-Thomson, 1958]. Furthermore, they can persist downstream of an aircraft for many chord lengths before they dissipate, affecting traffic control operations and preventing the application of optimal scheduling procedures [Spalart, 1998, Rossow, 1999].

The flow physics of the near wingtip field is very complex due to the highly turbulent and three-dimensional nature comprising multiple cross-flows [Craft et al., 2006]. More specifically, wingtip flows involve roll-up of vortex sheets, shear layer instabilities and boundary layer separation [Green, 2012]. Traditional turbulence models (that employ the eddy-viscosity concept) cannot capture the effect of rotation that characterizes strongly vortical flows, and this has led to over-prediction of turbulence production in wings with rounded tip profiles [Churchfield and Blaisdell, 2009]. Similarly, for Large Eddy Simulation (LES), the under-resolution of the boundary layer has been identified as one of the key causes for the over-prediction and fast decay rates of wing tip vortices [Wood-Bowyer et al., 2021].

On the other hand, experimental works on wingtip flows encounter the problem of vortex meandering, which can distort measurements if not detected and filtered out [Devenport et al., 1996]. Nevertheless, the importance of this flow has led to many insightful and detailed experimental and numerical studies that characterise the mean velocity and vorticity dynamics in a

wide range of aerofoil geometries and angles of attack [Giuni, 2013, Birch et al., 2003, Bailey et al., 2006, Katz and Galdo, 1989]. Chow et al. [1997] performed a very detailed experimental study of time-average quantities, that include turbulence measurements in the near-field wingtip vortex formation region; this work has been used as a benchmark for a large number of turbulence modeling studies. Related flow settings, such as the impingement of vortices on surfaces, the study of unsteady pitching behaviour and vortex breakdown have also been analysed [Wood-Bowyer et al., 2021, Novak and Sarpkaya, 2000, Visbal, 2017, Garmann and Visbal, 2015].

Several works have studied wingtip vortices in the far-field with a special focus on their persistence [Craft et al., 2006, Jacquin and Pantano, 2002]. Zeman [1995] linked the weak decay to the fact that in the vortex core the velocity has solid-body rotation profile, resulting in nearly zero turbulence production, effectively suppressing the Reynolds shear stress generation. Recently, the instability characteristics of vortex wandering were studied experimentally and using linear stability analysis under different flow conditions [Cheng et al., 2019]. The effect of active control, such as fluidic actuation, in the development of wingtip vortices in the presence of wandering has also been investigated [Dghim et al., 2020].

Three-dimensional flow around low-aspect-ratio finite wings at low Reynolds number (laminar flow) have been investigated [Taira and Colonius, 2009a,b, Zhang et al., 2020b], focusing mainly on post-stall conditions and the effect of different sweep angles [Zhang et al., 2020a]. High-fidelity simulations at higher Reynolds numbers in the presence of turbulence have also been made [Uzun and Hussaini, 2010, Lombard et al., 2016, Visbal, 2017]. In these simulations, shear layers and separated boundary layers have been reported as the leading sources of turbulence in the tip-flow [Jiang et al., 2008]. The study of Garmann and Visbal [2017] reports both instantaneous and time-average flows, and shows that the formation, separation, and entrainment of shear-layer substructures within the tip vortex feeding sheet are stationary whereas interactions with the wake are unsteady. Smith and Ventikos [2021] conducted a DNS study, and presented details related to the roll-up process and the behaviour of mean axial velocity and mean pressure profiles at relatively low angles of attack.

1.3 Separated shear flows and recirculating bubbles over wings

The generation of aerodynamic force and the resulting creation of lift can be attributed to the curvature of the aerofoil [Milne-Thomson, 1958]. When an aerofoil is symmetric and is at an angle of attack greater than zero, the points of lowest pressure are found at the leading edge on the suction side. If the angle of attack is increased, the curvature of the leading-edge streamline and the amount of suction increase. This process continues until a maximum angle is reached at which the flow is subject to a strong adverse pressure gradient which causes it to separate. In separated flows, vorticity is carried away from the surface through convection, leading to the formation of vortex sheets, vortices [Hirschel et al., 2020] or a free shear layer [Wu et al., 2015]. At the locations of separation on the body surface, the boundary layer equations are not applicable [Hirschel et al., 2020]. A shear layer is a flow region with a difference in mean velocity between adjacent fluid layers. This difference leads to a gradient in the velocity field across the thickness of the shear layer [Batchelor, 1967].

As flow separates from the suction side, a recirculating bubble forms between the shear layer and the surface. This shear layer is susceptible to disturbances and transition to turbulence occurs due to Kelvin-Helmholtz instability. This initial stage of the transition process has been reported extensively [He et al., 2017, Zhang et al., 2015, Shan et al., 2005]. When the turbulent shear layer over an aerofoil reattaches back to the surface, it forms a closed bubble. On the other hand, when the shear layer does not reattach on the surface, it forms an open bubble which is common in wings at high angles of attack and the flow is said to be massively separated. A fully stalled flow over an aerofoil is a problem of great interest particularly in the design of turbo-machines components [Tucker, 2011] and UAVs that operate at low Reynolds numbers. This bubble is referred to in the literature as Laminar Separation Bubble (LSB) because the bubble forms near the aerofoil's leading edge, where the flow remains fully laminar (at least at moderate Reynolds numbers). However, as the separated shear layer transitions and becomes turbulent, the flow can reattach at fully turbulent conditions.

A separation bubble compromises the aerodynamic efficiency, leading to a decrease in the

lift, unfavorable changes in moment, and an increase in drag [Anderson, 1991]. The aerofoil shape and the external disturbance environment can determine the location where transition to turbulence occurs [Sandham, 2008] and thus they can influence the overall performance. Gaster [1967] found that the size and behaviour of the bubble can be influenced by both the Reynolds number of the separated shear layer and the pressure gradient.

The presence of wingtip vortices prevents flow separation near the tip and this induces complex three-dimensional flow patterns in the suction side. Previous studies on finite wings have mainly concentrated on the surface patterns of three-dimensional flows [Tobak and Peake, 1982, Délery, 2013, 2001] whereas the exploration of the three-dimensional flow fields of the separated shear layer and recirculating flows on finite wings is still limited.

In a separated flow, the time-average strain rate $\langle S_{ij} \rangle$ undergoes rapid change due to the curved path of the streamlines as they pass around the recirculating bubble. When it comes to turbulence models that use the Bousinesq approximation, turbulence adjusts to the change in the mean strain rate in a time scale unrelated to $\langle S_{ij} \rangle$ [Wilcox et al., 1998]. Rotta [1962], as cited in [Wilcox et al., 1998], indicates that when a boundary layer is disturbed, it requires a distance equivalent to ten times the thickness of the boundary layer, downstream, to return to a state of equilibrium. This would make an approximation of a separated aerofoil using eddy viscosity models very challenging. LES, an economical alternative to DNS, proves to be effective in situations where separation occurs in sharp edges and when the principal features of interest are associated with shear layers that are remote from walls and are not affected by the viscous wall processes [Leschziner, 2006].

1.4 Anisotropic and inhomogeneous turbulence

In this section, we review of the work of A.N. Kolmogorov, who laid the foundation for the study of turbulent flows and provided insights into the role of small-scales and their statistical characteristics. Subsequently, we will discuss in more detail the dynamics of small-scales, which involve intricate interactions and nonlinear processes. We will also describe the Schur decomposition, which is an important theorem used in the analysis of the statistics in this thesis. Finally, we will conclude with a review of the existing literature, specifically emphasizing gaps

in the study of inhomogeneous and anisotropic flows.

1.4.1 K41 and the scales of turbulence

The Navier Stokes Equations (NSE) for incompressible flows take the form,

$$\frac{\partial U^*}{\partial t^*} + U^* \cdot \nabla U^* = -\frac{1}{\rho}\nabla P^* + \nu \nabla^2 U^* \,, \tag{1.1}$$

and

$$\nabla \cdot U^* = 0 \,, \tag{1.2}$$

where the time t^*, velocity ${U_i}^*$, distance x^* and pressure P^* are the dimensional variables. The variables are non-dimensionalized as follows: $t = t^* \frac{C}{U_\infty}$, $x = \frac{x^*}{C}$, $U_i = \frac{U^*}{U_\infty}$ and $P = \frac{P^*}{\rho {U_\infty}^2}$. The fluid is assumed incompressible, therefore density ρ is constant. Any new terms, including higher-order derivatives that will be introduced later derived from these variables can be appropriately scaled.

We use the Reynolds decomposition to express all variables in terms of time-average and fluctuating quantities, i.e. $U = \langle U \rangle + u$, $P = \langle P \rangle + p$. In this section, we assume that the mean-field vanishes i.e. $\langle U \rangle = 0$. For isotropic turbulence, statistics are independent of orientation, thus the normal Reynolds stresses are equal, $\langle u_1 u_1 \rangle = \langle u_2 u_2 \rangle = \langle u_3 u_3 \rangle$ and the shear stresses are zero, $\langle u_i u_j \rangle = 0$ for $i \neq j$ [Taylor, 1935, Stanisic, 2012].

On the other hand, anisotropy is caused by the presence of mean shear, buoyancy, magnetic fields or the presence of solid boundaries [Davidson, 2015]. Homogeneity implies that statistics in a turbulent flow are independent of spatial location. In an inhomogeneous flow, turbulent fluctuations have different statistics in different regions of the flow.

In this subsection, we review the groundbreaking work of A.N. Kolmogorov on the understanding of turbulent flows based on a statistical description. The fundamental building block in his work was the well-known energy cascade [Richardson, 1922], which he emphasized [Kolmogorov, 1962]. The turbulent cascade represents in a phenomenological way the transfer of turbulent kinetic energy from larger to smaller scales. Large eddies break up into smaller eddies through a nonlinear, inviscid, process. This fragmentation continues until the size of the

eddies reaches a point where viscosity starts to play a significant role. As the energy cascade proceeds it is expected that the small-scale velocity variations will gradually forget or become independent of the larger-scale fluctuations. A.N. Kolmogorov published a number of papers [Kolmogorov, 1941a, 1991a, 1941b] that established a strong foundation for the aforementioned phenomenological description[1]. These papers became widely known as "the 1941 Kolmogorov theory" or K41 due to their significant contribution and impact [Eckert, 2019, Davidson et al., 2011, Vulpiani and Livi, 2003].

As his first hypothesis, A.N. Kolmogorov introduced the notion of "local isotropy", which postulates that turbulence at small-scales becomes independent from the larger scales and can thus attains statistical homogeneity and isotropy. To achieve this, it is necessary for the Reynolds number $Re = \frac{Ul}{\nu}$, defined using a characteristic velocity U and the integral length scale l, to be very high i.e. implying a large separation of scales. Kolmogorov's second and third hypotheses rely on the principles of similarity. The first similarity hypothesis indicates that in turbulent flows with high Reynolds numbers, the statistics of the small-scales have a universal form that is uniquely determined by viscosity and dissipation. The second similarity hypothesis states that in turbulent flows with high Reynolds numbers, the statistical properties of motions with scales smaller than the integral length scale and larger than the dissipative scales have a consistent and universal pattern that is solely determined by energy transfer rate and not influenced by viscosity. The theory has been successful in a great variety of flows where the assumption of isotropy or inhomogeneity does not hold such as such as boundary layers, wakes, grids, ducts, pipes, jets, oceans and others [Saddoughi and Veeravalli, 1994, Davidson, 2015].

The continuous range of scales in turbulence makes the spectral representation of energy a convenient tool for analysis. A Fourier decomposition is employed, where the wavenumber vector κ and the eddy size l_e exhibit the following correspondence, $\kappa \sim \frac{\pi}{l_e}$ [Davidson, 2015]. $E(\kappa)\, d\kappa$ represents the amount of kinetic energy that is present within a specific range of

[1]Even though the theory is often described as purely phenomenological, the outcome came after half a year of studying empirical data [Vulpiani and Livi, 2003], as cited in [Eckert, 2019]. More specifically, A.N. Kolmogorov studied measurements of wind tunnel turbulence carried out by Dryden et al. [1937] which included intensity and decay rates.

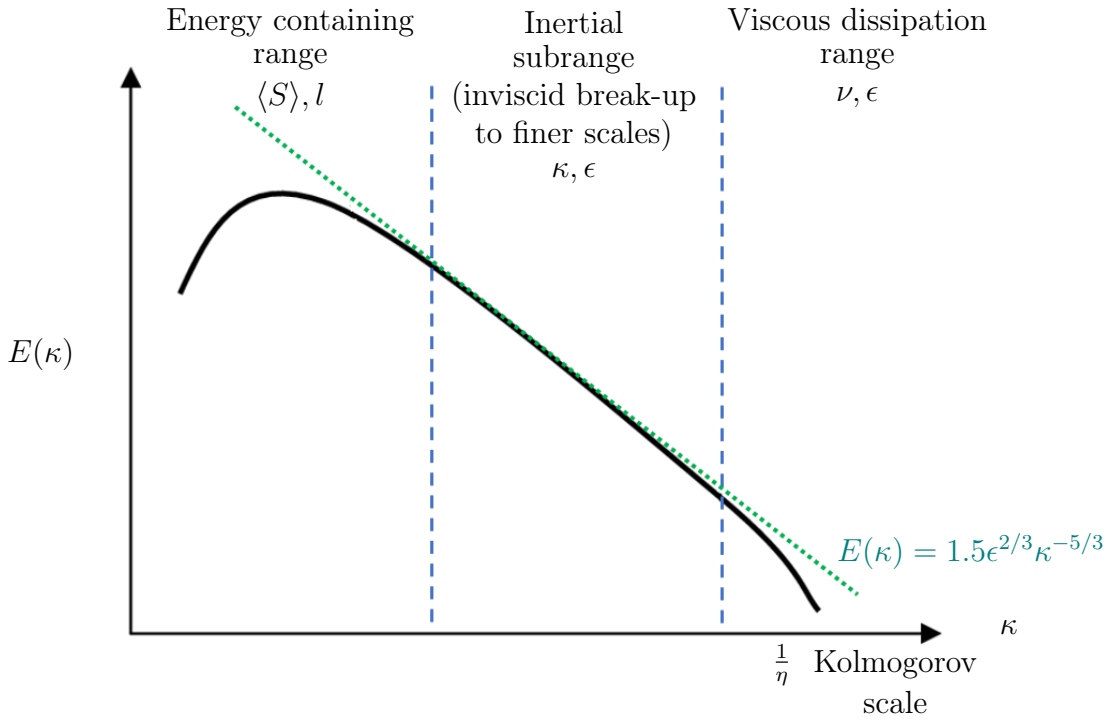


Figure 1.2: Sketch of energy spectrum and different regions.

wavenumbers κ and $\kappa + d\kappa$, therefore

$$k = \int_0^\infty E(\kappa)\, d\kappa\,. \tag{1.3}$$

Figure 1.2 shows a schematic representation of $E(\kappa)$ and the different regions of the spectrum. The wavenumber κ is a measure of the size of the eddy, with larger wavenumbers corresponding to smaller eddies. The integral scale (l) represents the characteristic length scale of the largest energy-containing eddies in a turbulent flow. It is an important parameter in turbulence modelling and is often used to normalize the energy spectrum function. The Taylor microscale, denoted as ζ, is a characteristic length scale within the inertial range, defined as $\langle(\frac{\partial u_1}{\partial x_1})^2\rangle = \frac{\langle {u_1}^2\rangle}{\zeta^2}$ [Tennekes et al., 1972]. In comparison to the dissipative scales, Taylor microscales are larger ($\zeta \gg \eta$), but in relation to the large scales, they are still much smaller ($l \gg \zeta$); this is a consequence of the large Re number assumed. The relationship between these two scales can be expressed as $\frac{\zeta}{l} \sim \sqrt{15}(\frac{ul}{\nu})^{-1/2}$ [Davidson, 2015, Sreenivasan and Antonia, 1997]. It is important to note that the Taylor scale does not have a clear physical interpretation [Pope, 2000]. The interaction of eddies within the inertial subrange is not affected by

viscosity. The transfer of energy across this range is called energy cascade and it is an inviscid process. One of the assumptions of Kolmogorov's universal equilibrium theory (second similarity hypothesis) is the presence of a wide separation of scales. This enables the inertial range to be independent of the energy-containing eddies and not depend on viscosity. This means that the inertial range $\frac{1}{l} \ll \kappa \ll \frac{1}{\eta}$ depends solely on κ and ϵ thus for dimensional consistency, we have the following form [Friedrich, 2021]

$$E(\kappa) = C_k \epsilon^{2/3} \kappa^{-5/3}\,, \tag{1.4}$$

where ϵ is the dissipation rate, equal to the energy passed down the scales, and C_k is the Kolmogorov constant. This is the well-known $-5/3$ law, which has been extremely successful even in flow cases where the Kolmogorov assumptions are not formally valid. It is also employed in DNS and LES, where the replication of this law is one of the criteria that provide confidence in the reliability of the results [Wilcox et al., 1998]. In the viscous dissipation range, the Kolmogorov length scale, $\eta = \left(\frac{\nu^3}{\epsilon}\right)^{1/4}$, is the smallest scale within a turbulent flow. Based on Kolmogorov's first similarity hypothesis, the behavior of the smallest scales in turbulent flows is influenced by two key factors: the rate at which energy is dissipated into heat (expressed as $\epsilon = 2\nu\langle s_{ij} s_{ij}\rangle$) and the kinematic viscosity ν. Using ν and ϵ, the time scale $\tau = \left(\frac{\nu}{\epsilon}\right)^{1/2}$ and the velocity scale $\upsilon = (\nu\epsilon)^{1/4}$ can be computed. The Reynolds number based on the Kolmogorov scales is then unity, $Re = \frac{\eta\upsilon}{\nu} = 1$. This is consistent with the observation that the cascade continues towards progressively smaller scales until the Reynolds number is small enough for dissipation to occur.

The definition of large or small-scales is not precise. Small-scales can encompass the dissipative range, as well as the inertial range [Sreenivasan and Antonia, 1997, Davidson, 2015]. In a more unambiguous manner, small-scales are related to the field of velocity derivatives [Tsinober, 2009]. Large scales are approximately comparable to the thickness of a shear layer when are produced by the mean shear [Durbin and Reif, 2011]. These scales generally encompass the majority of the energy generation and have the greatest influence on the transfer of momentum, mass, and heat [Sreenivasan and Antonia, 1997]. Mean flows represent the time-average and smoothed-out fluid motion. They can have a size comparable to shear layer thickness, and we

can consider them as large scales.

1.4.2 Small-scale dynamics

In this subsection, we cover the mechanisms behind the energy cascade in the physical space, specifically the dynamics of small-scales. The velocity gradient tensor (VGT), defined as $A_{ij} = \frac{\partial u_i}{\partial x_j}$, provides a detailed description of the small-scale behaviour and plays a pivotal role in studying and analyzing turbulent motion [Sreenivasan and Antonia, 1997]. A standard decomposition of VGT is

$$A_{ij} = s_{ij} + W_{ij} \,. \tag{1.5}$$

The symmetric component, s_{ij} known as the rate-of-strain tensor, describes the local deformation rates of fluid elements and determines the rate at which kinetic energy is dissipated. The viscosity of a fluid measures its resistance to deformation caused by the rate of strain. As a result of its resistance to deformation kinetic energy is turned into heat. The antisymmetric component of the VGT, is known as the rate-of-rotation tensor, $W_{ij} = -\frac{1}{2}\epsilon_{ijk}\omega_k$ where ω_k are the components of the vorticity vector and ϵ_{ijk} is the Levi-Civita tensor. It provides information about vorticity which measures the rotation rate of a fluid particle at a specific location.

The transport equations for enstophy, $\omega_i\omega_i$, and strain-squared, $s_{ij}s_{ij}$ can be directly derived from the Navier-Stokes equations and take the form [Tsinober, 2009],

$$\frac{1}{2}\frac{\partial \omega_i\omega_i}{\partial t} = \omega_i\omega_j s_{ij} + \nu\omega_i\nabla^2\omega_i \tag{1.6}$$

$$\frac{1}{2}\frac{\partial s_{ij}s_{ij}}{\partial t} = -s_{ij}s_{jk}s_{ki} - \frac{1}{4}\omega_i\omega_j s_{ij} - s_{ij}\frac{\partial^2 p}{\partial x_i \partial x_j} + \nu s_{ij}\nabla^2 s_{ij} \,. \tag{1.7}$$

In equations 1.6 and 1.7 enstrophy production via vortex stretching $\omega_i\omega_j s_{ij}$ and strain generation via self-amplification $-s_{ij}s_{jk}s_{ki}$ play a significant role in the dynamics of turbulence. The dynamical equation for strain squared 1.7 is the most complex of the two; in addition to self-amplification and viscous dissipation, strain interacts with the vorticity field and is subject

to the non-local action due to the pressure Hessian. In Appendix A the transport equation of $\frac{1}{2}\frac{\partial\langle s_{ij}s_{ij}\rangle}{\partial t}$ is derived directly from the NSE for inhomogeneous and anisotropic flows with non-zero mean flow.

The importance of using the VGT lies in its sensitivity to the non-Gaussian characteristics of turbulence which is related to the property of internal intermittency [Tsinober, 2009]. Internal intermittency refers to the temporal or spatial concentration (spottiness) of fine-scale structures in turbulent flows. This differs from external intermittency, which occurs when the flow field includes randomly varying turbulent and non-turbulent patches, along with the presence of an interface for example in transitional flows [Townsend, 1949, Kollmann, 2019, Gauding et al., 2021]. In mathematical terms, external intermittency is usually represented using an indicator function that takes the value of one in turbulent areas and zero in non-turbulent (laminar) areas. Both external and internal intermittency can be viewed as random processes [Dinesh et al., 2012]. Another crucial aspect concerning the VGT is its role in determining critical points based on the information it provides. This theory enables the precise definition of local topological properties, as it will be seen later in this section [Perry and Chong, 1987].

Vortex stretching appears when a vortex, which is a compact region of vorticity, is strained by the flow in an extensional sense along the rotational axis. This leads to a reduced cross section and increase of the rotational speed due to conservation of angular momentum. The opposite can also happen: in vortex compression, the cross section expands and the rotation rate decreases. As the process of vortex stretching takes place, smaller vortices with higher rotational speeds are formed, which is in agreement with the energy cartoon of Richardson [Richardson, 1922]. Eventually, this action alters the strain field as we see in figure 1.3 which shows a sketch of the interactions between the different processes. Strain self-amplification occurs when regions with high strain rate naturally undergo a process of thinning.

In the case of incompressible flow, the volume of a fluid particle remains constant. This means that if a fluid particle gets stretched in one direction, it will be compressed in the other. The strain rate tensor is symmetric, thus its eigenvalues λ_1, λ_2, and λ_3, are real numbers. The

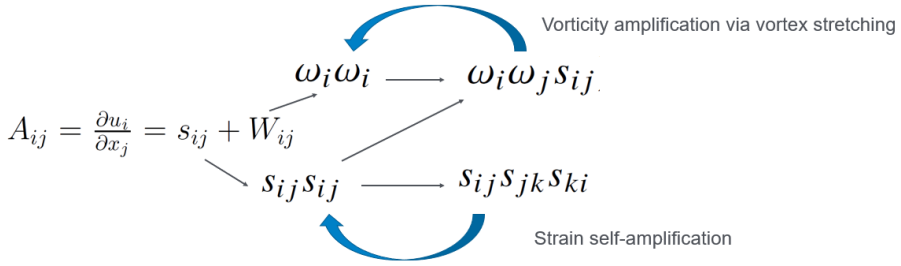


Figure 1.3: Illustration of the interaction between the strain self-amplification and vortex stretching process (adapted from Sagaut and Cambon [2008]).

corresponding eigenvectors are orthogonal. In the case of incompressible flows,

$$\lambda_1 + \lambda_2 + \lambda_3 = 0\,. \tag{1.8}$$

The largest eigenvalue, λ_1 is always extensional ($\lambda_1 > 0$) and the corresponding eigenvector, represents the direction of maximum extension or stretching. The smallest eigenvalue, $\lambda_3 < 0$ and the corresponding eigenvector represents the direction of maximum compression. The intermediate eigenvalue, λ_2, may be positive or negative. When $\lambda_2 > 0$ there are two directions of stretching and one direction of compressing. As a result, it favors the formation of disc-like structures. On the other hand, if $\lambda_2 < 0$, it results in two directions of compression and one direction of stretching. This leads to the formation of flow structures that are more tube-like on average. Betchov [1956] postulated that disc-like structures would be more common in turbulence. However, it is interesting to note that high-amplitude vorticity structures are actually more tube-like in nature as evidence of elongated, high-intensity patterns within the vorticity field were found [Siggia, 1981, Davidson, 2015]. It has been reported that in moderate-amplitude vorticity regions disc- and ribbon-like structures dominate [She et al., 1991].

The symmetric properties of s_{ij} result in

$$-s_{ij}s_{jk}s_{ki} = -(\lambda_1^3 + \lambda_2^3 + \lambda_3^3)\,. \tag{1.9}$$

Betchov [1956] discovered the kinematic equality

$$\langle \omega_i\omega_j s_{ij} \rangle = -\frac{3}{4}\langle s_{ij}s_{jk}s_{ki} \rangle\,. \tag{1.10}$$

In this context, the tendency towards disc-like structures results in a positive value of the production term $-\frac{3}{4}\langle s_{ij}s_{jk}s_{ki}\rangle$, ensuring a positive enstrophy production (see equation 1.6). Moreover, from 1.7, it is worth noting that enstrophy acts as a sink term in the generation of strain. This observation has led some people to believe that vortex stretching, which prevents energy from dissipating in the flow, also acts as a barrier to the energy cascade. However, it is important to note that Vortex stretching is not the dynamic cause of energy dissipation. While it does play a role in the transfer of energy, it simultaneously limits the rate of dissipation [Carbone and Bragg, 2020].

Taking the spatial gradient of the NSE 1.1 results in the transport equation of the VGT,

$$\frac{\partial A}{\partial t} + u \cdot \nabla A = -A^2 - H + \nu \nabla^2 A \,. \tag{1.11}$$

A is advected along with the velocity field, and it undergoes a process of self-amplification. H is the pressure Hessian term. Perry and Chong [1987] and Chong et al. [1990] conducted an analysis on the topological properties of local streamlines by employing critical point analysis. They examined the invariants of A to understand the characteristics of these streamlines. This analysis has proven to be a useful way to study some of the local flow properties in the so called QR plane [Cantwell, 1993, Ooi et al., 1999, Tsinober, 2009]. The characteristic equation containing the invariants of the VGT tensor is obtained by applying the Cayley-Hamilton theorem,

$$\lambda^3 + P_A\lambda^2 + Q_A\lambda + R_A = 0 \,. \tag{1.12}$$

The three invariants are

$$P_A = \mathrm{Tr}(A) = \lambda_1 + \lambda_2 + \lambda_3 \tag{1.13}$$

$$Q_A = \frac{1}{4}(\omega_i\omega_i - 2s_{ij}s_{ij}) \tag{1.14}$$

$$R_A = -\frac{1}{3}(s_{ij}s_{jk}s_{ki} + \frac{3}{4}\omega_i\omega_j s_{ij}) \,. \tag{1.15}$$

For incompressible flows, $P = 0$. Researchers have discovered a consistent and distinctive tear-drop shape in the joint probability density function (pdf) of Q and R when examining various types of turbulent flows. This finding suggests that the tear-drop shape is a universal

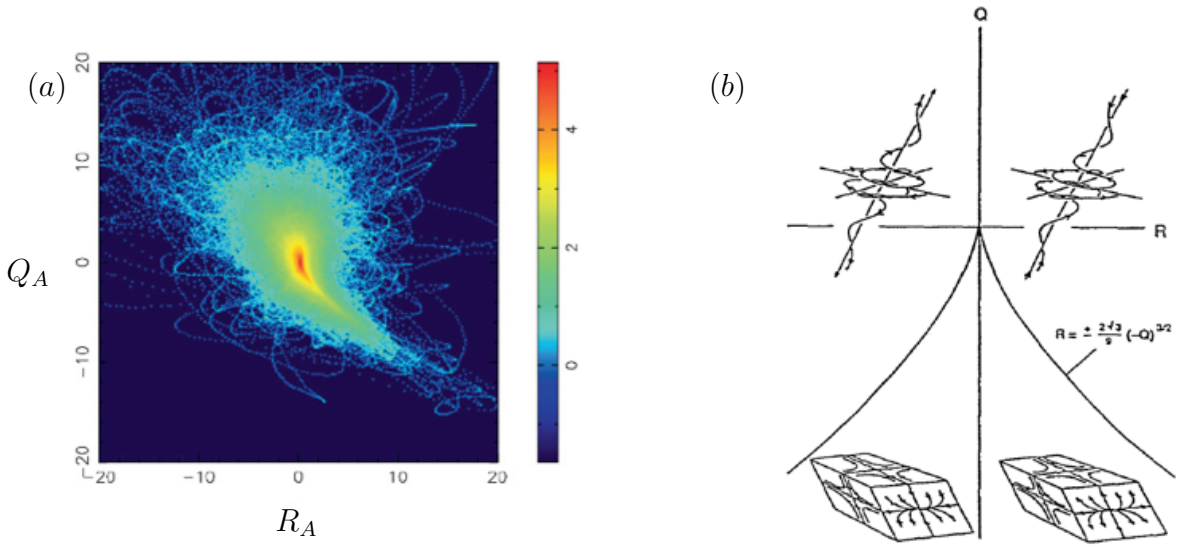


Figure 1.4: (a) Example of a joint pdf of Q_A and R_A invariants in the form of a teardrop [Galanti and Tsinober, 2004, Tsinober, 2009] and (b) three-dimensional topologies in the $Q_A R_A$ plane obtained from Soria et al. [1994], Perry and Chong [1994].

characteristic of the small-scale motion in the sense that it is an inherent feature of turbulence itself regardless of where it originates [Tsinober, 2009, Meneveau, 2011, Chacin and Cantwell, 2000].

Under incompressiblity conditions, the VGT can be divided up into six sectors according to the signs of Q_A, R_A and the discriminant $\Delta_A = Q_A^3 + \frac{27}{4}R_A^2$. The features of this invariant map and the invariants themselves have been studied in great detail, see [Kerr, 1985, Ashurst et al., 1987, Tsinober, 2009, Buxton and Ganapathisubramani, 2010] for further information. Δ_A is the discriminant that separates between purely real eigenvalues from a complex conjugate pair. More specifically, for $\Delta_A < 0$ all eigenvalues are real, for $\Delta_A > 0$ there is one real and two complex eigenvalues (that come in a conjugate pair). The Vieillefosse tail [Vieillefosse, 1984] (figure 1.4(a) bottom right quadrant) refers to an elongated accumulation of points located near where $\Delta_A = 0$ (figure 1.4(b) bottom right quadrant). In this quadrant, the preference for positive values of R_A is associated with the dominant presence of disc-like structures in the flow. This preference directly impacts the sign and magnitude of $-s_{ij}s_{jk}s_{ki}$, as discussed earlier, and leads to lower values of $\omega_i\omega_j s_{ij}$ due to the strain-dominated region in which it operates ($Q_A < 0$).

1.4.3 Studies on small-scale dynamics

In this subsection, we examine the existing research on the analysis of small-scale dynamics in turbulent flows with particular attention to inhomogeneous and anisotropic flows. The literature in this area is vast and only a few, relatively recent, studies will be presented.

Laizet et al. [2015] indicated that in order to accurately replicate the strain rate and rotation tensors, it is crucial to have a spatial resolution finer than $\Delta x = 2\eta$. This is one of the reasons for the selection of DNS as a research tool in this work. It is important to emphasize the pioneering work conducted by Soria et al. [1994], which utilized DNS to investigate an incompressible mixing layer. This study involved computing all nine partial derivatives of the velocity field at each grid point within the flow and analyzing various invariants and associated quantities derived from the velocity gradient tensor. Paul et al. [2017], employing DNS, conducted an investigation into the dynamics of the VGT for a spatially developing flow generated by a single square element of a fractal square grid at low Taylor-based Reynolds numbers (in the range of 30 to 40). Their study resulted in the observation of a teardrop-shaped QR distribution and the alignment of the vorticity vector and intermediate eigenvector in the region of decay. Furthermore, in the irrotational regions near the centerline of the grid element, it was noted that the pressure Hessian term, rather than the strain self-amplification, is responsible for the generation of strain. Hao et al. [2021] used DNS to analyze the spatial development of a dual-plane jet flow. The pdfs of the alignment between the vorticity vector and the stretching eigenvector exhibited a relatively constant distribution across various locations whereas the alignment with the intermediate eigenvector becomes increasingly pronounced as the flow progresses downstream and the orthogonality with the compressive eigenvector becomes more prominent at distant locations. Bechlars and Sandberg [2017a], using DNS, conducted a study on the relationship between strain and rotation in a boundary layer. They discovered that the strain rate and rotation rate exhibit gradual changes in the outer-layer, while the contracting vortical structures peak in the near-wall region. Wu et al. [2015] conducted a study on the effect of pressure gradient on the development of turbulent structures in a weakly compressible flow over an aerofoil and the evolution equations of Q and R at different positions along the suction side of the aerofoil's chord were analysed. It was found that both the wall and the

average adverse pressure gradient hinder the vortical stretching characteristics of the flow.

The subgrid-scale (SGS) stress tensor, which is is a symmetric tensor that represents the effects of small-scale fluid motions that cannot be resolved on a computational mesh in LES, has been modeled using the velocity gradient tensor [Lund and Novikov, 1993, Nicoud and Ducros, 1999, Zhou et al., 2019] and more recently with the aid of the Schur decomposition [Yu and Lu, 2020, Yu et al., 2021]. Traditionally, the SGS stresses are modelled using the filtered strain rate tensor [Chacin and Cantwell, 2000]. Yu and Lu [2020] analysed the filtered VGT in compressible mixing layers and identified the normal effect as the primary factor influencing compressibility, whereas the behaviour of SGS energy dissipation is primarily linked to the non-normal effect. In addition, a SGS model incorporating the non-local effect was proposed to improve the accuracy of predicting SGS energy dissipation.

1.4.4 Schur decomposition of the VGT

Recently, the complex form of the Schur decomposition (see Appendix B for more details) was proposed for the VGT [Keylock, 2018]. This decomposition splits the VGT into two parts: a normal part and a non-normal part. The normal part is associated with the eigenvalues of the VGT, acts locally and is connected to the dynamics represented by the restricted Euler equation. On the other hand, the non-normal part is responsible for the non-local dynamics of the flow, such as the deviatoric part of the pressure Hessian, and baroclinic effects (which involve interactions between temperature and pressure gradients) in the case of compressible flows [Yu et al., 2021]. Beaumard et al. [2019] conducted a study on the characteristics of the velocity gradient tensor on various types of flows, including a near-wake, two axisymmetric jets, and a planar mixing layer. They noted that the impact of non-normality on the dynamics of the system is more significant than what is typically observed in HIT attributing this to the role of the pressure Hessian. Yu et al. [2021] determined that the non-normal component has a substantial impact on the behaviour of the VGT in wall-bounded compressible turbulent flows where non-normal effects influence both enstrophy and dissipation. Keylock [2022] studied the connection between the dynamics of VGT and ejection-sweep occurrences in a boundary layer of channel flow. The study revealed that the sweeps demonstrated unique characteristics when

compared to the other quadrants or the overall flow. Specifically, the non-normal terms above the viscous sub-layer had a significantly diminished impact on the dynamics of the sweeps.

1.5 Decompositions of the Velocity Gradient Tensor

For clarity, we present again the Navier-Stokes equations (equations 1.1 and 1.2) in the context of incompressible flow, involving only fluctuating values. These equations can be expressed as

$$\frac{\partial u}{\partial t} + u \cdot \nabla u = -\frac{1}{\rho}\nabla p + \nu \nabla^2 u \tag{1.16}$$

$$\nabla \cdot u = 0\,. \tag{1.17}$$

The transport equation of the Velocity Gradient Tensor (VGT), defined as $A_{ij} = \frac{\partial u_i}{\partial x_j}$, can be derived directly from equation 1.16 (see Cantwell [1993])

$$\frac{\partial A}{\partial t} + u \cdot \nabla A = -A^2 - H + \nu \nabla^2 A\,, \tag{1.18}$$

where $H_{ij} = \frac{\partial^2 p}{\partial x_i \partial x_j}$ is the pressure Hessian tensor. For incompressible flow, H_{ij} is decomposed into two parts: an isotropic component and a deviatoric part,

$$H_{ij} = \frac{\mathrm{Tr}(H)}{3}\delta_{ij} + H_{ij}^{dev}\,, \tag{1.19}$$

where Tr is the trace operator (sum of diagonal elements). The deviatoric part H_{ij}^{dev} describes the influence of non-local effects through the pressure field. The characteristic equation of A is

$$\lambda_i^3 + P_A \lambda_i^2 + Q_A \lambda_i + R_A = 0\,, \tag{1.20}$$

where λ_i are the tensor eigenvalues and the tensor invariants P_A, Q_A, R_A can equivalently be defined as (in accordance with the definitions in section 1.4.2)

$$P_A = \mathrm{Tr}(A) = \lambda_1 + \lambda_2 + \lambda_3 = 0\,, \tag{1.21}$$

this is due to incompressibility, as indicated in equation 1.2,

$$Q_A = -\frac{1}{2}\mathrm{Tr}(A^2) = \lambda_1\lambda_2 + \lambda_2\lambda_3 + \lambda_3\lambda_1 \tag{1.22}$$

$$R_A = -\frac{1}{3}\mathrm{Tr}(A^3) = -(\lambda_1\lambda_2\lambda_3)\,. \tag{1.23}$$

The discriminant given by

$$\Delta_A = Q_A^3 + \frac{27}{4}R_A^2\,, \tag{1.24}$$

characterises the eigenvalues; for $\Delta_A < 0$ all eigenvalues are real, for $\Delta_A > 0$ there is one real and two complex eigenvalues (that come in a conjugate pair).

Traditionally, the VGT is decomposed into a Hermitian $S_A = \frac{1}{2}(A + A^T)$ and a skew-Hermitian tensor, $\Omega_A = \frac{1}{2}(A - A^T)$, where S_A and Ω_A are known as the strain rate and rotation rate tensors respectively, forming $A = S_A + \Omega_A$. Recently, Keylock [2018] has shown that A can be decomposed also into a normal tensor B (which is fully characterised by its eigenvalues) and a non-normal tensor C,

$$A = B + C\,. \tag{1.25}$$

The normal tensor B is associated with the local dynamics which is the eigenvalue-dominated part of the VGT due to its association with the isotropic part of the pressure Hessian. The non-normal part C on the other hand is related to the non-local effects (see Keylock [2018] for details). The connection between the non-locality and non-normality in fluid flow can be demonstrated using the Poisson equation for pressure, which leads to an expression that involves the isotropic part of the pressure Hessian,

$$H^{iso} = \frac{1}{3}\mathrm{Tr}(H)I = \frac{1}{3}\nabla^2 pI = -\frac{1}{3}\mathrm{Tr}(A^2)I = \frac{2}{3}Q_A I\,, \tag{1.26}$$

where I is the identity matrix. This equation demonstrates that H^{iso} is determined purely by the eigenvalues of A, thus linking it to the local behaviour of the flow. Ohkitani and Kishiba [1995] showed that the H^{dev}, can be expressed as a principal value integral of the pressure field in the neighbourhood of a point. This means that H^{dev} is a non-local quantity, and it is not

simply determined by the local properties of the flow.

The decomposition (1.25) is accomplished by performing the complex Schur transform of the VGT

$$A = UTU^* \,, \tag{1.27}$$

where an asterisk denotes conjugate transpose, U is a unitary matrix, i.e. $UU^* = I$. Matrix T is upper triangular and has the form

$$T = \begin{bmatrix} \lambda_1 & N_{1,2} & N_{1,3} \\ 0 & \lambda_2 & N_{2,3} \\ 0 & 0 & \lambda_3 \end{bmatrix} = L + N \,. \tag{1.28}$$

where L is a diagonal matrix that contains eigenvalues of A and N is strictly upper triangular. B is defined as

$$B = ULU^*. \tag{1.29}$$

B is a normal matrix, satisfying the condition $B = B^*$. C is defined as

$$C = UNU^*. \tag{1.30}$$

It is clear that C is a non-normal matrix. A ratio is defined to measure the degree of non-normality of the flow field

$$k_{BC} = \frac{\|B\| - \|C\|}{\|B\| + \|C\|} \,, \tag{1.31}$$

where $\|\cdot\|$ denotes the Frobenious norm of a tensor, for example $\|B\| = \sqrt{\mathrm{Tr}(BB^*)}$. Positive values of k_{BC} indicate that the dynamics are dominated by the eigenvalues; on the other hand, negative values indicate that dynamics stemming from non-locality are enhanced. The second invariant Q_A can be written as

$$Q_A = -\frac{1}{2}\mathrm{Tr}\left(A^2\right) = \frac{1}{2}\left[-\mathrm{Tr}\left((S_A + \Omega_A)^2\right)\right] = -\frac{1}{2}\left[\mathrm{Tr}\left(S_A^2\right) + \mathrm{Tr}\left(\Omega_A^2\right)\right] \,, \tag{1.32}$$

because $\mathrm{Tr}\left(S_A\Omega_A\right) = \mathrm{Tr}(\Omega_A S_A) = 0$. Based on (1.32), two quantities can be defined

$$Q_A^S = -\frac{1}{2}\mathrm{Tr}\left(S_A^2\right) \tag{1.33}$$

$$Q_A^\Omega = -\frac{1}{2}\mathrm{Tr}\left(\Omega_A^2\right)\ . \tag{1.34}$$

We can decompose B and C as the sum of corresponding strain and rotation tensors, i.e. $B = S_B + \Omega_B$, $C = S_C + \Omega_C$, and since $A = B + C$, we have $S_A = S_B + S_C$ and $\Omega_A = \Omega_B + \Omega_C$. The following expressions can be easily derived

$$Q_A^S = -\frac{1}{2}\mathrm{Tr}\left(S_A^2\right) = -\frac{1}{2}\left[\mathrm{Tr}\left(\left(S_B + S_C\right)^2\right)\right] = -\frac{1}{2}\left[\mathrm{Tr}\left(S_B^2\right) + \mathrm{Tr}\left(S_C^2\right)\right]\ , \tag{1.35}$$

because $\mathrm{Tr}\left(S_B S_C\right) = \mathrm{Tr}\left(S_B S_C\right) = 0$,

$$Q_A^\Omega = -\frac{1}{2}\mathrm{Tr}\left(\Omega_A^2\right) = -\frac{1}{2}\left[\mathrm{Tr}\left(\left(\Omega_B + \Omega_C\right)^2\right)\right] = -\frac{1}{2}\left[\mathrm{Tr}\left(\Omega_B^2\right) + \mathrm{Tr}\left(\Omega_C^2\right)\right]\ , \tag{1.36}$$

because $\mathrm{Tr}\left(\Omega_B\Omega_C\right) = \mathrm{Tr}\left(\Omega_C\Omega_B\right) = 0$. Note that $Q_A = Q_B$ because A and B have the same eigenvalues and $Q_C = 0$ thus $Q_C^S = -Q_C^\Omega$ because non-normality is partitioned equally across these two terms. It can be easily shown that

$$\|S_A\|^2 = \|S_B + S_C\|^2 = \|S_B\|^2 + \|S_C\|^2 \tag{1.37}$$

$$\|\Omega_A\|^2 = \|\Omega_B + \Omega_C\|^2 = \|\Omega_B\|^2 + \|\Omega_C\|^2\,, \tag{1.38}$$

and $\|S_C\|^2 = \|\Omega_C\|^2$ (see Appendix C for the proof). Since A and B have the same eigenvalues, we have for the third invariant,

$$R_A = -\frac{1}{3}\mathrm{Tr}(A^3) = R_B = -\frac{1}{3}\mathrm{Tr}(B^3)\,, \tag{1.39}$$

thus

$$R_A = -\frac{1}{3}\mathrm{Tr}(S_A^3) - \mathrm{Tr}(\Omega_A^3 S_A) = R_B = -\frac{1}{3}\mathrm{Tr}(S_B^2) - \mathrm{Tr}(\Omega_B^2 S_B)\,. \tag{1.40}$$

1.5.1 Transport equations for the invariants of A

We derive the transport equations for the invariants of A in terms of normal and non-normal quantities. We are interested in particular for the expressions of strain-self amplification and enstrophy production. We start with the transport equations for S_A and Ω_A,

$$\frac{DS_A}{Dt} = -S_A S_A - \Omega_A \Omega_A - \frac{1}{\rho}H + \nu\nabla^2 S_A \tag{1.41}$$

$$\frac{D\Omega_A}{Dt} = -2\Omega_A S_A + \nu\nabla^2\Omega_A\,. \tag{1.42}$$

The transport equation of the second invariant Q_A^S is obtained by multiplying each term of (1.41) with $-\frac{1}{2}S_A$ and taking the trace,

$$\frac{DQ_A^S}{Dt} = \underbrace{\frac{1}{2}\mathrm{Tr}\left(S_A S_A S_A\right)}_{\mathcal{SA}_s} \underbrace{+\frac{1}{2}\mathrm{Tr}\left(\Omega_A\Omega_A S_A\right)}_{\mathcal{EF}_s} \underbrace{+\frac{1}{2}\frac{1}{\rho}\mathrm{Tr}\left(HS_A\right)}_{\mathcal{H}_s} \underbrace{-\frac{1}{2}\nu\mathrm{Tr}\left(S_A\nabla^2 S_A\right)}_{\epsilon_s}, \tag{1.43}$$

where $\mathcal{SA}_s$ represents strain-self amplification, $\mathcal{EF}_s$ represents the generation of enstrophy by vortex stretching, $\mathcal{H}_s$ and ϵ_s the pressure Hessian and dissipation terms respectively. The transport equation of Q_A^Ω is obtained in a similar way from (1.42) and reads,

$$\frac{DQ_A^\Omega}{Dt} = \underbrace{\mathrm{Tr}(\Omega_A^2 S_A)}_{\mathcal{EA}_\Omega} \underbrace{-\frac{1}{2}\nu\mathrm{Tr}(\Omega_A\nabla^2\Omega_A)}_{\epsilon_\Omega}, \tag{1.44}$$

where $\mathcal{EA}_\Omega$ represents enstrophy production due to vortex stretching and ϵ_Ω is the dissipation term. To derive equivalent expressions in terms of normal and non-normal quantities, we

substitute $S_A = S_B + S_C$ and $\Omega_A = \Omega_B + \Omega_C$ in the right hand side of (1.41) to get,

$$\begin{aligned}\frac{DS_A}{Dt} = &-\left(S_BS_B + S_CS_B + S_BS_C + S_CS_C\right) - \left(\Omega_B\Omega_B + \Omega_C\Omega_B + \Omega_B\Omega_C + \Omega_C\Omega_C\right) \\ &-\frac{1}{\rho}H + \nu\nabla^2\left(S_B + S_C\right) .\end{aligned} \tag{1.45}$$

We multiply with $S_A = S_B + S_C$, take the trace and multiply by $-\frac{1}{2}$ to get,

$$\begin{aligned}\frac{DQ_A^S}{Dt} = &\underbrace{\frac{1}{2}\left[\mathrm{Tr}\left(S_BS_BS_B\right) + \mathrm{Tr}\left(S_CS_CS_C\right) + 3\mathrm{Tr}\left(S_CS_CS_B\right)\right]}_{\mathcal{SA}_s} \\ &\underbrace{\frac{1}{2}\left[\mathrm{Tr}\left(\Omega_B\Omega_BS_B\right) + \mathrm{Tr}\left(\Omega_C\Omega_CS_C\right) + \mathrm{Tr}\left(\Omega_C\Omega_CS_B\right)\right]}_{\mathcal{EA}_s} \\ \underbrace{+\frac{1}{2}\frac{1}{\rho}\mathrm{Tr}\left(H^{dev}S_C\right)}_{\mathcal{H}_s} &\underbrace{-\frac{1}{2}\nu\mathrm{Tr}\left(S_B\nabla^2S_B\right) - \nu\mathrm{Tr}\left(S_B\nabla^2S_C\right) - \frac{1}{2}\nu\mathrm{Tr}\left(S_C\nabla^2S_C\right)}_{\epsilon_s} .\end{aligned} \tag{1.46}$$

For $\mathcal{SA}_s$ we have taken into account that cyclical permutation does not alter the trace $\mathrm{Tr}(S_CS_CS_B) = \mathrm{Tr}(S_BS_CS_C) = \mathrm{Tr}(S_CS_BS_C)$ thus $\mathrm{Tr}(S_CS_CS_B) + \mathrm{Tr}(S_BS_CS_C) + \mathrm{Tr}(S_CS_BS_C) = 3\mathrm{Tr}(S_CS_CS_B)$. Likewise $\mathrm{Tr}(S_BS_BS_C) = \mathrm{Tr}(S_CS_BS_B) = \mathrm{Tr}(S_BS_CS_B) = 0$ (see Appendix D for details). The term $\mathcal{H}_s$ has been split into $\frac{1}{2}\frac{1}{\rho}\mathrm{Tr}(H^{iso}S_B)$ which is zero due to the incompressibility constraint applied to S_B and $\frac{1}{2}\frac{1}{\rho}\mathrm{Tr}(H^{dev}S_C)$ which is non-zero.
For $\mathcal{EA}_s$, the trace of the terms of the type "BBC" are unaffected by permutation $\mathrm{Tr}(\Omega_BS_C S_B)$, $\mathrm{Tr}(\Omega_CS_B\Omega_B)$ and $\mathrm{Tr}(\Omega_BS_B\Omega_C)$ and are zero (see Appendix D for details). The two terms of the type $\mathrm{Tr}(S_C\Omega_CS_B)$ have also zero trace.

We follow a similar procedure for the transport equation of Q_A^Ω. Substituting $\Omega_A = \Omega_B + \Omega_C$ in the right hand side of equation (1.42) we get

$$\frac{D\Omega_A}{Dt} = -2(\Omega_BS_B + \Omega_BS_C + \Omega_CS_B + \Omega_CS_B + \Omega_CS_C) + \nu\nabla^2(\Omega_B + \Omega_C) . \tag{1.47}$$

As before, we multiply each term with $\Omega_A = \Omega_B + \Omega_C$, take the trace and multiply with $-1/2$

to get,

$$\frac{DQ_A^{\Omega}}{Dt} = \underbrace{\left(\mathrm{Tr}\left(\Omega_B\Omega_B S_B\right) + \mathrm{Tr}\left(\Omega_C\Omega_C S_C\right) + \mathrm{Tr}\left(\Omega_C\Omega_C S_B\right)\right)}_{\mathcal{EA}_\Omega} \underbrace{-\frac{1}{2}\nu\left(\Omega_B\nabla^2\Omega_B\right) - \nu\left(\Omega_B\nabla^2\Omega_C\right) - \frac{1}{2}\nu\left(\Omega_C\nabla^2\Omega_C\right)}_{\epsilon_\Omega}, \tag{1.48}$$

where $\mathcal{EA}_\Omega = 2\mathcal{EA}_s$. Matching and rearranging the terms corresponding to the strain self-amplification $\mathcal{SA}_s$ in equations (1.43) and (1.46) and keeping in mind that $\mathrm{Tr}(S_AS_AS_A) = 3\det(S_A)$ and $\mathrm{Tr}(S_CS_CS_C) = 3\det(S_C)$ and $\mathrm{Tr}(S_CS_CS_B) = -\mathrm{Tr}(\Omega_C\Omega_CS_B)$, we obtain the following new expression for $\det(S_A)$:

$$-\det(S_A) = -\det(S_B) - \det(S_C) + \mathrm{Tr}(\Omega_C\Omega_CS_B)\,, \tag{1.49}$$

where $-\det(S_A) = -\frac{1}{3}s_{ij}s_{jk}s_{ki}$ in index notation. In the same way, rearranging the terms corresponding to the enstrophy production $\mathcal{EA}_\Omega$ in equations (1.44) and (1.48) while keeping in mind that $\mathrm{Tr}(S_CS_C\Omega_C) = -\det(S_C)$ based on $R_C = 0$ (since $R_A = R_B$),

$$\mathrm{Tr}(\Omega_A^2S_A) = \mathrm{Tr}(\Omega_B\Omega_BS_B) - \det(S_C) + \mathrm{Tr}(\Omega_C\Omega_CS_B)\,, \tag{1.50}$$

where $\mathrm{Tr}(\Omega_A^2S_A) = \frac{1}{4}\omega_i\omega_js_{ij}$ in index notation. We will investigate the distribution of these quantities along the recirculating and transitional flow regions in the next sections.

1.6 The Lamb vector

Following the discussion on the significance of vorticity in small-scale dynamics, this section explores the Lamb vector, named in honour of Horace Lamb. The vector elucidates the connection between the vorticity and velocity fields, and is related to the energy cascade trough vortex stretching. Defined as the cross product of the vorticity and velocity vectors (i.e., $L = \Omega \times U$), the subsequent section provides an overview of the research encompassing this vector.

1.6.1 Properties and physical importance

An alternative formulation of the acceleration term also named Lagrange's acceleration formula in the NSE (1.1)[Truesdell, 1954] is

$$\frac{\partial U}{\partial t} + U \cdot \nabla U = \frac{\partial U}{\partial t} + \Omega \times U + \nabla \frac{1}{2} (U \cdot U) \ . \tag{1.51}$$

In equation 1.51, $L = \Omega \times U$ is the Lamb vector and is directly linked to the convective nonlinear term of the NSE and it is the major source of vortical flow non-linearity [Gibbon and Holm, 2012]. Substituting 1.51 into 1.1, the NSE in rotational form is obtained [Wu et al., 2015]

$$\frac{\partial U}{\partial t} + \Omega \times U = -\nabla \alpha - \nu \nabla \times \Omega \, , \tag{1.52}$$

where we have applied the vector identity $\nabla \times \Omega = -\nabla^2 U$ (due to continuity) to write the dissipative term in terms of vorticity. The above form clearly shows that viscosity has no effect on the transport of momentum if vorticity is zero. In 1.52, the Bernoulli function α is defined as [Hamman et al., 2008, Gibbon and Holm, 2012, Wu et al., 2015]

$$\alpha = \frac{P}{\rho} + \frac{1}{2} U^2 \, , \tag{1.53}$$

which is the total energy of a fluid particle (per unit mass) in an incompressible flow. For an idealised steady, inviscid, incompressible flow, and in the absence of external forces, α is constant along the streamlines but it can vary from one streamline to another. Under these ideal conditions equation 1.52 turns into

$$\Omega \times U = -\nabla \alpha \, . \tag{1.54}$$

In order α to be constant throughout the domain, the Lamb vector should vanish; this would be the case of an irrotational flow (where $\Omega = 0$) and Beltrami flow. We will go back to these conditions and their implications later in this section.

The generation of small-scale fluctuations that result in the dissipation of turbulence and

enstrophy at the end of the cascade process is due to the nonlinearity [Davidson, 2015]. By taking the curl of equation 1.52 we obtain the transport equation for vorticity,

$$\frac{\partial \Omega}{\partial t} + \nabla \times (\Omega \times U) = \nu \nabla^2 \Omega \,, \tag{1.55}$$

where

$$\nabla \times (\Omega \times U) = \overbrace{U \cdot \nabla \Omega}^{\text{convective term}} - \overbrace{\Omega \cdot \nabla U}^{\text{vorticity stretching}} \,, \tag{1.56}$$

where $U \cdot \nabla \Omega$ is the convective term and $\Omega \cdot \nabla U$ is the vorticity stretching term. Equation 1.55 is more convenient as pressure is absent. The following relation can be obtained by vector algebra [Wu et al., 2015]

$$\underbrace{\frac{|\Omega \times U|^2}{|U|^2 |\Omega|^2}}_{\text{Nonlinear term}} + \underbrace{\frac{|U \cdot \Omega|^2}{|U|^2 |\Omega|^2}}_{\text{Helical density}} = 1 \,, \tag{1.57}$$

where the helicity density is the dot product $U \cdot \Omega$. The cosine of the angle between Ω and U,

$$\cos(U, \Omega) = \frac{U \cdot \Omega}{|U||\Omega|} \,, \tag{1.58}$$

measures the level of three-dimensionality of the flow. When $L = 0$, equation 1.1 turns into

$$\frac{\partial U}{\partial t} = -\nabla \left(P + \frac{1}{2} U \cdot U \right) . \tag{1.59}$$

Here, there is no source of vortical non-linearity however nonlocal effects of pressure are present. These nonlocal effects refer to the fact that pressure gradients can influence the flow of fluid at a distance from the pressure source. In 2D or plane flows, vortex stretching is absent as there is no out-of-plane velocity component , thus $U \cdot \nabla \Omega = 0$ and helicity defined as $U \cdot \Omega$ is zero. However $\Omega \times U \neq 0$ does not vanish. In this case equation 1.1 can be simplified to

$$\frac{\partial \Omega}{\partial t} + U \cdot \nabla \Omega = \nu \nabla^2 \Omega \,. \tag{1.60}$$

On the other hand, when the streamlines are exactly parallel to the vorticity lines we refer to

Flow	$\boldsymbol{\Omega} \times \mathbf{U}$	$\boldsymbol{\Omega} \cdot \mathbf{U}$	**Condition**
Irrotational	0	0	$\Omega = 0$
2D	finite	0	Absence of vortex stretching
Beltrami	0	finite	Ω parallel to U
Generalized Beltrami	finite	finite	$\nabla \times (\Omega \times U) = 0$

Table 1.1: Summary of the types of flow conditions.

Beltrami, where $L = \Omega \times U = 0$ and $|\cos(\langle U \rangle, \langle \Omega \rangle)| = 1$. The following expression is valid

$$\Omega \times U = \zeta U \,, \tag{1.61}$$

ζ is the constant that determines the strength of the Beltrami flow and its sign determines if there is a right- or left-hand helical wave [Wu et al., 2015]. In these flows, the fluid motion has a clearly defined helical shape, with the rotation's axis representing the direction of motion. In a Beltrami flow, the Helmholtz vorticity equation 1.55 becomes linear,

$$\frac{\partial \Omega}{\partial t} = \nabla^2 \Omega \,. \tag{1.62}$$

A generalized Beltrami condition refers to the relaxation of $L = \Omega \times U = 0$ to [Wu et al., 2015]

$$\nabla \times (\Omega \times U) = 0 \,, \tag{1.63}$$

where $(\Omega \times U) = -\nabla \alpha$ is a solution. This condition is more general than the Beltrami condition and also allows the linearization of the Helmholtz vorticity equation 1.55, where accurate vortex flow solutions can be analytically attainable. This category belongs to one of three major types of exact solutions of steady-state NSE, there other two being parallel flows and similarity solutions [Wang, 1991]. We summarize the types of flows in table 1.1.

By taking the divergence of equation 1.52, we obtain the following expression in which α is the only term that remains non-zero after the divergence operation [Hamman et al., 2008],

$$\nabla \cdot L = -\nabla^2 \alpha \,. \tag{1.64}$$

Positive values mean that the fluid is being stretched or strained, while negative values mean that the fluid is rotating [Hamman et al., 2008]. By analyzing the distribution of divergence of the Lamb vector, researchers can gain valuable insights into regions of flow separation, recirculation, and areas that are prone to turbulence. In the subsequent subsection, we proceed with a review of previous research on the Lamb vector.

1.6.2 Studies on the Lamb vector

Most of the research involving the Lamb vector has been conducted in the last 20 years and has focused on specific flow settings. The literature on this subject can be divided into studies in aerodynamics, flow diagnosis, compressible flows, acoustics, boundary layer theory, turbulence modeling, and to a lesser extent, studies related to HIT.

In aerodynamics, the Lamb vector is responsible for the generation of lift and is closely tied to the development of the universal theory of steady lift and drag [Wu et al., 2018]. The forces could be fully determined by the integration of the Lamb vector. More specifically, the volume integral of the Lamb vector corresponds to the lift and induced drag, while the surface integral represents the profile drag. This implementation within the framework of viscous flow led to the rediscovery of the conventional Kutta-Joukowski formula which is commonly used in inviscid aerodynamics [Wu et al., 2015]. Also, a series of works related to the use of the Lamb vector integrals in aerodynamics is available [Marongiu and Tognaccini, 2010, Mele and Tognaccini, 2014, Marongiu et al., 2013].

The Lamb vector divergence $\nabla \cdot L$ can provide a systematic approach to investigate coherent structures and motions. This approach enables the description of the interaction between neighbouring fluid motions with high and low momentum which result in a change in momentum over time [Hamman et al., 2008]. The authors formulated the transport equation of $\nabla \cdot L$ and mentioned that $\nabla \cdot L < 0$, indicates vortical movements characterized by a reduction of energy. On the other hand, when $\nabla \cdot L > 0$, it indicated straining motions with localized energy concentration. This finding can be attributed to equation 1.64, which establishes a direct association between the divergence of L and the Laplacian of the Bernoulli function α, where the following relationship holds: $\alpha \sim \frac{1}{2} U \cdot U$. The paper also mentioned that drag reduction can

be achieved by reducing the zone of interaction between positive and negative levels of $\nabla \cdot L$. Recently, Yu et al. [2023] conducted a LES study where the dynamical mechanism of energy loss caused by cavitation in a hydrofoil was examined using the Lamb vector and its divergence. Also, Xu et al. [2022] conducted a simulation of compressible flow around a wavy-axis square cylinder. They identified and analyzed the two-layer structure of the shear layer using the instantaneous divergence of the Lamb vector. It was revealed that as compressibility increases, the transfer of momentum between high- and low-momentum fluid regions is hindered. Zhang et al. [2023b] investigated the impact of the installation of aerofoil probes on the unsteady behaviour and transport characteristics of a transonic compressor cascade. The Lamb vector divergence was able to represent the transport of momentum between regions during unsteady motion related to vortex folding or expansion. By studying the noise characteristics of transonic deep buffeting in an aerofoil, Zhang et al. [2023a] employed the curl of the Lamb vector $\nabla \times L$ to examine the influence of the interaction between shock waves and turbulent boundary layers, as well as the distribution of sound source strength. Chen et al. [2022] conducted a numerical investigation on the mechanisms of flow and noise control involving a cylinder with a wavy surface up to a Reynolds number of 2.4×10^6. It was shown that the reduction in the interaction area between the positive and negative Lamb vector divergence values, which is closely linked to noise generation, leads also to a decrease in drag and noise.

Wu et al. [1999] studied the characteristics of the Lamb vector within the framework of turbulence modeling. Their findings suggest that the task of modeling turbulent force ($\nabla \cdot \langle u_i u_j \rangle$) can be effectively addressed by focusing on modeling the mean turbulent Lamb vector. The structure of the Lamb vector in the viscous sublayer was also studied in [che, Chen and Liu, 2022]. It was demonstrated that the near-wall Lamb vector was related to both the skin friction divergence and the boundary vorticity divergence. Furthermore, a series of studies have explored the Lamb vector in the context of boundary layers [Chen and Liu, 2022, Xu et al., 2021, Tong et al., 2017]. The Lamb vector has been reported to offer a means of defining a hydrodynamic charge that resembles the electric charge found in electromagnetism [Rousseaux et al., 2007, Marmanis, 1998].

In relation to turbulent flows, there is a small number of studies that have studied the

magnitudes of solenoidal and irrotational parts of the Lamb vector in relation to the reduction of nonlinearity in HIT [Tsinober, 1990, Shtilman, 1992, Speziale, 1987]. Here, the solenoidal component of the nonlinear advection is employed to measure the degree of nonlinearity as this is related to vortex stretching. In HIT, the behaviour of vorticity depends solely on the solenoidal component of the Lamb vector where the average of the enstrophy production due to vortex stretching is [Shtilman, 1992] $\langle \omega_i \omega_j s_{ij} \rangle = -\langle \omega \nabla \times \nabla \times \beta \rangle$. The suppression of nonlinearity is also known as "Eulerization". There is a hypothesis that turbulent flows spend a significant amount of time near Euler solutions, which are dissipation-free and possess weak Beltrami characteristics [Levich, 1987, Moffatt, 2005]. Speziale [1987] found that there is no notable inverse relationship between helicity and dissipation in isotropic turbulence, even at higher Taylor based Reynolds number Re_{ζ_i} values where ζ_i indicates the Taylor microscale in the i-th direction. Recently, Iyer et al. [2022] using a DNS database of HIT with Taylor Reynolds numbers in the range of 38 and 1500 determined ratios between the potential and solenoidal parts of the Lamb vector. As the logarithm of Re_{ζ_i} increases, this ratio exhibits growth. For $Re_{\zeta_i} = 1300$, the ratio of the solenoidal part to the potential part was ≈ 0.9. Furthermore, the authors also observed a substantial amount of dissipation in areas when nonlinearity was not present.

1.7 Aims and objectives of the thesis

The following is an outline of the thesis. Chapter 2 provides a description of the numerical methods used to conduct DNS with our setting. To ensure the reliability and accuracy of the code, a validation campaign was carried out against published results, including a grid convergence study. We then proceed with the results chapters 3, 4, and 5, where the above questions are explored. Chapter 6 concludes the thesis; it summarizes the work carried out in this thesis and offers some suggestions for further research. The aims and objectives of the thesis will be presented next.

Currently, there is little discussion in the literature on the mechanisms that result in the inception, growth and intensification/suppression of vortical structures, in three-dimensional flows around wings. Likewise, there is a need to assess the interaction of vortical structures

with the developed turbulence field. The main goal of chapter 3 is therefore to conduct a thorough analysis of the main vorticity dynamics and turbulence production mechanisms in the separated flow around a finite wing with a square wing tip. We focus on the near field, an area where the flow is far from being self-similar. More specifically, we consider a moderate chord-based Reynolds number of $Re_c = U_\infty C/\nu = 10^4$, where U_∞ is the inlet velocity, C is the chord length and ν is the dynamic viscosity, and we fully resolve all scales of the flow using DNS. The flow has multi-scale character and we investigate in detail the multiple developing vortical patterns. The thesis has the following aims and objectives:

(i) Elucidate the formation of the primary streamwise vortices, specifically in the early stages before they separate from the wing surface. Investigate and reveal the key mechanisms governing their motion. What is are the key mechanisms to sustain (or suppress) the strength or rotational intensity of each vortex?

(ii) To what extent does the separation of flow at the leading edge impact the dynamics of the vortices?

In chapter 4, we aim to investigate the properties of small-scale statistics in a transitioning separated shear flow undergoing large-scale straining. The motivation behind this research arises from the fact that there is a lack of understanding regarding the impact of mean sheared flows on the dynamics in both the inertial and dissipative range, even though they are common in industrial applications. The flow field is obtained from a direct numerical simulation of the same configuration as in the chapter 3 however at the lower $Re_c = 5000$ for a higher resolution. We compute of the balance of the enstrophy and strain rate transport equations without any simplifications. Furthermore, the Schur decomposition of the VGT is used to provide further insight into the small-scales. The research conducted in this chapter has the following interconnected objectives.

(iii) With only a few exceptions for example the works of Paul et al. [2017] in square grids and Gurka et al. [2004] in boundary layers, the effect of mean strain on small-scale statistics remains elusive despite its prevalence in industrial flows. Our objective to determine the degree to which the presence of mean shear alters the generation of enstrophy and

total strain compared to HIT. Our objective is to measure and analyze key geometrical properties of the mean strain rate along the transitional and recirculating bubble.

(iv) How the occupancy in the QR distribution changes in the sections where an abrupt growth (or decay) in shear occurs remains elusive in the literature. It is clearly of interest to investigate how "efficient" each region is towards the production of enstrophy and strain vs. the percentage occupancy.

(v) What is the role of large events (defined as greater than 10 times their time-average value) on the dynamics? What is the time-occupancy of these large events along the two flow sections? How much do they contribute to the overall production terms of enstrophy and strain-squared?

(vi) Evaluate the influence of non-normality by performing the Schur decomposition of the VGT [Keylock, 2018]. What are the leading terms of enstrophy and total strain production in sections that deviate largely from HIT and where mean shear is active? What are the circumstances that enable these terms to prevail?

(vii) Incorporate mean flows into the Schur decomposition and uncover their topological organization and the resulting implications. What are the key distinctions and new intricacies in the communication between fluctuating-fluctuating and mean-fluctuating correlations that arise from incorporation of mean flows into the Schur decomposition?

The Lamb vector is directly linked to the convective nonlinear term of the NSE and it is the major source of vortical flow non-linearity. In chapter 5, we investigate the physical properties and spatial development of the Lamb vector and its divergence in a separated, transitional flow around a finite wing. To this end, we decompose the Lamb vector into irrotational (potential) and solenoidal parts and analyse the relative magnitude and spatial development of the two components. We include the effect of time-average flow in the Lamb vector formulation. Inter-scale energy transfer is intrinsically related to the Lamb vector as it provides a measure of the local interaction between vorticity (enstrophy) and velocity. We aim to identify the role of the mixed terms containing fluctuating and mean flow components and analyse their interaction

and how they are geometrically connected with each other as they evolve. The flow field is obtained from a direct numerical simulation of the same configuration as in chapter 4.

(viii) Analysis of the Lamb vector and its divergence in the flow around a finite wing.

(ix) The ratio between the potential term of the Lamb vector and the magnitude of the Lamb vector itself is known for HIT of different Reynolds numbers. How does this ratio behaves in a transitional flow and within a recirculation zone?

1.8 Journal papers, conferences, seminars and competitions

In this section, we present the scholarly contributions, conference presentation and participation in competitions stemming from the research described in this thesis.

Journals papers

- J. C. Bilbao-Ludena and G. Papadakis. Structure of vorticity and turbulence fields in a separated flow around a finite wing: Analysis using direct numerical simulation. *Phys. Rev. Fluids*, 8:014704, Jan 2023. doi: 10.1103/PhysRevFluids.8.014704.

- J. C. Bilbao-Ludena and G. Papadakis. Non-normality and small-scale statistics in a three-dimensional separated shear flow. *Under preparation.*

- J. C. Bilbao-Ludena and G. Papadakis. The structure of the Lamb vector in a separated three-dimensional shear flow. *Under preparation.*

Conferences and seminars

- J. C. Bilbao-Ludena and G. Papadakis. On the structure of the vorticity field in a separated wing flow; analysis using Direct Numerical Simulation . UK Turbulence Consortium Annual Review 2022 held at the South Kensington Campus, Imperial College London.

- J. C. Bilbao-Ludena and G. Papadakis. On the structure of turbulence fields in a separated flow around a finite wing; analysis using direct numerical simulation. Twelfth International Symposium on Turbulence and Shear Flow Phenomena (TSFP12) 2022 held in Osaka, Japan (Online).

- J. C. Bilbao-Ludena and G. Papadakis. Analysis of small-scale statistics in a turbulent recirculating flow around a wing. UK Fluids Conference 2022 held at the University of Sheffield in Sheffield, UK.

- J. C. Bilbao-Ludena and G. Papadakis. Analysis of small-scale statistics in a turbulent

recirculating flow around a wing. UK Turbulence Consortium Annual Review 2023 held at the South Kensington Campus, Imperial College London.

- J. C. Bilbao-Ludena and G. Papadakis. The structure of large events in the production mechanisms of enstrophy and strain rate in the transitioning and recirculating flow around a wing. European Turbulence Conference (ETC18) 2023 held in Valencia, Spain.

- J. C. Bilbao-Ludena and G. Papadakis. UK Fluids Conference 2023 held in Glasgow, UK.

- J. C. Bilbao-Ludena. The self-amplification and the structured chaotic sea. *The Science behind the Image Competition* seminar (online) 2023 organized by ARCHER2 and Edinburgh Parallel Computing Centre (EPCC).

Competitions

- J. C. Bilbao-Ludena. The emergence and coexistence of small-scale turbulence in an anisotropic and inhomogeneous flow. Entry submitted to the ARCHER2 Image and Video Competition 2021, organized by the ARCHER2 UK National Supercomputing Service, and image was chosen to feature in the ARCHER2 Calendar 2022.

- J. C. Bilbao-Ludena. The self-amplification and the structured chaotic sea. Entry submitted to the ARCHER2 Image and Video Competition 2022, organized by the ARCHER2 UK National Supercomputing Service, and image was chosen to feature in the ARCHER2 Calendar 2023.

Chapter 2

Numerical methodology and validation

In this chapter, we introduce the numerical solver based on the Finite Volume Method (FVM) that was used for the DNS simulations. We delve into the specifics of our solver and provide information into the parallelization strategy employed. Furthermore, we outline the computational setup for two types of simulations conducted at Reynolds numbers of 10000, validated against published data, and a Reynolds number of 5000 where we show the grid resolution adequacy for investigating small-scale phenomena. The chapter's content is drawn from the works of Papadakis [2019], Maliska [2023], Schlander [2023], Tsagkaridis [2022], Portela [2017], Paul [2017], Xiao [2017].

2.1 Solver

For the numerical simulations, we use the in-house code PANTARHEI that solves the incompressible Navier-Stokes equations using the fractional step method, see Guermond et al. [2006]. The code has been used extensively to simulate transitional and turbulent flows in several geometries [Xiao and Papadakis, 2019, Yao et al., 2022, Mikhaylov et al., 2021, Schlander et al., 2022], including flows around airfoils [Thomareis and Papadakis, 2017, 2018]. We make the assumption that the flow is incompressible and solve the Navier-Stokes equations (1.1 and 1.2).

Equation 1.1 can be generalized and expressed as the transport equation for a scalar variable ϕ. This equation governs the evolution of the quantity $\rho\phi$ over time and space

$$\overbrace{\frac{\partial(\rho\phi)}{\partial t}}^{\text{Transient term}} + \overbrace{\nabla\cdot(\rho U\phi)}^{\text{Convection term}} = \overbrace{\nabla\cdot(\rho\Gamma_\phi\nabla\phi)}^{\text{Diffusion term}} + \overbrace{S_\phi(\phi)}^{\text{Source term}} \quad . \tag{2.1}$$

Here, the vector ϕ_j, represents unknown variables, such as components of the velocity

vector U and pressure P. The transient term captures the temporal evolution, meanwhile, the convection term represents the transportation of ϕ by the fluid velocity U. The diffusion term accounts for the spatial spread or dissipation of ϕ attributed to concentration gradients, characterized by the diffusion coefficient Γ_ϕ. For momentum, it reflects the impact of fluid viscosity, whereas for temperature, it embodies thermal diffusivity. The source term includes external influences on the scalar variable ϕ.

In this study, the FVM is employed, which entails dividing the physical domain into a finite number of control volumes. Within the FVM framework, the Gauss divergence theorem is utilized to convert volume integrals into surface integrals,

$$\iiint_{\mathcal{CV}} \frac{\partial f_i}{\partial x_i}\, dV = \iint_{\partial \mathcal{CV}} f_i n_i\, dS\,. \tag{2.2}$$

This equation represents the conversion of the volume integral of the divergence of a flux f to the surface integral of the fluxes ($f_i n_i$) across the boundaries of a control volume $\mathcal{CV}$. Here, $\partial\mathcal{CV}$ denotes the surface bounding $\mathcal{CV}$, and n represents the outward-normal on that surface. Importantly, the FVM preserves the fundamental principle of conservation in the discrete equations. The main goal of a discretization method is to transform a set of often nonlinear partial differential equations, such as the one represented by 2.1, into a system of linear algebraic equations,

$$A_{ij}\phi_j = b_i\,. \tag{2.3}$$

The vector ϕ_j represents unknown variables, such as components of the velocity vector and pressure at the j-th node, while b_i encompasses all known information, including source terms, effects of external forces, and boundary conditions, at the i-th node. The solution of 2.3 results in the values of ϕ_j at discrete locations within the domain of interest, namely at the cell centers. Here, A_{ij} is a coefficient matrix influenced by both the mesh topology and the discretization scheme employed.

2.1.1 Fractional step method

The fractional step method allows the computation of pressure in a consistent and efficient way. The velocity is first calculated using the pressure from the previous time step,

$$\rho\Delta t\left(\frac{11}{6}\tilde{U}_i^{t+1}-3U_i^t+\frac{3}{2}U_i^{t-1}-\frac{1}{3}U_i^{t-2}\right)-\frac{\partial}{\partial x_j}\left(\mu\frac{\partial\tilde{U}_i^{t+1}}{\partial x_j}\right)=-\frac{\partial p^t}{\partial x_i}+f(t^{t+1})\,. \tag{2.4}$$

The subscript i denotes the velocity component in the i direction. The equation operates at discrete time steps, labeled as t, $t-1$, and $t-2$. It calculates the velocity at the next time step $t+1$, denoted as $\tilde{U}_i^{t+1}$. The discretisation of the transient term entails a weighted combination of the velocities at the current and previous time steps. The coefficients $(11/6, -3, 3/2, -1/3)$ are determined based on the employed time discretization scheme, which in this case is a 3rd order backward scheme. The term f encompasses convective effects, non-orthogonal diffusion, and any source terms.

Equation 2.4 will be substracted from a momentum equation involving the corrected velocity which takes the following form

$$\frac{\rho}{\Delta t}\left(\frac{11}{6}U_i^{t+1}-3U_i^t+\frac{3}{2}U_i^{t-1}-\frac{1}{3}U_i^{t-2}\right)-\frac{\partial}{\partial x_j}\left(\mu\frac{\partial\tilde{U}_i^{t+1}}{\partial x_j}\right)=-\frac{\partial P^{t+1}}{\partial x_i}+f(t^{t+1})\,. \tag{2.5}$$

This equation involves the corrected velocity at the next time step, denoted as U_i^{t+1}, in contrast to the estimated velocity $\tilde{U}_i^{t+1}$. The left-hand side of the equation represents now the momentum equation with the corrected pressure.

After the subtraction the following expression is obtained

$$\frac{\rho}{6\Delta t}\left(11U_i^{t+1}-11\tilde{U}_i^{t+1}\right)+\frac{\partial\Delta P^{t+1}}{\partial x_i}=0\,. \tag{2.6}$$

Equation 2.6 yields a relation involving the corrected and estimated velocities, along with the pressure gradient. Here, ΔP represents the pressure correction, while the corrected velocity field conforms to incompressibility. It is noteworthy that the corrected velocity and the viscous

terms utilize $\tilde{U}_i^{t+1}$ instead of U^{t+1}. Taking the divergence of equation 2.6 leads to

$$\frac{11\rho}{6\Delta t}\left(\frac{\partial U_i^{t+1}}{\partial x_i} - \frac{\partial \tilde{U}_i^{t+1}}{\partial x_i}\right) - \frac{\partial}{\partial x_i}\left(\frac{\partial \Delta P^{t+1}}{\partial x_i}\right) = 0\,. \tag{2.7}$$

Due to the incompressibility condition, the divergence of the corrected velocity field is zero. Simplifying Equation 2.7 by considering incompressibility results in

$$\frac{\partial}{\partial x_i}\left(\frac{\partial \Delta P^{t+1}}{\partial x_i}\right) = \frac{11\rho}{6\Delta t}\frac{\partial \tilde{U}_i^{t+1}}{\partial x_i}\,. \tag{2.8}$$

Equation 2.7 represents the Poisson equation for ΔP^{t+1}. On the right-hand side, it captures the deviation from incompressibility of the estimated velocity $\tilde{U}_i^{t+1}$.

Following the discretization approach of the FVM, the velocities at the faces of the control volumes are computed using the interpolation scheme proposed by Rhie and Chow [1983] to avoid a checkerboard pressure field. A second-order central discretization scheme is used in space for both convection and viscous terms. The orthogonal viscous terms are treated implicitly while the non-orthogonal viscous and convective terms are treated explicitly and advanced in time with a 3rd-order extrapolation.

The Fractional Step Method offers the flexibility to select different time-stepping schemes for convection and diffusion terms, making it advantageous for simulating problems with varying time scales. Importantly, the coefficient matrix remains constant throughout the simulation, regardless of the velocity component's direction, eliminating the need for repeated computation and enabling efficient memory usage. Once calculated at the simulation's outset, the coefficient matrix is stored in memory and utilized in each time step, optimizing the computational process. The algebraic multigrid preconditioner BoomerAMG, implemented in the Hypre library [Falgout and Yang, 2002], is used to accelerate the solution of the linear systems resulting from the discretization process. In contrast to methods like PISO, which often require multiple iterations for velocity and pressure corrections, the described approach avoids this iterative process, streamlining the simulation and enhancing overall computational efficiency.

2.1.2 Hardware and parallelization strategy

This work extensively utilized the ARCHER2 supercomputer [ARCHER2, 2024], which is an HPE Cray EX supercomputing system with an estimated peak performance of 28 Pflop/s. The machine comprises 5,860 compute nodes, each equipped with dual AMD EPYCTM 7742 64-core processors clocked at 2.25GHz, resulting in a total of 750,080 cores. ARCHER2 is ranked 39th in the TOP500 (most powerful non-distributed computer systems in the world) as of November 2023, and achieved the 22nd place in November 2021 [TOP500, 2024]. Pantarhei employs PETSc (Portable, Extensible, Toolkit for Scientific Computation) library for its parallelization strategy [Balay et al., 2018, 1997]. PETSc is widely recognized for its capability in efficiently solving large parallelized matrices, rendering it an important asset in scientific and computational uses.

The parallelization process begins with partitioning the computational domain into multiple subdomains. The mesh created by ICEMCFD is partitioned using METIS [METIS, 2024]. Each subdomain is allocated to a dedicated processor for concurrent processing, enabling simultaneous computation of different parts of the problem. Each processor independently handles its assigned subdomain, while communication at the boundaries between subdomains is managed through the MPI protocol. The cells at these boundaries are handled similarly to traditional boundary cells, such as cyclic boundary cells. In order to maintain a balanced computational load, the number of cells per processor is constrained to approximately 80,000 based on prior scalability studies using the code [Tsagkaridis, 2022, Xiao, 2017]. We proceed with the description of the computation setup and validation next.

2.2 Computational setup and validation

We consider the flow around a NACA 0018 wing with a square wingtip at a chord-based $Re_c = 10^4$ and 10° angle of attack (AoA). This wing has been employed in the study of the aerodynamics of small and medium scale unmanned aircrafts and its thickness allows to fit equipment within the compact size of the vehicle [Crivellini and D'Alessandro, 2014]. This airfoil has also been employed in wind turbines [Mohamed et al., 2020] where it has been

reported to improve blade stiffness and loading [Timmer, 2008]. The selected Re number and AoA correspond to parts of the operational envelope of Unmanned Aerial Vehicles (UAVs) [Taira and Colonius, 2009b].

For validation purposes, we compare our results against those of Zhang and Samtaney [2015]. The wing is placed within a uniform flow with velocity U_∞, at an angle of attack of $\alpha = 10^\circ$ and the simulation is performed at the chord-based $Re_c = 10^4$. The mesh consists of approximately 10 million cells distributed across 32 planes in the spanwise direction with the domain length and boundary conditions set according to Zhang and Samtaney [2015]. The simulation was initially run for $35t^*C/U_\infty$, a period sufficient for the flow to reach statistically steady state. It was then restarted and time-average statistics were collected over a period of $18t^*C/U_\infty$. For clarity in presenting the results, we will consistently express the non-dimensionalized distance explicitly as x_i/C (rather than x_i^*/C).

Figure 2.1(a) presents comparison of time- and spanwise averaged profiles of streamwise velocity at different x/C locations. There is very good agreement with the results from the literature. Panel (b) shows the $\langle C_p \rangle$ distribution (the angular brackets $\langle \cdot \rangle$ indicate time-averaging, and in the case of infinite wing, also spanwise-averaging). Separation occurs at $x/C \approx 0.2$ and the recirculation zone on the suction side creates a $\langle C_p \rangle$ plateau that extends almost until the trailing edge (note a slight increase close to $x/C = 1$). The distribution of the skin friction coefficient $\langle C_f \rangle$ on the suction side is shown in panel (c). It reaches a peak due to flow acceleration around the leading edge and quickly decreases due to the adverse pressure gradient, finally reaching the value of zero, which marks the beginning of the flow separation region. Within the recirculation region, $\langle C_f \rangle$ has very low values, as can be also detected from the shape of the velocity profiles of panel (a). The good matching with the literature data allows us to proceed with the simulation of the finite wing.

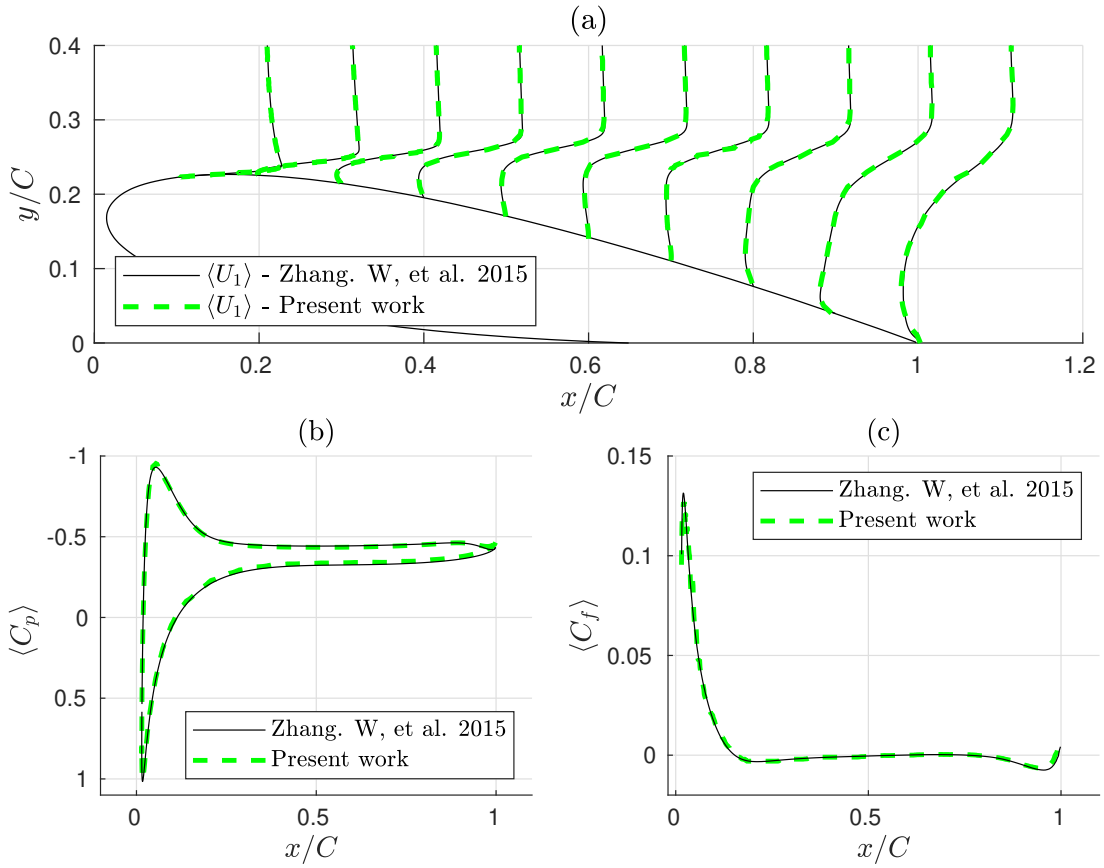


Figure 2.1: Comparison of time- and spanwise-averaged (a) streamwise velocity profiles at equally spaced intervals $x/C = 0.1, 0.2, \ldots, 1.0$. (b) $\langle C_p \rangle$ distribution and (c) $\langle C_f \rangle$ distribution. Present results are compared with those of Zhang and Samtaney [2015].

2.3 Computational details for the simulation of the finite wing for $Re_c = 10000$

In this thesis, we have opted for squared wingtips instead of the traditional rounded wingtips for specific reasons. While rounded wingtips are known for reducing induced drag and enhancing stability our study focuses on vortex dynamics near sharp edges. The sharp edges of squared wingtips generate intricate airflow patterns and a greater number of secondary structures with increased strength, deviating from the smoother transitions associated with rounded tips [Giuni, 2013, Birch et al., 2003, Bailey et al., 2006, Katz and Galdo, 1989].

Furthermore, when considering the wingtip geometry for UAVs or UAM vehicles, various factors are taken into account, with each type offering distinct advantages based on the specific requirements and objectives of the aircraft. Squared wingtips could present several practical advantages for structural integration in these vehicles compared to rounded tips. Their simpler

geometry facilitates the attachment of additional structural elements or features, particularly beneficial for accommodating or integrating multiple sensors, cameras, or communication devices. This design contributes to a more uniform load distribution across the wing, simplifying the design and implementation of structural elements [Barbarino et al., 2011, Vourtsis et al., 2023].

From a computational perspective, particularly when utilizing the FVM, choosing a squared wingtip over a rounded one offers certain benefits related to mesh generation and grid conformity. The generation of a structured mesh around the squared tip provides a more uniform grid representation compared to the complex spanwise mesh representation required to accommodate the curvature associated with a rounded tip. This can lead to better overall grid quality, crucial for achieving convergence and stability. It is important to note that in order to accommodate the features of the spanwise projected mesh, which involves cells projected from the finite trailing edge on the tip-side, the use of skewed cells was necessary. Consequently, the use of a squared tip helped alleviate the level of non-orthogonality in the cells in this section.

The dimensions of the computational domain used for the finite aspect ratio wing with square tip is shown in Figure 2.2. A C-type body-fitted grid is wrapped around the airfoil and enables very good resolution of the near wall flow features. The mesh comprises about 60 million cells, which are clustered in the vicinity of the wing, the tip and the near wake. To reduce the computational cost, only half of the wing is simulated. The aspect ratio of the whole wing is equal to 2 and the domain extends one chord length beyond the wingtip in the spanwise direction. Post processing of the results has shown that at a spanwise distance $0.8C$ from the wingtip, $\langle C_p \rangle$ converges to the free-stream value. The (x, y, z) coordinates, used interchangeably with (x_1, x_2, x_3), are along with the streamwise, cross-stream, and spanwise directions respectively. The trailing edge is located at $x/C = 1$, $y/C = 0$ and the wingtip at $z/C = -1$, refer to the bottom right panels of figure 2.2. A no-slip wall boundary condition is imposed at the wing surface, whereas the top and bottom planes (of the front view) are defined as symmetry planes. At the spanwise planes $z/C = -2$ and 0 symmetry conditions are also imposed. The flow velocity is prescribed at the inlet, while a convective boundary condition is employed at the outlet.

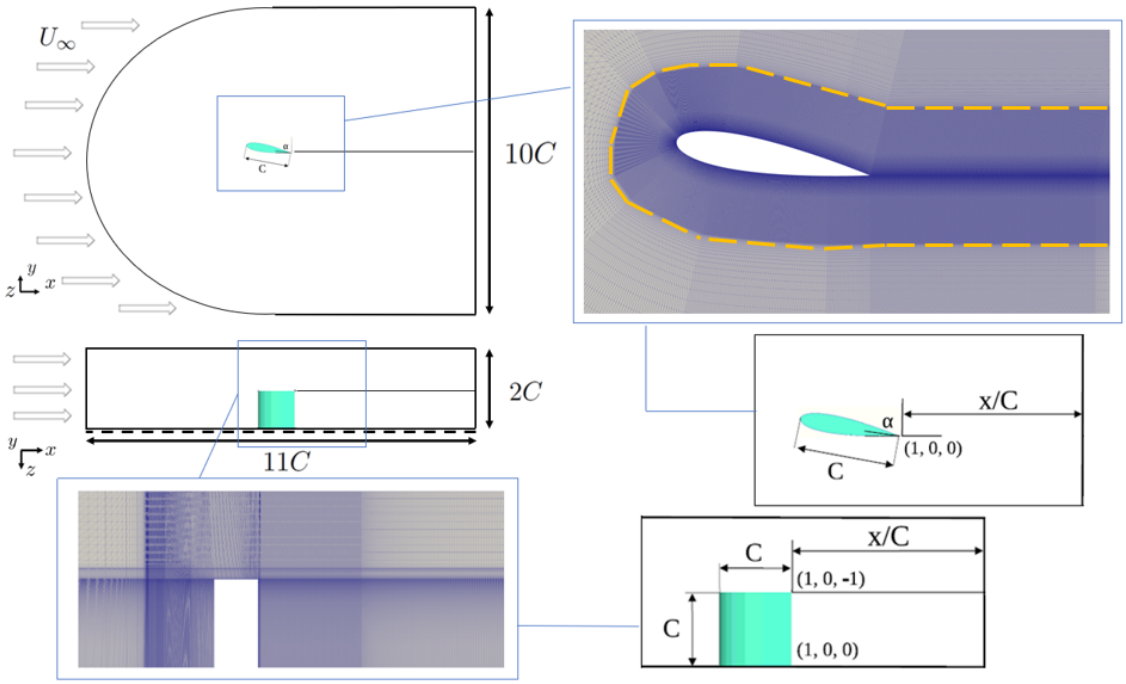


Figure 2.2: Computational domain (front and top views) and mesh layout for the finite wing simulation. The trailing edge is located at $x/C = 1$, $y/C = 0$ and extends in the spanwise direction $z/C = -1 \ldots 0$. Only half of the wing is simulated (and shown). The dotted orange curve demarcates the region of the mesh inside which a constant cell thickness growth rate (equal to 1.01) is employed. Around the airfoil, this curve is located at a distance $0.25C$ in the wall-normal direction).

The flow was simulated using 787 cores. In total, 214 probe points were placed at different locations to monitor the velocity field. After all transients died out and the flow reached a statistical steady state (which took about $60C/U_\infty$), the simulation was restarted and continued for another $120C/U_\infty$ to collect statistics.

The thickness of the cell closest to the wall has $\Delta y^+ < 0.5$ and the grid spacings in the streamwise and spanwise directions have $\Delta x^+ < 3$ and $\Delta z^+ < 1$ respectively (the plus superscript, $^+$, indicates wall units, as usual). This is very fine resolution, that exceeds the standard DNS requirements for wall-bounded flows, $10 < \Delta x^+ < 20$, $\Delta y^+ < 1$, $5 < \Delta z^+ < 10$ [Piomelli and Balaras, 2002]. The time step was set to $0.0004C/U_\infty$ and the maximum CFL was about 0.5.

The quality of the mesh was further checked by computing the ratio of the grid size (taken to be equal to the cubic root of the cell volume, $V^{1/3}$) to the Kolmogorov length scale, η. The latter was calculated from $\eta = (\nu^3/\epsilon)^{1/4}$, where $\epsilon = 2\nu\langle s_{ij}s_{ij}\rangle$ is the turbulent kinetic energy

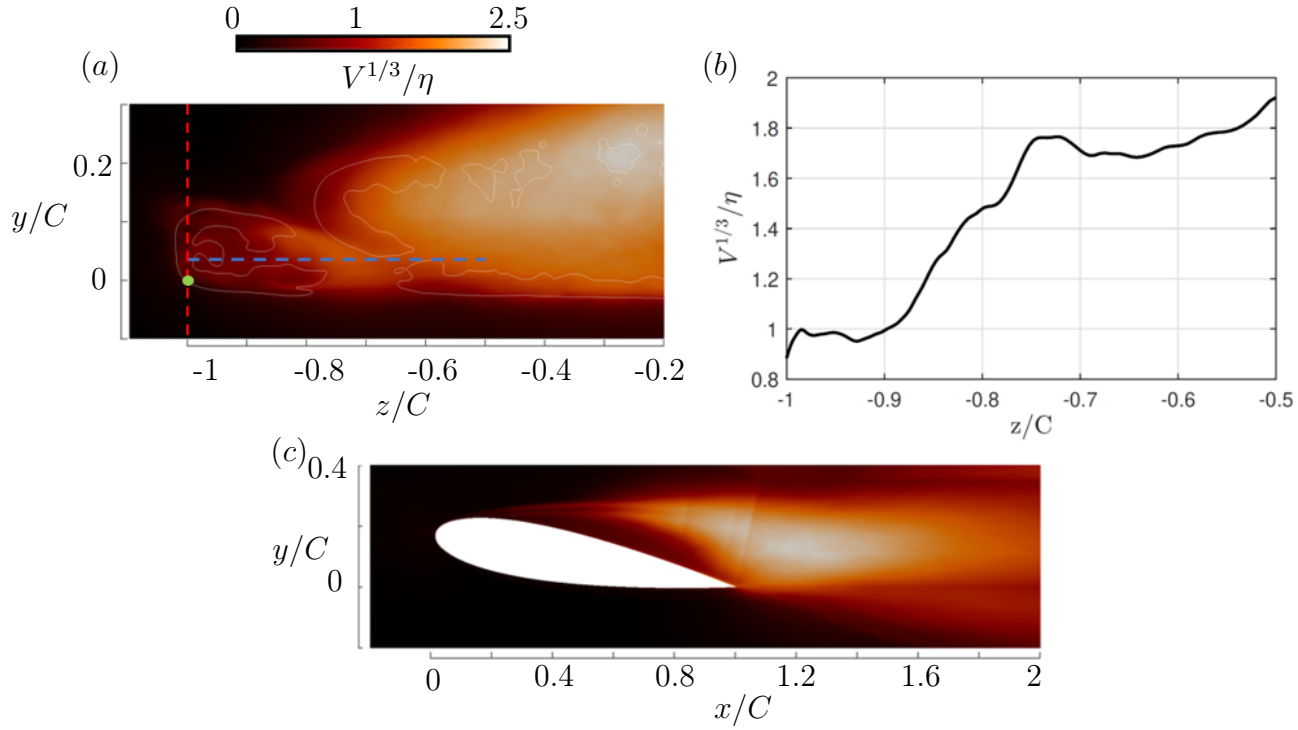


Figure 2.3: Plots of the grid size to Kolmogorov length scale ratio, $V^{1/3}/\eta$. (a) Contours in the $y-z$ plane at $x/C = 1.1$. The white curve represents the $Q = 5$ isoline, the red dotted line marks the location of the wingtip plane, and the green dot the trailing edge tip corner. (b) Variation of $V^{1/3}/\eta$ along the dashed blue line shown in (a) at $y/C = 0.04$. (c) Contours of $V^{1/3}/\eta$ at $x-y$ plane at $z/C = -0.5$ (quarter-span).

dissipation rate, and s_{ij} are the components of the fluctuating strain-rate tensor. Figure 2.3(a) shows a contour plot of this ratio in the $z-y$ plane downstream of the trailing edge; the maximum value is below 2.5. In panel (b), the values along the blue dashed line shown in panel (a) are found to be below 2. Figure 2.3(c) shows contours in the $x-y$ plane located at quarter span; again the ratio does not exceed 2.5. The values are sufficiently small and in accordance with the recommendations of Yeung and Pope [1989].

Figure 2.4 shows two streamwise velocity profiles obtained with approximately 10, 30, 60 and 80 million cells. The results with 60 and 80 million cells are almost indistinguishable. This figure also demonstrates that the size of the computational domain in the streamwise (5C downstream of the trailing edge) and spanwise (1C normal to the tip-side) directions is big enough to capture the free-stream values. With respect to the domain size in the cross-stream direction (10C), figure 3.18 (discussed later in the thesis) shows that the blockage ratio (wake size/domain size) is about 5%.

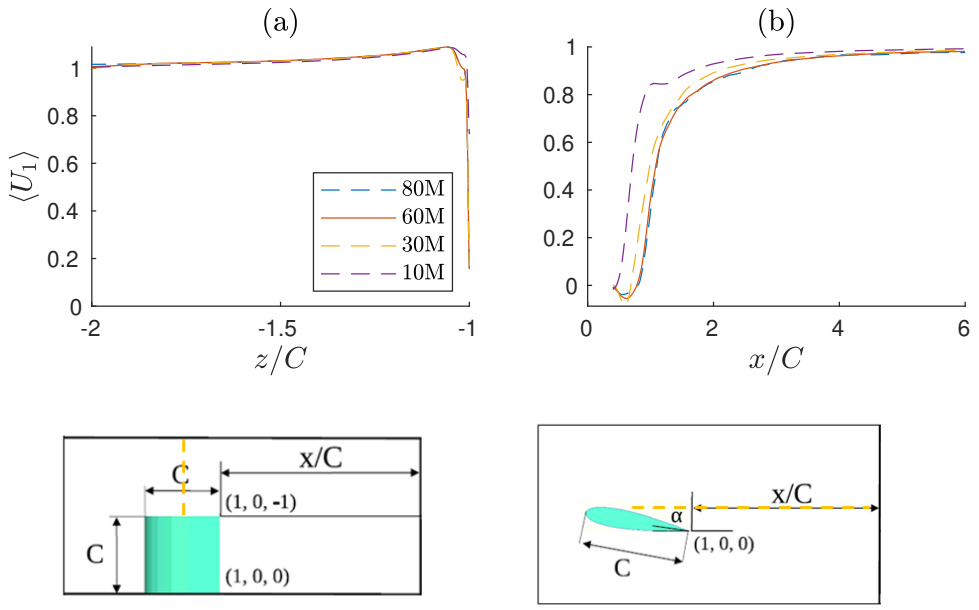


Figure 2.4: Comparison of distribution of $\langle U_1 \rangle$ velocity obtained using different mesh sizes along the (a) spanwise and (b) streamwise directions, along the dashed lines placed at $x/C = 0.5$ and $y/C = 0.12$ for (a), and $y/C = 0.2$ and $z/C = -0.5$ for (b).

2.4 Computational details for the simulation of the finite wing for $Re_c = 5000$

The flow configuration, geometry, angle of attack and domain size are similar to those of chapter 2. The Reynolds number Re_c is 5000 and the number of cells is $\approx 80M$ and the flow was simulated using 1024 cores. In total, 214 probe points were placed at different locations to monitor the velocity field. After all transients have passed and the flow reached a statistically steady state (which took about $60C/U_\infty$), the simulation was restarted and continued for another $200C/U_\infty$ to collect statistics. Validation against reference data from the literature and full assessment of the grid convergence was presented at $Re_c = 10^4$ in chapter 2. Figure 2.5 shows contours of the ratio of the grid size (taken to be equal to the cubic root of the cell volume, $V^{1/3}$) to the Kolmogorov length scale; the maximum value is approximately 1.2 at the tip of the recirculation zone. Such fine resolution is required to balance the enstrophy and total strain transport equations. Long simulation time enables capturing the rare and large events in the form of spiky bursts (short-lived and high-intensity events) that are part of the intermittent nature of turbulence; they are analysed in later sections. Two lines are shown in figure 2.5. Line A crosses the recirculation zone, while along line B, the flow is

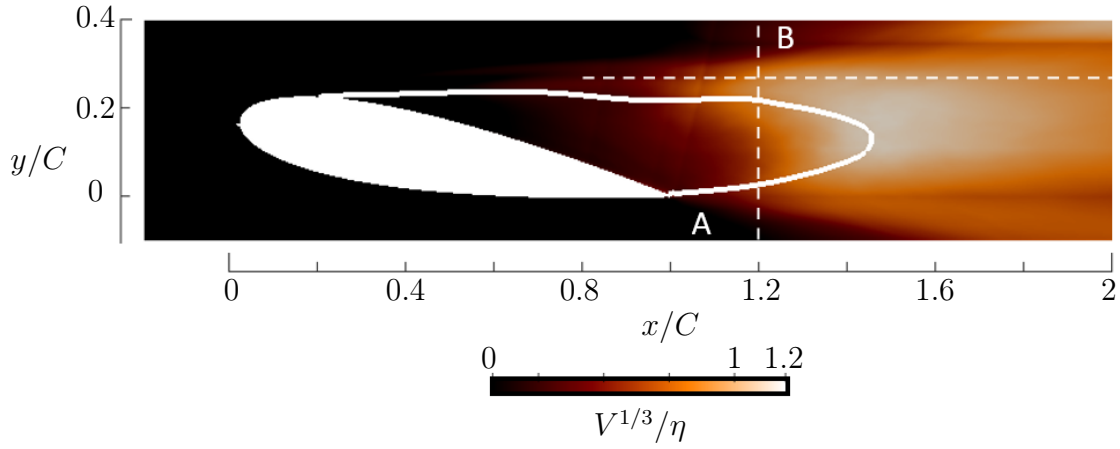


Figure 2.5: Contours of $V^{1/3}/\eta$ in the $x-y$ plane at $z/C = -0.2$. The white dotted line A goes through the recirculating zone and B through the transition.

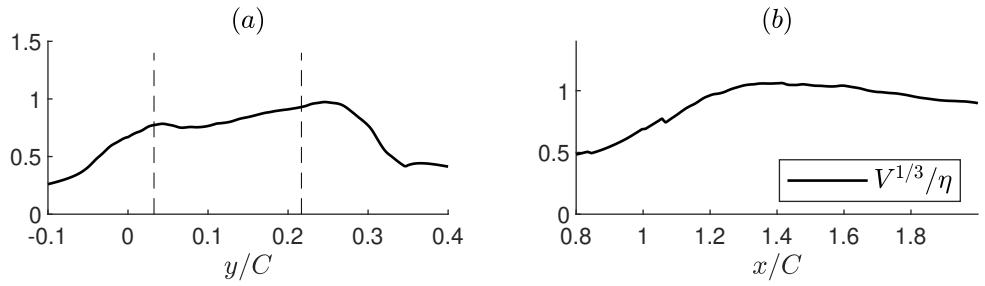


Figure 2.6: Variation of grid size to Kolmogorov length scale ratio, $V^{1/3}/\eta$ along (a) line A and (b) line B. The vertical dashed lines in (a) denote the boundaries of the recirculation zone.

transitioning. Figure 2.6(a) shows that along line A, the resolution is sub-Kolmogorov. Figure 2.6(b) corresponding to line B, shows that from $x/C \approx 1.3 - 1.8$ the resolution is very close to Kolmogorov. We are interested in analysing the small-scale dynamics in the recirculating and transitional flow regions. A total of 30 and 90 probes were placed along lines A and B respectively to obtain measurements for post-processing analysis.

The values obtained in terms of resolution are notably smaller than the recommendations put forth by Yeung and Pope [1989], Laizet et al. [2013]. To further validate the reliability of the results presented in this study, in figure 4.14 and 4.15, the balance of the transport equation of enstrophy and strain, respectively, is shown. Some terms involve tensor contractions using cubic velocity gradients. The minimal residual values ensure that the data obtained has converged sufficiently to provide reliable statistics. Additionally, despite the inhomogeneous condition of

the present flow, figure 4.18 shows a very close resemblance to HIT. Furthermore, the joint pdf of the second and third invariants of the VGT, as depicted in figure 4.23, in a section where the flow approximates HIT conditions, clearly demonstrates the teardrop form, which is notably challenging to replicate using advanced LES modeling strategies [Chevillard and Meneveau, 2006, Wilczek and Meneveau, 2014]. The fact that our work covers sections outside of HIT conditions in the flow makes DNS the only available source to conduct our research.

Chapter 3

Structure of vorticity and turbulence fields in a separated flow around a finite wing

The chapter is organized as follows. Section 3.1, 3.2 and 3.3 present and analyse the main features of the three-dimensional velocity field, the generation and evolution mechanisms of the streamwise vortices, and the spatially developing turbulence field, respectively. We conclude in section 3.4. The work presented in this chapter has been published in Bilbao-Ludena and Papadakis [2023][1].

3.1 Main features of the near wake velocity field

Contours of the time-averaged streamwise velocity at different streamwise planes are shown in figure 3.1. A separation bubble starts at $x/C \approx 0.2$ and does not close on the suction side of the wing. Close to the leading edge, the separating region occupies most of the span, but once the secondary flow in the wingtip starts to develop, the left boundary is displaced inboard. This creates a recirculating bubble with the outboard end forming an angle with the streamwise direction; this will be seen more clearly in subsequent figures. A 3D separated region with a similar trapezoidal shape has been also observed in [Garmann and Visbal, 2017] for a wing with a rounded tip profile. It is very interesting to see that at $x/C \approx 0.8$ another small recirculating bubble (indicated by a deep blue color) appears close to the wingtip; this bubble closes in the

[1]Part of the work in this chapter was also presented at following conferences: UK Turbulence Consortium Annual Review 2022 held at the South Kensington Campus, Imperial College London, Twelfth International Symposium on Turbulence and Shear Flow Phenomena (TSFP12) 2022 held in Osaka, Japan (Online). Entry submitted to the ARCHER2 Image and Video Competition 2021, organized by the ARCHER2 UK National Supercomputing Service, and image was chosen to feature in the ARCHER2 Calendar 2022.

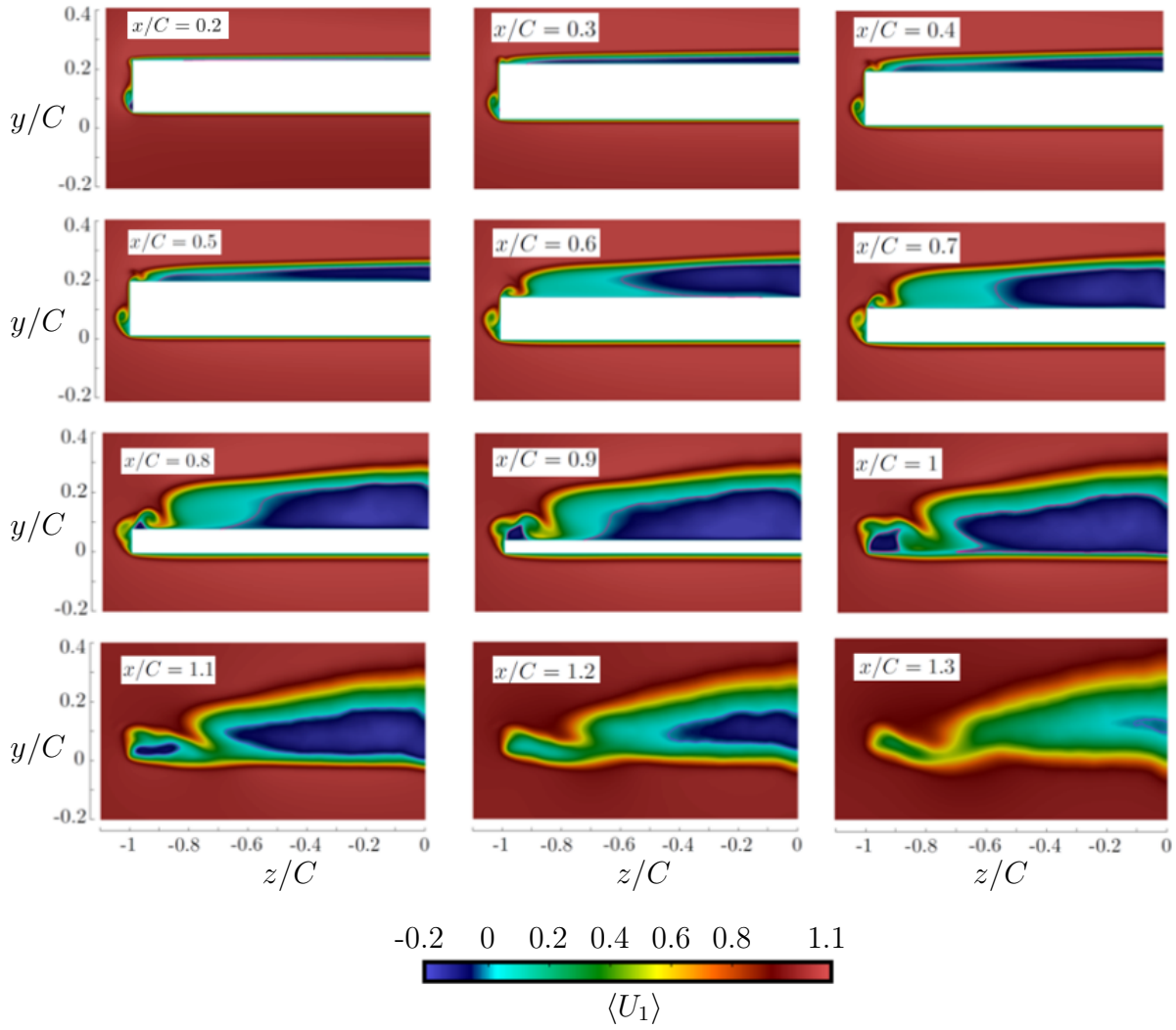


Figure 3.1: Contours of the mean axial velocity $\langle U_1 \rangle$ at equally spaced planes $x/C = 0.2, \ldots 1.3$. The purple-coloured contour line represents $\langle U_1 \rangle = 0$.

near wake at $x/C \approx 1.2$. Between the two recirculation regions, a jet with positive velocity appears. As will be seen later, the shear layers in the wall-normal and spanwise directions play a very important role in the turbulence production and distribution of Reynolds stresses across the span. The flow has a wake-like behaviour, i.e $\langle U_1 \rangle < 1$ at all planes. The only region where $\langle U_1 \rangle > 1$ is observed slightly above the wake where the velocity magnitude reaches a value of approximately 1.1.

The Q-criterion was used to identify the emerging coherent structures of the finite wing flow. The identification method λ_2 [Jeong and Hussain, 1995] was also implemented and resulted in similar structures. Q is defined as the second invariant of velocity gradient tensor $\frac{\partial U_i}{\partial x_j}$, i.e. $Q = 0.5\,(\Omega_{ij}\Omega_{ij} - S_{ij}S_{ij})$, where Ω_{ij} and S_{ij} are the components of the instantaneous rotation

and strain-rate tensors respectively. Values $Q > 0$ denote a rotation-dominated region, which can be used for vortex identification purposes.

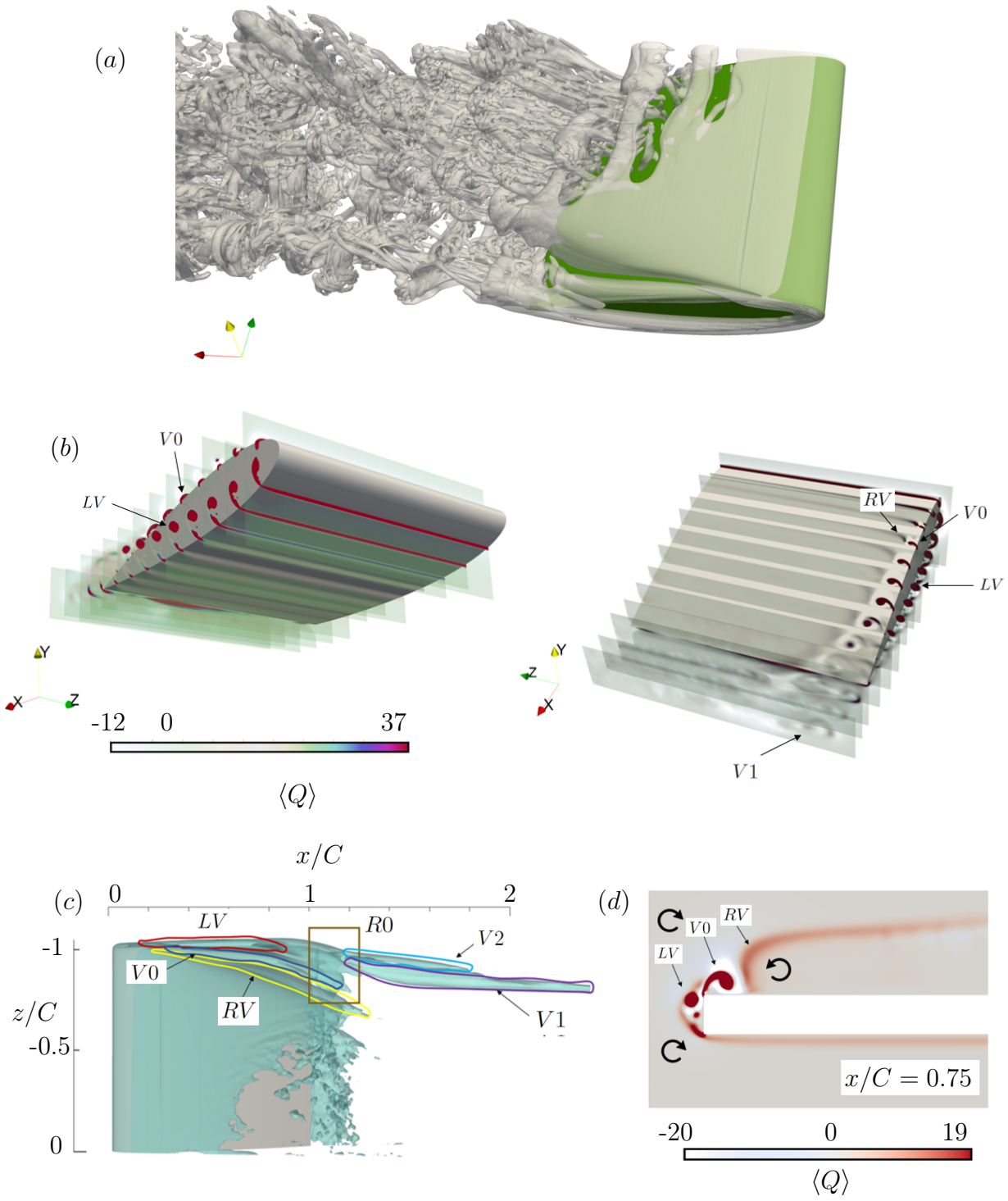


Figure 3.2: (a) Instantaneous isosurface of $Q = 5$. The wing is shown in green colour in the background. (b) Contours of the time-average $\langle Q \rangle$ at equally spaced planes $x/C = 0.1, 0.2, ..., 1.3$. with designated vortical structures. (c) Visualization and designation of vortical structures using the iso-surface $\langle Q \rangle = 5$. (d) Organization of the vortex structure topology at $x/C = 0.75$.

Figure 3.2(a) shows the instantaneous isosurface $Q = 5$. The laminar flow separates at the leading edge and the separated shear layer undergoes Kelvin-Helmholtz (KH) instability, leading to roll-up and the formation of KH vortices. Such vortices have also been seen in other works on infinite wings [Rosti et al., 2016, Shan et al., 2005, Jiang and Liu, 2004]. Further downstream the vortices break down resulting in transition to turbulence and the emergence of fine eddies in the proximity of the trailing edge. This process does not extend over the whole span though, and it is absent around the wing tip (up to $x/C \approx 0.7$, between $z/C \approx -1$ and -0.9). In this area, the secondary flow from the pressure side distorts the shear layer emerging from the leading edge and prevents separation, keeping the flow laminar; there is no evidence of KH instability either.

Visualization of isosurfaces of the time-average Q-criterion from different viewing angles enables us to understand better the structures that originate in the pressure area and the tip region. Figure 3.2(b) shows clearly one vortex that starts at the flat tip side and grows. This vortex is designated as Left Vortex (LV) and arises due to the spanwise separation of the shear layer emanating from the pressure side of the wing. Below LV (panel (b) and (d)), the Q-criterion reveals a smaller structure that is approximately $\approx 10\%$ (panel (d) of the size of LV. Despite displaying persistence in the streamwise direction, its relatively small core size and minimal impact on the development of the tip vortex wake (as demonstrated in the following sections), we do not consider this structure as one of the main vortical structures. However, we will describe its characteristics and connection with the other structures. Near the sharp edge on the suction side, a concentrated vortex starts developing at around $x/C = 0.1$, it grows and subsequently weakens as it approaches the trailing edge; we designate this vortex as V0. The evolution of this vortex can be visualized better in figure 3.2(c); we see that V0 has decayed shortly after the trailing edge. Starting at the same initial plane as V0, the Right Vortex (RV) develops in parallel but its trace is lost at a short distance downstream of the trailing edge.

The vortical region $R0$ is defined as the area where the separated shear layers taking part in the roll-up process amalgamate and readjust downstream of the tip. The main trailing vortex V1 originates at $R0$ and persists throughout the computational domain. V2 is another vortex that originates also from $R0$ but it is absorbed further downstream into V1. The organization

of the vortex structure topology at $x/C = 0.75$ is shown in figure 3.2(d) and shows good agreement with visualizations reported in experimental [Katz and Galdo, 1989, Bailey et al., 2006, Giuni, 2013, Birch et al., 2003] as well as computational studies [Smith and Ventikos, 2021] despite employing different Re_c and geometrical setups. In the next section, we explore in more detail the origins of these vortices and their evolution.

3.2 Origins of streamwise vortical structures and their evolution due to vortex stretching/tilting mechanisms

3.2.1 Generation of streamwise structures

We start by analysing the early formation of the vortices in the wing surface. Close to the leading edge the flow is laminar, transition occurs downstream, at around $x/C \approx 0.8 - 0.9$, see section 3.3. Figure 3.3 shows contours of streamwise vorticity, $\langle\Omega_x\rangle$, close to the wing tip. Starting at $x/C = 0.05$, the pressure difference between the lower and upper surface induces a relatively uniform spanwise flow leaking towards the tip. This creates the expected positive $\langle\Omega_x\rangle > 0$ at the pressure side, however a rather unexpected negative $\langle\Omega_x\rangle$ appears on the suction side (indicating a spanwise velocity directed towards the tip). This plane is located very close to the leading edge, and the secondary flow has not yet reached the suction side, as can also be seen from figure 3.1.

To explain this unexpected behaviour very close to the leading edge, it is instructive to consider a three-dimensional view of the distribution of the pressure coefficient $\langle C_p\rangle = \frac{\langle P\rangle - \langle P_\infty\rangle}{0.5\rho U_\infty^2}$, where ρ is the fluid density, as shown in the left panel of figure 3.4, where the isosurface $\langle U_1\rangle = 0$ is also superimposed. A zoomed-in view close to the leading edge is shown in the right panel. This figure elucidates very clearly the underlying mechanism that explains the observed behaviour of streamwise vorticity. As the flow approaches and impinges on the leading edge, the pressure grows reaching $\langle C_p\rangle \approx 1$ as expected, see panel (a). Close to the tip however, the flow is diverted in the spanwise direction and separates around the sharp round edge, creating a small recirculation zone, as shown in panel (a). Note that underneath the recirculation zone a patch of very low pressure forms, see dark blue region in the flat tip in panel (b). As the flow accelerates around the suction side, the pressure is also reduced (see light blue strip in

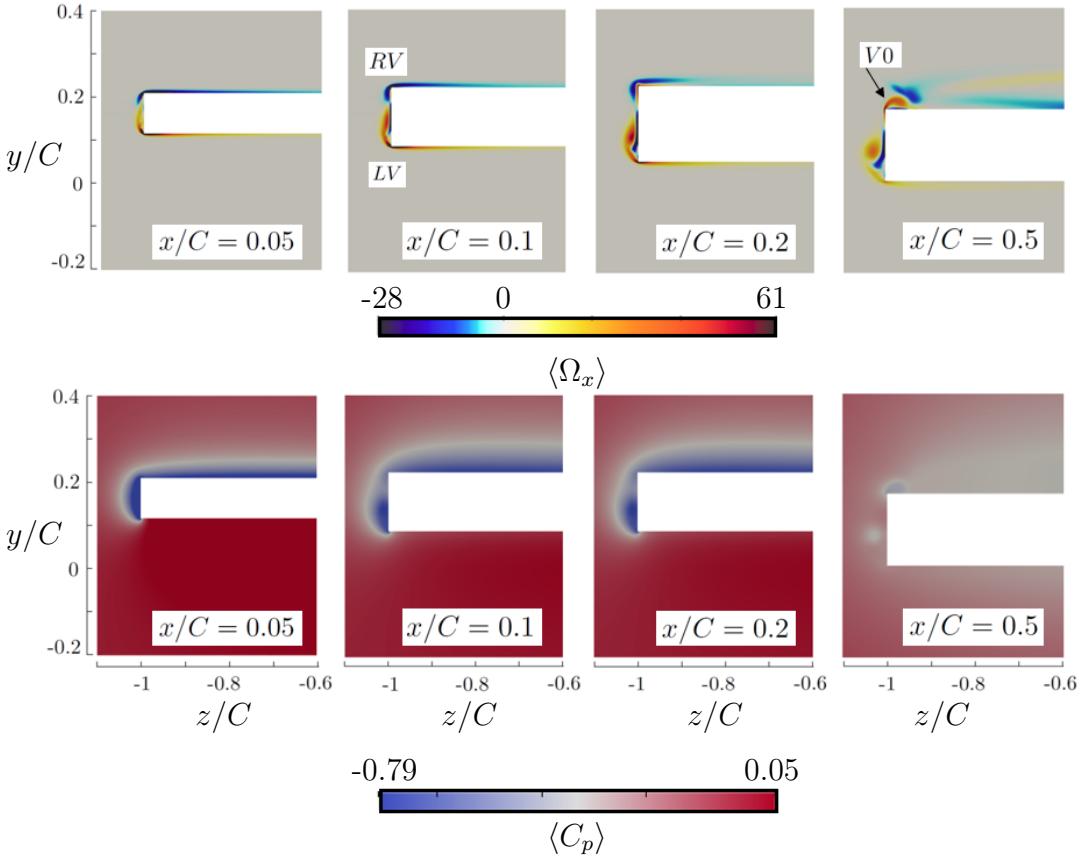


Figure 3.3: Contours of time-averaged streamwise vorticity (top row) and pressure coefficient (bottom row) at different x planes, highlighting the early formation of vortical structures RV, LV and V0.

panel (b)), however it remains larger compared to the pressure on the flat tip side (this is corroborated by the pressure contours shown in the bottom row of figure 3.3). This pressure difference between the top surface and the flat tip results in negative spanwise velocity that is responsible for the negative $\langle\Omega_x\rangle$. Essentially the flow is sucked towards the low pressure region forming on the tip surface. Note that the mechanism that creates this secondary motion is the pressure difference between top surface and the tip, and not between the top and bottom surfaces as in the standard lifting line theory. It is expected that the same mechanism will be also at play for rounded tips, depending on the radii of curvature in the $x-z$ and $x-y$ planes. If for example, the acceleration around the rounded tip in the $x-z$ plane is faster compared to that in the x-y plane, lower pressure will appear on the surface of the tip resulting in a similar streamwise vorticity development as observed in Garmann and Visbal [2017].

The subsequent evolution of spanwise vorticity is shown in figure 3.3. At $x/C = 0.1$, the

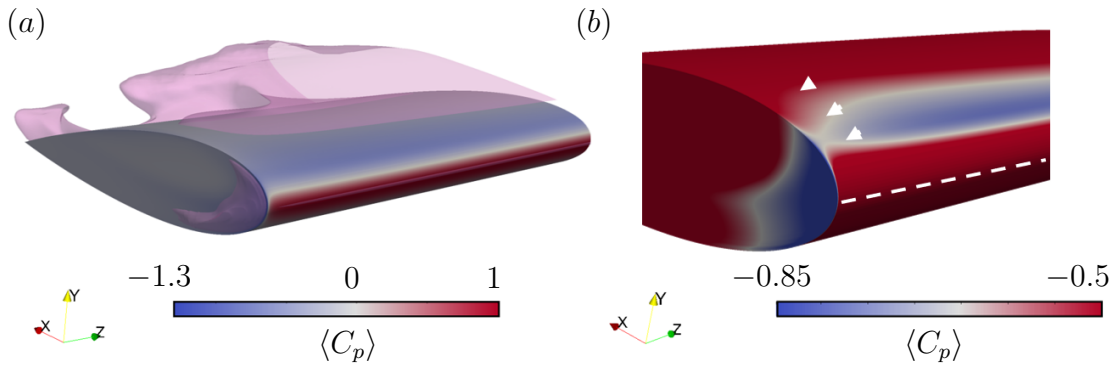


Figure 3.4: Contours of $\langle C_p \rangle$ over the wing (a) superimposed with the $\langle U_1 \rangle = 0$ isosurface, (b) zoomed-in view around the leading edge. The white dashed line marks the stagnation line across the span. The three white triangles indicate the streamwise locations $x/C = 0.05$, 0.1, and 0.2.

positive streamwise vorticity that was generated at the pressure side starts moving towards the suction side, creating the LV vortex, see also panel (b) of figure 3.2. Further downstream, starting at $x/C = 0.2$, the flow starts to separate also at the top tip corner, providing the earliest signs of V0 vortex, which is more clearly visible at $x/C = 0.5$. This vortex grows underneath the shear layer with negative Ω_x that is already present in the suction side, and displaces it in the inboard direction, thus creating a bent RV shear layer. The three vortices, LV, V0, RV leave their footprint very clearly in the $y - z$ plane, as can be seen from panel (d) of figure 3.2. This analysis shows that the separating shear layer from the leading edge (see figure 3.1) acquired negative streamwise vorticity very early on (due to the developed pressure distribution as already mentioned), and vortex RV is the result of intrusion and bending of this shear layer by V0. It is worth noting that starting from $x/C = 0.2$ a significant patch of negative $\langle \Omega_x \rangle$ begins to emerge beneath and between LV and the tip surface. This corresponds to the origins of the aforementioned unnamed small structure mentioned in the previous section (3.2). This patch takes the form of a secondary structure that appears to be influenced by the behavior of LV and the pressure variation in this specific location of the surface. The confined space in which it develops, constrained by LV and the tip surface, limits its evolution and thus its size further downstream.

Figure 3.5 shows contour plots of $\langle \Omega_x \rangle$, $\langle \Omega_y \rangle$ and $\langle \Omega_z \rangle$ at different streamwise planes further downstream. This figure clearly highlights the multiple and diverse vortical structures formed

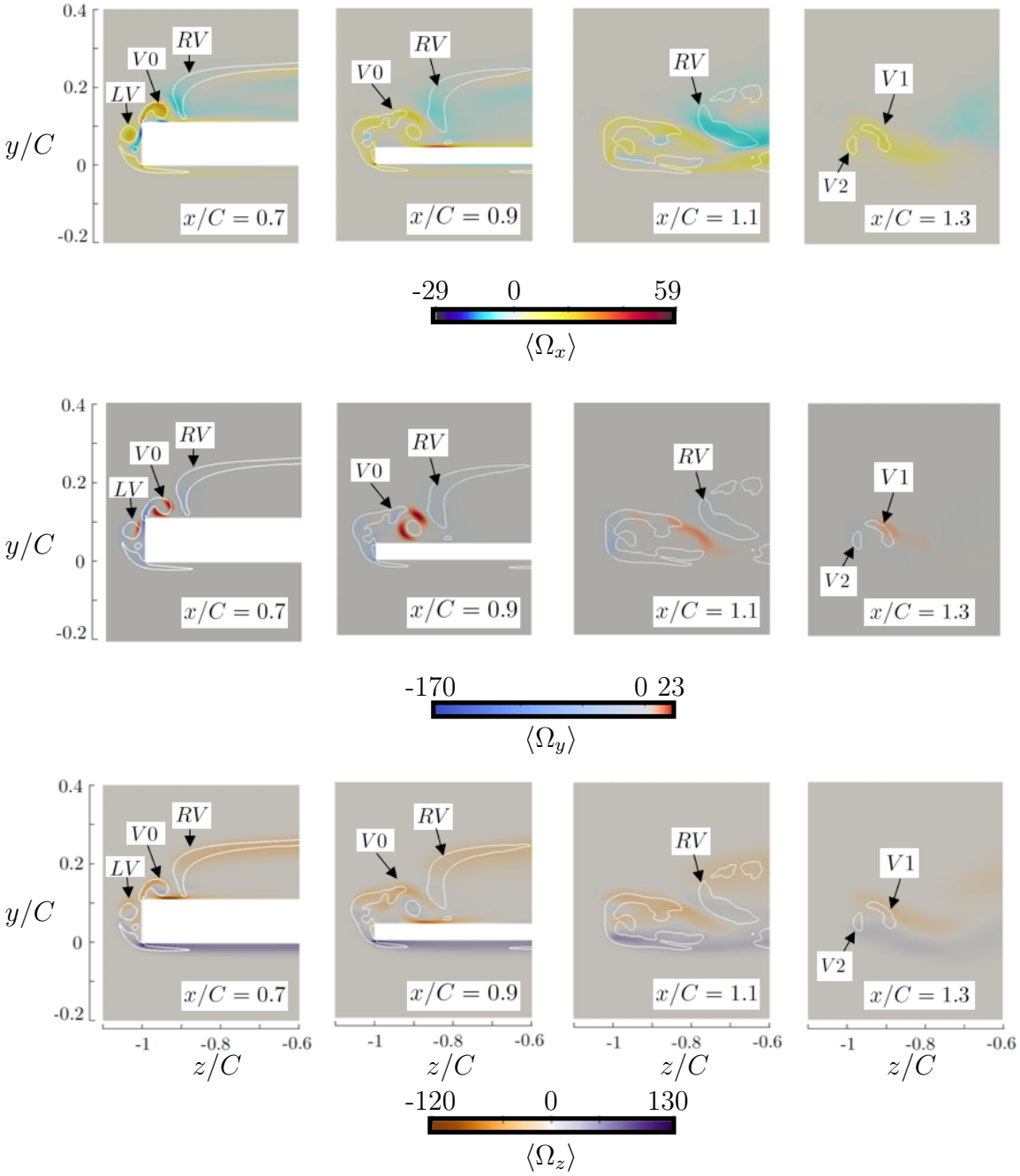


Figure 3.5: Contour plots of time-averaged vorticity components (streamwise at top row; wall-normal at middle row; spanwise at bottom row) at different x/C planes. The isoline $\langle Q \rangle = 7$ is indicated in white colour.

around the sharp corners of the wingtip. The $\langle \Omega_x \rangle$ component maintains its coherence at $x/C = 0.7$, and all the three aforementioned vortical structures are visible. Additionally, the smaller unnamed vortical structure developing beneath LV counter-rotates with respect to the direction of this vortex. Further downstream, at $x/C = 0.9$, V0 and LV (that have the same sense of rotation) seem to merge, leading to a large vortex structure, which retains its

coherence at $x/C = 1.1$. On the other hand, regarding of the small unnamed vortical structure that counter-rotates beneath LV, no further evidence can be identified in the wake beyond $x/C = 1.1$. It is interesting to observe the formation of a thin layer of strong positive $\langle\Omega_x\rangle$ close to the wall, in the gap between V0 and RV at $x/C = 0.9$. It is difficult to explain the origin of this layer, but probably it is related to the spanwise pressure gradient generated by the unequal vorticities of V0 and RV.

The wall-normal component, $\langle\Omega_y\rangle = \dfrac{\partial\langle U_1\rangle}{\partial x_3} - \dfrac{\partial\langle U_3\rangle}{\partial x_1}$, which encodes the spanwise inhomogeneity of $\langle U_1\rangle$ velocity, peaks at two regions located in the boundaries between the three vortices (see contours at $x/C = 0.7$ and 0.9). Further downstream, only one peak remains, while in the wake $\langle\Omega_y\rangle$ decays.

The stronger vorticity component as expected is $\langle\Omega_z\rangle$, but its detailed structure is significantly distorted by the strongly three-dimensional nature close to the wing tip. Note that both positive and negative values appear at $x/C = 0.7 - 1.3$ in the suction side. The positive ones are due to the recirculation zone close to the tip shown in figure 3.1. In the near wake, at $x/C = 1.3$, the shape is dictated by the two wakes from the top and bottom sides, and the strong three-dimensionality has subsided.

3.2.2 The role of vortex stretching and tilting on the evolution of vortical structures - early stage

We now investigate how the three vortices identified earlier sustain or lose their strength. To this end, we employ the evolution equation of the time-average vorticity component $\langle\Omega_i\rangle$, which takes the form [Tennekes and Lumley, 2018]:

$$\langle U_j\rangle\frac{\partial\langle\Omega_i\rangle}{\partial x_j} + \langle u_j\frac{\partial\omega_i}{\partial x_j}\rangle = \langle\omega_j s_{ij}\rangle + \langle\Omega_j\rangle\langle S_{ij}\rangle + \nu\frac{\partial^2\langle\Omega_i\rangle}{\partial x_j^2}\,, \tag{3.1}$$

where lower case variables denote fluctuations, i.e. the Reynolds decomposition is $\Omega_i = \langle\Omega_i\rangle + \omega_i$. Vorticity can be amplified or suppressed due to the vortex stretching/tilting term $\langle\omega_j s_{ij}\rangle + \langle\Omega_j\rangle\langle S_{ij}\rangle$ [Wu et al., 2015]. In the following, we will investigate this term in more detail. In particular, we consider only the streamwise vorticity $\langle\Omega_x\rangle$ and the vorticity intensification $\langle\Omega_j\rangle\langle S_{xj}\rangle$, which can be decomposed into vortex stretching (or axial elongation) and tilting

terms,

$$\underbrace{\langle\Omega_j\rangle\langle S_{xj}\rangle}_{\text{vorticity intensification}} = \underbrace{\langle\Omega_x\rangle\langle S_{xx}\rangle}_{\text{vortex stretching}} + \underbrace{\langle\Omega_y\rangle\langle S_{xy}\rangle + \langle\Omega_z\rangle\langle S_{xz}\rangle}_{\text{vortex tilting}}. \tag{3.2}$$

Stretching and tilting represent features of vorticity kinematics which act only in 3D flows. From conservation of angular momentum, a vortex tube undergoing mean stretching, i.e. $\langle S_{xx}\rangle = \frac{\partial\langle U_1\rangle}{\partial x_1} > 0$, will become more narrow and have increased streamwise vorticity. On the other hand, under mean compression i.e. $\langle S_{xx}\rangle < 0$, the vorticity tube will grow thicker, resulting in a reduced rotational rate [Wu et al., 2015].

Vortex V0 emerging from the top sharp edge of the wing tip

We start with V0 and analyse the different terms of the vorticity transport equation at $x/C = 0.6$, where the flow is still laminar. Figure 3.6(a) shows (filled) contours of axial elongation superposed with (blue/red) line contours of $\langle\Omega_x\rangle$. We also plot in white line the contour of $\langle Q\rangle = 5$. The coloured line contours of vorticity and Q-criterion match well and demarcate the boundaries of V0. It can be seen that this vortical structure consists of a separating shear layer emanating from the sharp top edge of the tip and a vortex core. In the shear layer the axial strain rate $\langle S_{xx}\rangle$ is positive indicating elongation, while in the core it is negative. Axial vorticity is therefore intensified in the shear layer and subsequently feeds the core. This mechanism is confirmed in panel (c) which shows the variation of the stretching and tilting terms along a horizontal line that crosses V0 (yellow dashed line in panel (a)). The vertical line in the panel (c) demarcates the areas of positive and negative vortex stretching. Note that the tilting terms have opposite signs compared to the stretching term, but the latter is stronger in the shear layer region, resulting in a region of vorticity intensification. In the core region however, a region of vorticity suppression is identified, leading to the eventual decay of V0. Contours of the convection term $-\langle U_j\rangle\frac{\partial\langle\Omega_1\rangle}{\partial x_j}$ are shown in panel (b). This term takes positive values in the middle of the shear layer and the core (see also panel c), indicating the transport of diminishing $\langle\Omega_x\rangle$ downstream.

Figure 3.7 displays an isosurface of $-\langle U_j\rangle\frac{\partial\langle\Omega_1\rangle}{\partial x_j}$ with positive value. The isosurface consists of two legs that correspond to the two areas mentioned above. The outboard leg terminates at the point where the separated flow at the tip (shown in pink colour) starts to form. The

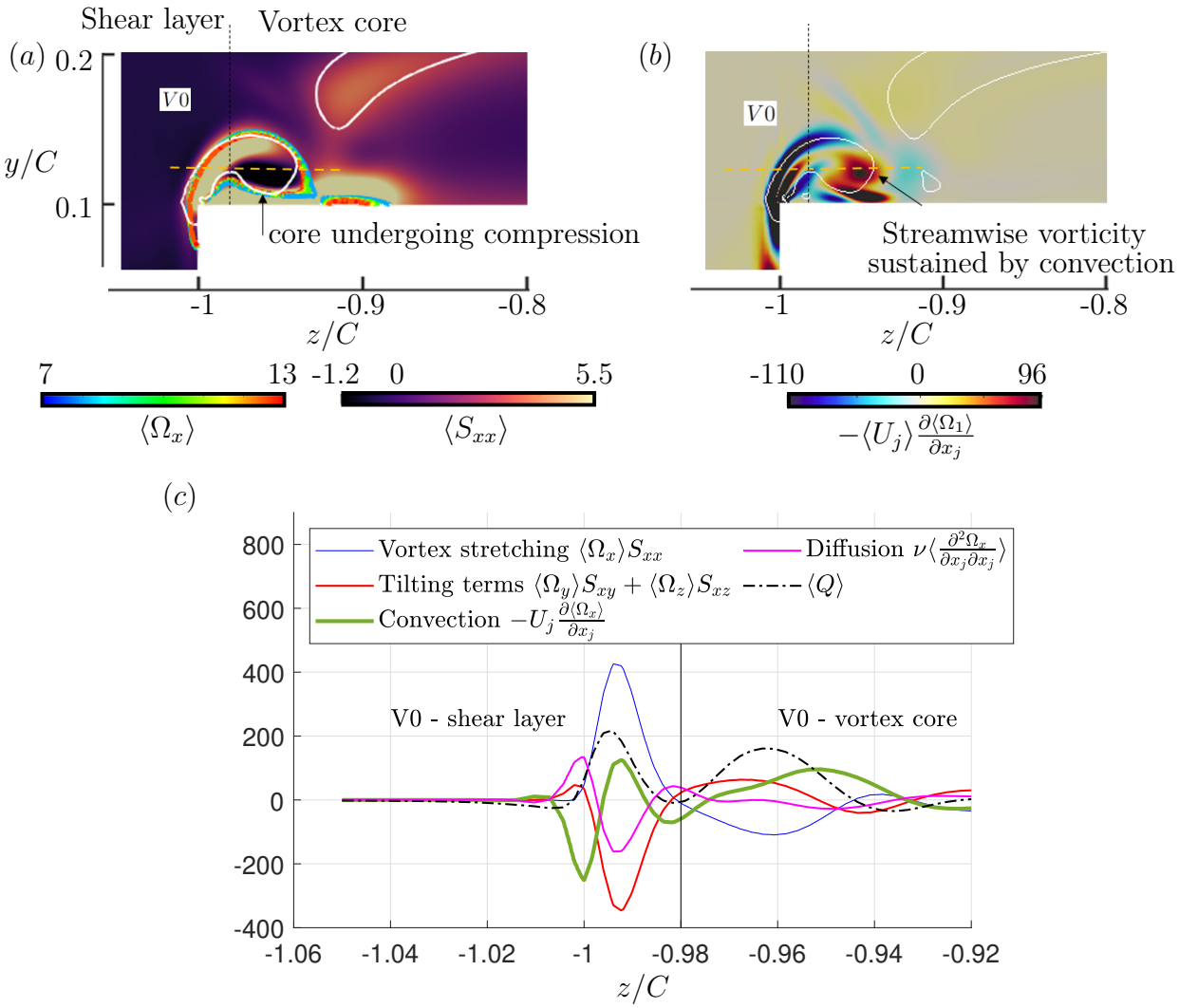


Figure 3.6: (a) Axial elongation rate (filled purple contours) superposed with streamwise vorticity (blue/red) line contours, (b) Convection term (filled contours) and (c) budgets of the vorticity transport equation along the horizontal yellow dashed line shown in panels (a) and (b). The white isoline depicts $\langle Q \rangle = 5$. The vertical solid black line in (c) demarcates the boundary between the shear layer and vortex core regions. Vertical dashed lines are placed in the same spanwise location in (a) and (b). Results at plane $x/C = 0.6$.

inboard leg continues slightly further downstream. Note the disintegration and amalgamation of V0 with LV close to the trailing edge.

Regions undergoing strong vorticity stretching or compression over the wing surface are shown in figure 3.8. The strong three-dimensionality of the flow is once again evident. The feeding shear layer emanating from the tip is a continuous source of positive vorticity to the core of V0 through stretching as can be seen from panel (a). This mechanism, first identified in figure 3.6 for a particular plane, is found to persist along the downstream direction but

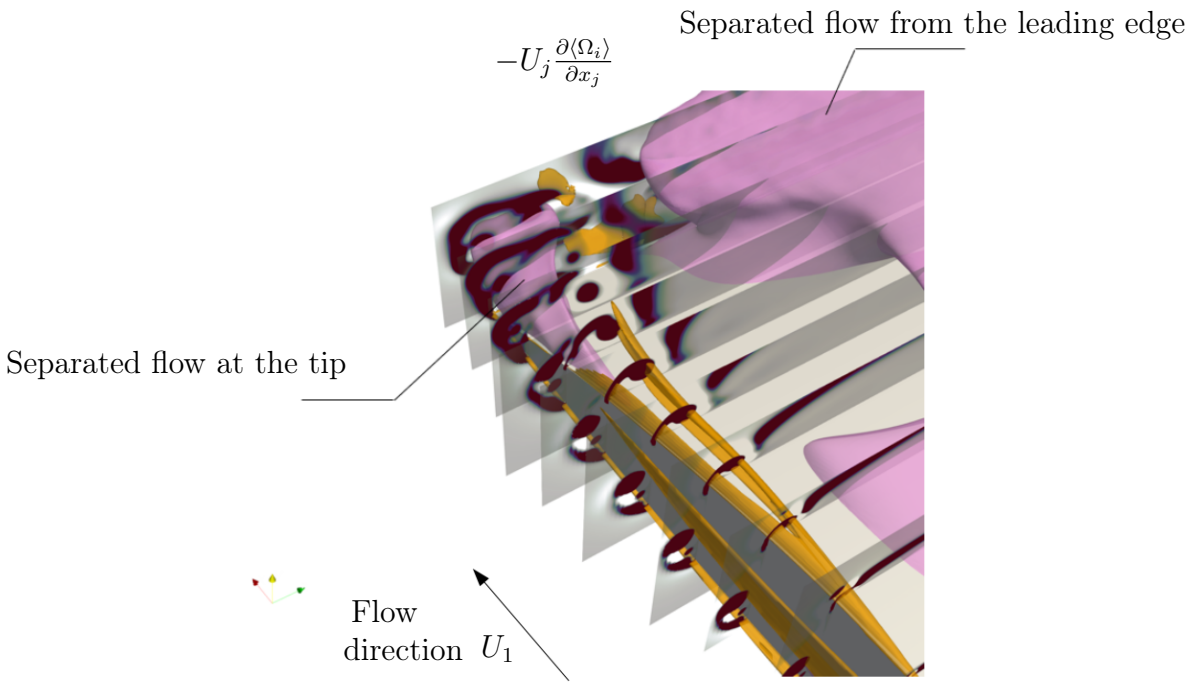


Figure 3.7: Isosurface of vorticity convection $-U_j \frac{\partial \langle \Omega_1 \rangle}{\partial x_j} = 78$ (orange colour). Vortex V0 is visualised by $\langle Q \rangle$ criterion (same values as in figure 3.2(b)) at equally spaced planes $x/C = 0.4 - 1.2$. The pink isosurface represents $\langle U_1 \rangle = 0$ and encloses the two separated flow regions (one that starts in the leading edge, and the other in the trailing edge, around the tip). The vorticity convection isosurface value corresponds to $\approx 52\%$ of the positive maximum value found within the core of V0 at the $z - y$ plane located at $x/C = 0.6$.

is distorted due to the presence of the separated region at the tip. In particular, the vortex stretching region lifts above the recirculating bubble. The region of vortex compression, shown in panel (b), is more compact and is localised around the core of vortex V0. As the latter is deflected inboard due to the recirculation zone around the tip, so does the compression region. Note that the presence of the recirculation zone severs the ties between the feeding shear and the core of V0. This has important implications for this vortex. While the compression mechanism is present from the early stages of V0 and persists throughout, once the tip recirculation bubble forms, the feeding shear can no longer provide a source of vorticity through stretching, leading to the eventual demise of V0.

This can be attested in figure 3.9 that shows the vortical structures at two planes close to the trailing edge, at $x/C = 0.85$ and 0.99. The mean axial strain rate is displayed in the background with filled contours, on which coloured isolines of $\langle \Omega_x \rangle$ are superposed together with

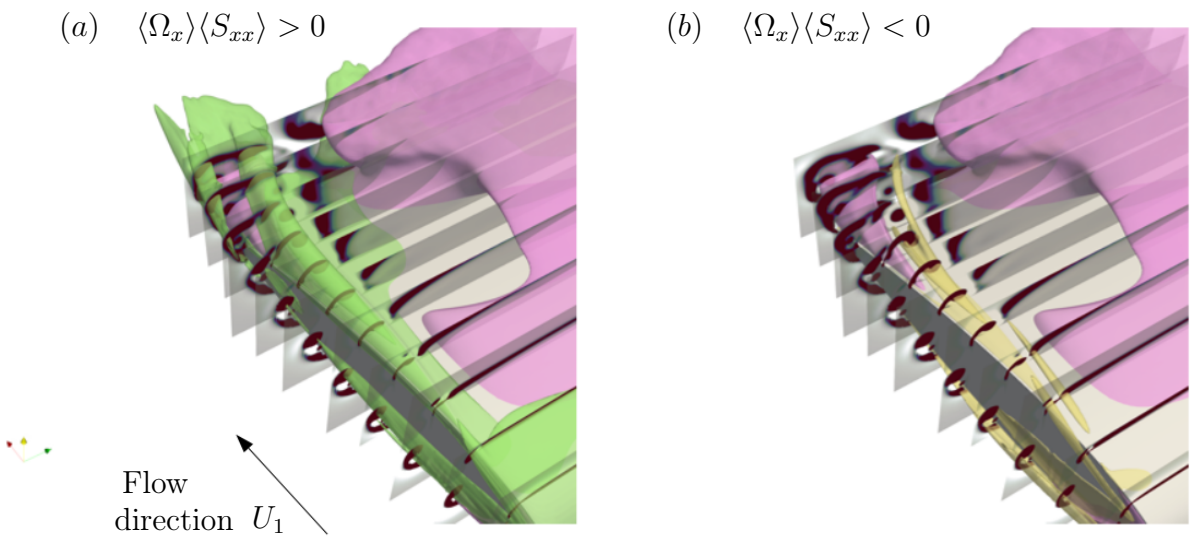


Figure 3.8: Isosurfaces of (a) vorticity stretching rate $\langle\Omega_x\rangle\langle S_{xx}\rangle = 14$ (in green colour) (b) vorticity compression rate $\langle\Omega_x\rangle\langle S_{xx}\rangle = -30$ (in yellow colour). The pink isosurface represents $\langle U_1\rangle = 0$. Results are shown at equally spaced planes $x/C = 0.2 - 1.2$. The isosurface values of the vortex stretching/compression rate correspond to $(a) \approx 32\%$ of the positive maximum value found within V1 at $x/C = 1.2$ and $(b) \approx 44\%$ of the minimum negative value within the core of V0 at the z-y plane located at $x/C = 0.85$. the reach self-similarity

the $\langle Q\rangle = 5$ white isoline. Note how the arc-shaped shear layer originating from the pressure side is further lifted away from the surface of the areofoil as x/C grows from 0.85 to 0.99. This is due to the presence of the recirculating bubble, as already mentioned. Vortex V0, shown here enclosed within a rectangle with dashed-lined perimeter, is disconnected from the feeding shear, thus losing its feeding source. Although it is still a coherent vortex in these two planes, shortly downstream it completely disintegrates and merges with the wake in the periphery of the trailing edge. This figure further corroborates the fact that compression effects play the dominant role in the annihilation of V0. On the other hand, the lifted shear layer carries strong streamwise vorticity (in the form of LV) which, after some readjustment, will eventually develop into the trailing vortex V1. This shear layer displaces the RV vortex further inboard. Note again the presence of a wall layer with strong positive streamwise vorticity. The layer has a finite extent in the spanwise direction and is confined between V0 and RV.

Using the components of R_A and Q_A (introduced in section 1.4.2) provides an alternative viewpoint, enabling a direct correlation between vortex intensification through the interaction of enstrophy production and strain production to be established. In this context, the definition

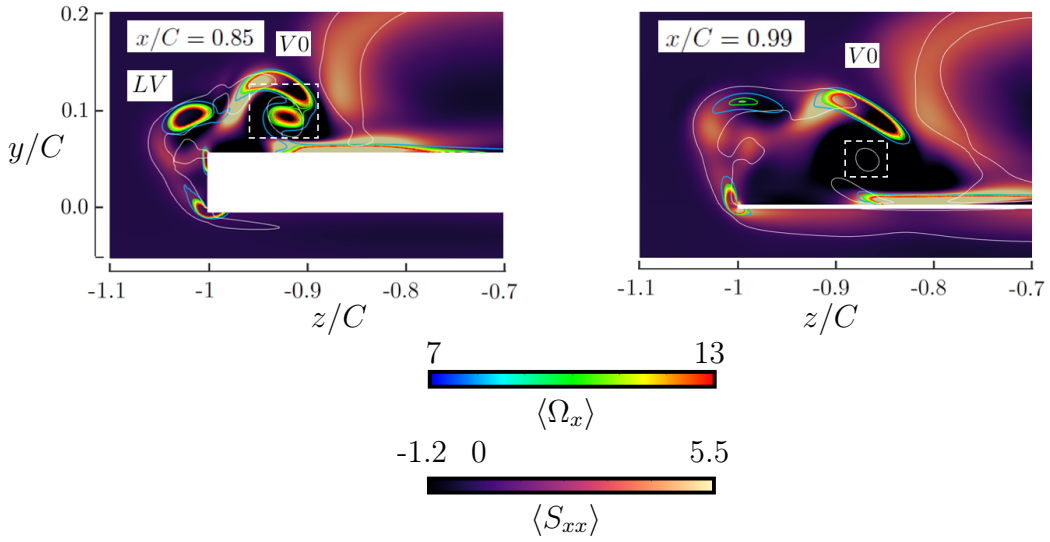


Figure 3.9: Coloured (filled) contours of elongation rate superposed with coloured (line) contours of $\langle\Omega_x\rangle$ at two planes $x/C = 0.85$ (left) and $x/C = 0.99$ (right). The white isoline depicts $\langle Q\rangle = 5$.

of $\langle R\rangle$ depends on the large-scale enstrophy production $\langle\Omega_i\rangle\langle\Omega_j\rangle\langle S_{ij}\rangle$ and the large-scale strain self-amplification $-\langle S_{ij}\rangle\langle S_{jk}\rangle\langle S_{ki}\rangle$ [Tsinober, 2009]. This yields an equivalent expression with respect to R_A

$$\langle R\rangle = -\frac{1}{3}(\langle S_{ij}\rangle\langle S_{jk}\rangle\langle S_{ki}\rangle + \frac{3}{4}\langle\Omega_i\rangle\langle\Omega_j\rangle\langle S_{ij}\rangle\langle\Omega_x\rangle)\,. \tag{3.3}$$

The coloured contours in figure 3.10 represent $\langle\Omega_i\rangle\langle\Omega_j\rangle\langle S_{ij}\rangle$ and the large-scale strain self-amplification $\langle S_{ij}\rangle\langle S_{jk}\rangle\langle S_{ki}\rangle$ at $x/C = 0.85$ where the isoline of $\langle Q\rangle = 10$ has been used for better visualisation purposes. A notable observation is the remarkable similarity in the distribution of contour lines for these two production terms, with slightly higher values originating from $\langle\Omega_i\rangle\langle\Omega_j\rangle\langle S_{ij}\rangle$, particularly in the feeding shear that is being disintegrated and in the developing boundary layer below the core. Conversely, the vortex core of V0 exhibits relatively lower values for both quantities. It is important to note that in the streamwise direction at this location, the contrast between turbulent and laminar regions is clearly defined (as we will see later in figure 3.18), compared to a fully developed turbulence case. Consequently, the spatial extent over which these two production terms operate is highly confined. This observation indicates that the levels of production activity influencing the dynamics of V0 are mostly concentrated in the vicinity of the core, consistent with our prior analysis. The presence of negative values

for these two quantities in the feeding shear of LV indicates a weakening of the feeding shear further downstream. This observation suggests that the LV core undergoes stretching (refer to figure 3.12) and maintains its strength through this mechanism rather than through convection (refer to figure 3.8), as the vorticity in this feeding shear at this streamwise location is being weakened.

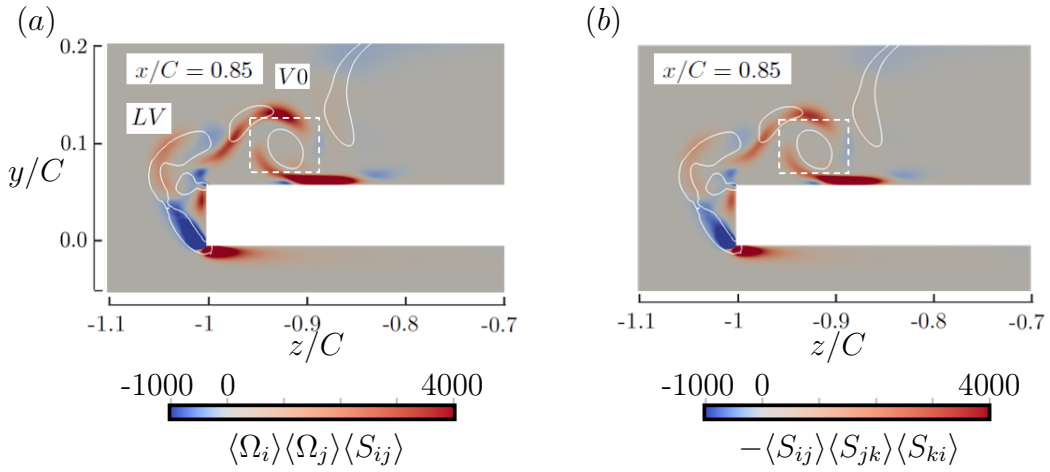


Figure 3.10: Coloured contours of (a) $\langle\Omega_i\rangle\langle\Omega_j\rangle\langle S_{ij}\rangle$ $\langle\Omega_x\rangle$ and (b) $\langle S_{ij}\rangle\langle S_{jk}\rangle\langle S_{ki}\rangle$ at $x/C = 0.85$. The white isoline depicts $\langle Q\rangle = 10$.

We now turn our attention to the exact extent in the difference between the two production terms, as well as the difference between vorticity and strain. Figure 3.11 displays contours of $\langle Q\rangle$ and $\langle R\rangle$ at $x/C = 0.85$. In panel (a), within the core of V0, vorticity prominently dominates over strain, as anticipated. This dominance is also observed in the feeding shear, which is undergoing disintegration. Outside the core, strong contours of excess strain are evident. This observation confirms the compression effects that is occurring within the surroundings of core as seen in figure 3.9. In panel (b), the contours reveal that an excess of large-scale enstrophy production is present in the feeding shear layer and a small portion inside the core of V0. On the other hand, an excess of large-scale strain self-amplification is observed below and above the core. Despite the subtle similarities observed in figure 3.10, certain areas of excess or deficit of the production terms are highly concentrated here with contour levels that are approximately an order of magnitude lower. In contrast to the clearly defined filled contours in the V0 core depicted in panel (a), in panel (b), the core appears significantly affected by the simultaneous occurrence of different dynamics. From an axial perspective, our prior analysis revealed axial compression.

However, the presence of negative values of $\langle R \rangle$ (indicating an excess of enstrophy production) in the core of V0 shows the impact of vortex tilting on sustaining the vortex strength. Upon closer examination of the topology of regions where vortex compression is active (which will be discussed in greater depth in Chapter 4), these regions are characterized by $\langle Q \rangle > 0$ and $\langle R \rangle > 0$. These regions encompass approximately $\approx 40\%$ of the core, predominantly affecting the upper part, indicating a clear indication of the overall weakening trend of the vortex strength.

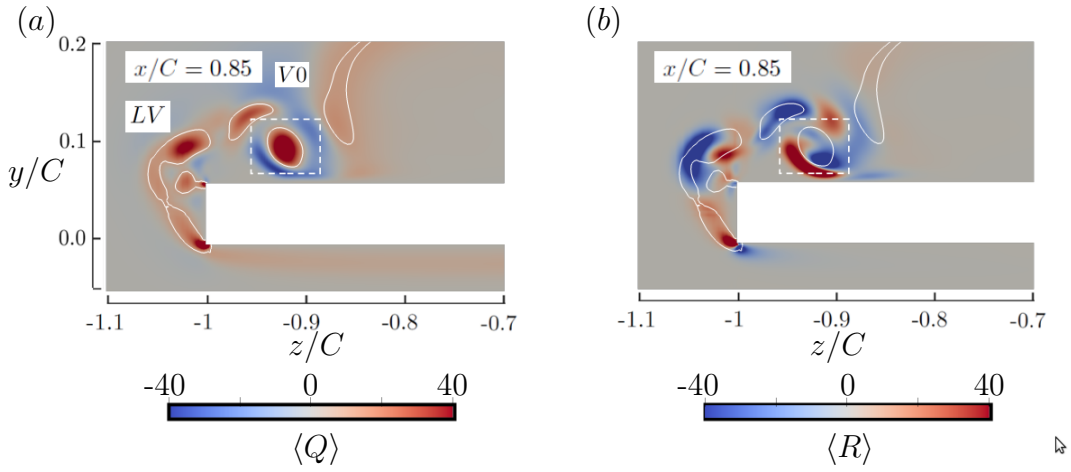


Figure 3.11: Coloured contours of (a) $\langle Q \rangle$ and (b) $\langle R \rangle$ at $x/C = 0.85$. The white isoline depicts $\langle Q \rangle = 10$.

Vortex LV

Attention is now turned to vortex LV, which originates on the pressure side and develops along the flat tip face. Figure 3.12 shows an isosurface of the vorticity stretching rate. Note that LV starts to develop early, at around $x/C \approx 0.2$, with its core forming slightly above the aforementioned recirculation bubble that appears in the flat tip close to the leading edge. This makes physical sense; outside the recirculation zone, the flow accelerates in the streamwise direction, leading to a positive strain rate that increases the streamwise vorticity of LV. The vorticity intensification however becomes weaker further downstream. As the flow develops, the core of LV is lifted up and at $x/C \approx 0.9$, it emerges on the suction side. In this region, it is amalgamated with the arch-shaped shear layer which feeds V0 with vorticity; this shear layer is found above the trailing edge recirculation pocket, as was seen more clearly in figure 3.8.

Figure 3.13 shows the distribution of the vorticity generation terms within the feeding shear

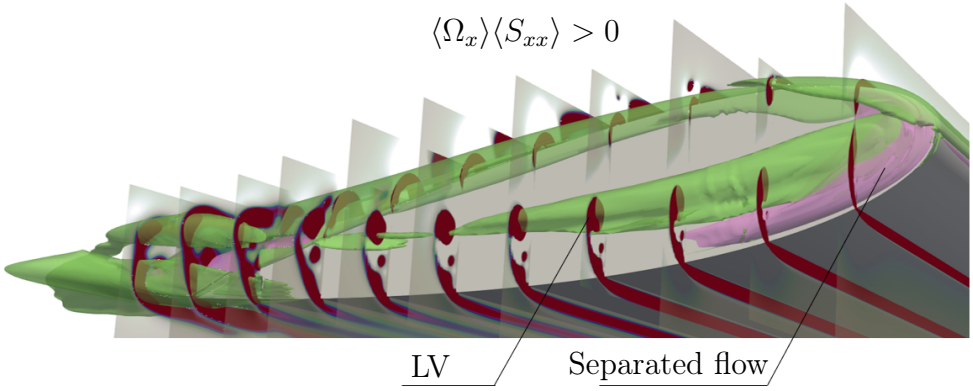


Figure 3.12: Isosurface of vorticity stretching rate $\langle S_{xx}\rangle = 14$ in the tip (green colour). Vortex LV is visualised by plotting the $\langle Q\rangle$ criterion (same values as in figure 3.2(b)) at equally spaced planes $x/C = 0.1 - 1.1$. The pink isosurface represents $\langle U_1\rangle = 0$. The isosurface $\langle S_{xx}\rangle$ value corresponds to $\approx 11\%$ of the positive maximum value found within the core of LV at the $z-y$ plane located at $x/C = 0.3$.

and the core of vortex LV at $x/C = 0.35$. The figure reveals the mechanism with which LV gains axial vorticity. Within the separated shear layer feeding LV, vortex tilting is the dominant positive term; this term is plotted with a solid red line in panel (d). Indeed strong spanwise vorticity is produced in the pressure side and the component $\langle\Omega_z\rangle\langle S_{13}\rangle$ of the tilting term is responsible for generating $\langle\Omega_x\rangle$ in the tip. The shear layer then feeds the LV core with streamwise vorticity. In the core itself, the tilting term is negligible, as shown in panel (c), and LV is sustained by a weakly positive stretching term.

The counter-clockwise rotating vortex RV

The generation mechanism of vortex RV close to the leading edge was elucidated earlier in section 3.2.1. Here we investigate the mechanism that sustains RV. Figure 3.14 (a) shows contours of vortex stretching rate $\langle\Omega_x\rangle\langle S_{xx}\rangle$ at plane $x/C = 0.85$. As already mentioned, RV is located to the right of V0 and is suspended at a higher wall-normal distance. The term $\langle\Omega_x\rangle\langle S_{xx}\rangle$ is negative, see colour scale at the bottom of panel (b). Since $\langle\Omega_x\rangle < 0$, RV is subject to stretching and this is the mechanism that sustains it. This can also be seen from panel (c) that plots the budgets of the vorticity equation along the yellow horizontal dashed line that crosses RV, as shown in panel (a). The tilting terms play a minor role. Figure 3.14

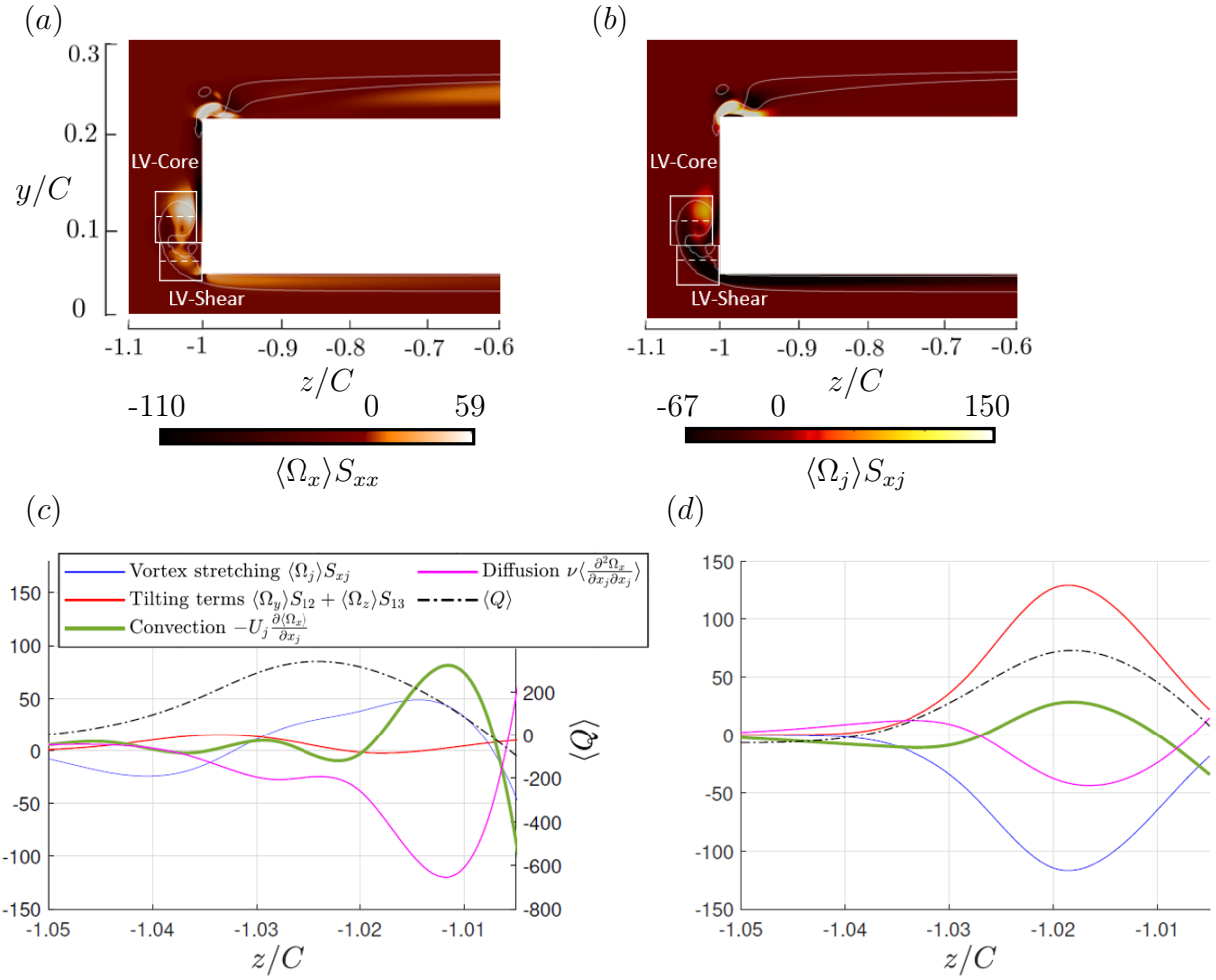


Figure 3.13: Contour plots of axial vorticity generation term (a) stretching only and (b) stretching and tilting, for vortex LV at $x/C = 0.35$. The solid white isoline depicts $\langle Q \rangle = 5$. Spanwise distribution of the budget terms of the vorticity transport equation along (c) the core and (d) the feeding shear of LV. The exact locations are marked as white dashed lines in panels (a) and (b).

(b) shows contours of stretching term in the $x - z$ plane with $y/C = 0.1$. The plots show all vortices examined so far, and clearly display the different signs of the stretching term. Strong positive values appear for LV, and negative for V0 and RV. But V0 carries positive vorticity, RV negative, so this term has the opposite effect, it is detrimental for the former and favourable for the latter. This explains why V0 is annihilated shortly downstream of the trailing edge while RV persists, as be clearly seen in panel (b). Eventually RV also disintegrates, but it does so further downstream, at around $x/C \approx 1.2$.

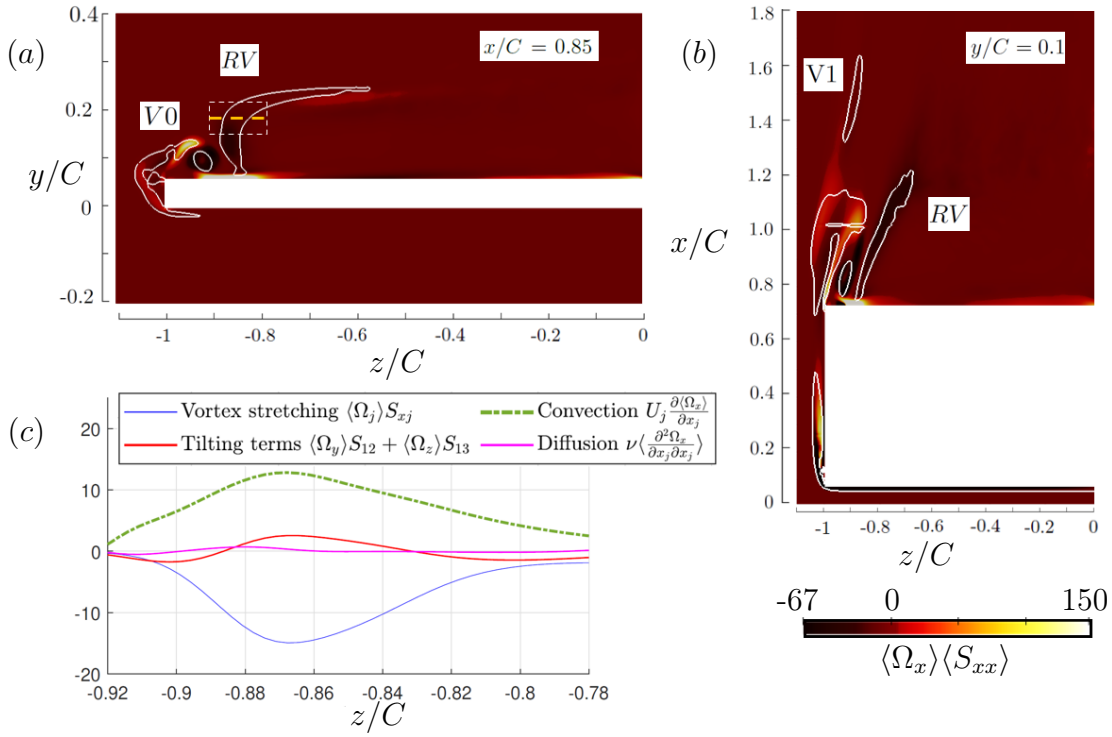


Figure 3.14: Contours of vortex stretching rate $\langle\Omega_x\rangle\langle S_{xx}\rangle$ at planes (a) $x/C = 0.85$ and (b) $y/C = 0.1$. (c) Balance of the vorticity transport equation along the dashed yellow line shown in panel (a) that crosses RV. The solid white isolines in (a) and (b) depict $\langle Q\rangle = 5$.

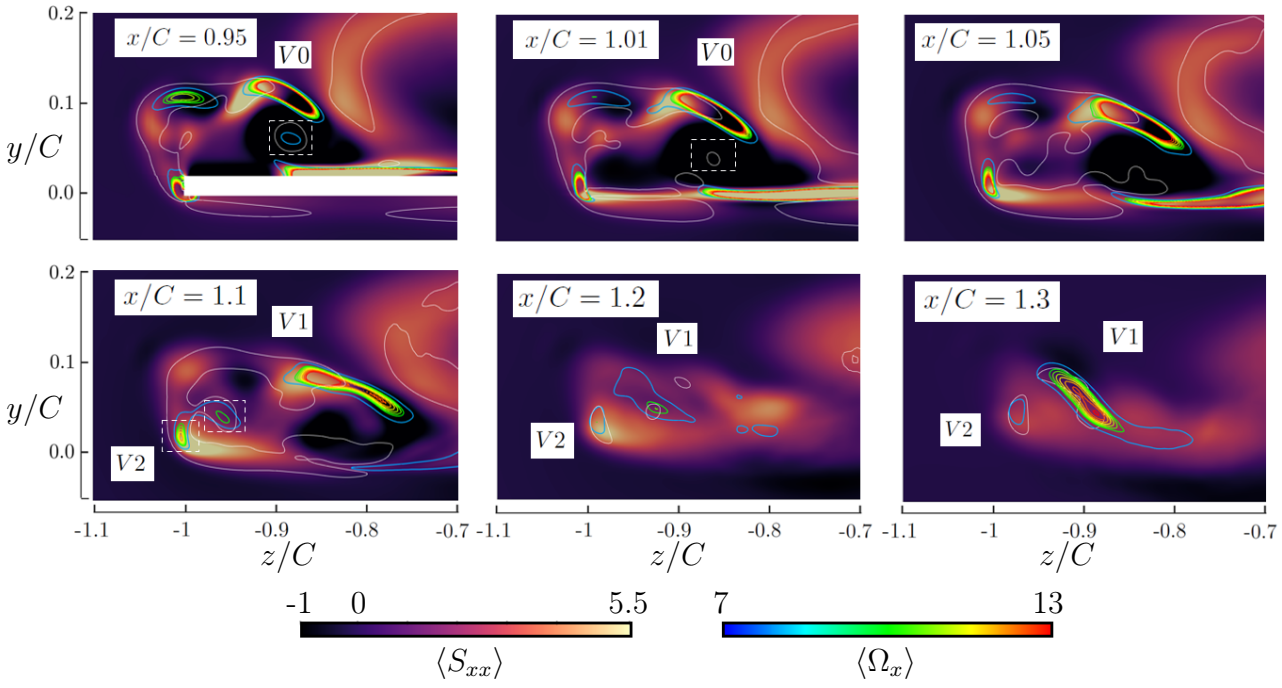


Figure 3.15: Emergence of the wake tip vortices V1 and V2. Contours (filled) of streamwise strain rate $\langle S_{xx}\rangle$ superposed to coloured isolines of positive $\langle\Omega_x\rangle$ at different x/C planes. The solid white line indicates $\langle Q\rangle = 5$.

3.2.3 Emergence of the wake tip vortices V1 and V2 - Late stage

Figure 3.15 presents (filled) contours of streamwise strain rate $\langle S_{xx} \rangle$ superposed with isolines of positive vorticity $\langle \Omega_x \rangle$. The arch-like structure that was formed from the secondary flow around the recirculation zone at the tip persists up to about $x/C = 1.1$. This structure carries two regions of concentrated vorticity, located at approximately the same wall normal distance, $y/C = 0.1$, and at spanwise locations $z/C = -1$ and -0.9. The former patch of vorticity quickly disappears, because it is located within a region of compression (dark contours), but the latter patch grows due to stretching (note the yellow-coloured spot of high acceleration at $z/C = 0.9$ in planes $x/C = 0.95 - 1.1$). Eventually this patch will evolve to form the tip vortex V1 that will persist in the wake, see plane $x/C = 1.3$. The core of this vortex is located slightly inboard with respect to the tip, at $z/C \approx -0.9$. This agrees with the theoretical analysis of Milne-Thomson [1958]. We conjecture that the high strain rate that leads to the intensification of V1 is due to the recovery of the streamwise velocity downstream of the recirculation bubble that forms around the tip of the trailing edge. It is also interesting to observe that the near wall vorticity patch (that forms between V0 and RV) is immersed in a region of compression shortly downstream of the trailing edge and quickly disappears (it is detected until $x/C \approx 1.1$). Vortex V2 starts to be visible in the lower tip corner in planes $x/C = 0.95 - 1.05$ and undergoes stretching in all planes. It eventually gets absorbed into V1, as shown in 3.2(c).

Isosurfaces of the vortex intensification terms, stretching and/or tilting, are shown in figure 3.16. Panel (a) depicts the isosurface of the stretching term which occupies a large part of the wing tip region but has a fine extent downstream. Comparison with the $\langle \Omega_x \rangle$ isosurface, shown in panel (d), indicates a high degree of correlation. The tilting terms, panel (b), are more sporadic (we have used the same isosurface value for the stretching and tilting terms in order to make the comparison meaningful). Finally the total intensification term shown in panel (c), indicates a high degree of resemblance to the stretching term. This indicates that the tilting term is very important in the shear layer feeding LV with vorticity, see figure 3.13), but once this function is completed, the stretching term takes over and is the dominant factor in enhancing or suppressing the local vorticity. In this sense, the mechanism is consistent with the standard lifting line theory [Milne-Thomson, 1958]. Standard lifting line theory, developed

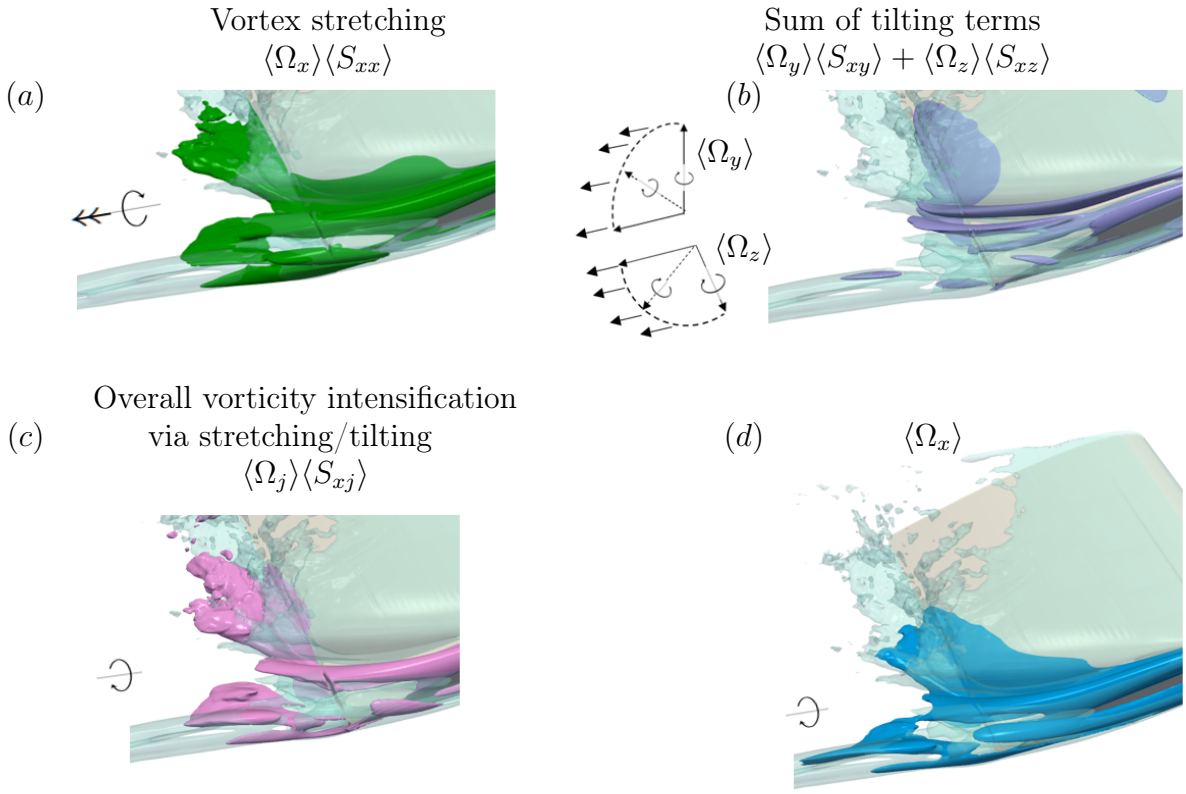


Figure 3.16: Isosurfaces of vortex intensification terms, stretching and/or tilting, superimposed on $\langle Q\rangle = 5$. (a) Stretching term $\langle\Omega_x\rangle\langle S_{xx}\rangle = 14$, (b) Tilting terms $\langle\Omega_y\rangle\langle S_{xy}\rangle + \langle\Omega_z\rangle\langle S_{xz}\rangle = 14$, (c) Sum of all terms, $\langle\Omega_j\rangle\langle S_{xj}\rangle = 12$. (d) $\langle\Omega_x\rangle = 8$. The isosurface values correspond to (a) $\approx 32\%$, (b) $\approx 67\%$, (c) $\approx 54\%$ and (d) $\approx 72\%$ of their corresponding positive maximum values within V1 in the z-y planes located at $x/C = 1.2$ (at $x/C = 1.3$ for (b)).

by Prandtl and Glauert [Tollmien et al., 1961], is an aerodynamic analytical approach that simplifies the study of lift distribution along the span of a finite wing. It assumes that the wing generates lift through a series of horseshoe-shaped vortices shed from each spanwise station. This theory views the wing as a lifting line and uses the Kutta-Joukowski theorem to establish a relationship between the lift per unit span and the circulation around the vortices [Green, 2012].

Figure 3.17 shows an isosurface of the total intensification term in the region $x/C = 1 - 2.2$ superposed with the $\langle Q\rangle = 5$ to visualise the V1 and V2 vortex structures. At $x/C = 1.5$, V1 and V2 have core area ratio $A^{V2}/A^{V1} = 0.26$ and a circulation ratio of $\langle\Gamma_x^{V2}\rangle/\langle\Gamma_x^{V1}\rangle = 0.28$. These differences prevent these two vortices from undergoing mutual induction that results in twisting and merging [Meunier et al., 2005, Leweke et al., 2016]. Instead, at $x/C = 1.8$, V2 gets stretched by the strain field of V1 whose circulation remains unaffected [Dritschel and Waugh,

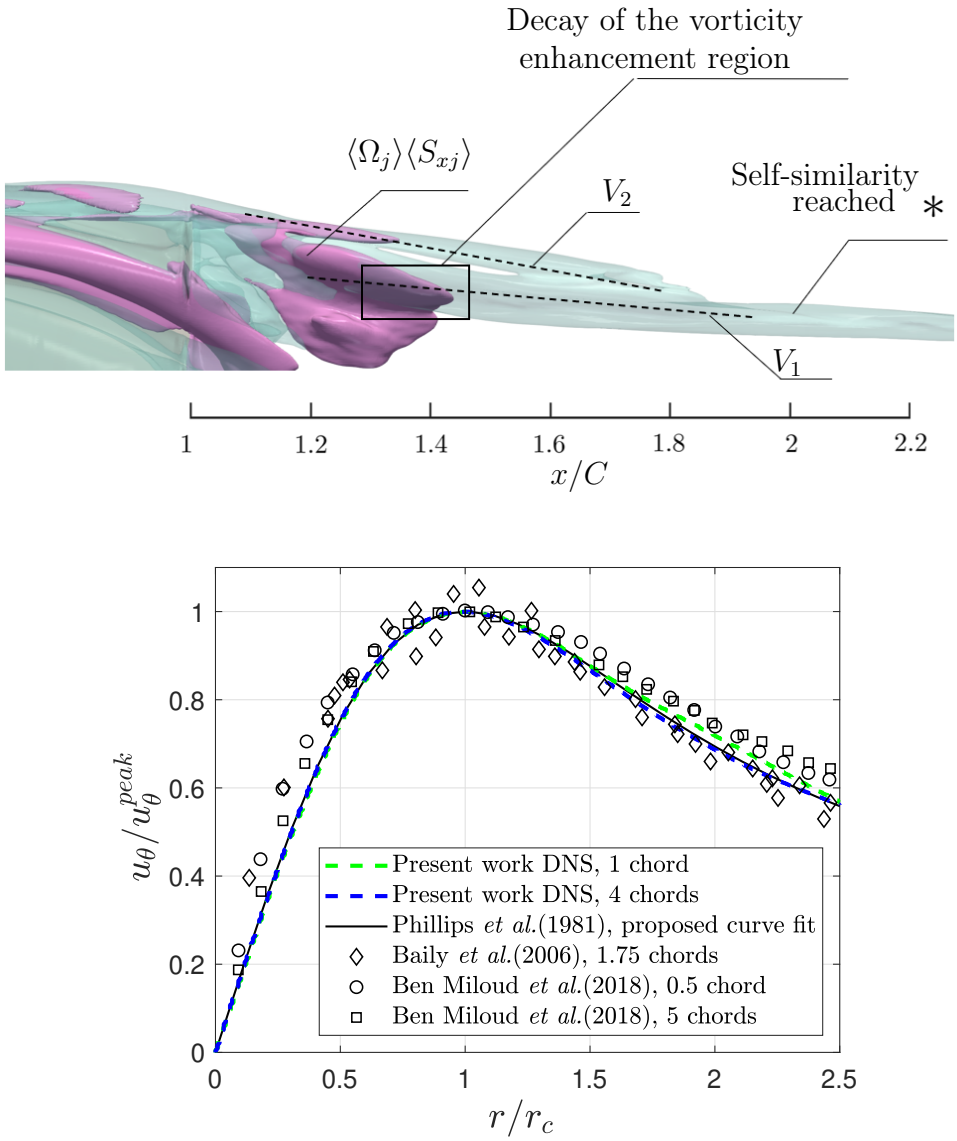


Figure 3.17: Isosurface of the vorticity intensification term $\langle\Omega_j\rangle\langle S_{xj}\rangle = 12$ (purple colour) superimposed on $\langle Q\rangle = 5$ (top). Normalised azimuthal velocity profile inside V1 at two positions $x/C = 2$ and 5, and comparison with self-similar profiles from the literature (bottom). The distances in the figure inset are measured downstream of the trailing edge.

1992], and is eventually absorbed by V1. Note that the isosurface value of $\langle\Omega_j\rangle\langle S_{xj}\rangle = 12$ is the same as one plotted in panel (c) of figure 3.16. Once the vorticity intensification term has decayed in the wake (at a location indicated by an asterisk), the azimuthal velocity profile in the radial direction inside V1 becomes self-similar. This is clearly evidenced in the bottom panel, which demonstrates very close agreement with self-similar velocity profiles reported in the literature [Phillips, 1981, Bailey et al., 2006]. The matching is very good, both in the inner part where solid-body rotation is found (linear variation), and also in the outer region $r/r_c \approx$

$[0.7 - 2.5]$, where the effect of the potential external flow is felt (r_c indicates the radial location of the maximum azimuthal velocity). Further downstream, the only mechanism affecting V1 is viscous diffusion, thus it decays slowly and persists until the end of the computational domain.

The sustained presence of V1 in its elongated form strongly suggests its manifestation as a vortex tube. Although enstrophy production becomes negligible upon reaching self-similarity between $x/C = 1 - 1.4$, it undergoes a significant amount of enstrophy production prior to this phase, as illustrated in figure 3.15. Betchov [1956] introduced the following equation under homogeneity constraints: $\langle \omega_i \omega_j s_{ij} \rangle = -\frac{3}{4} \langle \lambda_1 \lambda_2 \lambda_3 \rangle$. A positive value of this equation would require the presence of one large compressive strain, denoted by λ_3, accompanied by two weaker extensional strains, λ_1 and λ_2, associated with disc-like behavior or bi-axial stretching. However, when applying these findings to our case involving large scale production terms, it would suggest that the term λ_1^M, λ_2^M, and λ_4^M (where M denotes the large scale structure) would attain a similar disc-like strain field. However, this interpretation does not align with the evident display of the vortex tube form of V1 throughout its trajectory, where the uni-axial effect of the mean axial flow is visible. This disparity highlights the significant contrast between the time-average small scale turbulence under homogeneity and the geometry of highly anistropic large scale structures. Furthermore, it is intriguing to observe that the configuration of the strain eigenvalues as they reach self-similarity, even with minimal input of the production terms, preserve tubular configuration.

3.3 Turbulence structure of the separated wake

In this section, we examine the spatial distribution of turbulent kinetic energy (TKE), k, and its production. The objective is to identify the most intense regions and uncover the main production mechanisms. We focus on the near-field, i.e. distance $5\% - 30\% C$ from the trailing edge. In this region, the flow is far from being self-similar, thus well known viscous vortex models, such as the Burgers or Sullivan vortex [Green, 2012, Wu et al., 2015], do not apply.

The distribution of k across the span at different planes is shown in figure 3.18. Between $x/C = 0.5 - 0.8$ k, grows rapidly in the area just above the $\langle U_1 \rangle = 0$ isoline (marked with a solid black line). The high shear in this localised region triggers the formation and growth

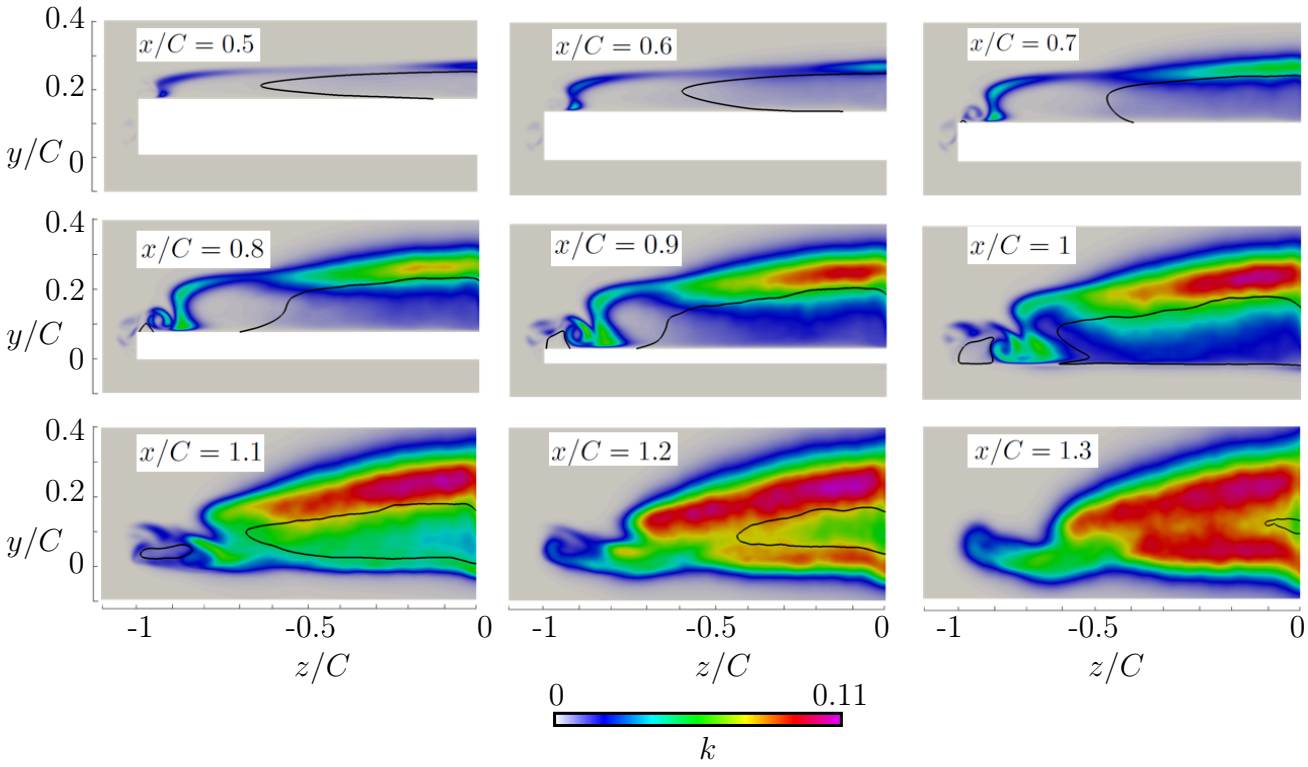


Figure 3.18: Contours of k plotted at equally spaced planes $x/C = 0.5 - 1.3$. The black contour line represents $\langle U_1 \rangle = 0$.

of Kelvin-Helmholtz instabilities, shown earlier in figure 3.2. Inside the recirculation bubble the value of k is low. The transition point is located approximately between $x/C \approx 0.8 - 0.9$. Note that the k contours in the suction side closely follow the shape of the distorted shear layer that carries the RV vortex. Close to the tip, low values of k are encountered. In the near wake at $x/C = 1.2$, two regions of high turbulent intensity can be detected, one originates from the suction side and the other from the pressure side, with the former being more widespread. Further downstream, at $x/C = 1.3$, the two regions merge.

Figure 3.19 shows contour plots of the production term $P = -\langle u_i u_j \rangle \langle S_{ij} \rangle$ in the same planes. The plots confirm the presence of a high production region just above the recirculation bubble; this explains the shape of k contours shown in the previous figure 3.18. The extent of the high P region in the spanwise direction closely follows the extent of the recirculation bubble, as can be seen in planes $x/C = 0.7 - 1.1$. Further downstream, at $x/C = 1.1 - 1.2$, the high P region envelops the shrinking bubble. The mixing in the wake fills the regions of low P with substantial values of k, as can be more clearly seen at plane $x/C = 1.3$ (compare with previous

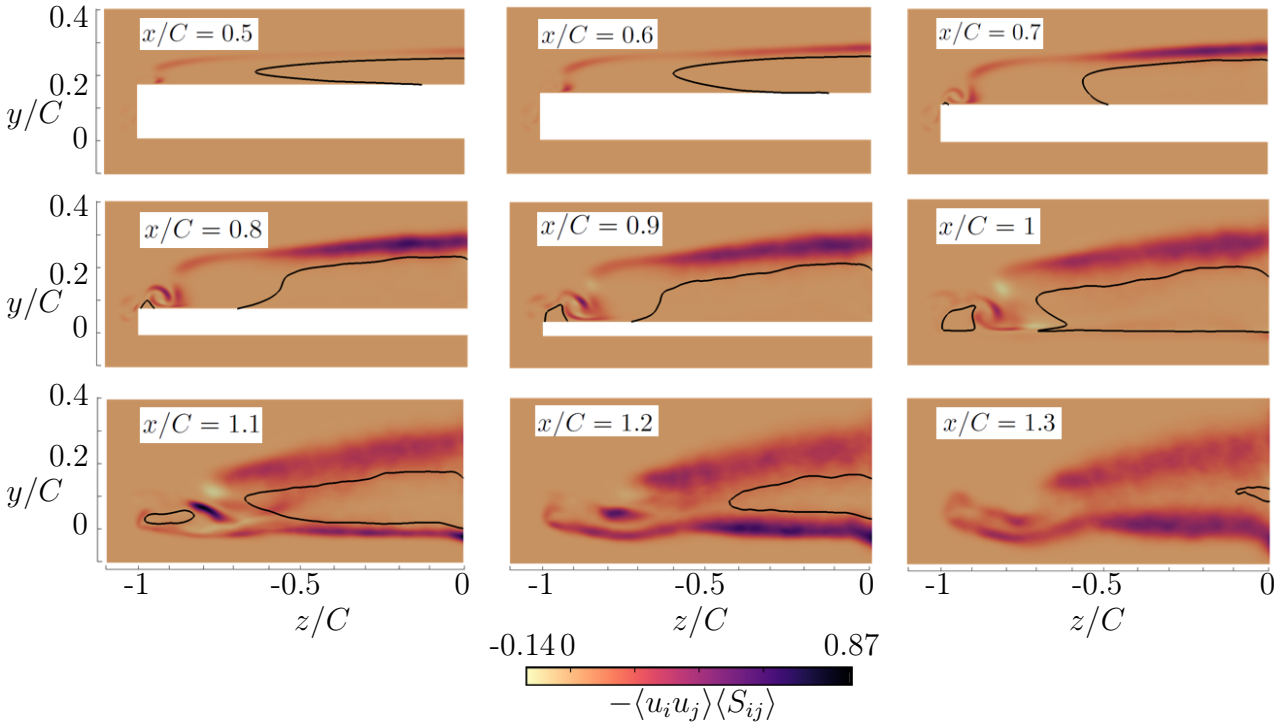


Figure 3.19: Contour plots of TKE production $P = -\langle u_i u_j \rangle \langle S_{ij} \rangle$ at equally spaced planes $x/C = 0.5 - 1.3$. The black contour line represents $\langle U_1 \rangle = 0$.

figure 3.18).

The above broad brush picture needs to be complemented with some additional details. For example, notice the localised pockets of high production in the area between the two recirculation zones. These pockets first appear at $x/C = 0.8$ but can be detected even at $x/C = 1.3$. They can explain the local overshoot of k, visible in figure 3.18 at all planes between $x/C = 0.8 - 1.2$, at the spanwise location $z/C \approx -0.8$. Further outboard, at $z/C = -0.9$, where the centre of the fully formed wing tip vortex V1 is located (refer to figure 3.15) both k and P attain very low values.

The increased turbulent activity between the two recirculation bubbles can be also detected in the Reynolds stresses isosurface plots shown in figure 3.20. Analysis shows that $\langle u_1 u_1 \rangle$ and $\langle u_2 u_2 \rangle$ dominate over $\langle u_3 u_3 \rangle$. It can be seen that k and $\langle u_1 u_1 \rangle$ isosurfaces wrap around the outer boundary of V0 and the large bubble originating from the leading edge. The levels of turbulent production and k are small in the V0 core, most likely due to the stabilizing effect of solid body rotation [Zeman, 1995].

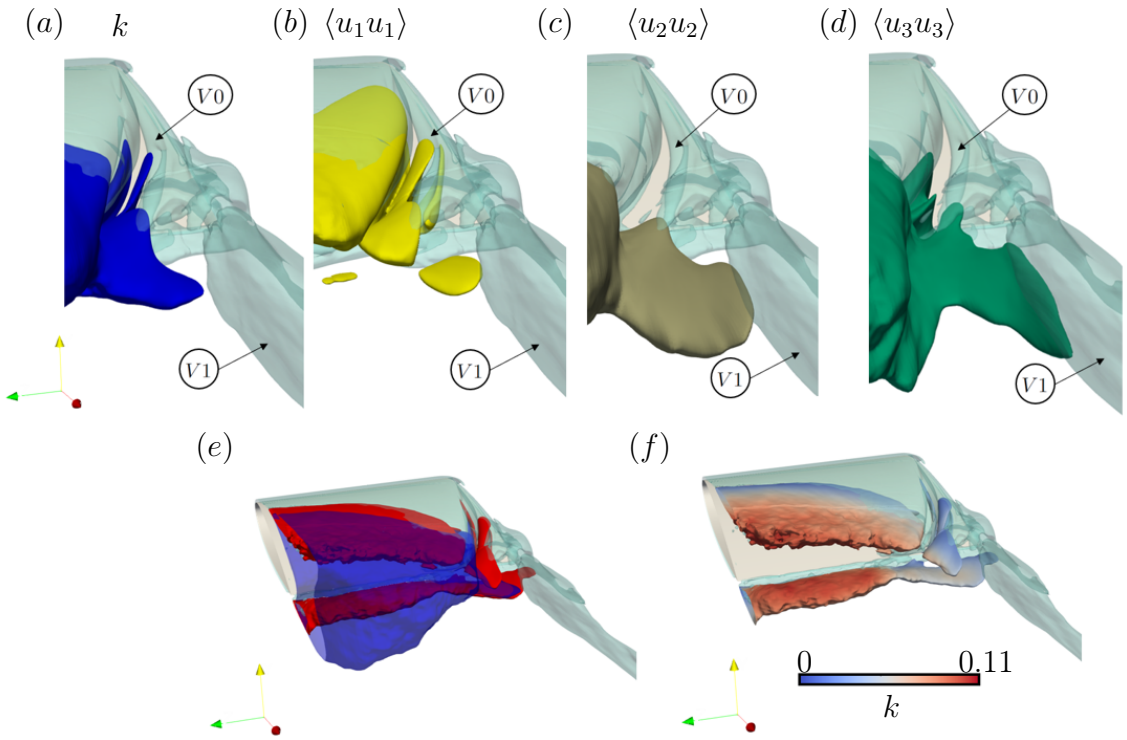


Figure 3.20: Isosurfaces of (*a*) k, (*b*) $\langle u_1u_1\rangle$, (*c*) $\langle u_2u_2\rangle$ and (*d*) $\langle u_3u_3\rangle$ with values 0.05, 0.05, 0.04 and 0.02 respectively. These values correspond to (*a*) $\approx 45\%$, (*b*) $\approx 55\%$, (*c*) $\approx 49\%$, and (*d*) $\approx 29\%$ of the maximum value of the corresponding quantities at the $z-y$ plane located at x/C=1.2. (e) Isosurfaces of k with value 0.5 (blue) and turbulence production with value 0.2 (red). The isosurface values correspond to $\approx 55\%$ and $\approx 31\%$ of the maximum value of k and $\mathcal{P}$ respectively in the $z-y$ plane located at $x/C = 1.2$. (f) Turbulence production $\mathcal{P}$ colored by k. The isosurface $\langle Q\rangle = 5$ is superimposed in all plots to visualise the vortical structures.

3.3.1 Production mechanisms for normal Reynolds stresses

We now proceed to study the production terms of the Reynolds stresses of $\langle u_1u_1\rangle$ and $\langle u_2u_2\rangle$, given by Pope [2000],

$$\mathcal{P}_{11}^{R-s} = -2\left[\langle u_1u_1\rangle\frac{\partial\langle U_1\rangle}{\partial x_1} + \langle u_1u_2\rangle\frac{\partial\langle U_1\rangle}{\partial x_2} + \langle u_1u_3\rangle\frac{\partial\langle U_1\rangle}{\partial x_3}\right], \tag{3.4}$$

$$\mathcal{P}_{22}^{R-s} = -2\left[\langle u_2u_1\rangle\frac{\partial\langle U_2\rangle}{\partial x_1} + \langle u_2u_2\rangle\frac{\partial\langle U_2\rangle}{\partial x_2} + \langle u_2u_3\rangle\frac{\partial\langle U_2\rangle}{\partial x_3}\right]. \tag{3.5}$$

The magnitude of $\langle u_3u_3\rangle$ (and its production) is smaller in comparison with the other two stresses and is not investigated.

Figures 3.21 and 3.22 show isosurfaces of $\mathcal{P}_{11}^{R-s}$ and $\mathcal{P}_{22}^{R-s}$ respectively. In each plot, iso-

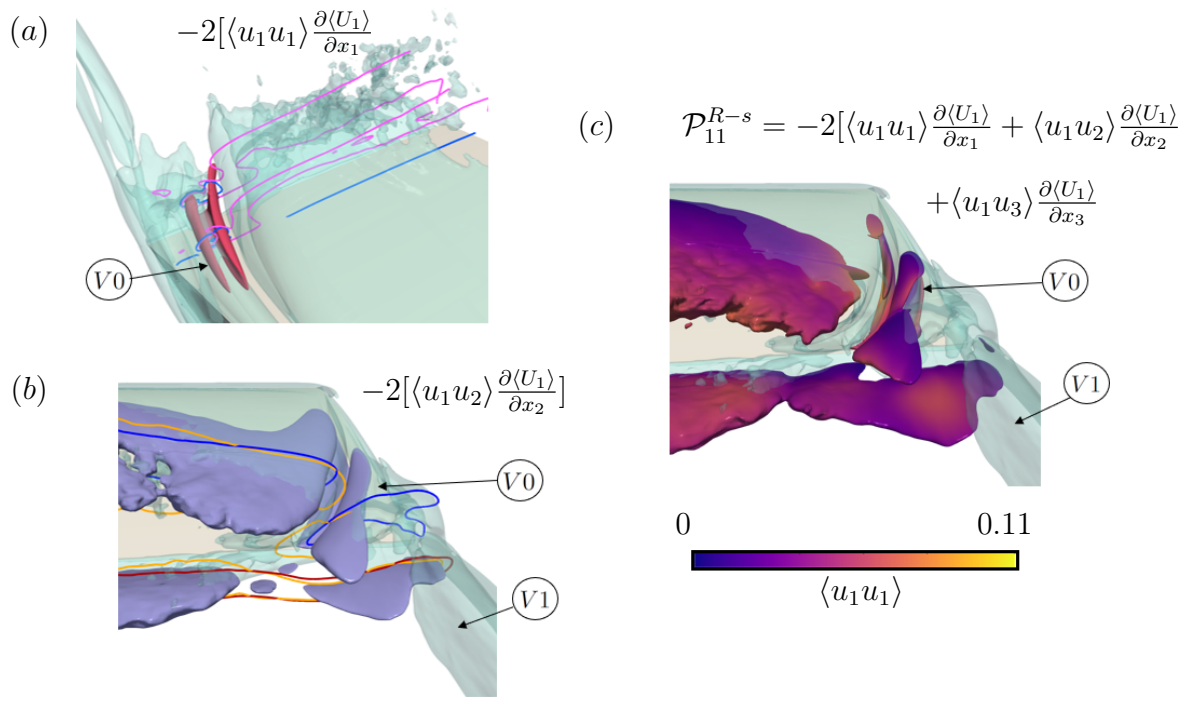


Figure 3.21: Production terms of $\langle u_1u_1\rangle$ (a) The magenta isosurface represents $-2[\langle u_1u_1\rangle \frac{\partial\langle U_1\rangle}{\partial x_1}] = 0.4$ with pink lines representing the contours of $\langle u_1u_1\rangle = 0.03$ and blue line representing compression $\frac{\partial\langle U_1\rangle}{\partial x_1} = -2$. (b) The purple isosurface represents $-2[\langle u_1u_2\rangle \frac{\partial\langle U_1\rangle}{\partial x_2}] = 0.5$, blue lines represent the contours of shear strain coming from the top wing surface with $\frac{\partial\langle U_1\rangle}{\partial x_2} = -7$ and orange lines $\langle u_1u_2\rangle = 0.01$, the red line represents shear from the bottom wing surface with $\frac{\partial\langle U_1\rangle}{\partial x_2} = 7$ and the corresponding orange line $\langle u_1u_2\rangle = -0.01$ and (c) total production of $\langle u_1u_1\rangle$: iso-surface $\mathcal{P}_{11}^{R-s} = 0.3$ colored by $\langle u_1u_1\rangle$. The isosurface values are equal to $(a) \approx 45\%$, $(b) \approx 36\%$ and $(c) \approx 27\%$ of the positive maximum value of the corresponding quantities in the $z-y$ plane located at $x/C = 1.2$ (at $x/C = 0.9$ for (a)). The isosurface $\langle Q\rangle = 5$ is superimposed in all plots to visualise the vortical structures.

surfaces of the most important components that make up the production terms according to (3.4) and (3.5) are also plotted. Figure 3.21 indicates that the term $-2\langle u_1u_2\rangle \frac{\partial\langle U_1\rangle}{\partial x_2}$ is by far the largest contributor of $\mathcal{P}_{11}$, compare panels (b) and (c). This is of course expected since both the separating shear layer on the suction side and the attached flow in the pressure side are associated with strong shear $\frac{\partial\langle U_1\rangle}{\partial x_2}$ (note however that the production is stronger in the suction side because flow separation results in higher shear). It is also interesting to notice the localised contribution of the normal term, $-2\langle u_1u_1\rangle \frac{\partial\langle U_1\rangle}{\partial x_1}$, which wraps around vortex V0, as can be seen in panel (a).

The production term $\mathcal{P}_{22}^{R-s}$ is shown in panel (b) of figure 3.22. The dominant component is $-2\langle u_2u_2\rangle \frac{\partial\langle U_2\rangle}{\partial x_2}$, which is shown in panel (a). The two other components are not included because

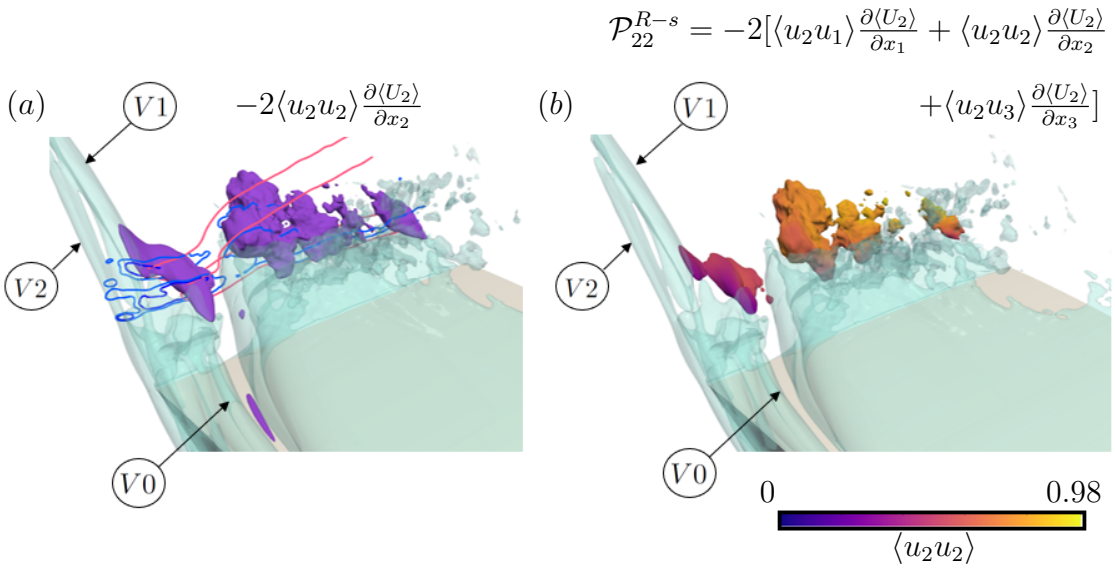


Figure 3.22: Production terms of $\langle u_2u_2\rangle$ (a) Isosurface of $-2\langle u_2u_2\rangle\frac{\partial\langle U_2\rangle}{\partial x_2} = 0.3$, blue lines represent contours $\frac{\partial\langle U_2\rangle}{\partial x_2} = -3, -4$ and the pink line represents $\langle u_2u_2\rangle = 0.04$ (b) Isosurface of $\mathcal{P}_{22}^{R-s} = 0.3$ colored by $\langle u_1u_1\rangle$. The contour values correspond to $(a) \approx 61\%$ and $(b) \approx 64\%$ of their respective positive maximum value in the $z-y$ plane located at $x/C = 1.2$. The isosurface $\langle Q\rangle = 5$ is superimposed in all plots to visualise the vortical structures.

their contribution is negligible; this can be attested by the resemblance of the isosurfaces in the two panels. The production term is maximised downstream of the trailing edge, where higher local values of negative normal strain $\frac{\partial\langle U_2\rangle}{\partial x_2}$ are encountered. Assuming that $\frac{\partial\langle U_3\rangle}{\partial x_3}$ is small, from the continuity equation we get $\frac{\partial\langle U_2\rangle}{\partial x_2} = -\frac{\partial\langle U_1\rangle}{\partial x_1}$, so the regions of strong $-2\langle u_2u_2\rangle\frac{\partial\langle U_2\rangle}{\partial x_2}$ are collocated with the areas of rapid streamwise velocity recovery, i.e. large $\frac{\partial\langle U_1\rangle}{\partial x_1}$ acceleration (or normal strain rate). This is the area shortly downstream of the closure of the recirculation region close to the tip.

In order to probe further the interaction between the elongation rate, $\langle S_{xx}\rangle$, vortex stretching, circulation and production of turbulent kinetic energy in the near wake, we integrate the aforementioned quantities in a number of cross-steam planes from $x/C = 1.1 - 2.4$. The boundary of the integration area S_z is shown with a closed dashed line in panels (a) and (b) of figure 3.23 and encloses vortex V1. In the same panels, contours of $-2\langle u_1u_2\rangle\frac{\partial\langle U_1\rangle}{\partial x_2}$ and $-2\langle u_2u_2\rangle\frac{\partial\langle U_2\rangle}{\partial x_2}$ are plotted respectively at plane $x/C = 1.2$. The locations of the planes themselves are marked in figure 3.23(c). The three areas of large production $-2\langle u_1u_2\rangle\frac{\partial\langle U_1\rangle}{\partial x_2}$ in panel (a) correspond to flow originating from the pressure side (bottom horizontal region), the suction

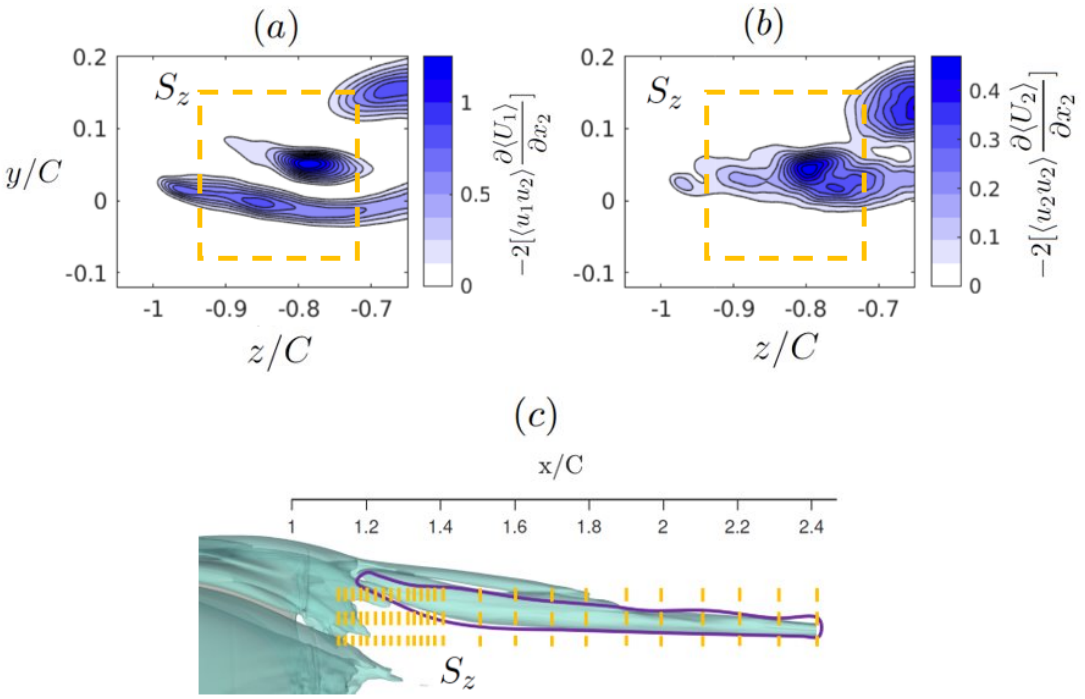


Figure 3.23: (a) Contours of $-2[\langle u_1u_2\rangle \frac{\partial\langle U_1\rangle}{\partial x_2}]$ (b) $-2[\langle u_2u_2\rangle \frac{\partial\langle U_2\rangle}{\partial x_2}]$ superimposed with the integration area S_z at $x/C = 1.2$. (c) Streamwise locations of the integration planes (that capture the spatial evolution of vortex V1) superimposed on $\langle Q\rangle = 5$ isosurface.

side (top right area) and between the two recirculation zones (middle region), see also contours of the total production $P = -\langle u_iu_j\rangle\langle S_{ij}\rangle$ at plane $x/C = 1.2$ at figure 3.19. The patches of large $-2\langle u_2u_2\rangle \frac{\partial\langle U_2\rangle}{\partial x_2}$ in panel (b) correspond to the two areas shown in figure 3.22(a).

In panel (a) of figure 3.24 we plot the variation along x/C of the surface integrals of vortex stretching, axial elongation and production terms over S_z. We also superimpose the circulation $\langle\Gamma_x\rangle$ (surface integral of $\langle\Omega_x\rangle$). This panel shows that the peaks of $\int_{S_z}\langle\Omega_x\rangle\langle S_{xx}\rangle\, dS_z$, $\langle\Gamma_x\rangle$ and $\int_{S_z}\langle S_{xx}\rangle\, dS_z$ are not in phase. The axial elongation term peaks at the streamwise location where $\langle U_1\rangle = 0$ (marked with the vertical dashed line). This is the result of flow recovery, as the flow comes out of the recirculation region around the tip. The vortex stretching term peaks slightly further downstream and causes the growth of circulation, $\langle\Gamma_x\rangle$ which peaks at about $x/C \approx 1.5$. Note the very weak decay of $\langle\Gamma_x\rangle$ with respect to the other two terms. The only mechanism responsible for the decay for $x/C > 2.0$ is viscous diffusion, which is a slow term and explains the persistence of V1 until the exit of the computational domain. Panel (b) shows that the production component due to shear $-\langle u_1u_2\rangle \frac{\partial\langle U_1\rangle}{\partial x_2}$ peaks earlier compared to the normal component $-2\langle u_2u_2\rangle \frac{\partial\langle U_2\rangle}{\partial x_2}$ and it reaches a higher value. The peak of the former term almost

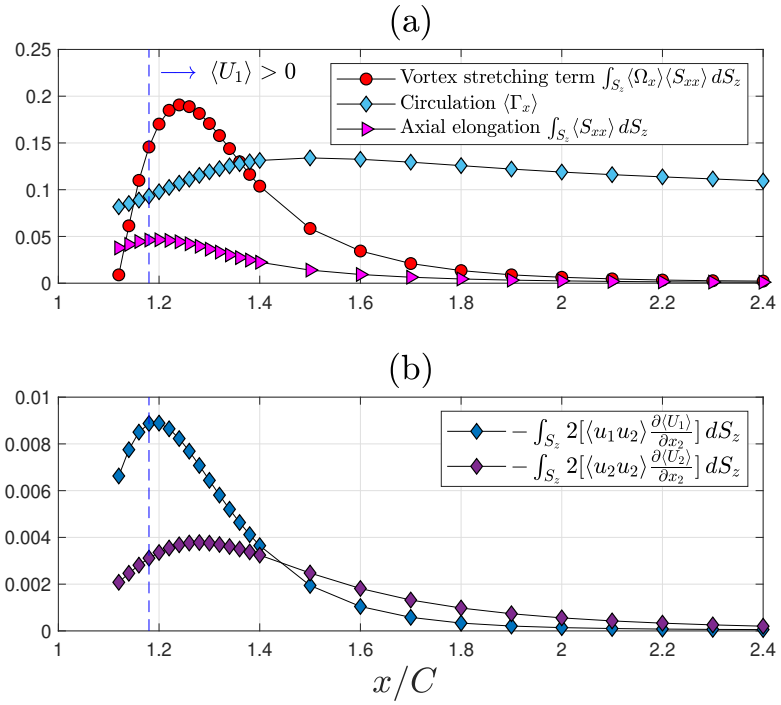


Figure 3.24: Streamwise evolution of quantities related to (a) the vorticity field and (b) the production of Reynolds stresses. The quantities shown are integrated over the surface S_z marked in panels (a) and (b) of figure 3.23. The vertical dashed line indicates the streamwise location where $\langle U_1 \rangle = 0$.

coincides with the location where $\langle U_1 \rangle = 0$. Note also the faster decay rate of $-2\langle u_1 u_2 \rangle \frac{\partial \langle U_1 \rangle}{\partial x_2}$ compared to $-2\langle u_2 u_2 \rangle \frac{\partial \langle U_2 \rangle}{\partial x_2}$. While circulation is (almost) constant, both production terms decay because of the solid body rotation velocity profile within V1, see bottom row of figure 3.17. The fast decay of $-2\langle u_1 u_2 \rangle \frac{\partial \langle U_1 \rangle}{\partial x_2}$ between $x/C \approx 1.2 - 1.4$ is probably due to the flow recovery away from the recirculation region that smooths the streamwise velocity in the x_2 (i.e. y) direction.

3.4 Summary

DNS of a half-span NACA 0018 wing with square wingtip profile was performed at a $Re_c = 10^4$ and 10° angle of attack. A thorough analysis of the spatial evolution of vorticity dynamics and turbulent production mechanisms above the wing and in the near wake was carried out. The flow was found to separate close to the leading edge and did not reattach on the suction side of the wing. Close to the leading edge, the separating region occupied most of the span, but once the secondary flow in the wingtip started to develop, the left boundary of the recirculating

bubble was displaced inboard. In the proximity of the tip, the flow remained attached, but another recirculation zone appeared close to the trailing edge.

In total 5 vortical structures were identified, with one of them rotating in the counter-clockwise direction. The underlying mechanism was traced to the low pressure region in the flat wingtip close to the leading edge, which created a spanwise motion in the outboard direction. This low pressure was associated with the formation of a small recirculation zone, arising from the flow separation at the sharp wingtip around the leading edge.

We analysed the terms of the vorticity transport equation and showed how each of the identified vortices sustained or lost their strength as they approached the trailing edge, with particular focus on the role of vortex stretching/compression and tilting. Different mechanisms were found to be at play in the separating shear layers and in the vortex cores. The emergence of the main wingtip vortex V1 from the amalgamation and interaction of the different vortices was also elucidated. The presence of the recirculation zone close to the trailing edge resulted in the distortion of the shear layers originating from the pressure side.

The distribution of turbulent kinetic energy around the main wing tip vortex V1 was found to be highly asymmetric and high values were concentrated on the right of its axis. Apart from the main separating shear layer, patches of strong production were also found in the area between the two recirculation bubbles in the near wake.

Analysis of the production terms of individual Reynolds stresses has enabled us to uncover the main production mechanisms. As expected, $-2\langle u_1 u_2\rangle \frac{\partial \langle U_1\rangle}{\partial x_2}$ was found to be one of the dominant terms responsible for maintaining high levels of $\langle u_1 u_1\rangle$; this is the standard production term for wall-bounded flows. Additionally, the wall-normal stress source term $-2\langle u_2 u_2\rangle \frac{\partial \langle U_2\rangle}{\partial x_2}$ was responsible for maintaining $\langle u_2 u_2\rangle$ primarily in the spiral wakes in the near field.

The vortex stretching rate, axial elongation, streamwise vorticity and production terms were integrated over square y-z areas containing the V1 vortex, and plotted against the streamwise direction x/C. When the stretching rate became negligible, the circulation (surface integral of streamwise vorticity) reached a peak and then started to decay very slowly, explaining the persistence of V1 until the end of the computational domain. The production terms become negligible at $x/C \approx 2$ as expected, because the velocity profile within the core of V1 (solid

body rotation) cannot sustain turbulence.

The detailed analysis presented aims to contribute to a better understanding of separated vortical flows and can hopefully lead to actuation strategies to manipulate them.

Chapter 4

Non-normality and small-scale statistics in a separated shear flow

This chapter[1] begins by introducing the decompositions of the Velocity Gradient Tensors (VGT) in section 1.5. We simulate the flow around the finite wing for $Re_c = 5000$ introduced in section 2.4. In section 4.1, we analyze the key features of the three-dimensional velocity field. The subsequent sections present the main findings, starting with the eigencontributions to turbulence production in section 4.2, followed by the analysis of enstrophy and total strain in Section 4.3. The dynamics of vortex stretching due to the mean flow as well as the small scale strain are covered in sections 4.4 and 4.5 respectively. Section 4.6 focuses on the intermittent nature of vorticity and strain-self amplification, specifically analyzing large events, defined as greater than 10 times the time-average value. Section 4.7 examines the non-normality of the VGT and its production mechanisms. In Section 4.8, we extend the Schur decomposition to mean fields and analyze the non-normality in the interaction terms between mean flow and fluctuations. Finally, summary of this chapter is in section 4.9. mean strain

4.1 Flow characteristics

In this section, we discuss the key features of the recirculating and transitional flow regions. Figure 4.1(a) shows contours of mean axial velocity. The boundary of recirculation bubble is

[1]Part of the work in this chapter was presented at the following conferences: UK Fluids Conference 2022 held at the University of Sheffield in Sheffield, UK; the Turbulence Consortium Annual Review 2023 held at the South Kensington Campus, Imperial College London; and European Turbulence Conference (ETC18) 2023 held in Valencia, Spain. Entry submitted to the ARCHER2 Image and Video Competition 2022, organized by the ARCHER2 UK National Supercomputing Service, and image was chosen to feature in the ARCHER2 Calendar 2023. Entry presented at the *The Science behind the Image Competition* seminar (online) 2023 organized by ARCHER2 and Edinburgh Parallel Computing Centre (EPCC).

marked with a white line contour (contour value $\langle U_1 \rangle = 0$). There is no reattachment in the suction side due to the high angle of attack; instead, the recirculation extends up to $1.4C$ from the leading edge. Downstream of the bubble, figure 4.2(b) shows that the free-stream velocity is slowly recovered.

Figure 4.1(b) shows contours of the turbulent kinetic energy, k. Inside the recirculating bubble, the values of k are finite despite the fact that production is negligible (figure 4.2(c)). Instead, turbulence is sustained by turbulent diffusion from the top and bottom shear layers. Higher values of k are found outside the bubble and extend over a wider region compared to production. In the transitional region, k values peak at $x/C \approx 1.4$ (see also figure 4.2(b)) which is an indication that the transition process at this point has completed. Figure 4.1(c) shows contours of the production $-\langle u_i u_j \rangle \langle S_{ij} \rangle$. Regions of strong production are found above and below the recirculation zone due to the presence of the separating and attached shear layers in the suction and pressure sides respectively. On the other hand, inside the bubble, there are negligible values.

Figure 4.3 shows the profiles of Reynolds stresses along lines A and B. As expected, the streamwise normal stresses $\langle u_1 u_1 \rangle$ dominate outside the recirculation zone, but inside the bubble, the flow is closer to isotropic. In figure 4.3(b), it can be seen that streamwise and cross-stream stresses attain almost equal values at the peak, while the spanwise component is smaller. There is a non-negligible spanwise component at the start of the transition process though. In our previous work in chapter 3 (also in Bilbao-Ludena and Papadakis [2023]) with the same geometry and $Re_c = 10^4$, it was shown that the transition was due to Kelvin-Helmholtz instabilities that develop on top of the separated shear layer. This is a two-dimensional mechanism. The fact that the spanwise component at the initial stages of transition is non-zero is probably because a finite wing is studied and the 3D effect has penetrated into the flow and reached the shear layer at the location $x/C = 1$. Downstream of the peak all stresses decay, indicating that the flow will re-laminarise (due to the low Re number). The peak of the shear stress $\langle u_1 u_2 \rangle$ follows exactly the peaks of the streamwise and cross-stream peak as expected.

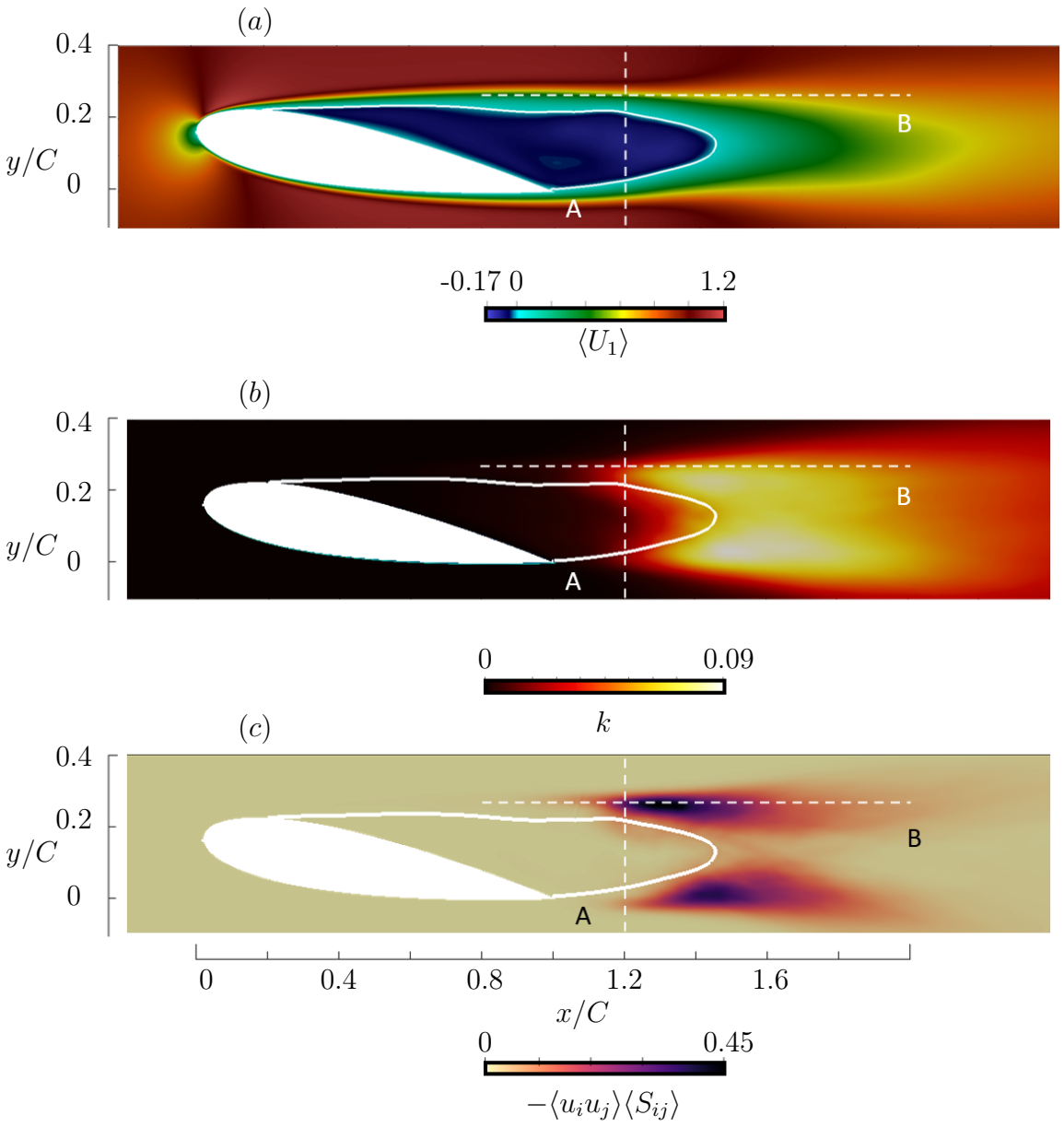


Figure 4.1: Contours of (a) $\langle U_1 \rangle$, (b) turbulent kinetic energy (TKE) k and (c) its production term $-\langle u_i u_j \rangle \langle S_{ij} \rangle$ in the $x - y$ plane at $z/C = -0.2$.

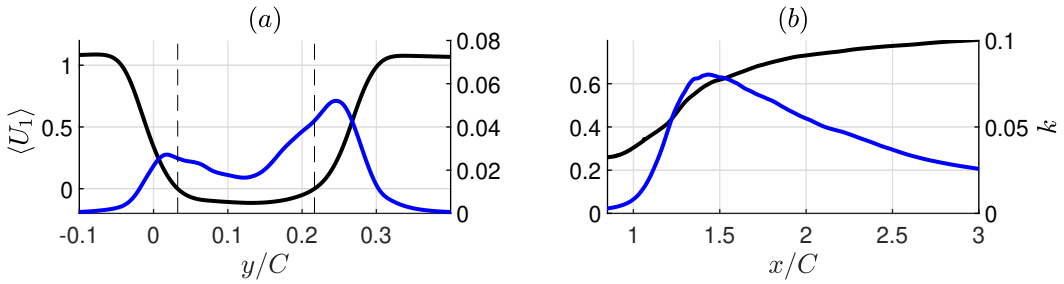


Figure 4.2: Distribution of $\langle U_1 \rangle$ (blue line) and k (black line) for (a) along line A and (b) along the transition line B. The dashed vertical lines in (a) indicate the boundaries of the recirculation zone.

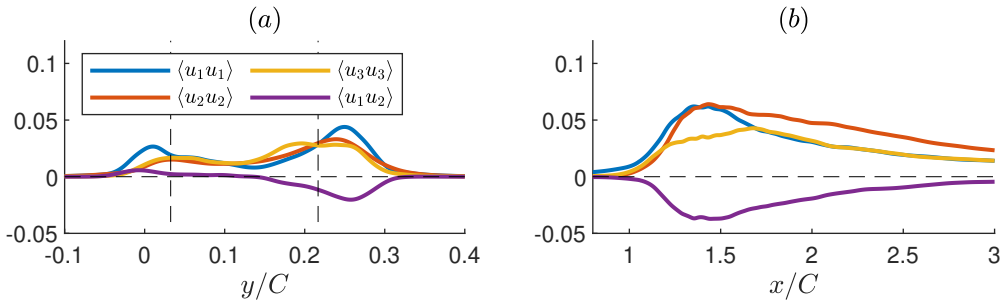


Figure 4.3: Reynolds stresses (a) along line A and (b) along line B.

The Taylor microscale in the i-th direction is defined as,

$$\zeta_i = \sqrt{\frac{\langle u_i u_i \rangle}{\langle \frac{\partial u_i}{\partial x_i} \rangle^2}}\,, \tag{4.1}$$

and the corresponding Reynolds number

$$Re_{\zeta_i} = \frac{\sqrt{u_i u_i}\zeta_i}{\nu}\,. \tag{4.2}$$

Figure 4.4, shows the distributions of Taylor and Kolmogorov length-scales along lines A and B. Inside the recirculation zone, panel (a), ζ_2 and ζ_3 have similar values. ζ_1 is larger just outside the recirculation region because of the high values of k and moderate values of dissipation. Further away, close to free-stream, the Taylor microscales take unrealistically high values because dissipation tends to zero faster than k. In the transition region, figure 4.4(b), ζ_1 decays rapidly until $x/C \approx 1$ which correlates with the location of the rapid increase of k due to transition, see figure 4.2(b). Further downstream, the three components maintain similar magnitudes. On average, the values of the Taylor microscale are about 5% of the chord length. Figure 4.5 shows the variation of Re_{ζ_i}; peak values of ≈ 80 are reached. This value is rather small, and is due to the low Reynolds number (based on global scales). The flow is complex and a very fine resolution and long integration times are needed in order to balance the transport equation of enstrophy and total strain and get converged statistics of the large and rare events that will be presented in the next sections. The range of Re_{ζ_i} values corresponds to the lower end of HIT studies [Iyer et al., 2022] but are higher than other DNS works involving the study of small-scales turbulence generated by a square grid-elements where $Re_{\zeta_i} = 30-40$ [Paul et al.,

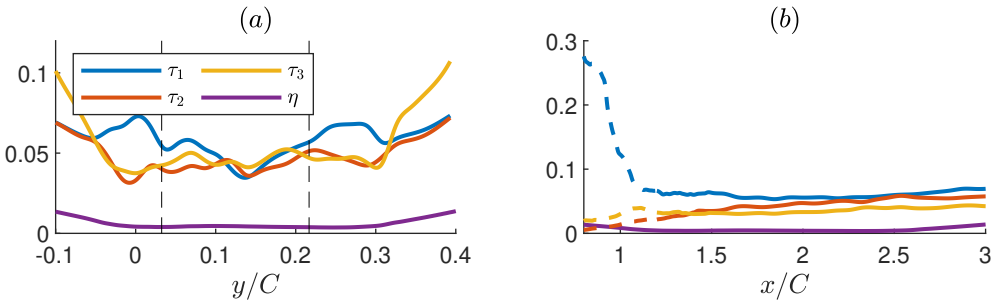


Figure 4.4: Taylor microscales ζ_i and Kolmogorov scale along (a) line A and (b) line B. The dashed lines indicate the region upstream of transition.

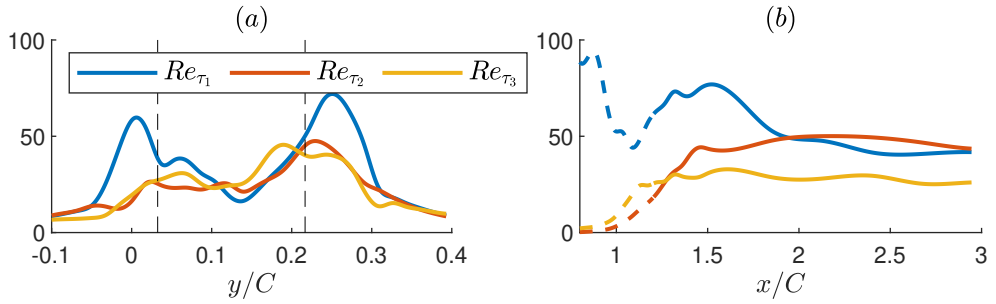


Figure 4.5: Reynolds number based on the Taylor microscale (a) along line A and (b) along line B. Dashed lines indicate the region upstream of transition.

2017, Zhou et al., 2016a,b, 2014a,b]. Figure 4.5(a) shows the biggest deviations between the three Reynolds numbers are outside the recirculation zone. Note that the high values of Re_{ζ_1} upstream of transition are unrealistic as k values are close to zero (see figure 4.5(b)); we mark this region with dashed lines.

4.2 Eigencontributions to turbulence production

We proceed with an eigenanalysis of turbulence production. We use the following eigendecomposition for the turbulent energy production [Liberzon et al., 2005]:

$$P = -\langle u_i u_j \rangle \langle S_{ij} \rangle = -\Sigma_{i=1}^{3} \Lambda_i^M \langle u^2 \cos^2 \left(u, e_i^M\right) \rangle = \Sigma_{i=1}^{3} P_{\Lambda_i^M} \,, \tag{4.3}$$

where u_i are the fluctuating velocities, $u^2 = u_1^2 + u_2^2 + u_3^2$, $\langle S_{ij} \rangle = \frac{1}{2}\left(\frac{\partial \langle U_i \rangle}{\partial x_j} + \frac{\partial \langle U_j \rangle}{\partial x_i}\right)$ is the mean strain rate and Λ_i^M and e_i^M are the eigenvalues and eigenvectors of $\langle S_{ij} \rangle$ respectively. The eigendecomposition of the turbulence production superimposed with the eigenvalues Λ_i^M are shown in figure 4.6. By definition $\Lambda_1^M > \Lambda_2^M > \Lambda_3^M$, where due to incompressibility $\Lambda_1^M > 0$,

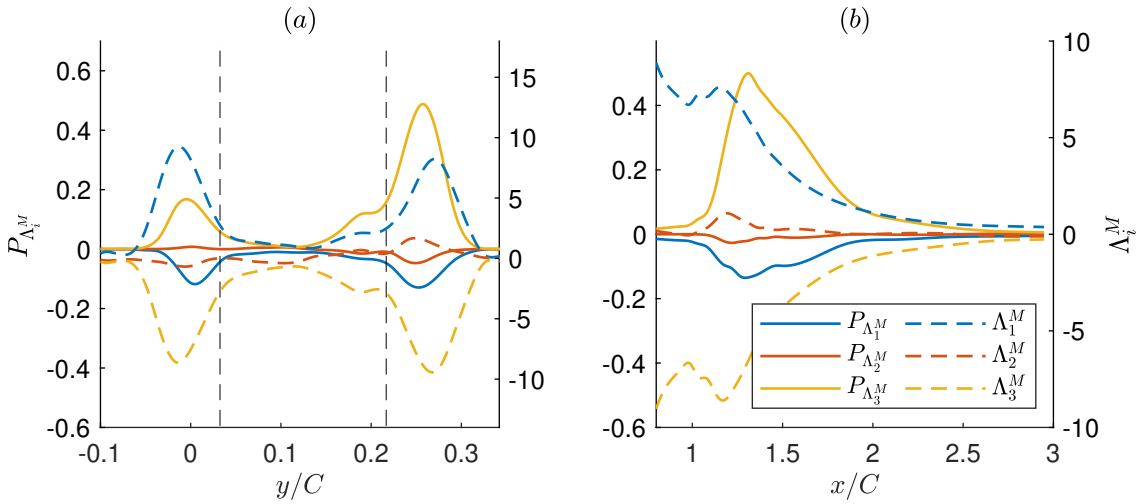


Figure 4.6: Eigendecomposition of turbulent production (left axis) and eigenvalues of the mean strain rate tensor (right axis) (a) along line A and (b) along line B.

$\Lambda_3^M < 0$ and Λ_2^M can be either positive or negative. In the two peaks at $y/C \approx -0.02$ and 0.28, the major contribution for overall net positive production stems from the compressing eigenvalue Λ_3^M (i.e. $P_{\Lambda_3^M}$) consistent with previous findings on wall boundary flows [Liberzon et al., 2005] and confined three-dimensional shear flows [Gurka et al., 2004]. Inside the recirculation zone, panel (a), the shear is weak and this is reflected by small eigencontributions. Note the very low values of Λ_2^M (it fluctuates around 0) and its eigencontribution. In the transitional region, panel (b), $P_{\Lambda_3^M}$ shows a similar dominance with its contribution decreasing steadily after the peak. Upstream of transition, the eigenvalues are large but $P_{\Lambda_i^M}$ is small because the flow is laminar. Thus there is a spatial gap between the peak of the eigencontribution and the eigenvalue; the former is downstream of the latter. The rapid growth of $P_{\Lambda_3^M}$ denotes that the transition location is located between $x/C \approx 1.2 - 1.3$, consistent with previous figures. Interestingly the intermediate eigenvalue is weakly extensional throughout transition, which indicates that the shear layer is exhibiting characteristics similar to a disk-like structure with bi-axial stretching nature [Davidson, 2015]. Figure 4.7 shows the time-average alignments between u_i and the principal directions of the mean strain rate tensor. In the transitional flow as $P_{\Lambda_i^M}$ starts to increase at $x/C \approx 1.2$, the alignments maintain a clear order $\langle|\cos\left(u, e_3^M\right)|\rangle > \langle|\cos\left(u, e_2^M\right)|\rangle > \langle|\cos\left(u, e_1^M\right)|\rangle$. This alignment order starts to form at $x/C \approx 1.2$, and is completed at $x/C \approx 1.5$. Within this region, transition takes place, see figure 4.6 (b) suggesting that the alignments are a product of re-organization of the structure. Moreover, the

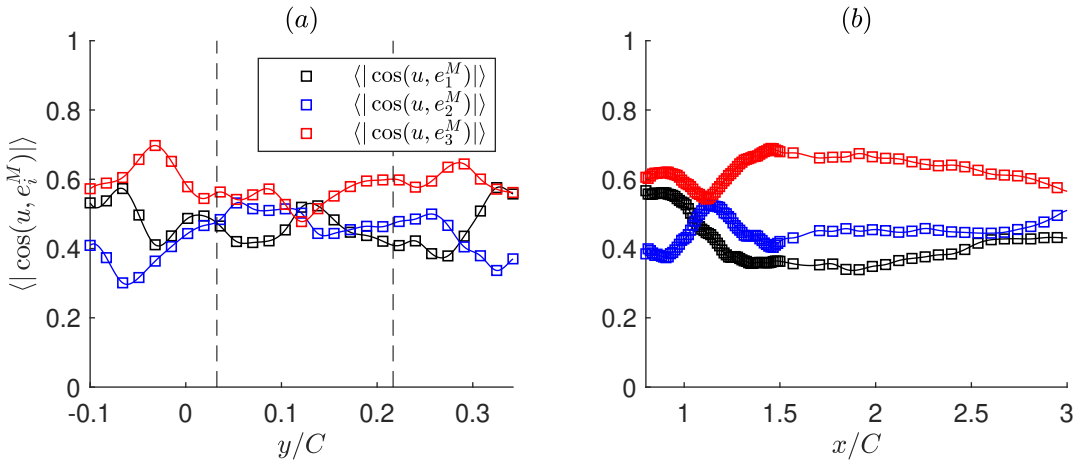


Figure 4.7: Time-average alignment of u and the principal components of the mean-strain rate fields (a) along line A and (b) along line B.

rapid increase of $\langle|\cos\left(u,e_3^M\right)|\rangle$ from $x/C \approx 1.2$ to ≈ 1.4 explains the rapid increase $P_{\Lambda_3^S}$ and the location of its peak. The peak observed shortly before reaching $x/C = 1.5$ in figure 4.7(b) may indicate a manifestation of the active effects of the mean strain rate on the flow field in general. As the flow re-laminarises, the alignments start to converge towards 0.5 however at a slow pace as $\langle|\cos\left(u,e_3^M\right)|\rangle$ still keeps some coherence (compared to Λ_3^M which has lost $\approx 80\%$ of its value beyond $x/C \approx 2$). This convergence is also visible inside the recirculating flow section (panel (a)). At this point, it can be inferred that the notable decrease in turbulence production primarily stems from the weakening of the eigenvalues rather than a deterioration in the alignments. The pdf's of $|\cos\left(u,e_i^M\right)|$ are displayed in figure 4.8 at two locations, along the transition region, $x/C = 1.32 - 1.43$ (around the peak of turbulence production) and at $x/C = 2.74 - 3.36$ where the production is minimal. In the first location, the distribution of $|\cos\left(u,e_3^M\right)|$ is skewed towards 1. However, further downstream, as shown in panel (b), the pdf's are slowly converging toward a flat distribution. The particular distribution observed in panel (a) might be facilitated by the disc-like structure of the strain field. The lower probabilities of parallel alignment in $|\cos\left(u,e_1^M\right)|$ and $|\cos\left(u,e_2^M\right)|$ might be attributed to the extensional properties of Λ_1^M and the weaker (and thus more random) nature of Λ_2^M respectively.

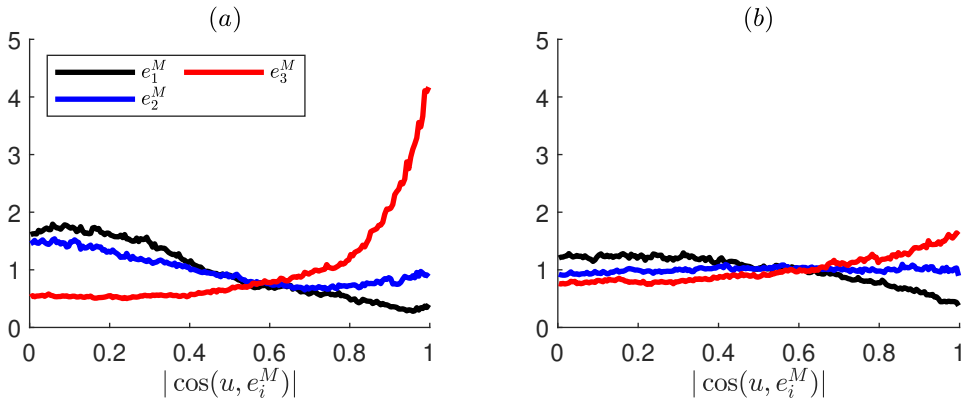


Figure 4.8: Pdf's of the absolute alignments between u and the principal direction of mean strain rate for (a) transitional flow between $x/C = 1.32 - 1.43$ and (b) $x/C = 2.74 - 3.36$.

4.3 Analysis of enstrophy and total strain

Figure 4.9 shows contours of $0.5\langle\omega_i\omega_i\rangle$ and $\langle s_{ij}s_{ij}\rangle$. The two quantities are maximized at the tip of the recirculation zone and have similar values. Figure 4.10 shows the distribution along lines A and B and it can be seen that $0.5\langle\omega_i\omega_i\rangle$ has slightly higher values in the two peaks above and below the recirculation zone. The difference between $0.5\langle\omega_i\omega_i\rangle$ and $\langle s_{ij}s_{ij}\rangle$, which is the second invariant of the characteristic equation of the VGT $\langle Q\rangle = 0.5\langle\omega_i\omega_i\rangle - \langle s_{ij}s_{ij}\rangle$ (see equation 1.32), takes the form of a divergence which for the case of homogeneous isotropic turbulence $\langle Q_A^{HIT}\rangle = 0$.

Figure 4.11 illustrates the sequential development of the instantaneous fields of $0.5\omega_i\omega_i$ and $s_{ij}s_{ij}$. The vortical structures identified by $Q = 2$ are marked with green contour lines. In the left column, the contours of $0.5\omega_i\omega_i$ are either pronounced in specific parts of the vortical structures (as seen in $E1$, $E2$, and $E3$) or they fill the entire structure (as observed in $E4$ and to a lesser extent, in the structure forming $E5$). Moreover, the dense areas of $0.5\omega_i\omega_i$ are in close proximity to contours of $s_{ij}s_{ij}$ as seen in the right column. Depending on whether the entire structure (as is the case of $E4$) or only certain parts of it are subjected to strain, a distinction can be made between "vortex stretching" and "vorticity stretching". At $t = 194$, $E1$ and $E2$ are a direct product of strained mean flow and are clustered around the border the bubble. As these elongated, complex, and swirling eddies are advected downstream by the mean flow, they interact with vortical structures that are shed from the trailing edge, like $E3$, generating complex vorticity and strain fields ($t = 194 - 194.4$). Simultaneously, break up of the larger

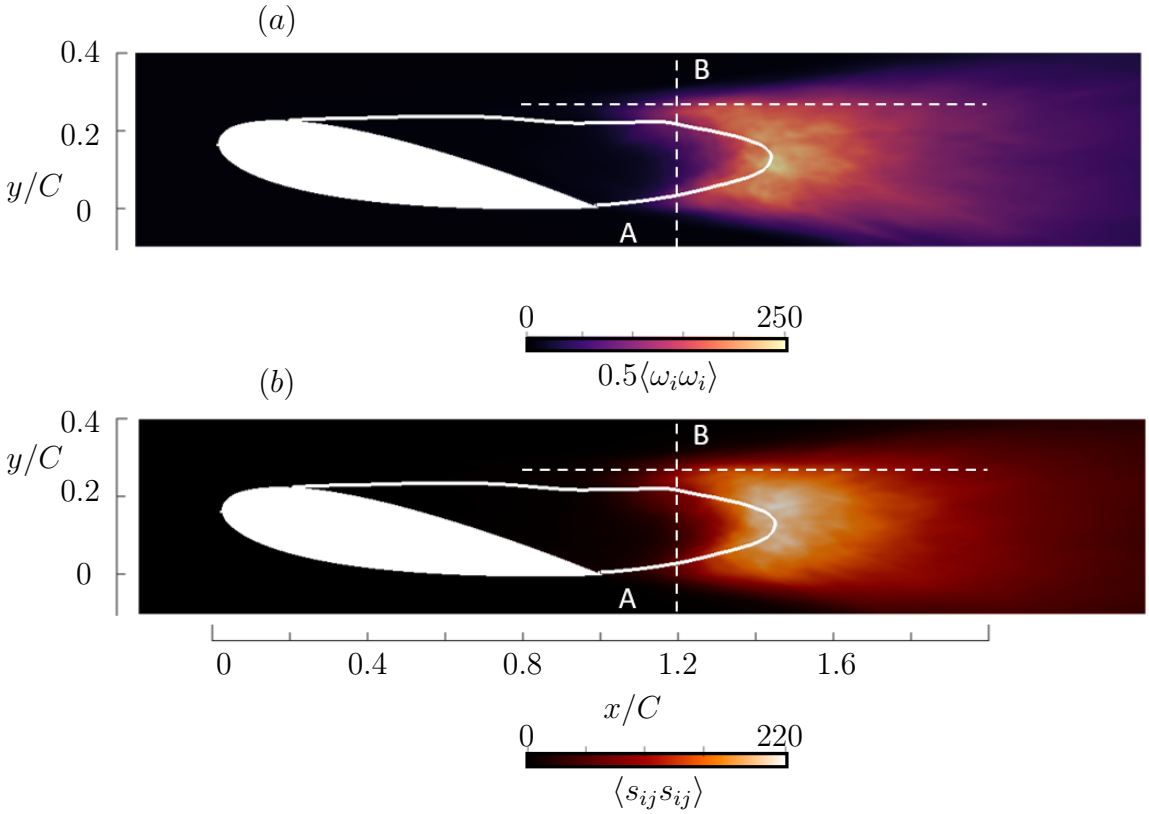


Figure 4.9: Contours of (a) $0.5\langle\omega_i\omega_i\rangle$ and (b) $\langle s_{ij}s_{ij}\rangle$ in the $x-y$ plane at $z/C=-0.2$.

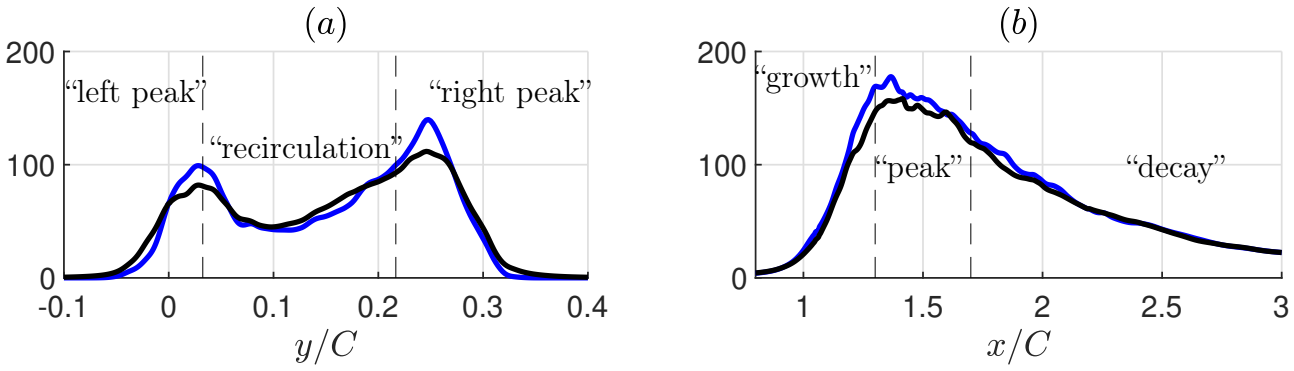


Figure 4.10: $0.5\langle\omega_i\omega_i\rangle$ (blue line) and $\langle s_{ij}s_{ij}\rangle$ (black line) distribution (a) along line A and (b) along line B.

structure into smaller structures with a wide range of sizes takes place, as it is the case of $E3$ during $t = 194 - 194.4$. $E4$ is the case of an isolated spiky blob of vorticity which forms parts of what we call a large event (see the next sections for further details) and displays a high value of $0.5\omega_i\omega_i$. Further downstream, in panel (a), structures are more randomly aligned and less densely packed, as exemplified by $E5$. Here, shear forces are weaker, allowing the vortices to become more randomly oriented.

Figure 4.12 shows the spatial variation of $\langle\omega_i\omega_i\rangle$ and $\langle\omega_1\omega_2\rangle$. It is clear that there is small-scale anisotropy, especially around the peaks of enstrophy where $\langle\omega_1\omega_1\rangle$ and $\langle\omega_3\omega_3\rangle$ are larger than $\langle\omega_2\omega_2\rangle$. However, in the middle of the recirculating bubble and for $x/C > 2.3$ the small-scale anisotropy vanishes and the flow approaches homogeneous isotropic turbulence. It is interesting to note that along line B, isotropy for enstrophy is achieved earlier than isotropy of the Reynolds stresses, compare with figure 4.3(b).

We now focus on the dynamical equations of $0.5\langle\omega_i\omega_i\rangle$ and $\langle s_{ij}s_{ij}\rangle$, and their main production mechanisms i.e. enstrophy production via vortex stretching $\langle\omega_i\omega_j s_{ij}\rangle$ and strain rate self-amplification $-\langle s_{ij}s_{jk}s_{ki}\rangle$. Enstrophy production $\omega_i\omega_j s_{ij}$ is a non-linear process because it involves the multiplication of vorticity by strain which means that even a small amount of vorticity can amplify under stretching. This is an inviscid process, where vortical filaments are elongated and thinned due to the strain in the flow. As these filaments are stretched, they spin faster, leading to an amplification of vorticity. The resulting vortices can strain other vortices, leading to even more intense vorticity generation. This thinning of vortex filaments signifies transfer of energy from larger scales to smaller scales through a cascade process. For this reason, vortex stretching is considered as the main driver in the transfer of kinetic energy down the scales until it is finally dissipated [Taylor, 1937] in a similar way as it is described by the Richardson–Kolmogorov cartoon of turbulent cascade [Richardson, 1922, Kolmogorov, 1991b, 1962]. The cartoon is supported by physical evidence, in the sense that inertial-range vortices of a given size range receive their energy predominantly through the stretching action of eddies which are about three to five times larger [Davidson, 2015, Leung et al., 2012]. On the other hand the strain self-amplification term $-s_{ij}s_{jk}s_{ki}$ represents the process in which the compressive strain rates in a fluid are amplified (or become steeper and more intense) through

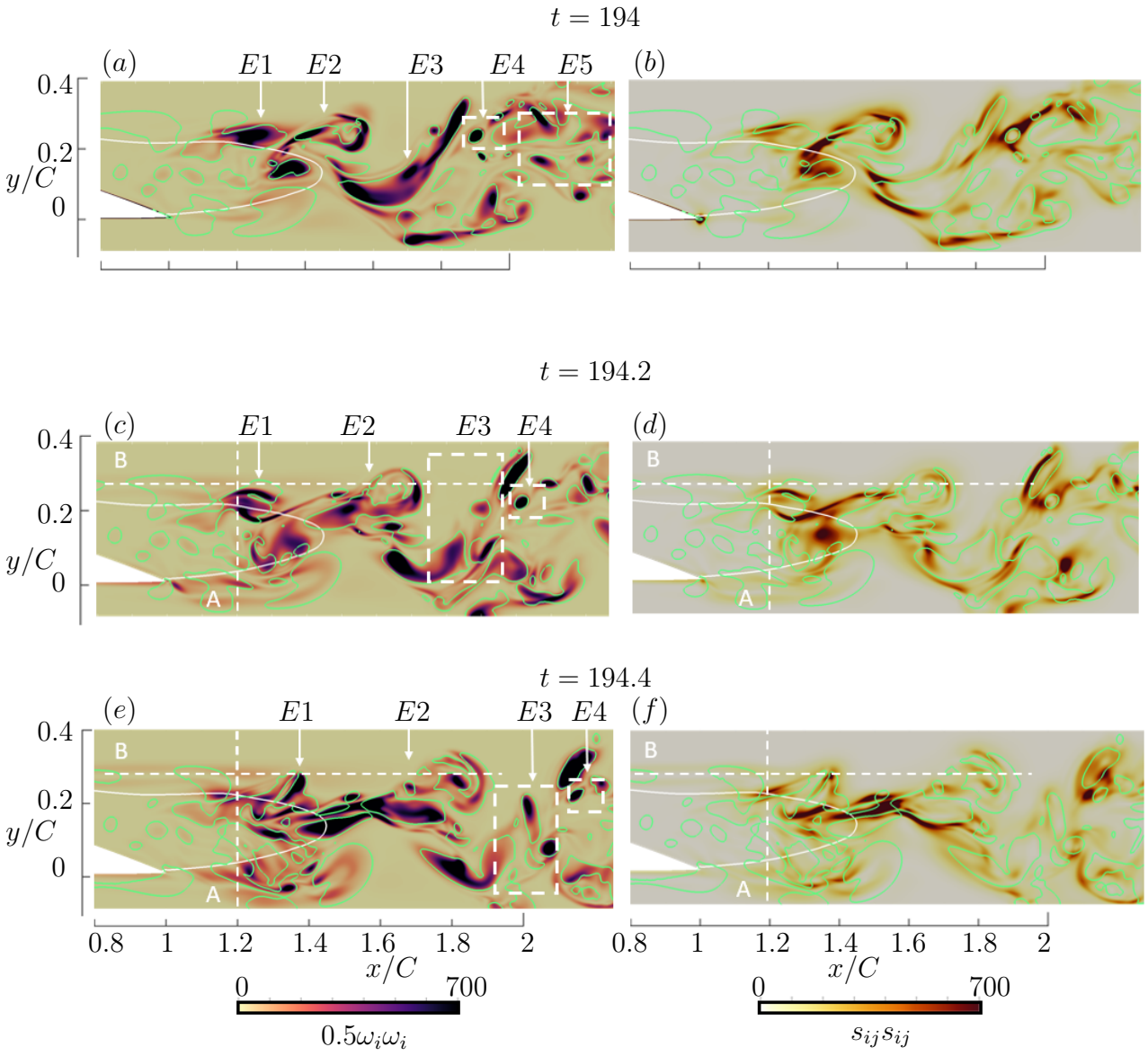


Figure 4.11: Sequence of instantaneous contours of $0.5\omega_i\omega_i$ ((a) $t = 194$, (c) $t = 194.2$, (e) $t = 194.4$) and $s_{ij}s_{ij}$ ((b) $t = 194$, (d) $t = 194.2$, (e) $t = 194.4$). The light green line represents the instantaneous vortical structures with $Q = 2$. The white line represents the recirculation zone boundary.

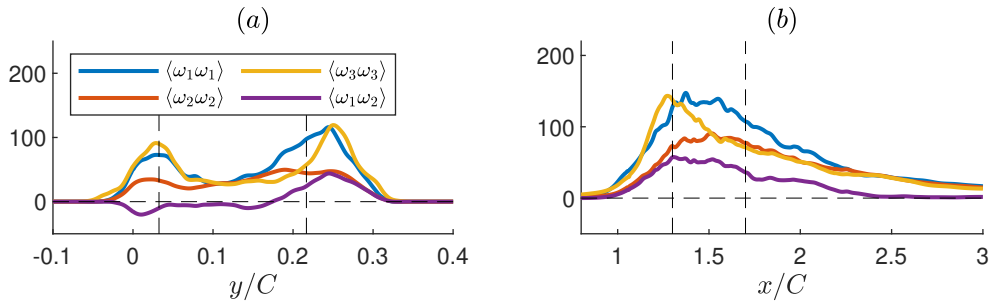


Figure 4.12: Main components of enstrophy and $\langle\omega_1\omega_2\rangle$ in (a) along line A and (b) along line B.

nonlinear self-advection [Sagaut and Cambon, 2008]. While the standard notion is that vortex stretching plays the main role in the energy cascade, there is evidence suggesting that strain self-amplification may actually be more significant [Carbone and Bragg, 2020, Yang et al., 2023].

The enstrophy transport equation is [Tennekes et al., 1972]:

$$\begin{aligned}\frac{1}{2}\frac{\partial\langle\omega_i\omega_i\rangle}{\partial t} = &\underbrace{-\langle U_j\rangle\frac{\partial}{\partial x_j}\frac{1}{2}\langle\omega_i\omega_i\rangle}_{\mathcal{C}_\omega}\underbrace{-\langle u_j\omega_i\rangle\frac{\partial\langle\Omega_i\rangle}{\partial x_j}}_{\mathcal{P}_\omega}\underbrace{-\frac{1}{2}\frac{\partial}{\partial x_j}\langle u_j\omega_i\omega_i\rangle}_{\mathcal{T}_\omega}\underbrace{+\langle\omega_i\omega_j s_{ij}\rangle}_{\mathcal{EF}_\omega}\\ &\underbrace{+\langle\omega_i\omega_j\rangle\langle S_{ij}\rangle}_{\mathcal{EM}_\omega}\underbrace{+\langle\omega_i s_{ij}\rangle\langle\Omega_j\rangle}_{\mathcal{M}_\omega}\underbrace{+\nu\frac{\partial^2}{\partial x_j\partial x_j}\langle\frac{1}{2}\omega_i\omega_i\rangle}_{\mathcal{D}_\omega}\underbrace{-\nu\left\langle\frac{\partial\omega_i}{\partial x_j}\frac{\partial\omega_i}{\partial x_j}\right\rangle}_{\epsilon_\omega},\end{aligned} \tag{4.4}$$

where $\mathcal{C}_\omega$ is convection by mean flow, $\mathcal{P}_\omega$ represents production by mean-field, $\mathcal{T}_\omega$ is transport by turbulent fluctuations, $\mathcal{EF}_\omega$ is the production or destruction via vortex stretching or compression respectively due to fluctuating strain fields, $\mathcal{EM}_\omega$ is production or destruction due to mean strain rate fields, $\mathcal{M}_\omega$ is the mixed production term and $\mathcal{D}_\omega$ and ϵ_ω are the viscous diffusion and dissipation of enstrophy respectively. Note that in the case of HIT besides the terms depending on the mean flow, the terms $\mathcal{T}_\omega$ and $\mathcal{D}_\omega$ also vanish since they take a divergence form.

Figure 4.13 shows isosurfaces of $\mathcal{EM}_\omega$ and $\mathcal{EF}_\omega$ (light green and pink colour respectively with a value of 300) within the vortical structures (visualized with the Q criterion with value 2). The isosurfaces indicate that the quantities emerge right after transition occurs. It can be observed that $\mathcal{EM}_\omega$ starts earlier than $\mathcal{EF}_\omega$. Balancing the enstrophy equation is challenging due to the lack of homogeneous directions in our case. In order to increase the sample size, however, we consider data over a spanwise distance $0.08C$ around $z/C = -0.2$. The budgets of the transport equation for enstrophy are shown in figure 4.14. The balancing error is measured with respect to the absolute value of the largest production peak. The maximum error along lines A and B is approximately $\approx 13 - 14\%$. Outside the recirculation zone, there are two peaks in the source term due to $\mathcal{EM}_\omega$ but within the recirculation bubble the small scale vortex stretching term $\mathcal{EF}_\omega$ becomes dominant and it is balanced by dissipation, refer to panel (a). The turbulent transport term $\mathcal{T}_\omega$ change signs outside the recirculation zone and inside this zone it has negligible values. The convection term $\mathcal{C}_\omega$ also plays a crucial role to balance the equation

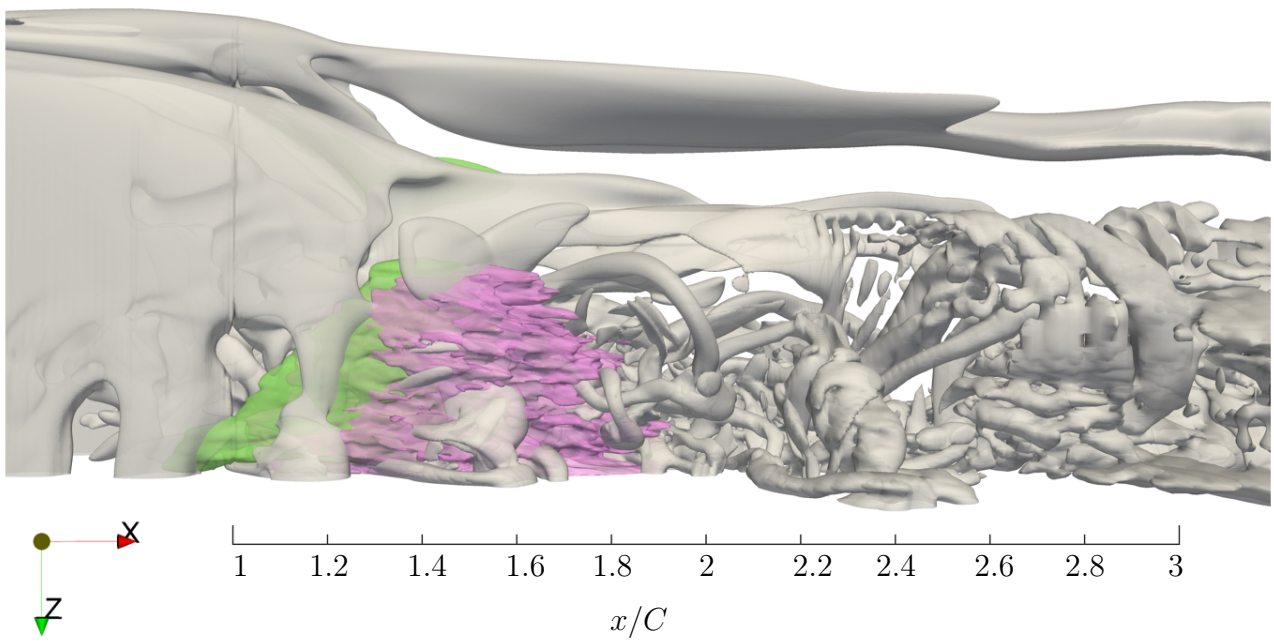


Figure 4.13: Isosurfaces of enstrophy production due to vortex stretching by the mean flow $\mathcal{EM}_\omega$ and fluctuations $\mathcal{EF}_\omega$ (light green and pink colour with a value of 300 respectively). Vortical structures are represented by the Q-criterion value of 2.

outside the recirculation zone. In the transitional region, panel (b), the primary contributor to the rapid increase in enstrophy in the "growth" section was the generation term $\mathcal{EM}\omega$. This term reaches its maximum before the peak of enstrophy, while $\mathcal{EF}\omega$ continues to grow at a much slower pace reaching its peak further downstream. $\mathcal{EM}\omega$ reaches values approximately $\approx 30\%$ higher than the maximum values of $\mathcal{EF}\omega$. The presence of $\mathcal{EM}\omega$ activates the turbulent transport terms around its peak. Compared to the recirculating flow, $\mathcal{EM}_\omega$ decays smoothly due to the lack of input from the mean shear. It is interesting to note that the peak of $\mathcal{EF}_\omega$ develops downstream of the peak of $\mathcal{EM}_\omega$. We will investigate this issue further in the next sections.

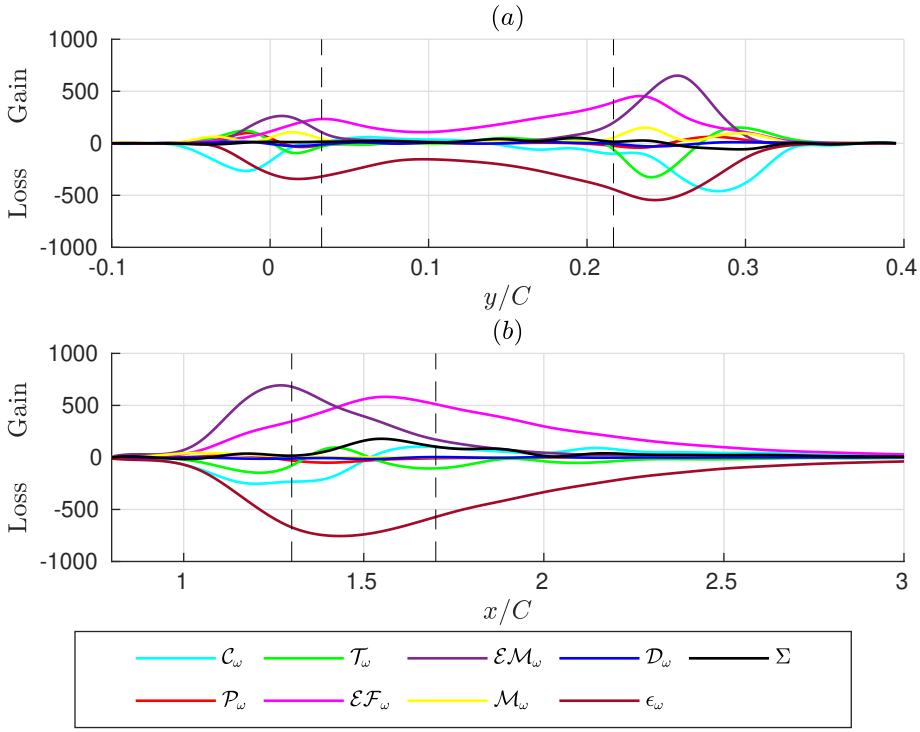


Figure 4.14: Budgets of the transport equation of $0.5\langle\omega_i\omega_i\rangle$ for (a) along line A and (b) along line B. Spanwise averaging over a distance $0.08C$ centered around $z/C = -0.2$ was performed to increase the sample size.

The transport equation for $\langle s_{ij}s_{ij}\rangle$ is [Tsinober, 2009]:

$$\begin{aligned}\frac{1}{2}\frac{\partial\langle s_{ij}s_{ij}\rangle}{\partial t} = &\underbrace{-\langle U_k\rangle\frac{\partial}{\partial x_k}\frac{1}{2}\langle s_{ij}s_{ij}\rangle}_{\mathcal{C}_s}\underbrace{-\langle u_k s_{ij}\rangle\frac{\partial\langle S_{ij}\rangle}{\partial x_k}}_{\mathcal{P}_s}\underbrace{-\frac{1}{2}\frac{\partial}{\partial x_k}\langle u_k s_{ij}s_{ij}\rangle}_{\mathcal{T}_s}\\ &\underbrace{-2\langle s_{ij}s_{ik}\rangle\langle S_{kj}\rangle}_{\mathcal{SM}_s}\underbrace{+\frac{1}{2}\langle\omega_i s_{ij}\rangle\langle\Omega_j\rangle}_{\mathcal{M}_s}\underbrace{-\langle s_{ij}s_{jk}s_{ki}\rangle}_{\mathcal{SF}_s}\underbrace{-\frac{1}{4}\langle\omega_i\omega_j s_{ij}\rangle}_{\mathcal{EF}_s}\\ &\underbrace{-\langle s_{ij}\frac{\partial^2 p}{\partial x_i\partial x_j}\rangle}_{\mathcal{H}_s}\underbrace{+\nu\langle s_{ij}\nabla^2 s_{ij}\rangle}_{\mathcal{D}_s},\end{aligned} \tag{4.5}$$

where $\mathcal{C}_s$ is convection by mean flow, $\mathcal{P}_s$ represents production by mean-field, $\mathcal{T}_s$ is transport by turbulent fluctuations, $\mathcal{SM}_s$ is strain amplification by mean strain rate, $\mathcal{M}_s$ corresponds to mixed production, $\mathcal{SF}_s$ is strain-self amplification, $\mathcal{EF}_s$ is the enstrophy production or destruction via vortex stretching or compression respectively due to fluctuating strain rate, $\mathcal{H}_S$ and $\mathcal{D}_s$ is the deviatoric pressure Hessian term and viscous dissipation terms respectively. Likewise, in the case of HIT besides the terms depending on the mean flow, $\mathcal{T}_s$ and $\mathcal{H}_S$ vanish. Budgets of the transport equation of total mean strain are shown in figure 4.15. In panel (a),

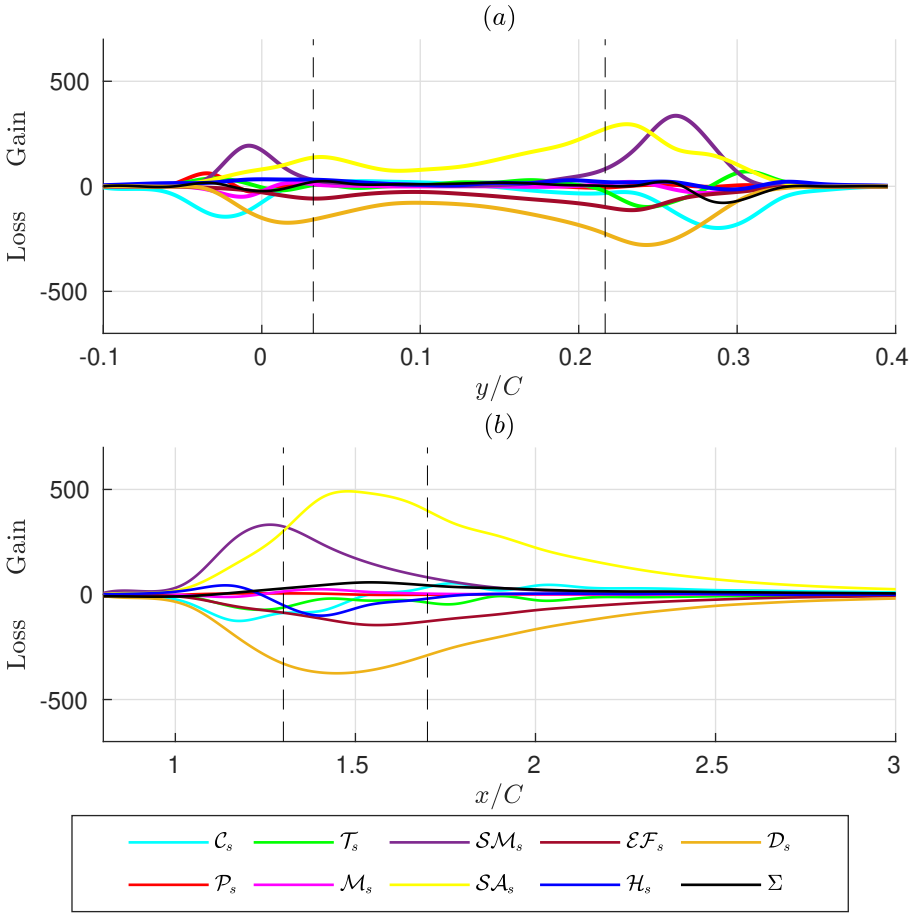


Figure 4.15: Budgets of the transport equation of $\langle s_{ij}s_{ij}\rangle$ for (a) along line A and (b) along line B. Spanwise averaging over a distance $0.08C$ centered around $z/C = -0.2$ was performed to increase the sample size.

inside the recirculation bubble, the generation of $\langle s_{ij}s_{ij}\rangle$ is sustained by the fluctuating strain self amplification term $\mathcal{SF}_s$ and balanced by dissipation. There are two peaks of $\mathcal{SM}_s$ outside the recirculation zone, while inwards two peaks of $\mathcal{SF}_s$ close to the recirculation boundary can be found. The convection term plays an important role outside the recirculation zone; in fact, in $y/C \approx 0.3$ it exceeds the dissipation term. In figure 4.15(b), $\mathcal{SF}_s$ and $\mathcal{SM}_s$ are the main source terms and the peak of $\mathcal{SF}_s$ is delayed with respect to that of $\mathcal{SM}_s$ but the value is higher. $\mathcal{SF}_s$ peak values are $\approx 60\%$ higher than $\mathcal{SM}s$. From $x/C \approx 1 - 1.5$ the role of $\mathcal{EF}_s$ as a sink is of comparable size with the rest of the budget terms. After this stage, $\mathcal{EF}_s$ together with dissipation act as the main sink terms. The balancing error is small along both lines and in the areas of interest of fully developed turbulence such at $y/C \approx 0.21$, it is negligible. In the case of the transitional flow, the maximum balancing error is $\approx 11\%$.

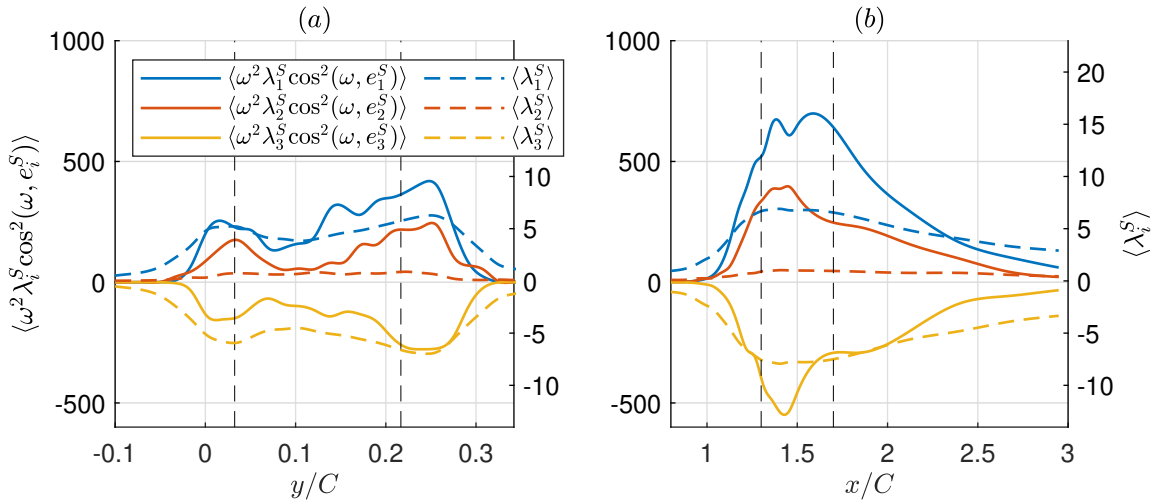


Figure 4.16: Eigencontributions to enstrophy production due to vortex stretching $\langle\omega_i\omega_j s_{ij}\rangle$ (left axis) and averaged eigenvalues of the fluctuating strain rate tensor (right axis) (a) along line A and (b) along line B.

4.4 Dynamics of vortex stretching due to small-scale strain

We turn our attention to vortex stretching term $\mathcal{EF}_\omega = \langle\omega_i\omega_j s_{ij}\rangle$ which can be decomposed as

$$\langle\omega_i\omega_j s_{ij}\rangle = \Sigma_{i=1}^{3}\langle\omega^2\lambda_i^s\cos^2(\omega,e_i^s)\rangle\,, \tag{4.6}$$

where $\omega^2 = \omega_i\omega_i$, λ_i^s and e_i^s are the eigenvalues and eigenvectors respectively of the fluctuating strain rate tensor s_{ij} [Tsinober, 2009]. Figure 4.16 shows the distribution of the eigendecompositions superimposed with $\langle\lambda_i^s\rangle$ along lines A and B. It can be seen that along both lines, the eigencontributions from the extensive and the intermediate eigenvalues act as source terms leaving the compressive eigencontribution as the sink. The eigenvalues of fluctuating strain tend to have a preferred ratio close to $(-4/1/3)$ which consistent with previous analysis, refer to Paul et al. [2017], Hamlington et al. [2008], Zhou et al. [2016a, 2015]. The intermediate eigenvalue is highly fluctuating, switching signs from positive to negative, but on average is weakly positive [Hamlington et al., 2008, Tsinober, 2009]. As can be seen from 4.17(a), within the recirculating region the alignments ω_i and e_i^s between take values that are close to those of HIT. In this scenario, vorticity typically tends to align parallel to the direction of the intermediate strain eigenvector and aligns orthogonally (perpendicularly) to the direction of compressive strain eigenvector [Tsinober et al., 1992, Mullin and Dahm, 2006]. With respect to the di-

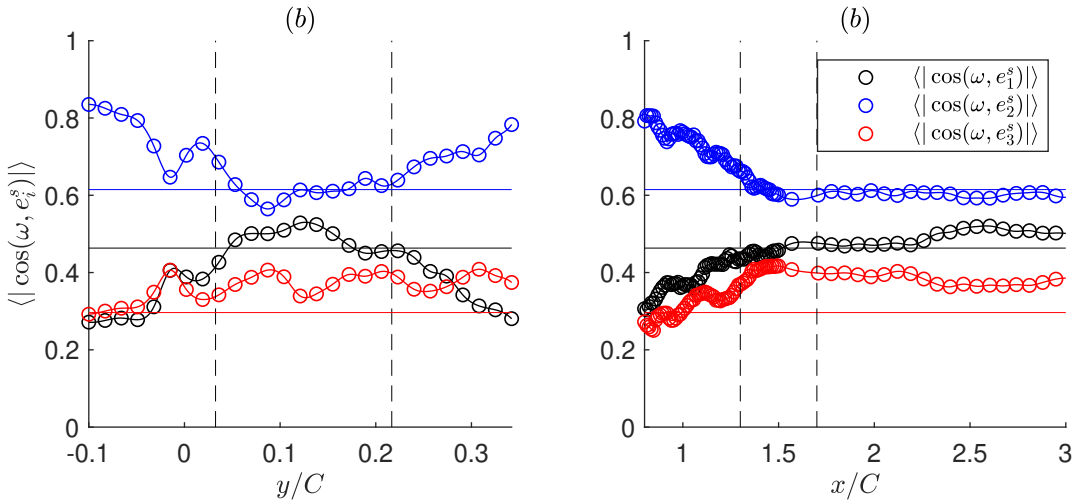


Figure 4.17: Average alignments between fluctuating vorticity and the eigenvectors of the fluctuating strain rate tensor (a) along line A and (b) along line B. Horizontal lines represent the average values for HIT $Re_{\zeta i} = 107$, data taken from Schumacher et al. [2007], Hamlington et al. [2008].

rection of extensive strain, the orientation of the vorticity is more arbitrarily or randomly determined. The particular high likelihood of favourable alignment between the intermediate eigenvector and ω_i merely reflects a vortex aligned with its own strain field according to the model proposed by Ashurst et al. [1987]. In these strongly vortical regions which resembles a quasi two-dimensional flow field, the strain field is dominated by the vorticity itself. The strain field is characterized by strong bi-axial strain field and the vorticity vector is aligned with the remaining, i.e. intermediate strain direction rather than any of the two other vectors (see Ni et al. [2014], Hamlington et al. [2008], Kholmyansky et al. [2001], Meneveau [2011] for further details). Outside the recirculation zone there are significant deviations from HIT however. Along the transition region, it can be observed in figure 4.17(b), that after the peak of $\mathcal{EF}_s$ at $x/C \approx 1.5$, the alignment between the vorticity and the intermediate eigenvector approaches values close to HIT.

In figure 4.18, the pdf's of the alignments between fluctuating vorticity and the eigenvectors of strain tensor for different regions of the transitional flow are presented. The regions are labeled as "growth" ($x/C = 1.22 - 1.33$), "peak" ($x/C = 1.4 - 1.63$), and "decay" ($x/C = 2.46 - 3.43$). The pdf's of HIT [Schumacher et al., 2007, Hamlington et al., 2008] are superimposed (dashed lines). The behaviour of the compressing eigenvector e_3 shows slight variations, but overall there is a strong similarity to HIT in all regions. The most significant deviation is

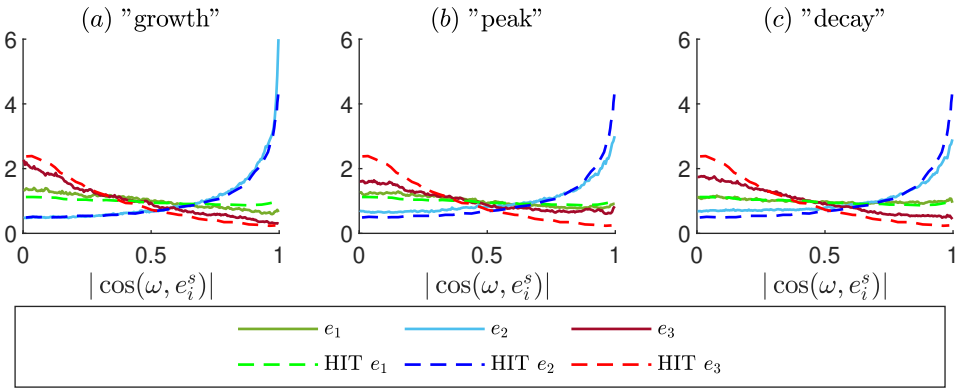


Figure 4.18: Pdf's of the alignments between vorticity and the principal directions of strain rate tensor in the transitional regions in different sections: (a) "growth" ($x/C = 1.2 - 1.3$), (b) "peak" ($x/C = 1.4 - 1.6$) and (c) "decay" ($x/C = 2.5 - 3.5$). Dashed lines indicate pdf's of HIT ($Re_{\zeta i} = 107$) data taken from Schumacher et al. [2007], Hamlington et al. [2008].

observed in the "growth" section, where there is a higher occurrence of perpendicularity in the alignment of compressive eigenvectors. This leads to a favourable scenario for the production of enstrophy.

4.5 Dynamics of vortex stretching due to the mean flow strain

We now turn our attention to $\mathcal{EM}_\omega$ which can be decomposed as,

$$\langle \omega_i \omega_j \rangle \langle S_{ij} \rangle = \Sigma_{i=1}^{3} \langle \omega^2 \Lambda_i^M \cos^2 \left(\omega, {e_i}^M\right) \rangle \ , \tag{4.7}$$

where $\omega^2 = \omega_i \omega_i$, Λ_i^M and ${e_i}^M$ are the eigenvalues and eigenvectors respectively of the mean strain rate tensor $\langle S_{ij} \rangle$ [Tsinober, 2009]. Figure 4.19 depicts the eigencontributions superimposed with the corresponding eigenvalues. For both flow regions Λ_1^M and Λ_3^M and the corresponding eingecontributions determine the overall value of $\mathcal{EM}_\omega$; the intermediate eigencontribution plays a minimal role. In the recirculation zone, the eigencontribution stemming from Λ_1^M is the dominant one, and attains maximum value near the peaks of k and enstrophy as expected. Note the very low values of all three components inside the recirculation bubble, which is due to the absence of mean shear. In figure 4.19(b), the same trends are observed with the eigencontribution from Λ_1^M as the dominant term. Compared to 4.16(b) the decay

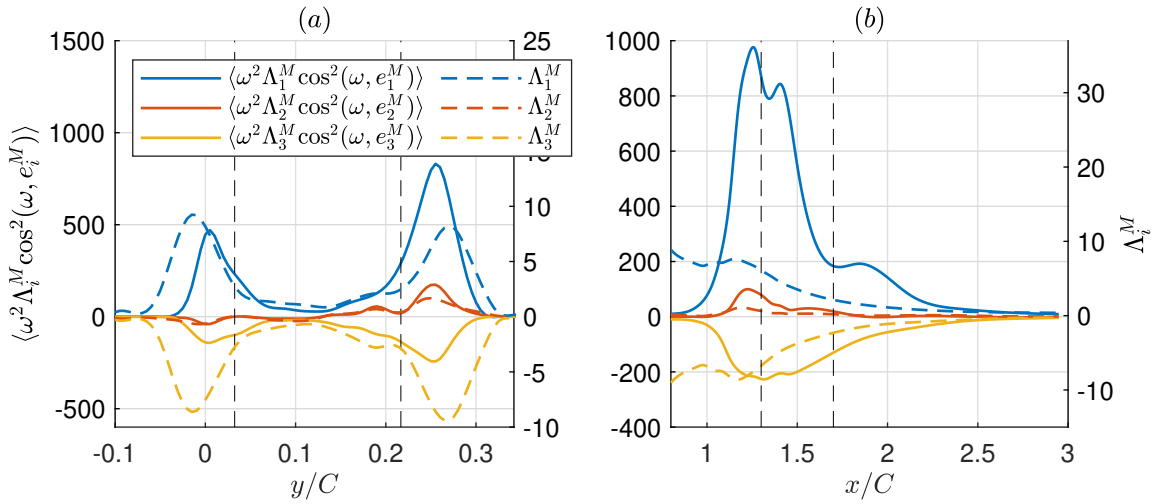


Figure 4.19: Eigencontribution of enstrophy production by mean strain rate $\langle\omega_i\omega_j\rangle\langle S_{ij}\rangle$ (left axis) and eigenvalues of the mean strain rate tensor (right axis) (a) along line A and (b) along line B.

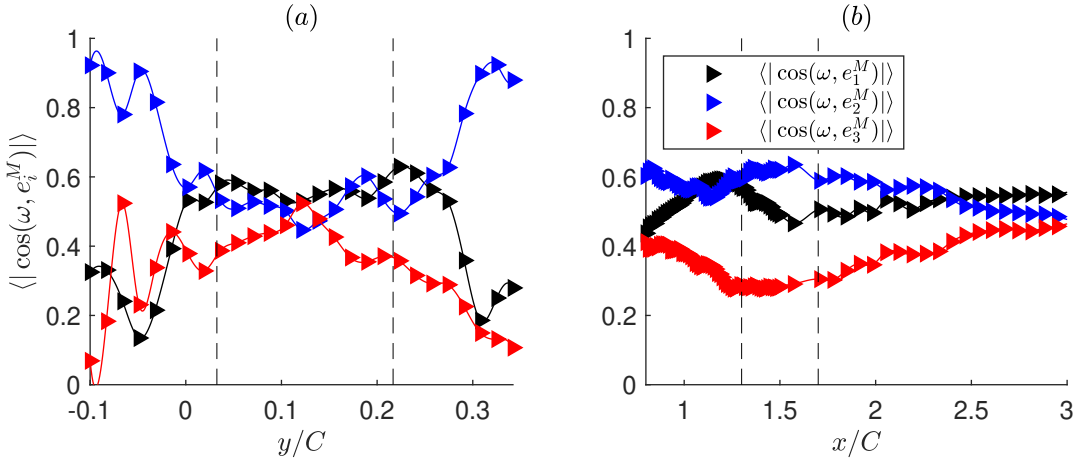


Figure 4.20: Alignment of fluctuating vorticity and the principal directions of the mean strain rate tensor (a) along line A and (b) along line B. Horizontal lines represent the values for HIT ($Re_{\zeta i} = 107$) [Schumacher et al., 2007, Hamlington et al., 2008].

(after $x/C \approx 2$) here is more abrupt due to the very low eigenvalues (again due to small mean shear). Note on the other hand the finite eigenvalues upstream of transition but due to the lack of fluctuating vorticity, the value of the eigencontribution is zero.

In figure 4.20, the average alignments $\langle|\cos\left(\omega, e_i^M\right)|\rangle$ are shown. Although these are alignments with respect to fixed (in time) principal strain directions, figure 4.20(b), shows that the alignments match for a short segment ($x/C \approx 1.4 - 1.6$) surprisingly well with HIT values. After $x/C \approx 2$ there is a loss of the coherence of the alignments. The lack of consistency becomes apparent when the values of Λ_i^M fall below ≈ 4. This implies that as the mean shear flow becomes weaker, its ability to affect the fluctuating vorticity diminishes, leading to a greater

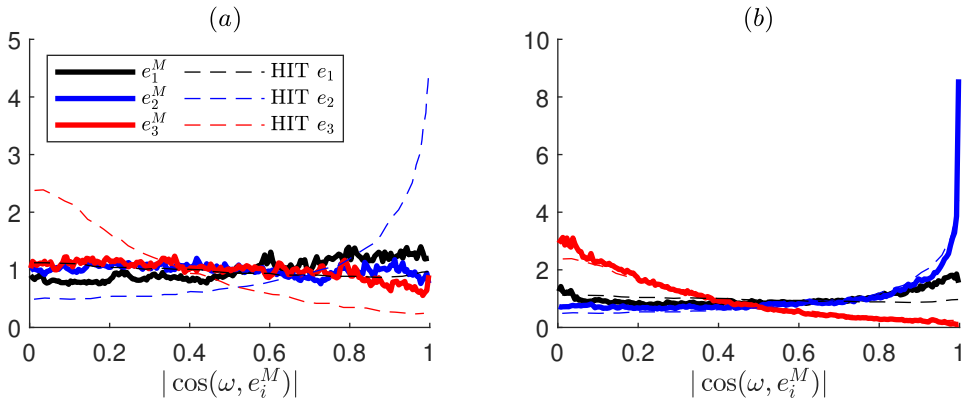


Figure 4.21: Pdf's of the absolute value of the cosine of the angle between fluctuating vorticity and the eigenvector of mean strain rate for (a) recirculating flow between $y/C = 0.87 - 0.155$ and (b) transitional flow between $x/C = 1.325 - 1.371$. Dashed lines represent values from HIT ($Re_{\zeta i} = 107$) , data from Schumacher et al. [2007], Hamlington et al. [2008] are superimposed.

independence between the two quantities. Specifically, the alignment is affected as ω and e_i^M tend to become uncoupled. In figure 4.20(a), outside of the recirculation bubble, the alignments mirror each other. Within the recirculation bubble, however there is a visible loss of coherence particularly $y/C = 0.8 - 0.15$ which the section where the eigenvalues have their lowest values.

Figure 4.21(a) shows the pdf of the absolute value of the cosine of the angle between vorticity and the eigenvectors of the mean strain rate tensor for recirculating flow between $y/C = 0.87 - 0.155$. Here, the magnitudes of Λ_i^M are negligible and the pdf shows a clear flat distribution which indicates that the alignments are random, i.e. there is on preference. On the contrary, in the transitional flow between $x/C = 1.325 - 1.371$ where the eigecontributions reach their maxima, figure 4.21(b) shows that the distributions attain a distribution typical of a HIT distribution as the ones observed in figure 4.18.

4.6 On the intermittent nature of vorticity and strain-self amplification

In this section, we turn our attention to rare events and their distribution in domain and time. We quantify their contributions on the production terms $\mathcal{EF}_w$ and $\mathcal{SF}_s$, and analyze their structure and the circumstances under which they appear.

The application of critical point theory to the topological classification of the flow introduced

Region (I)	Definition	F(I) for HIT	Flow topology [Ooi et al., 1999]
1.	$Q > 0$, $R > 0$	11.1	unstable-focus/ contracting (UF/C)
2.	$Q > 0$, $R < 0$	26.5	stable-focus/stretching (SF/S)
3.	$Q < 0$, $D > 0$, $R < 0$	9.9	stable-focus/stretching (SF/S)
4.	$Q < 0$, $D < 0$, $R < 0$	9.0	stable-node/saddle/saddle (SN/S/S)
5.	$Q < 0$, $D > 0$, $R > 0$	13.0	unstable-focus/ contracting (UF/C)
6.	$Q < 0$, $D < 0$, $R > 0$	30.5	unstable-node/saddle/ saddle (UN/S/S)

Table 4.1: Occupancy fractions F(I) of the 6 QR regions for $Re_{\zeta i} = 433$ (data obtained from Li et al. [2008] as cited by Keylock [2018]).

by Chong et al. [1990] is used to classify the topology of the flow and estimate the deviation from HIT. We compare later in this section the occupancy fractions in the 6 regions of the QR diagram against the HIT results taken from Li et al. [2008] as cited by Keylock [2018] which are shown in Table 4.1. According to the terminology used by Ooi et al. [1999] the regions can be regrouped in 4 divisions: unstable-focus/ contracting (UF/C)(regions 1 and 5), stable-focus/stretching (SF/S) (regions 2 and 3), stable-node/saddle/saddle (SN/S/S) (region 4) and and unstable-node/saddle/ saddle (UN/S/S) (region 6).

Figure 4.22 shows the instantaneous contours of discriminant Δ and the QR regions. In panel (a), Δ positive contours are very similar with Q, it is for the reason that this scalar is also used as a vortex identification tool [Chong et al., 1990]. The most abrupt changes in sign are found in the boundaries of the Q contours as in $E2$, $E3$ and $E4$. Particularly in $E4$, which is a region of concentrated vorticity, high positive values of Δ are surrounded by equally extreme negative values. Chacin and Cantwell [2000] revealed that the regions where Δ has a rapid change of sign are associated with the strongest generation of Reynolds stress and turbulent kinetic energy. In panel (b), the different regions are displayed with different colours. It can be seen that regions 1 and 2 are contained quite often inside Q as expected. This is because vortical structures often have a focus point. Within these regions, there is notable variability between the contracting and stretching nature of the focal structures, with a slight inclination towards region 2, aligning with the tear-drop-shaped pdf (refer to Section 1.4.2). Regions 3 and 5 are shown to be small or not frequently occupied. The rest of the domain is filled particularly by region 6, followed by region 4.

The Lagrangian perspective reveals that the dynamics of the local flow topology in the

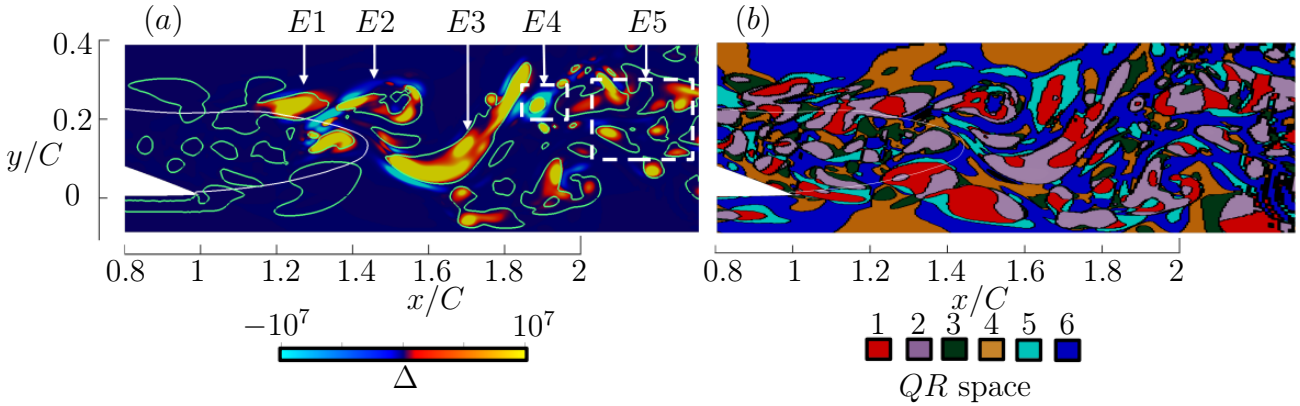


Figure 4.22: Contours of (a) Δ and (b) regions of the QR space based on fluctuations in the $x-y$ plane at $z/C=-0.2$. The light green isoline (a) represents $Q=2$.

incompressible regions are characterized by clockwise cycles around the origin of the QR map, following nearly closed trajectories in the order of $6-4-3-2-1-5$ [Martın et al., 1998]. An interesting observation from the Eulerian perspective is that there are many cases where the direct transfer from region 2 to 6 occurs without involving any intermediary region (such as 1 and 5), resulting in a change in phase from focal stretching to pure straining without involving focal compression. On the other hand, the common direct transfer from region 1 (focal compression) to region 6 (pure straining) is primarily facilitated through the passage of region 5, which aligns with the clockwise rotation of the trajectories found in Lagrangian studies. Additionally, in line with the Lagrangian feature, the clockwise trajectory $6-4-3$ can be observed, as it is noticeable that region 3 is mainly enclosed within region 4, reinforcing this trajectory.

Figure 4.23 shows the joint pdf of Q and R invariants in the "decay" section ($x/C=2.46-3.43$) of the transitional section with the 6 regions marked in the QR plane. At this spatial location, the flow is acquiring a quasi-HIT behaviour and contours that resemble the universal teardrop shape are obtained. Similar findings were reported at particular sections in mixing layers [Soria et al., 1994], boundary layers [Chacin and Cantwell, 2000, Bechlars and Sandberg, 2017b], turbulent jets [Beaumard et al., 2019] and single-square grid-generated turbulence [Zhou et al., 2015, Paul et al., 2017].

Figure 4.24 shows the occupancy fraction of each region inside the recirculation zone and the transitional region. The superposed dotted lines show the HIT values (for $Re_{\zeta i}=433$) cited in

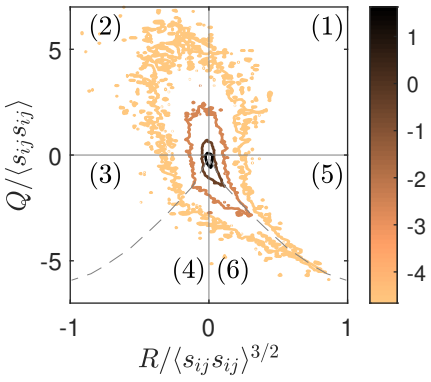


Figure 4.23: Joint pdf showing the QR regions for the transitional flow in the "decay" section ($x/C = 2.46 - 3.43$). The grey dashed line is the locus of points where $\Delta = 0$.

Keylock [2018]. In figure 4.24(a), the occupancy of region 2 has two clear peaks at $y/C \approx 0.05$ and $y/C \approx 0.25$ that corresponds with the peaks of k, $0.5\langle\omega_i\omega_i\rangle$ and $\langle s_{ij}s_{ij}\rangle$ while region 6 has a clear peak inside the bubble matching the HIT line at $y/C \approx 0.12$. At the furthest ends of the domain, enstrophy is zero. As a result, regions 4 and 6 share the total occupancy. In figure 4.24(b), there is a sharp change in the dominating region from Region 2 in the "growth" section to region 6 in the "peak" section which increases notably leading the occupancy for half of the "decay" section. Through instantaneous visualization of the flow topology (figure 4.22(b)), we observed that the increased presence of region 6 (between $x/C \approx 1.4$ and 2.5) could be attributed to the presence of less densely packed vortical structures (where region 2 tends to concentrate). These less dense vortical structures are made possible by the closure of the bubble, which provides additional space for the advection of larger structures that result from shear flows. At the end of the domain, there is a significant reduction in the size of these structures, which are more homogeneously distributed, closely resembling the values of HIT.

The contribution of each region to the mean values of the vortex stretching $\langle\omega_i\omega_j s_{ij}\rangle$ and strain self-amplification $-\langle s_{ij}s_{jk}s_{ki}\rangle$ are shown in figures 4.25 and 4.26 respectively. For $\langle\omega_i\omega_j s_{ij}\rangle$ regions 1 and 2 are the leading contributors while the other regions play a secondary role. The overall dominance of region 2 can be attributed to its higher occupancy, as indicated in figure 4.24. Region 1 which is determined by $Q > 0$, $R > 0$ is acting as a sink. In HIT, this particular region exhibits a slightly higher inclination for parallel alignment between ω and λ_3^s compared to other regions [Keylock, 2018]. Buxton and Ganapathisubramani [2010] showed that regions 1 and 5 were the only regions that showed a decrease in enstrophy due to time-

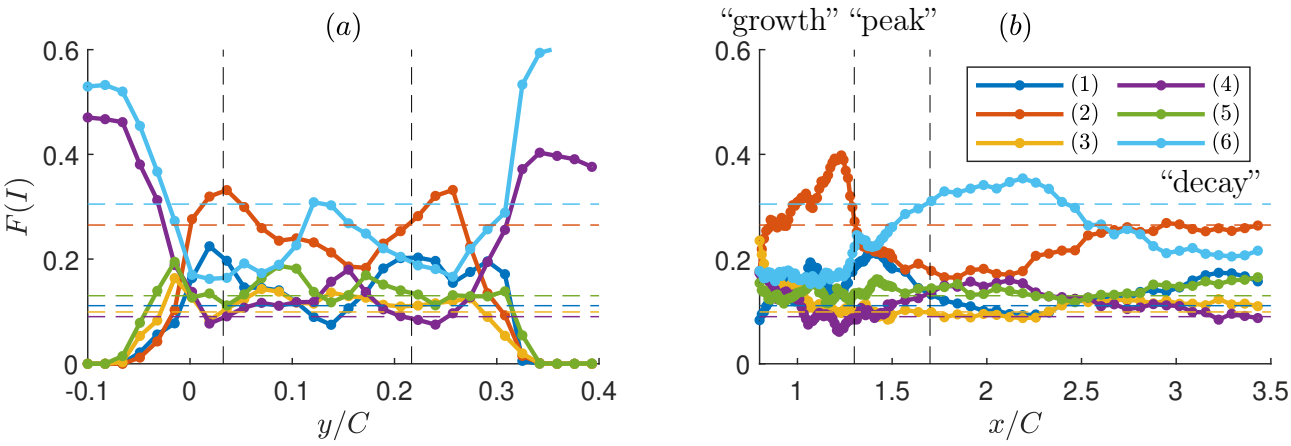


Figure 4.24: Occupancy fractions of QR regions (1)-(6) for the (a) along line A and (b) along line B. The dotted lines correspond to HIT values ($Re_{\zeta i} = 433$) obtained from Keylock [2018], see table 4.1.

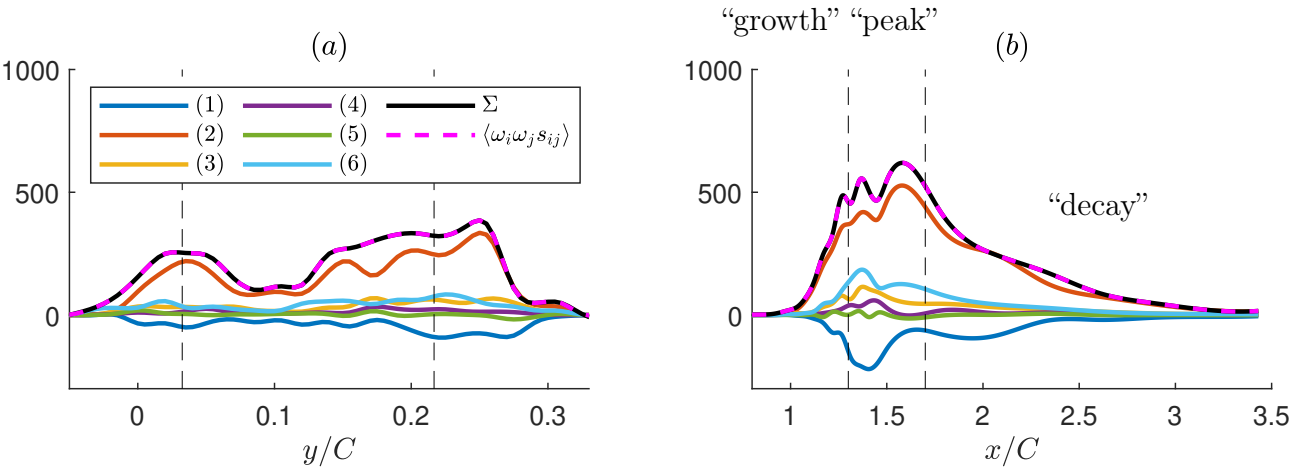


Figure 4.25: Contribution of different QR regions to $\langle \omega_i \omega_j s_{ij} \rangle$ (a) along line A and (b) along line B.

average vorticity compression. In Panel (a), even though the rest of the regions have similar occupancy as region 1, they account only for approximately 10%. In Panel (b) however, as transition occurs there is a significant contribution from region 6. Chu et al. [2014] discovered that the small-scale structures belonging to the SFS topology (region 2 and 3) in the outer layer of compressible turbulent boundary layers play the most important role in enstrophy production. For $-\langle s_{ij} s_{jk} s_{ki} \rangle$, region 6 is the main contributor while the rest of the regions collectively make up at least $\approx 45\%$ of values with regions 2 and 5 being the other most important contributors.

Figure 4.27 shows the pdf's at different locations in the recirculating and transitional flow. The highest probability values are centered around 0. The pdfs of both terms have long tails with a small probability indicating infrequent events. The $-s_{ij} s_{jk} s_{ki}$ distribution is skewed

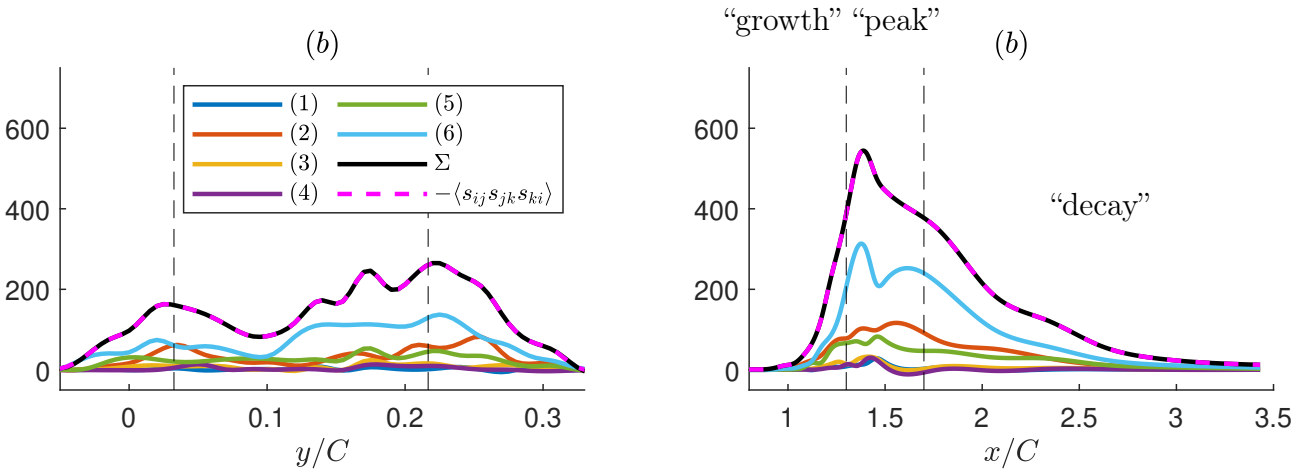


Figure 4.26: Contribution of different QR regions to $-\langle s_{ij}s_{jk}s_{ki}\rangle$ (a) along line A and (b) along line B.

towards a negative average which is a universal feature of turbulent flows due to the predilection of $\lambda_2^s > 0$. $\omega_i\omega_j s_{ij}$ on the other hand is less skewed showing a more symmetrical distribution due to the role of vortex compression which enables negative values. Here, however stretching prevails over compressing in all cases similar to HIT [Betchov, 1976, Davidson, 2015]. The fact that the distribution is not symmetric (which would turn $\omega_i\omega_j s_{ij} = 0$) is a reflection of the non-Gaussian nature of the velocity gradients [Tsinober, 2000]. In panel (a), the pdf in the "peak" section resembles the distribution of "recirculation" with the difference that the former section attains longer exponential tails and it is wider spread around 0. Similarly, in panel (b), the pdf of the "peak" is generally wider spread and has longer positive exponential tails respectively. Negative values however are of the same order of magnitude.

The exponential tails discussed above are rare events which in turbulence are often associated with the intermittent nature of large velocity gradients. Several studies have shown that strongly swirling structures in the dissipation range tend to be "tube-like" or "worm-like" in shape [Jiménez et al., 1993, Hosokawa and Yamamoto, 1990, Siggia, 1981, She et al., 1991]. These "worm-like" structures are reported to form from vortex sheets (thin layers of rotating fluid that separate regions of different velocities) that roll-up. This roll-up is believed to be a one-step process, driven by the Kelvin-Helmholtz instability [Ruetsch and Maxey, 1991, Vincent and Meneguzzi, 1991, McKeown et al., 2018]. However, ongoing research is still being conducted to determine whether these tubes dominate the inertial range of turbulence. Yeung et al. [2015]

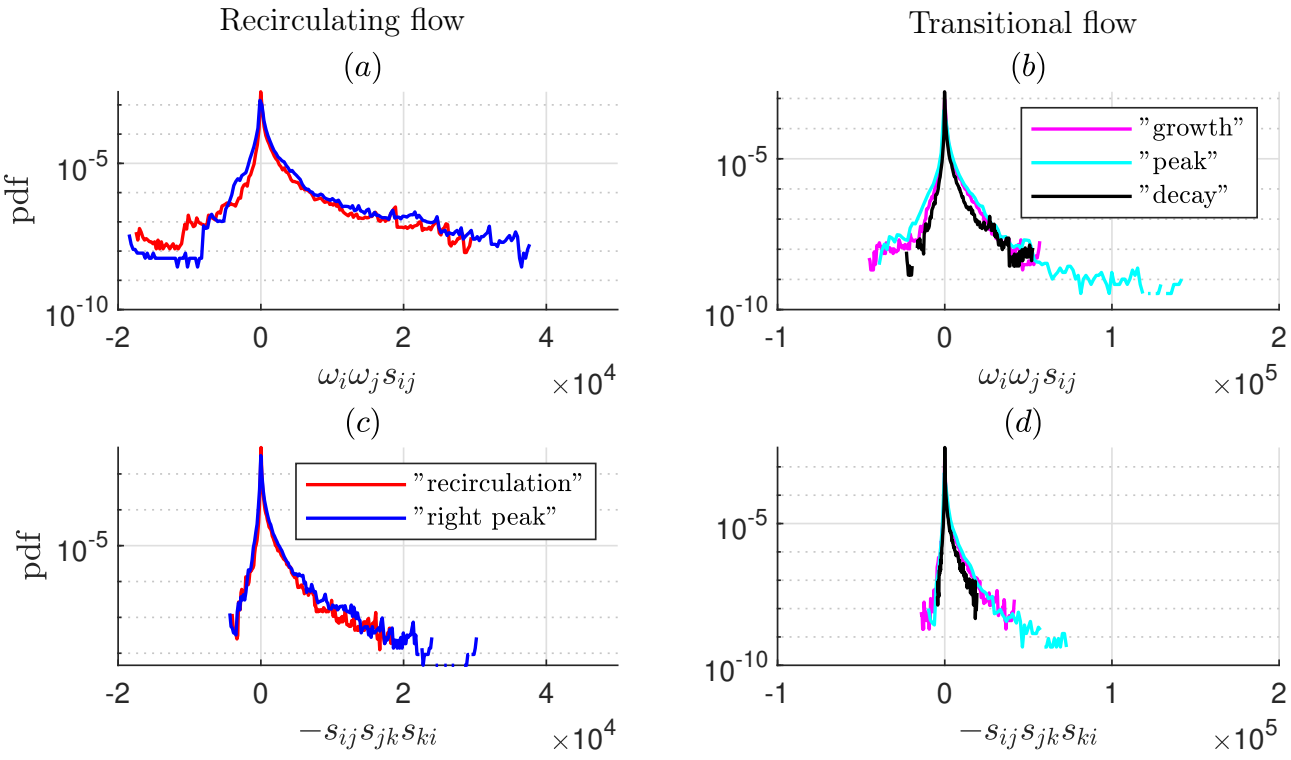


Figure 4.27: Pdf of $\omega_i\omega_j s_{ij}$ (top row) and $-s_{ij}s_{jk}s_{ki}$ (bottom row) at different locations. Recirculating flow sample locations (a), (c): "recirculation" ($y/C = 0.15 - 0.17$), "right peak" ($y/C = 0.21 - 0.25$). Transitional flow sample locations (b), (d): "growth" ($x/C = 1.2 - 1.3$), "peak" ($x/C = 1.4 - 1.63$) and decay ($x/C = 2.46 - 3.43$).

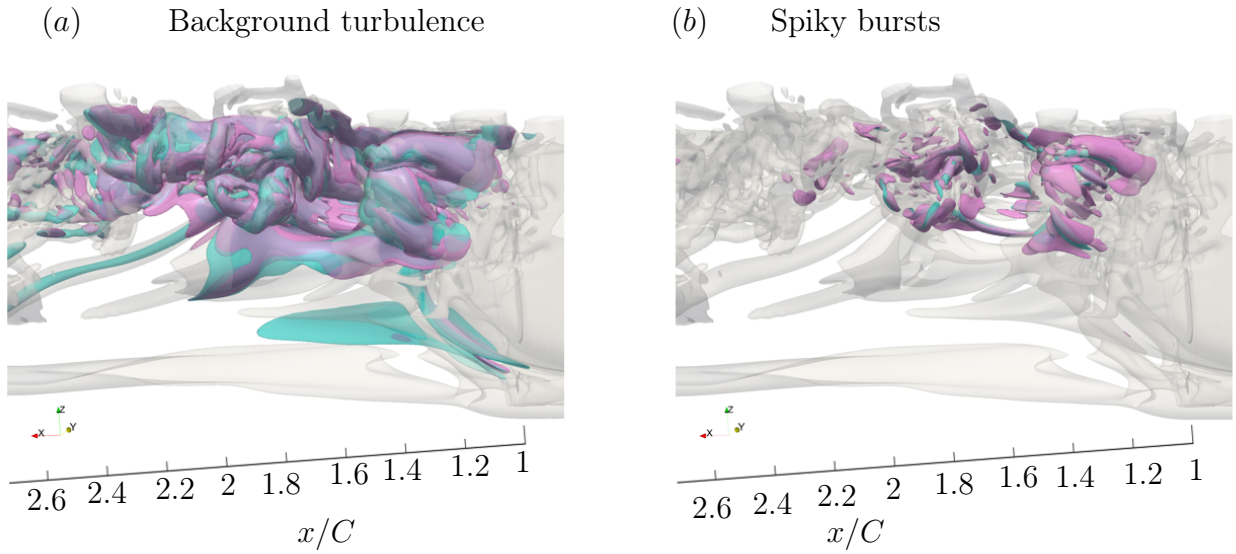


Figure 4.28: Isosurfaces of instantaneous enstrophy $0.5\omega_i\omega_i$ (cyan) and vortex stretching $\omega_i\omega_j s_{ij}$ (purple). (a) values of 100 and 300 respectively and (b) large events in the form of spiky bursts with values 1000 and 3000 (10 times higher). Vortical structures in the background are visualised in grey colour (value of Q-criterion equal to 2).

investigated in one of the largest simulations involving HIT to date ($Re_\zeta = 1300$), extreme events which are many orders of magnitude larger than the mean value and large events, which are greater than ten times the time-average value. It was found that the structures of these two types of events differ significantly. Unlike elongated vortex tubes, which are characteristic of large events, extreme events exhibit a chunky or compact structure. In this work, we focus our attention on large events of $\omega_i\omega_j s_{ij}$ and the circumstances in which these happen.

Figure 4.28 shows isosurfaces of instantaneous enstrophy $0.5\omega_i\omega_i$ (cyan) and vortex stretching $\omega_i\omega_j s_{ij}$ (purple) in the form of background turbulence with values equal to 100 and 300 respectively and large events with values 1000 and 3000 (10 times higher) representing intermittent spiky bursts. While it is known that large events are infrequent (sporadic) and spottier (small in volume) and therefore might have a relatively small kinetic energy content, their contribution to the time-average value is nor clear. In order to quantify this, in figure 4.29, we quantify the weighted contribution of the large events, defined as $\omega_i\omega_j s_{ij} > 10\langle\omega_i\omega_j s_{ij}\rangle$ and $-s_{ij}s_{jk}s_{ki} > -10\langle s_{ij}s_{jk}s_{ki}\rangle$, to the mean values at different spatial locations. Statistics were collected for $100t^*C/U_\infty$. the contribution of these large events to the mean value of enstrophy production is approximately 60%, whereas for strain-self amplification, it is around 40%. Notably, in the "growth" section, the large events of both production terms contribute in a similar magnitude towards their means, presenting a striking difference. As the flow progresses to the "decay" section, the contribution of these large events steadily decreases. Within the recirculating flow, the contribution of these events peaks in the middle of the bubble, reaching approximately 50% and 70% respectively. As the bubble begins to close and as we move outside of it, the contributions of large events tend to match.

In figure 4.30(a) and (b), for both types of flows, the frequency of these large events is less than 5% where the values corresponding to $\omega_i\omega_j s_{ij} > 10\langle\omega_i\omega_j s_{ij}\rangle$ are slightly more frequent than $-s_{ij}s_{jk}s_{ki} > -10\langle s_{ij}s_{jk}s_{ki}\rangle$. The trend is however less noticeable in the "growth" section (panel (b)), indicating that during the flow transition, large events of $-s_{ij}s_{jk}s_{ki}$ exhibit a comparable frequency. Furthermore, subplots (c) and (d) display the number of standard deviations $\sigma_{std} = \sqrt{\frac{1}{N}\sum_{i=1}^{N}(x_i^{\text{Data point}} - \langle x^{\text{Data point}}\rangle)^2}$, where N represents the sample size, x_i denotes each individual data point, and the time average of the entire set) between the

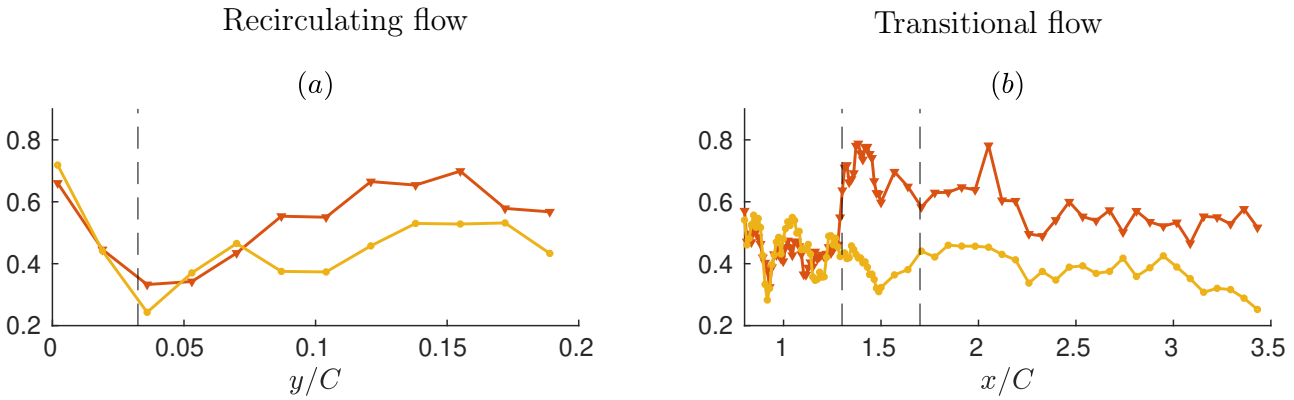


Figure 4.29: Contribution of events with values equal or larger than 10 times the time-average (large events) to the mean value (orange for $\omega_i\omega_j s_{ij}$ and yellow for $-s_{ij}s_{jk}s_{ki}$) (a) along line A and (b) along line B.

time-average and the fixed value of 10 times the mean of the production terms along lines A and B. It is important to note that each individual pdf distribution at each measurement point has a distinct σ_{std}. In a statistical context, a larger standard deviation indicates greater variability or dispersion in the values within that distribution. A higher number of standard deviations from the mean suggests that the occurrence of these large events significantly differs from the expected average behavior (becomes rarer). In panel (c), the values corresponding to $-s_{ij}s_{jk}s_{ki}$ exhibit a slightly higher degree of separation from the mean in terms of standard deviations, approximately around $\approx 3.5\sigma_{std}$, within the recirculating bubble. Moving to panel (d), it is notable that in the "growth" section, both values are similar. However, as the "peak" section commences, the value corresponding to $-s_{ij}s_{jk}s_{ki}$ predominantly surpasses $\omega_i\omega_j s_{ij}$, and the values of these two quantities gradually increase after the "peak" section, contrary to the trend observed in panel (b) where this increase is not very noticeable. This implies that as the "decay" phase is approached, the values within the distribution are getting closely clustered around the mean. Despite their minor differences in frequency and deviation from the mean, it is noteworthy that the contribution of $\omega_i\omega_j s_{ij} > 10\langle\omega_i\omega_j s_{ij}\rangle$ to the overall mean value (refer to figure 4.29) is approximately $\approx 20\%$ higher, with the exception of the "growth" section in the transitional region and certain areas within and outside of the recirculating bubble.

Figure 4.31 shows that for both the recirculating and transitional regions, about 80% of the large vortex stretching events occur when the flow field belongs to region 2. In the case of strain self-amplification, region 6 is the leading term and its contribution is approximately

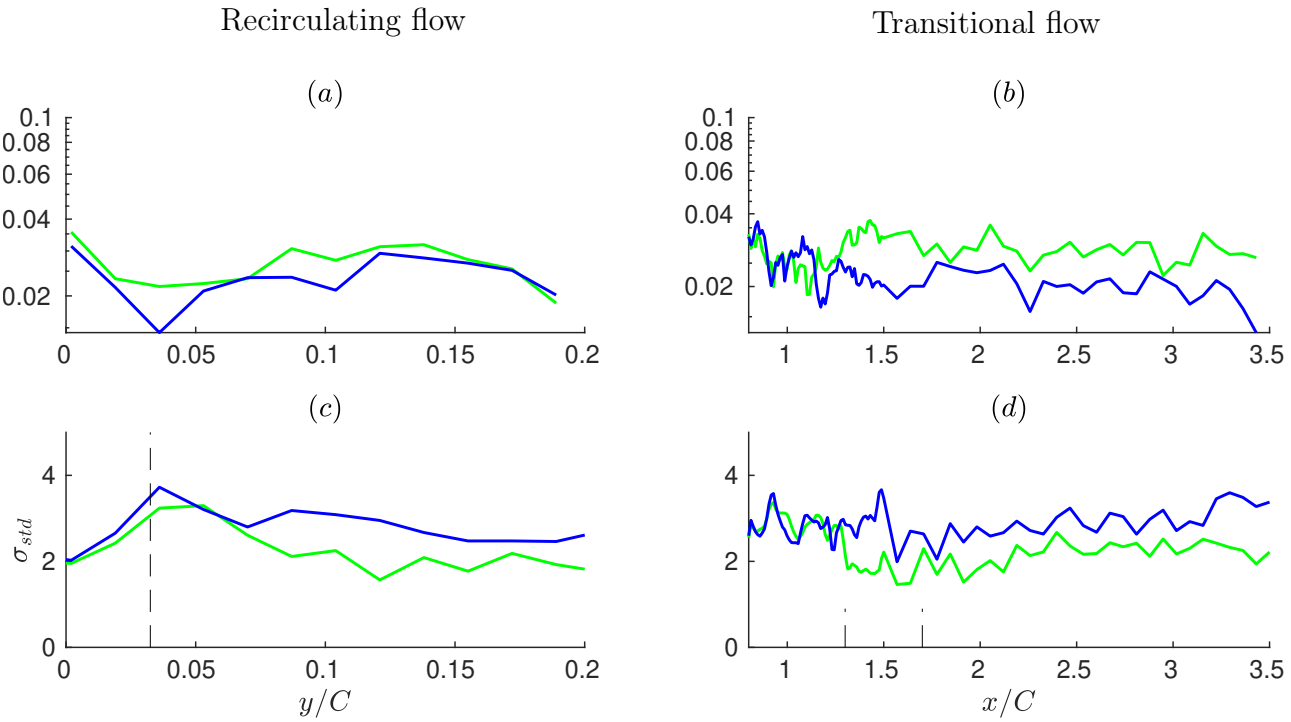


Figure 4.30: Frequency of events large events (a) along line A and (b) along line B (green line for $\omega_i\omega_j s_{ij}$ and blue line for $-s_{ij}s_{jk}s_{ki}$) and number of standards deviations σ_{std} between the time-average and the fix value of ten times the mean (c) along line A and (d) along line B.

$\approx 50\%$. Note that the remaining $\approx 50\%$ due to region 2 followed by 5. Region 2 is active in vortex stretching and acts as a sink in equation 4.5. The presence of region 2 might indicate the role of enstrophy production in limiting the levels of strain.

Figures 4.32 and 4.33 enable us to compare the topological contributions of the different QR regions of background turbulence and large events to mean values for the recirculation and transitional section respectively. With respect to $\omega_i\omega_j s_{ij}$, figures 4.32 (a) and (c) and 4.33 (a) and (c) show us that the topology between background and large events for the two types of flows is not significantly altered. Region 2 is still the most efficient region for enstrophy generation with the only difference that region 1 appears as a source term when constrained to large events. With respect to $-s_{ij}s_{jk}s_{ki}$, figure 4.32 (b) and (e) and figures 4.33 (b) and (e) show a very similar topology between background and large events. There is a higher presence of region 3 in the recirculating flow than in the transitional section in general.

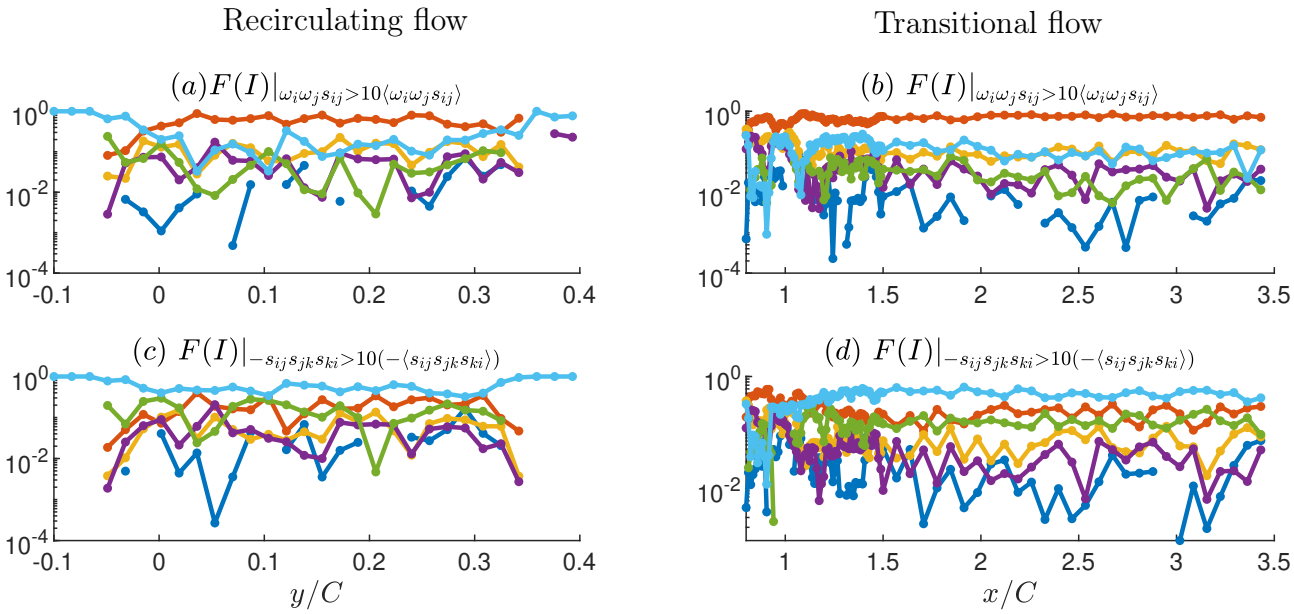


Figure 4.31: Occupancy fractions of QR regions for values of vortex stretching and strain-self amplification larger than 10 times the mean. Colours of different regions as in figure 4.24.

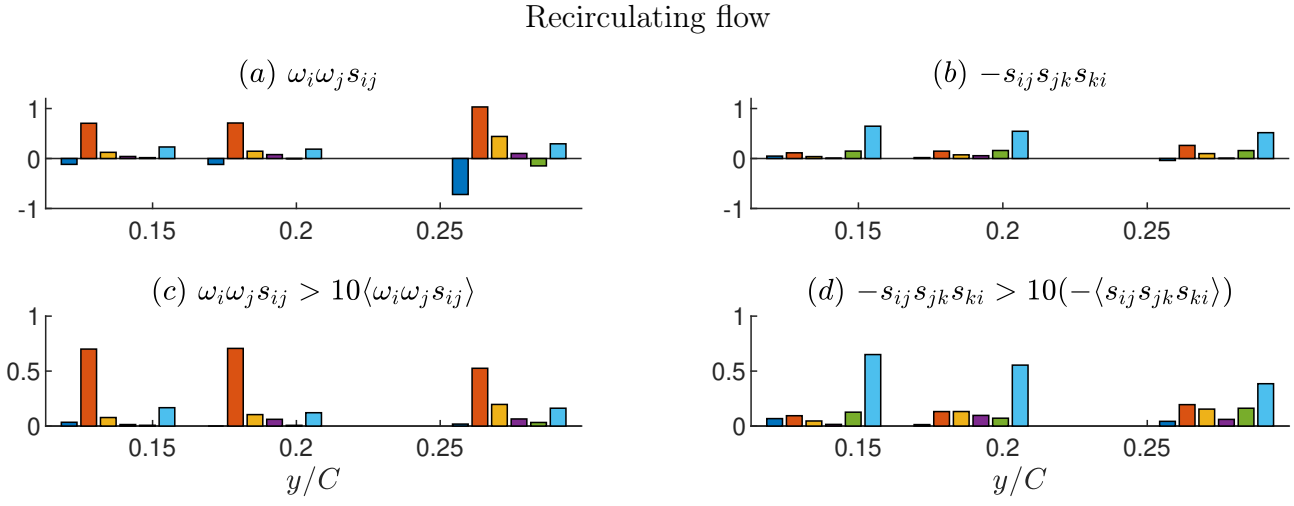


Figure 4.32: Contribution of each QR region to the mean at different locations within the recirculation zone. Measurement points at $y/C = 0.14$, 1.9 and 0.27. Colours of different regions as in figure 4.24.

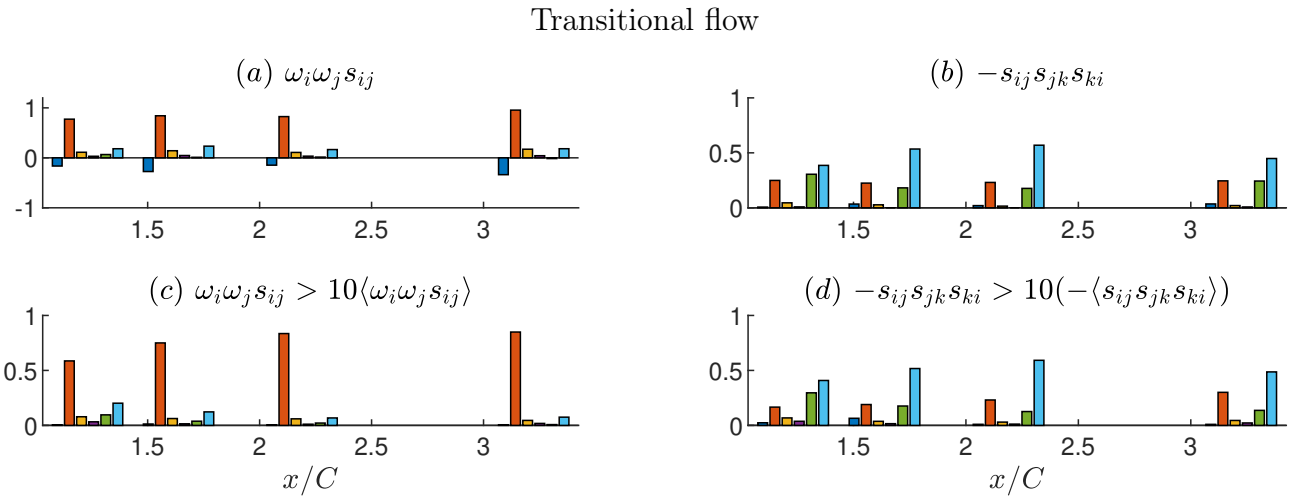


Figure 4.33: Contribution of each QR regions on the mean at different locations within the transitional region. Measurement points are $x/C = 1.23$, 1.63, 2.18 and 3.22. Colours of different regions as in figure 4.24.

4.7 Analysis of the non-normality of the velocity gradient tensor

In figure 4.34 (a) and (b), the spatial variation of the non-normality index k_{BC}, defined in equation 1.31, is shown for both flow sections. The regions that behave closer to HIT with respect to the alignments between the fluctuating vorticity and eigenvectors of the strain field, i.e. at $y/C \approx 0.1 - 0.2$ for recirculating and $x/C \approx 3 - 3.5$ for transitional flow yield k_{BC} values that match approximately with the HIT estimation obtained by Keylock [2018]. Indeed k_{BC} (black line) approaches zero but remains positive. The HIT pdf distribution reported by Keylock [2018] is slightly skewed towards -1, however, when the pdf is integrated the obtained value is marginally positive as the pink line indicates. The k_{BC} conditioned on events on the QR region 6 ($k_{BC}|^{QR=6}$), shows positive values, $k_{BC}|^{QR=3}$ negative values, and for $k_{BC}|^{QR=1}$ values are close to zero in agreement with previous findings [Keylock, 2018, 2022]. In panels (c) and (d) we estimate the occupancy of non-normal dominated flow field ($k_{BC} < 0$), the values for $y/C \approx 0.1 - 0.2$ and $x/C \approx 3 - 3.5$ are slightly above $\approx 50\%$. We conclude that the areas of non-normality are found in the peaks outside of the recirculating bubble reaching maximum value at $y/C \approx 0$ and $y/C \approx 0.28$ which coincides with the peaks of $\mathcal{EM}_\omega$ and $-\langle u_i u_j\rangle S_{ij}$ (see figure 4.19 (a) and 4.6 (a)). This is further evidence that the generation of $0.5\langle\omega_i\omega_i\rangle$ and k by

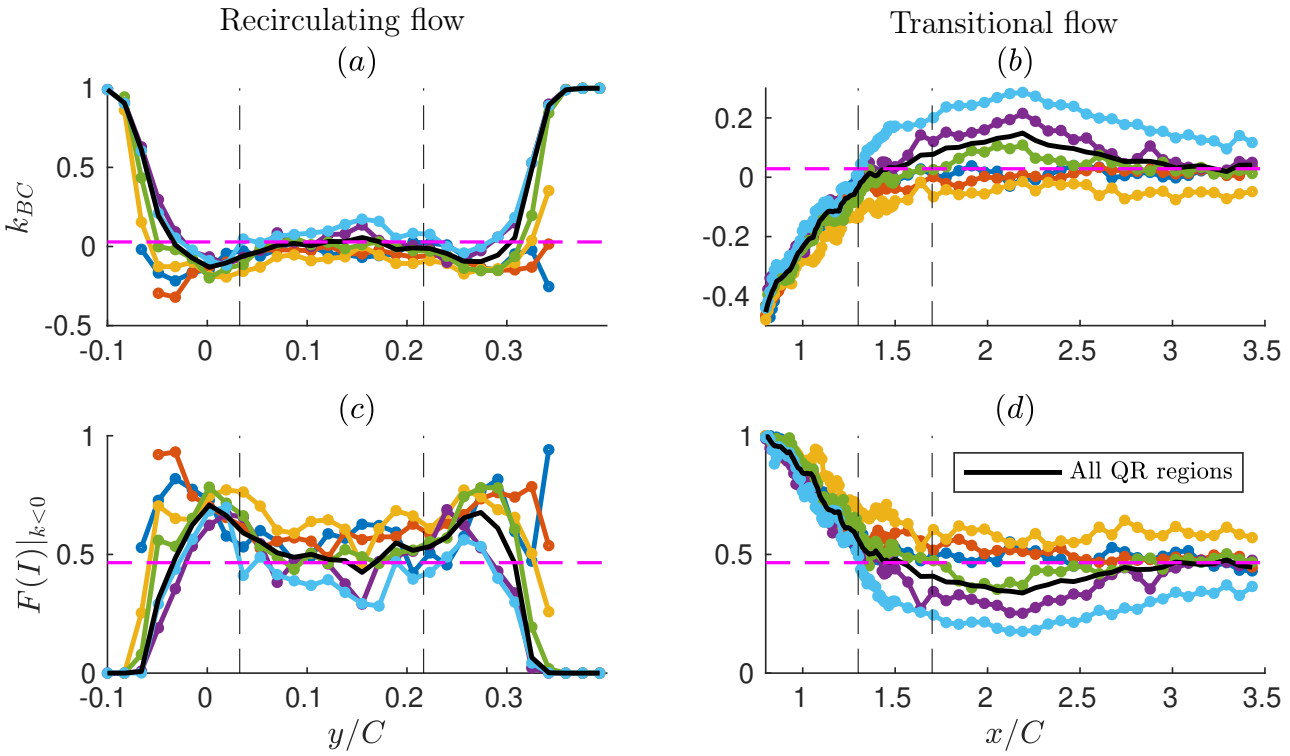


Figure 4.34: Variation of non-normality index k_{BC} conditioned on QR regions for the (a) recirculating and (b) transitional flow sections. Occupancy fractions of different QR regions at each measurement point where the non-normality index is $k_{BC} < 0$ (c) recirculating and (d) transitional flow. The dotted pink line corresponds to HIT values ($Re_{\zeta i} = 433$), data obtained from Keylock [2018].

mean strain fields is highly linked with non-local dynamics. In the case of the transitional flow, the "growth" section ($x/C = 1.2 - 1.3$) is highly non-normal whereas the section after "peak" ($x/C = 1.8 - 2.5$) is normal ($k_{BC} > 0$). In the section where turbulence is fully developed, the most normal section is found in the transitional flow at $x/C \approx 2.1$. Here, the non-normal dominated flow field reaches only $\approx 33\%$ which coincides with the location of the flow that is dominated by region 6 in terms of occupancy (see figure 4.24).

Figure 4.35 shows the magnitude of the normal and non-normal parts of $\|\Omega_A\|^2$ and $\|S_A\|^2$. Note $\|\Omega_C\|^2 = \|S_C\|^2$. In particular, in $E4$, we can see that in the middle of the circumference of the eddy, is predominantly normal $\|\Omega_c\|^2 \approx 0$ and $\|S_c\|^2 \approx 0$. Non-normality in this structure is however visible bordering the isoline of the Q contour (panel (c)). In the case of fluctuating strain around $E4$, we can see that $\|S_B\|^2 > \|S_C\|^2$. Non-normality is particularly pronounced in $E1$ and in the upper pars of $E2$ and $E5$ and also in the lower parts of the domain where the large scales of motion are highly active. This might confirm the significant impact that

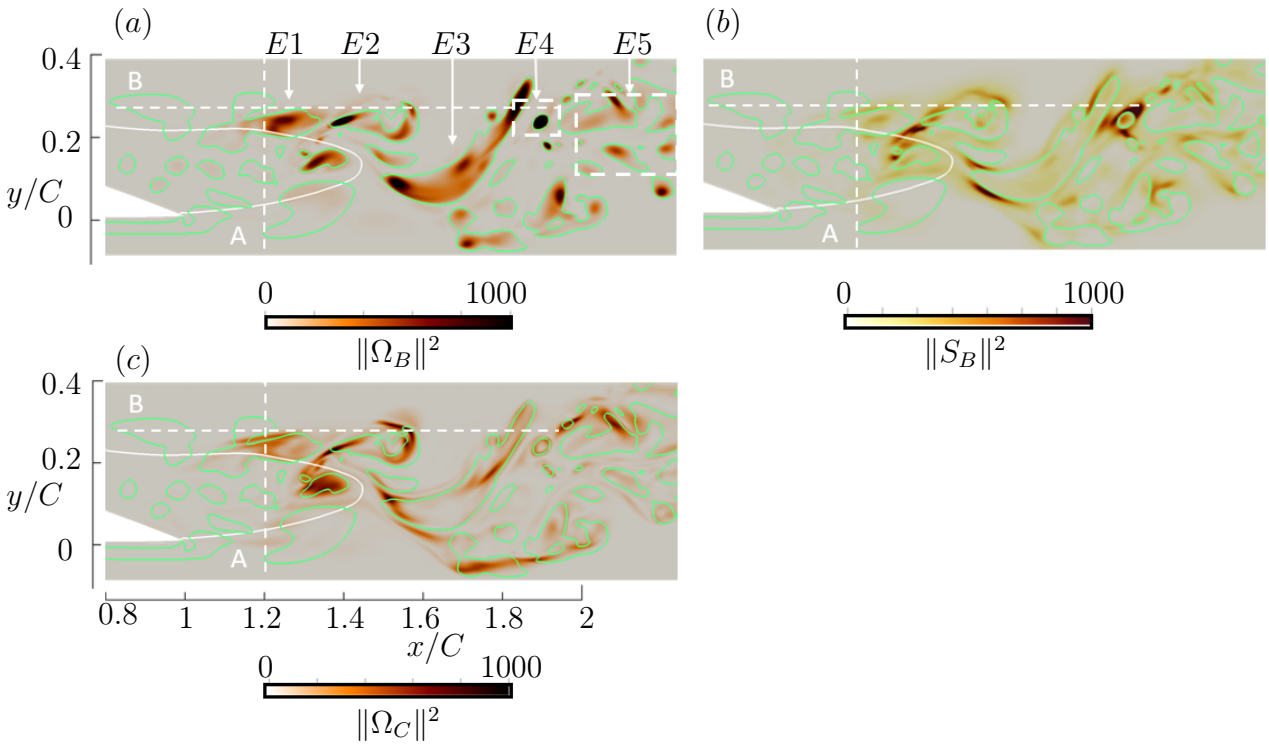


Figure 4.35: Contours of instantaneous (a) $\|\Omega_B\|^2$, (b) $\|S_B\|^2$, (c) $\|\Omega_C\|^2$ (note $\|\Omega_C\|^2 = \|S_C\|^2$) in the $x-y$ plane. Light green line represents the instantaneous vortical structures represented by the Q-criterion value of 2.

large scales have on the dynamics of the eddies via non-locality. The normal part of $\|\Omega_A\|^2$ is more concentrated within the boundaries of the vortical structures, while the non-normal part is more dispersed inside and around of these boundaries.

Figure 4.36 shows the variation of $\langle\|S_A\|^2\rangle$ and $\langle\|\Omega_A\|^2\rangle$ along with their normal and non-normal components (refer to equations 1.37 and 1.38). For $\langle\|\Omega_A\|^2\rangle$ refer to panels (a) and (b); in the recirculating region $\langle\|\Omega_C\|^2\rangle$ is slightly higher than $\langle\|\Omega_B\|^2\rangle$ over the entire range with larger differences in the peaks outside of the recirculating zone. In the transitional zone, both components are of similar magnitude, however after the peak at $x/C \approx 1.4$, $\langle\|\Omega_B\|^2\rangle$ attains slightly higher values. Panels (c) and (d) show $\langle\|S_B\|^2\rangle \approx \langle\|S_C\|^2\rangle$ inside the recirculating bubble between $x/C \approx 0.08 - 0.12$ whereas in the transitional region, this trend starts from $x/C \approx 1.6$ until the end of the domain. This trend approaches the HIT behaviour (dashed pink line) in figure 4.34(a)(b) where a quasi-normal distribution $k_{BC} \approx 0$. Outside the recirculating zone however there is a clear dominance of $\langle\|S_C\|^2\rangle$ over $\langle\|S_B\|^2\rangle$. The predominance of non-normality over normality in the strain peaks outside of the recirculation suggests that non-local

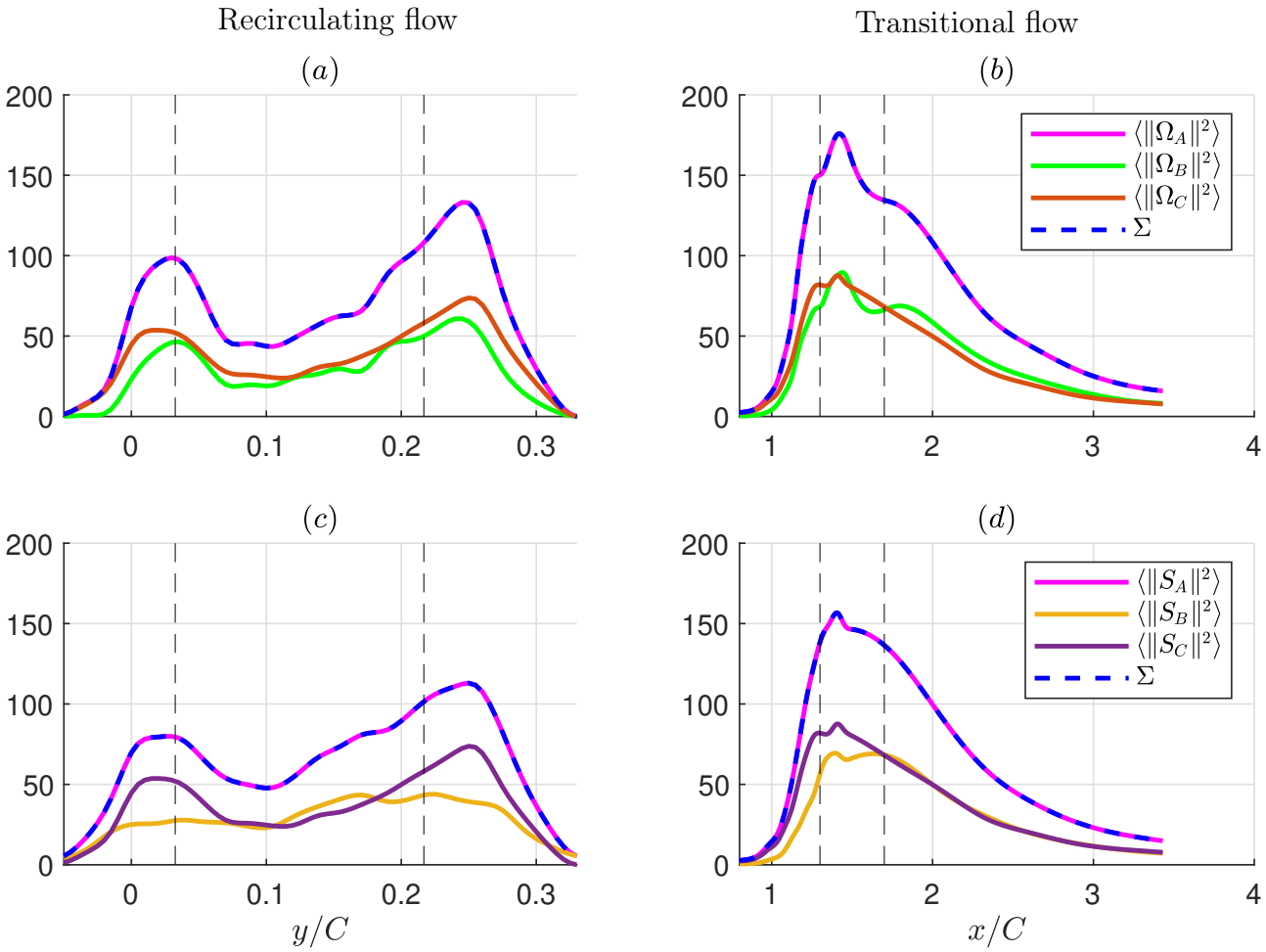


Figure 4.36: Distribution of the different components of $\langle\|S_A\|^2\rangle$ and $\langle\|\Omega_A\|^2\rangle$ for (a) and (c) along line A and (b), and (d) along line B.

strain may be more sensitive and prone to be generated in the transient sections of the flow. Region 6, (refer to figure 4.24) (a)), shows one of the most significant variations in the non-normality index when transitioning from the HIT conditions within the recirculation zone to the high shear region influenced by the mean flow production terms, reaching its peak non-normality value in this area. Similarly, in the transitional region, as turbulence starts to develop $\langle\|S_C\|^2\rangle$ grows faster than $\langle\|S_B\|^2\rangle$. When it comes to enstrophy, the reason why $\langle\|\Omega_B\|^2\rangle$ and $\langle\|\Omega_C\|^2\rangle$ are not approximately equal compared to their straining counterparts in the "decay" region might be linked to the fact that $\langle\|\Omega_B\|^2\rangle = 0$ in regions 4 and 6.

The QR regions that contribute most to the generation of the production terms of $\langle\omega_i\omega_j s_{ij}\rangle$ (Region 1 and 2) and $-\langle s_{ij}s_{jk}s_{ki}\rangle$ (Region 6) were identified in section 4.6. Since these three regions are responsible for shaping the dynamics of the production term, we proceed with our

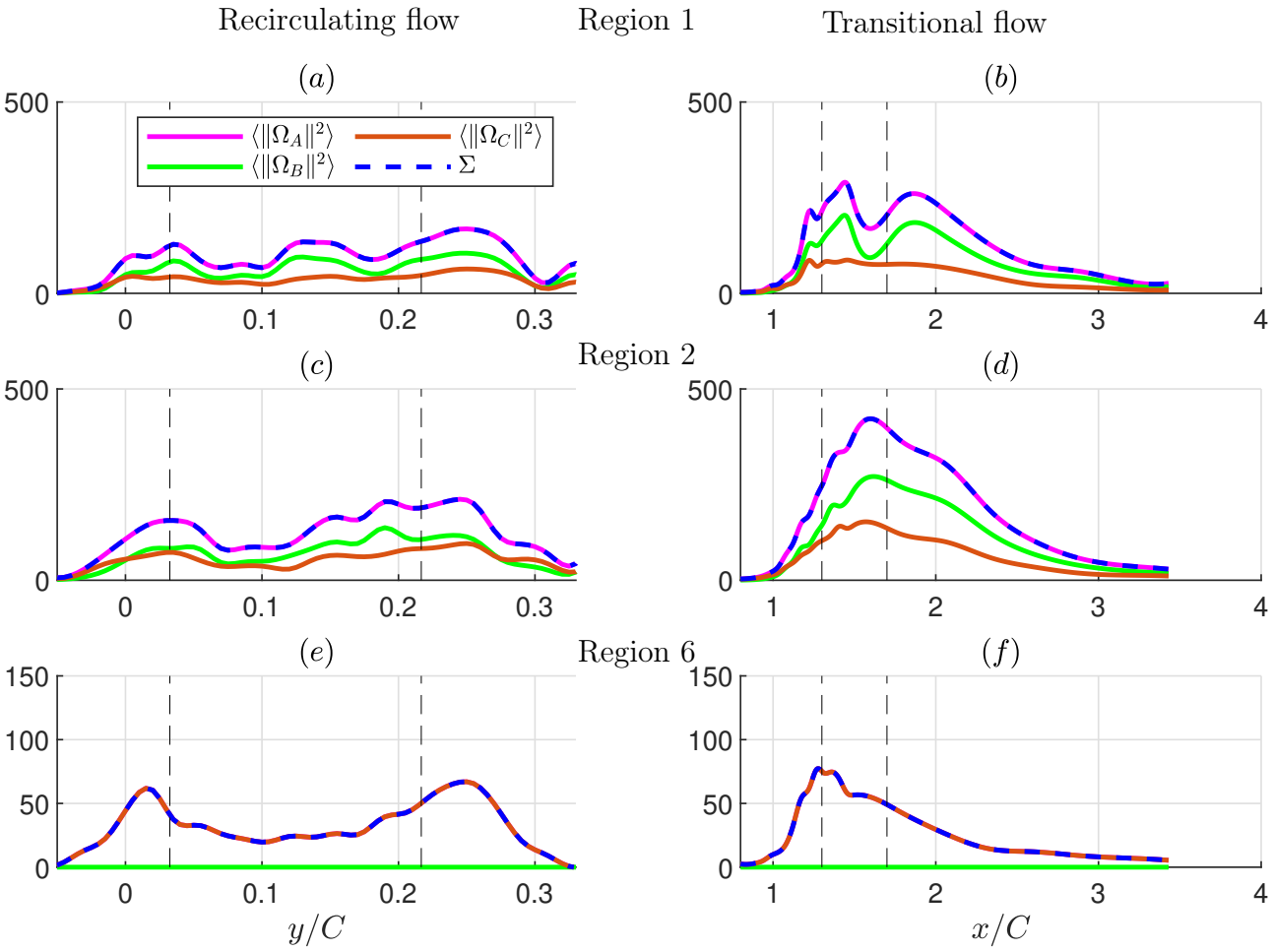


Figure 4.37: Distribution of $\langle\|\Omega_A\|^2|^{QR=1,2,6}\rangle$ for (a), (c), (e) along line A and (b), (d), (f) along line B.

analysis by focusing on these three regions only. Figure 4.37 shows the components of the conditionally averaged $\langle\|\Omega_A\|^2|^{QR=1,2,6}\rangle$ into normal and non-normal parts. Region 1 and 2 shows a clear dominance of $\langle\|\Omega_B\|^2\rangle$ over $\langle\|\Omega_C\|^2\rangle$ which agrees with the findings of Keylock [2018] where the pdf's are skewed towards 1 indicating fully normality. Region 6, which is defined by the condition $\Delta_A < 0$ i.e. no complex eigenvalues, has by definition $\langle\|\Omega_B\|\rangle = 0$. Here, only $\langle\|\Omega_C\|^2\rangle$ is present.

We repeat the analysis for the conditionally-averaged norm $\langle\|S_A\|^2|^{QR=1,2,6}\rangle$. In regions 1 and 2, the non-normal contributions are more prominent whereas the normal parts have very low values. Region 6 however shows $\langle\|S_B\|^2\rangle$ as the dominant term across the whole domain in both flow sections.

We proceed now with the analysis of the production terms and their Schur decomposition

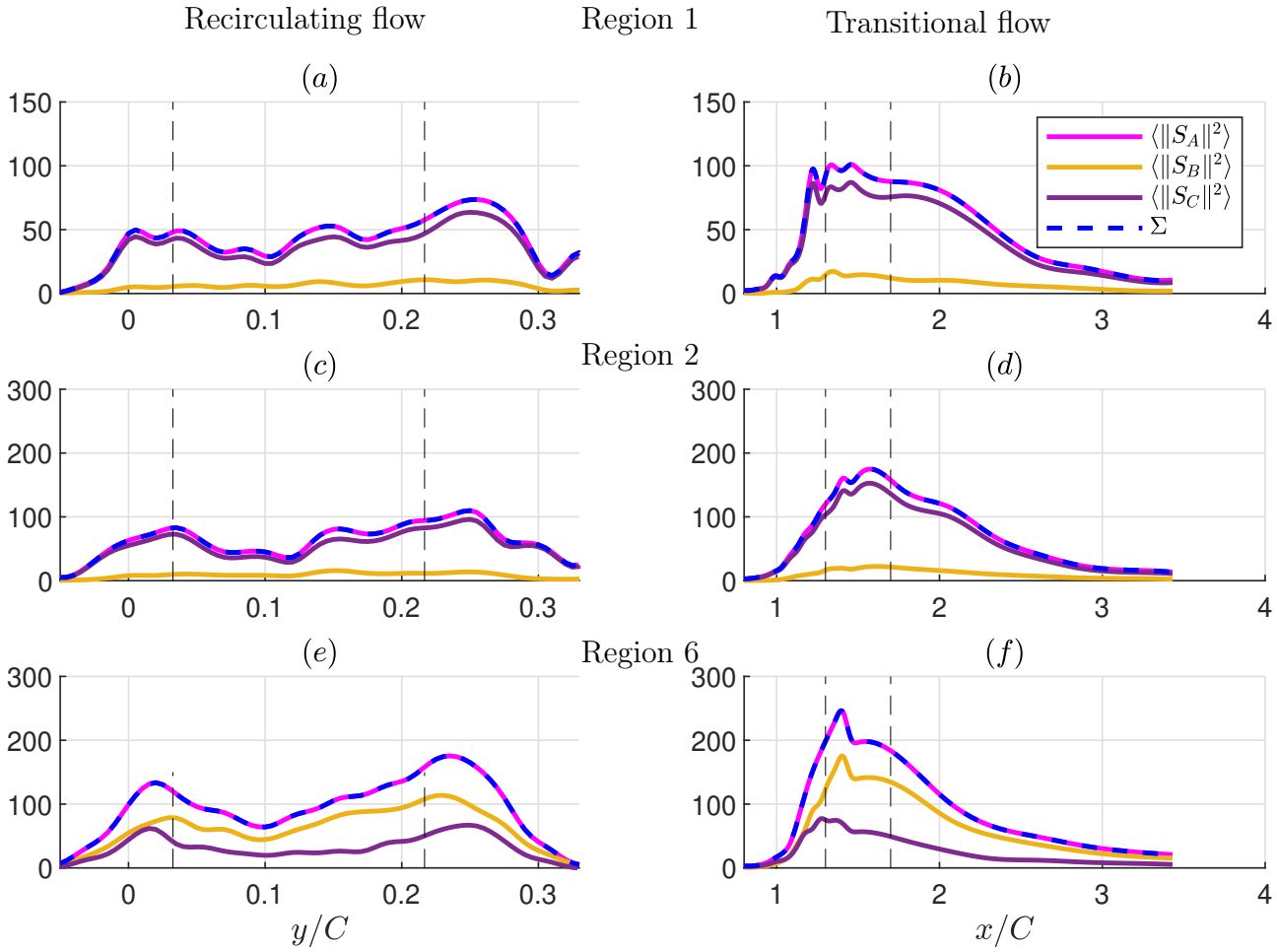


Figure 4.38: Distribution of $\langle \|S_A\|^2 |^{QR=1,2,6} \rangle$ accross all regions for (a), (c) along line A and (b), (d) along line B.

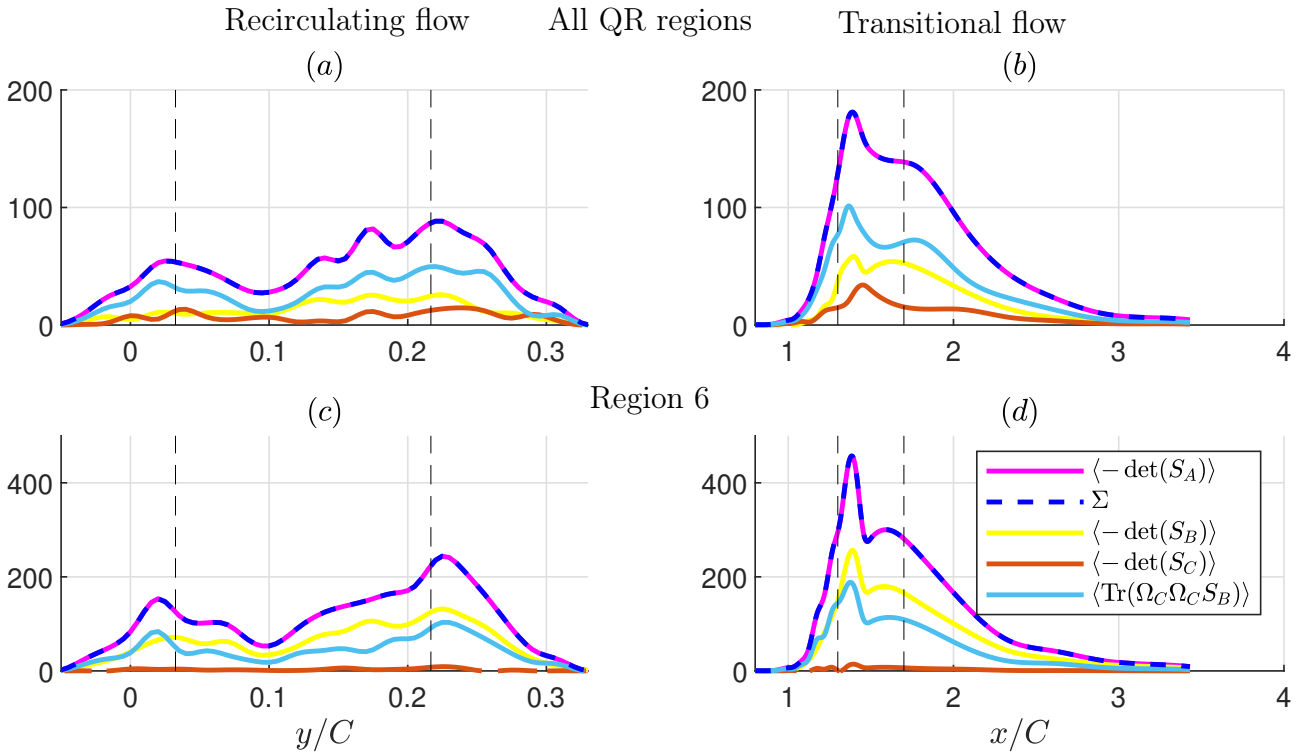


Figure 4.39: Distribution of $-\langle \det(S_A) \rangle$ (top row) and $-\langle \det(S_A)|^{QR=6} \rangle$ (bottom row) for (a), (c) along line A and (b), (d) along line B.

refer to equations 1.49 and 1.50. Figure 4.39 shows the decomposition of $-\langle \det(S_A) \rangle$ (top row) and $-\langle \det(S_A)|^{QR=6} \rangle$ (bottom row). When all regions are considered (top row) the mixed term $\langle \mathrm{Tr}(\Omega_C \Omega_C S_B) \rangle$ is the main contributor to $-\langle \det(S_A) \rangle$ followed by $-\langle \det(S_B) \rangle$ and $-\langle \det(S_C) \rangle$. When conditioning to events in region 6 (bottom row), $-\langle \det(S_B) \rangle$ is the dominant term followed by $\langle \mathrm{Tr}(\Omega_C \Omega_C S_B) \rangle$. The fact that the normal part is the dominant term in region 6 is in agreement with figure 4.34 that shows that this region displays a highly normal behaviour that can be high as $\approx 80\%$. The fact that the mixed term dominates slightly in panel (a)(instead of the normal component) when all regions are considered is due to the influence of regions 1-5 which collectively make up at least $\approx 45\%$ of the value (figure 4.26), and favour the dominance of the mixed term. The trend of significantly higher values of $\langle \mathrm{Tr}(\Omega_C \Omega_C S_B) \rangle$ compared to $-\langle \det(S_B) \rangle$ is more pronounced near the strain peaks (refer to figure 4.36(c)), which could also explain the prevalence of non-normality over normality in these regions. The values of $-\langle \det(S_C) \rangle$ are very low and it has been reported that the median values of this term are close to zero [Beaumard et al., 2019].

The spatial variation of $\langle \mathrm{Tr}(\Omega_A^2 S_A) \rangle$ (equivalent to $\frac{1}{4}\langle \omega_i \omega_j s_{ij} \rangle$ in index notation) and its

components, see equation 1.50, are shown in figure 4.40. The top row shows the results for all regions, while the bottom rows show the results for regions 1 and 2 which are the most effective in the production or destruction of this quantity (see figure 4.25). When considering all regions (top row), the dominant term is the mixed term $\langle \mathrm{Tr}(\Omega_C \Omega_C S_B) \rangle$ followed by normal term $\langle \mathrm{Tr}(\Omega_B \Omega_B S_B) \rangle$. This dominance can be attributed to the significant loss that the normal term, $\langle \mathrm{Tr}(\Omega_B \Omega_B S_B) \rangle$ undergoes through compression (negative values) in region 1 ($Q > 0$, $R > 0$) whereas $\langle \mathrm{Tr}(\Omega_C \Omega_C S_B) \rangle$ is negligible (see panel (c),(d)). It is important to note, that inside the recirculating bubble, when all regions are considered, these terms converge towards $\langle \mathrm{Tr}(\Omega_C \Omega_C S_B) \rangle \approx \langle \mathrm{Tr}(\Omega_B \Omega_B S_B) \rangle$ for a limited section when HIT conditions are reached (panel (a)). By taking a closer look to panel (e) and (f), constrained to region 2, the normal term $\langle \mathrm{Tr}(\Omega_B \Omega_B S_B) \rangle$ is indeed the dominant product which undergoes stretching. By considering all regions (top row) as stretching wins over compression, the normal term remains positive but the quantity is diminished, allowing the mix term $\langle \mathrm{Tr}(\Omega_C \Omega_C S_B) \rangle$ to take over. Lastly, $-\langle \det(S_C) \rangle$, similar to in figure 4.39, remains mostly positive in all panels, but with significantly lower values compared to the other terms.

It is interesting to note, that in panel (b), as the "peak" section section starts, a significant dominance of the the mixed term $\langle \mathrm{Tr}(\Omega_C \Omega_C S_B) \rangle$ is observed. This predominance can be attributed to the fact that for this short segment (between $x/C \approx 1.4$ and 1.6), the occupancy fractions of region 1 (and the effects of compression that come with it) is equal to the occupancy fractions of regions 2 and 6 (see figure 4.25(b)). Furthermore, in the first half of the "decay" section, even though the overwhelming normality of the flow (see figure 4.34(d)), the following approximation is found: $\langle \mathrm{Tr}(\Omega_C \Omega_C S_B) \rangle \approx \langle \mathrm{Tr}(\Omega_B \Omega_B S_B) \rangle$. This approximation highlights the fact that, despite that region 6 has the highest occupancy in this section, its contribution to enstrophy production is negligible (see figure 4.25(b)).

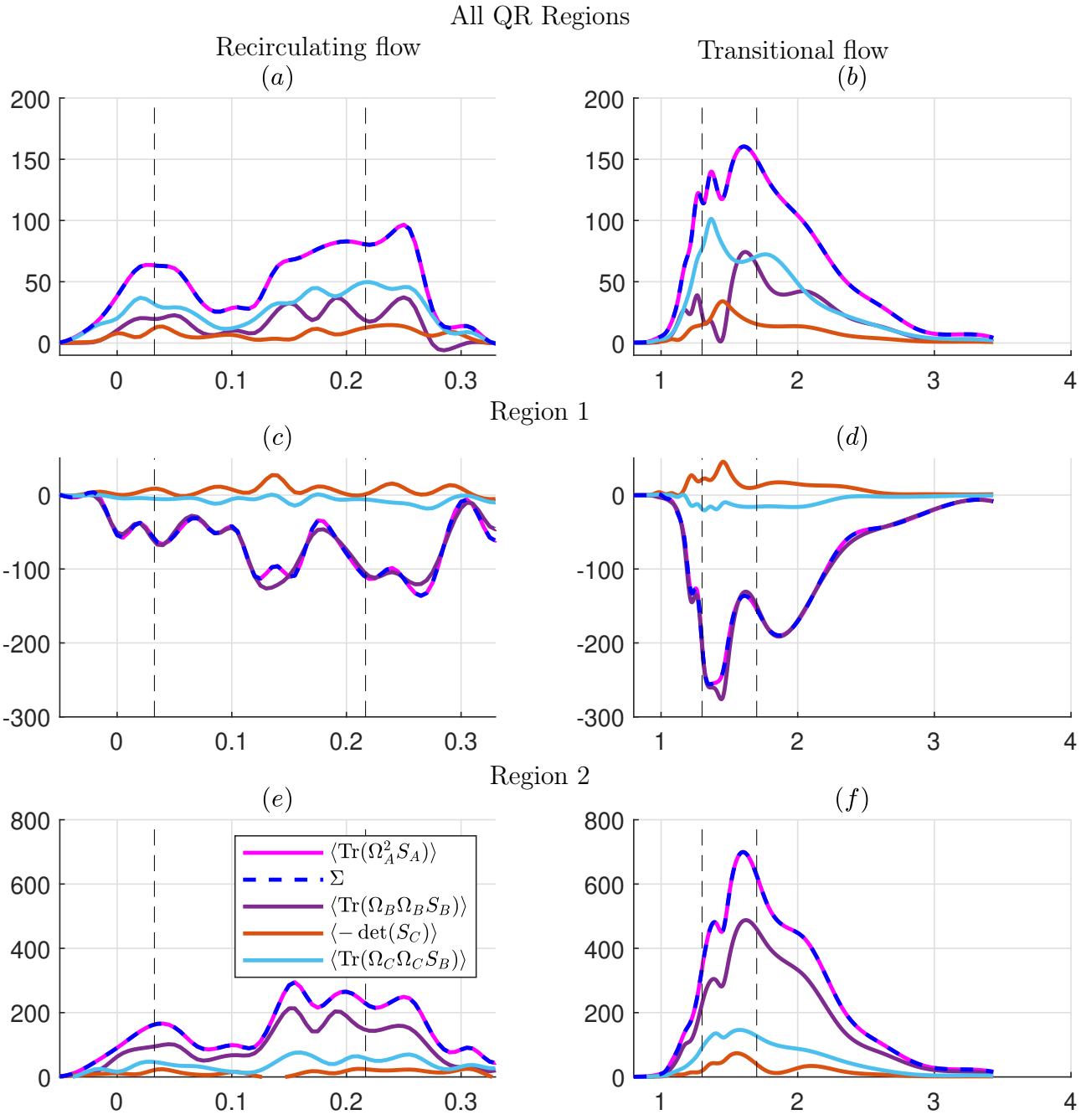


Figure 4.40: Distribution of $\langle \mathrm{Tr}(\Omega_A^2 S_A) \rangle$ (top rows) and $\langle \mathrm{Tr}(\Omega_A^2 S_A)|^{QR=1,2} \rangle$ (mid and bottom rows) for (a), (c), (e) along line A and (b), (d), (f) along line B.

4.8 Non-normality in interaction terms between mean flow and fluctuations

We now explore the Schur decomposition of term $\mathcal{EM}_\omega$, which represents the interaction between the mean and fluctuating flow in the generation of enstrophy. To this end, the terms responsible in the energy transfer $\|S_B^M\|^2$ and $\|S_C^M\|^2$ are first analyzed (the superscript M indicates a quantity related to the mean flow). Figure 4.41 shows the contours of these two quantities where it is observed that the peak values of $\|S_B^M\|^2$ are clustered in the leading edge of the wing and are an order of magnitude lower than the ones of $\|S_C^M\|^2$. The latter term is maximized in the separated shear layers at the suction side and the attached boundary layer at the pressure side.

Figure 4.42(a) show contours of $\Delta_A^M = \left(Q_A^M\right)^3 + \frac{27}{4}\left(R_A^{M\,2}\right)$. There is a clear demarcation in the focal (rotational character) and non-focal (straining character) sections. The light blue region where $\Delta_A^M < 0$ shows the section of the mean flow field where all eigenvalues are real and it is mainly found near the leading edge, close to the front stagnation point. Negative values are also found in the wake within the recirculating zone and outside. $\Delta_A^M > 0$, that results in two complex eigenvalues, on the other hand has a strong presence in the region where turbulence production is very active. This suggest that $\|S_C^M\|^2$ plays a pivotal role in the generation of k and $\frac{1}{2}\langle\omega_i\omega_i\rangle$.

Figure 4.42(b) shows the spatial localisation of the Q_A^M-R_A^M regions. It is observed that in the leading edge, the contours of $\|S_B^M\|^2$ and $\|S_C^M\|^2$ belong to region 6 and 2 respectively. Here, beside the change in Δ_A^M, there is a sharp change from $Q_A^M < 0$ and $R_A^M > 0$ to $Q_A^M > 0$ and $R_A^M < 0$ respectively. More specifically, the area of the separated flow stemming from the leading edge and mean shear in the suction side and along the boundary layer of the pressure side belongs to region 2. Region 1 is found in the pressure side as the flow approaches the trailing edge and in the proximity of the wake after the flow leaves the trailing edge and within the recirculating zone. Regions 3 and 5 are active further downstream in the section where turbulence has fully developed whereas region 5 has a small presence.

Figure 4.43 shows the distribution of $\mathrm{Tr}\left(\langle\Omega_A^2\rangle S_A^M\right)$ and its decomposition (see Appendix E

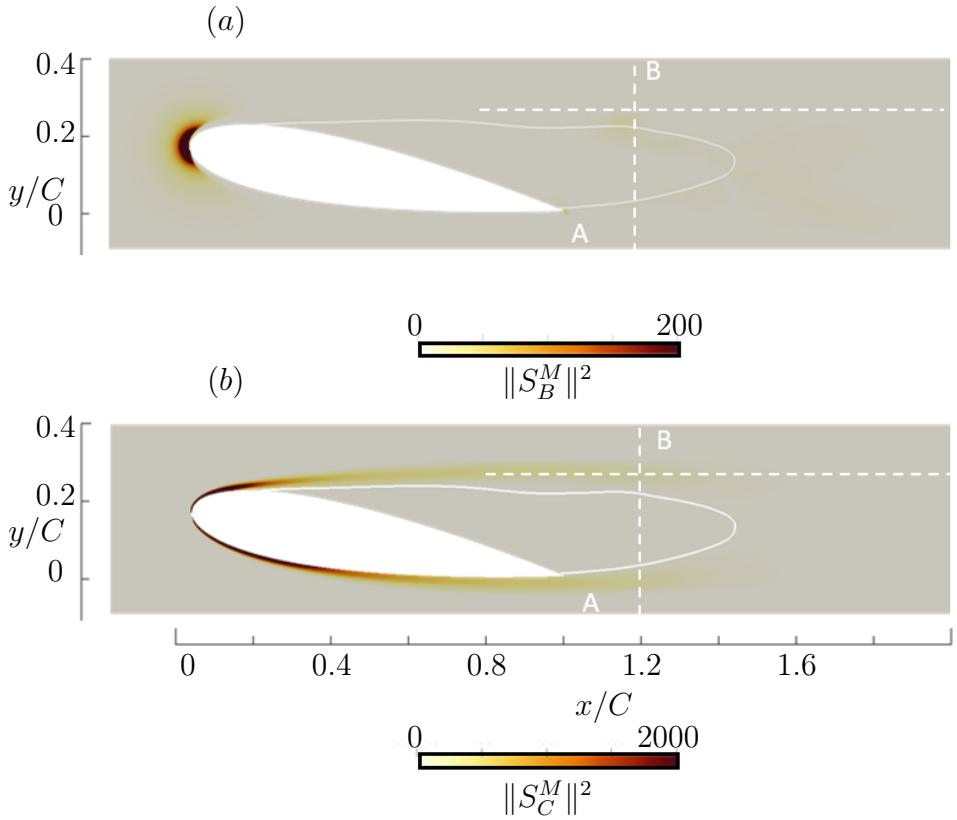


Figure 4.41: Contours of (a) $\|S_B^M\|^2$ and (b) $\|S_C^M\|^2$ in the $x-y$ plane at $z/C=-0.2$.

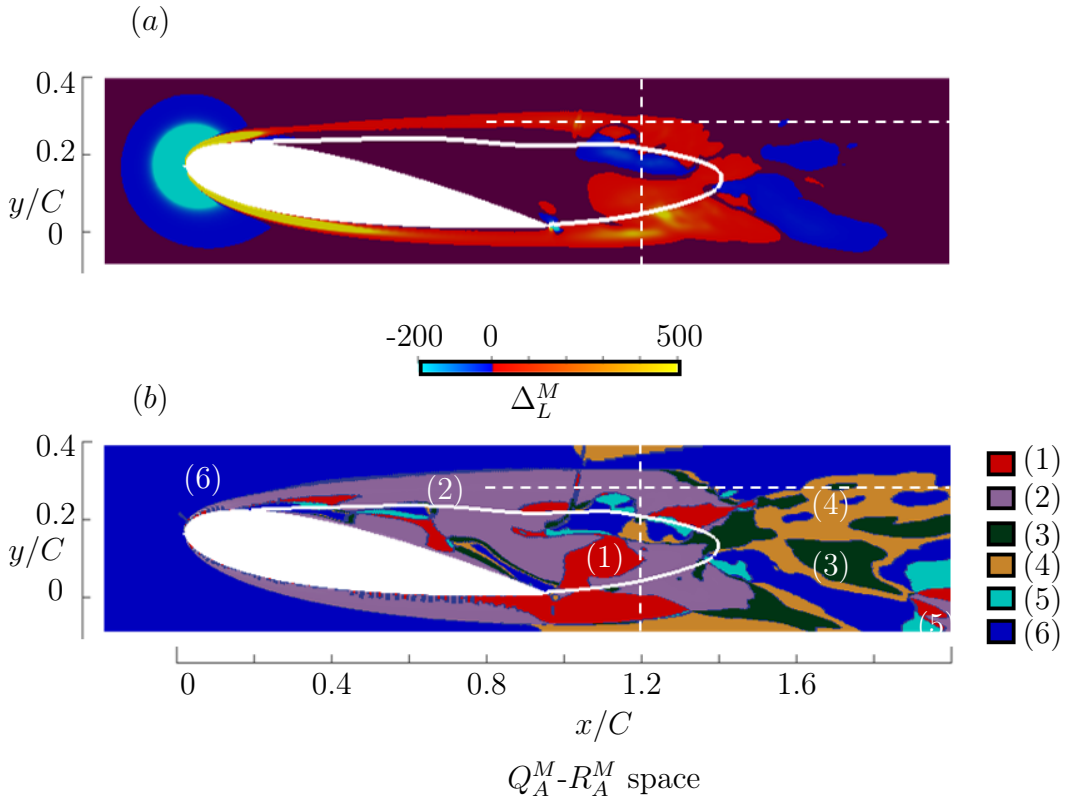


Figure 4.42: Contours of (a) Δ_A^M and (b) regions of the Q_A^M-R_A^M space based on the mean flow in the $x-y$ plane at $z/C=-0.2$.

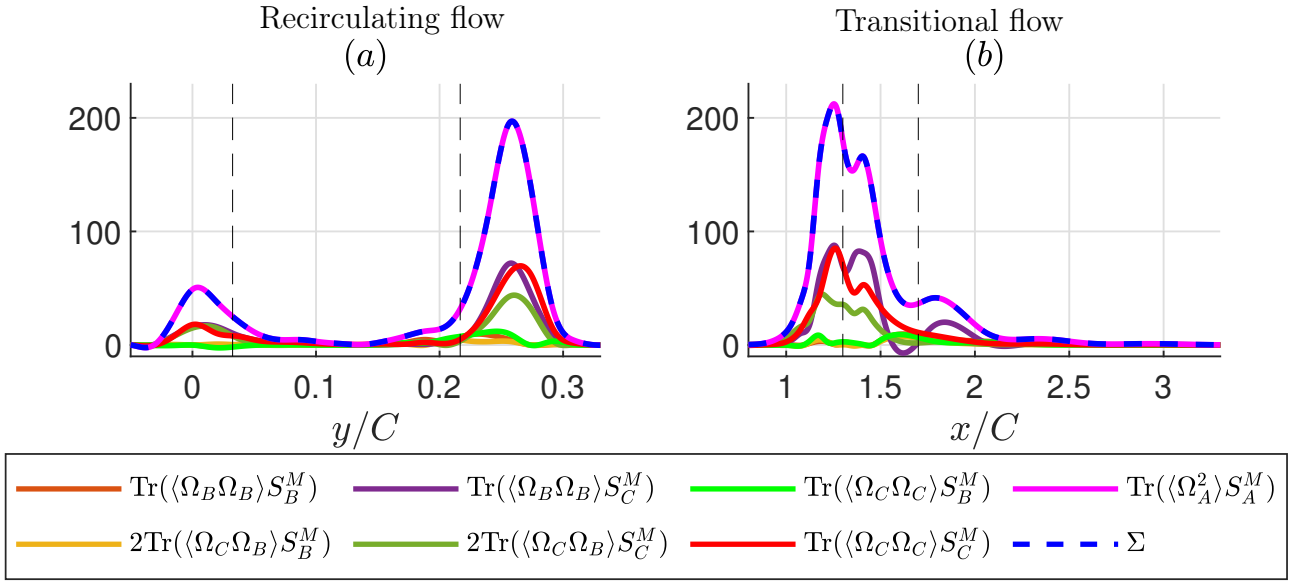


Figure 4.43: Distribution of the components of $\mathrm{Tr}(\langle\Omega_A^2\rangle S_A^M)$ where S_A^M, S_B^M and S_C^M are the mean strain rate fields.

for details). A clear trend is visible, $\mathrm{Tr}\left(\langle\Omega_B\Omega_B\rangle S_C^M\right)$, $\mathrm{Tr}\left(\langle\Omega_C\Omega_C\rangle S_C^M\right)$ and $\mathrm{Tr}\left(\langle\Omega_C\Omega_B\rangle S_C^M\right)$ are the main contributors in the location of the peaks for both cases whereas the terms coupled with S_B^M have significant lower values. The fact that these components coupled with the normal mean straining are low is in agreement with our previous finding where in figure 4.41 negligible values of S_B^M are found across the recirculating and transitional region. It should also be noted that all the terms of $\mathrm{Tr}\left(\langle\Omega_A^2\rangle S_A^M\right)$ are non-zero (see Appendix F for further details).

4.9 Summary

DNS was conducted on a NACA 0018 wing with a square wingtip profile to investigate the properties of small-scale statistics in a separated shear flow undergoing large-scale strain including the presence of a recirculating flow. The simulation was carried out at a Reynolds number of 5000 and a 10° angle of attack. The low Reynolds number allowed for achieving a grid size to Kolmogorov length ratio of approximately 1, and in certain sections sub-Kolmogorov resolution. This fine resolution is required to balance the transport equations and characterize rare and large events. Statistical analysis was conducted on two separate segments of the flow. The first segment follows line A, which is oriented perpendicular to the flow direction and intersects the recirculation zone. The second segment follows line B, and lies in the primary flow direction where the separated shear layer undergoes transition.

The enstrophy production term that depends on the mean strain rate $\mathcal{EM}\omega$ exhibited higher values compared to the enstrophy production mechanism due to fluctuating strain fields in limited sections of the flow. In these regions, the mean strain rate behaved similarly to the fluctuating strain rate in terms of alignment with the fluctuating vorticity. The presence of $\mathcal{EM}\omega$ activated the turbulent transport terms around its peak. The primary contributor to the rapid increase in enstrophy during the flow transition ("growth" section) along line A was the generation term $\mathcal{EM}\omega$. The contribution of the large events (greater than 10 times their time-average) to the mean value of enstrophy is $\approx 60\%$ whereas for strain-self amplification is $\approx 40\%$ along line A. In the "decay" section of the transitional flow, the contributions from large events gradually diminish. In the recirculating flow, the contribution of these events reach a peak in the middle of the bubble reaching $\approx 50\%$ and $\approx 70\%$ respectively. The occurrence of

these events however was found to be below 5% for both types of flows.

No point along lines A and B was found that matches exactly with the HIT parameters. However, when considering the fractions of occupied QR regions and alignments, it was observed that areas that approximate HIT were found in the middle section of the recirculating flow along line A. Similarly, in the turbulent shear flow along line B, to some degree, there were good approximations towards the end of the section.

We investigated the influence of non-normality by performing the Schur decomposition of the VGT. Through this analysis, we identified the primary factors responsible for enstrophy and total strain production in specific regions that significantly differ from HIT. Furthermore, we examined the conditions that facilitate the dominance of these factors in those particular sections. Finally, mean flows were incorporated into the Schur decomposition, and uncovered their topological organisation. We provided the key characteristics in the communication between fluctuating-fluctuating and mean-fluctuating correlations.

Chapter 5

The structure of the Lamb vector in a separated three-dimensional turbulent flow

In this chapter[1], the structure of the Lamb vector of the mean flow is presented in section 5.1 and of the turbulent fluctuations in section 5.2. We simulate the flow around the finite wing for $Re_c = 5000$ used in the previous chapter and introduced in section 2.4. We examine the sequence of events starting from the leading edge to the fully developed turbulent flow in the wake. This analysis aims to improve our understanding of the dynamics of the shear flow and is discussed in detail in section 5.3. In section 5.4, we will explore the alignments between velocity and vorticity vectors. Finally, we study the Lamb vector and its potential component in section 5.5. We conclude by giving a summary of the main findings in section 5.6.

5.1 The Lamb vector of the mean flow

Figure 5.1 shows contours of the three components of the Lamb vector formed by the time average velocity and vorticity, $\langle\Omega\rangle \times \langle U\rangle$, in the $x - z$ plane. High levels of the x-component of the Lamb vector in figure 5.1(a) are found around the leading edge, the attached flow in the pressure side and to a lesser extent to the area bordering the recirculation zone. There is a change in the sign after the flow passes the trailing edge. The change of sign is attributed to $\langle U_2\rangle$, which starts with negative values as the flow moves around the pressure side and turns positive as the recirculating bubble closes. $\langle\Omega_3\rangle$ maintains the same sign on the pressure side of the wing. The contour plot has an almost symmetric distribution because the distribution of

[1]Part of work in this chapter was presented at the UK Fluids Conference 2023 held in Glasgow, UK.

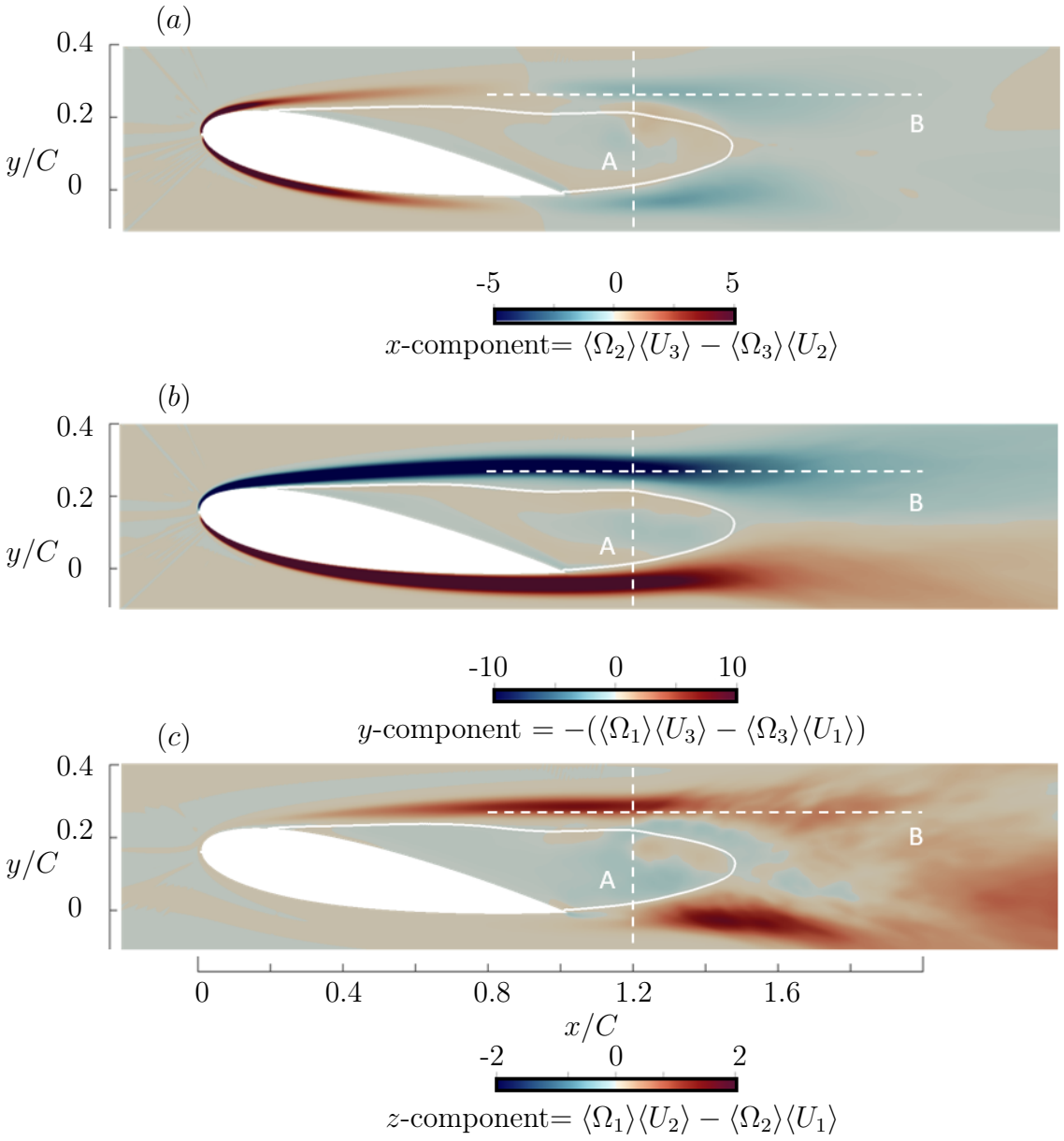


Figure 5.1: Contours of the three components of $\langle\Omega\rangle \times \langle U\rangle$ (a) x-component (b) y-component (c) z-component. The white dotted line A goes through the recirculating flow and B through the transition.

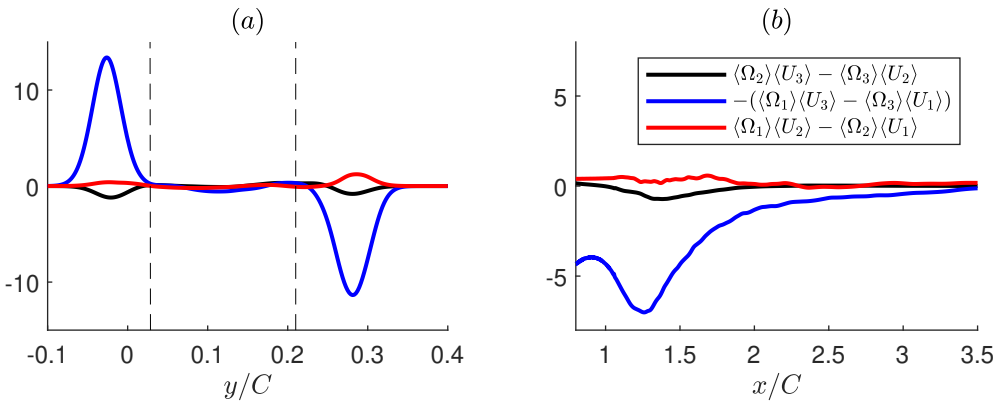


Figure 5.2: Variation of the three components of $\langle\Omega\rangle \times \langle U\rangle$ (a) along line A and (b) along line B.

$\langle U_2\rangle$ and $\langle\Omega_3\rangle$ in the separated shear layer is mirrored on the pressure side. The y-component of the Lamb vector (where $|\langle\Omega_3\rangle\langle U_1\rangle| \gg |\langle\Omega_1\rangle\langle U_3\rangle|$), see figures 5.2(a) and (b), is by far the largest one with two clear peaks of opposite sign outside of the recirculation zone along line A. Along line B, the y-component at $x/C \approx 1.3$ undergoes a rapid short increase downstream of the recirculating bubble. This is the area of streamwise velocity acceleration as discussed in chapter 3. Moreover, it has been reported that in the case of a closed bubble, the transition point is typically identified close to the area of the recirculating bubble at its maximum [O'Meara and Mueller, 1987]. The specific shape and size of the contours observed in figure 5.1(b) can be attributed to the relation between the leading edge spanwise vorticity and the average axial velocity, $\langle\Omega_3\rangle\langle U_1\rangle$. This also explains the change from positive to negative contours of the y-component found in the suction and pressure side of the wing respectively, which is primarily influenced by the sign of $\langle\Omega_3\rangle$. Even though there is an asymmetric disturbance of the flow by the wing, the lower shear peaks are only slightly higher than the leading edge separated flow, as seen in figure 5.2(a). The third component in figure 5.1(c) is a consequence of the three-dimensionality of the flow field due to the term $\langle\Omega_2\rangle\langle U_1\rangle$ as a consequence of the spanwise mean flow inhomogeneity stemming from the tip flow.

We now consider the divergence of the Lamb vector and employ the vector identity [Hamman et al., 2008]

$$\nabla \cdot (\langle\Omega\rangle \times \langle U\rangle) = \langle U\rangle \cdot \nabla \times \langle\Omega\rangle - \langle\Omega\rangle \cdot \langle\Omega\rangle\,, \tag{5.1}$$

where $\langle U\rangle \cdot \nabla \times \langle\Omega\rangle$ is the mean flexion product and $\nabla \times \langle\Omega\rangle$ is the mean flexion vector [Truesdell,

1954]. The flexion product can also be written as [Hamman et al., 2008]

$$\langle U\rangle \cdot \nabla \times \langle \Omega\rangle = \langle S\rangle : \langle S\rangle + \frac{1}{2}\left[\langle \Omega\rangle \cdot \langle \Omega\rangle - \nabla^2(\langle U\rangle \cdot \langle U\rangle)\right] , \tag{5.2}$$

leading to the alternative expression,

$$\nabla \cdot (\langle \Omega\rangle \times \langle U\rangle) = \langle S\rangle : \langle S\rangle - \frac{1}{2}\langle \Omega\rangle \cdot \langle \Omega\rangle - \frac{1}{2}\nabla^2(\langle U\rangle \cdot \langle U\rangle) . \tag{5.3}$$

Figure 5.3 shows the contours of the divergence of the Lamb vector of the mean flow and the terms of equation 5.3. $\nabla \cdot (\langle \Omega\rangle \times \langle U\rangle)$ is active in the separated shear flow where it is clearly split into two regions of positive and negative sign adjacent to each other. The enstrophy of the mean flow $\frac{1}{2}\langle \Omega\rangle \cdot \langle \Omega\rangle$ in (b) is clearly present in the shear layer surrounding the recirculating bubble. The isoline of $\langle S\rangle : \langle S\rangle = 250$ is superimposed and is present around the stagnation point of the leading edge. The term $\frac{1}{2}\nabla^2(\langle U\rangle \cdot \langle U\rangle)$ in (c) has a similar shape as $\nabla \cdot (\langle \Omega\rangle \times \langle U\rangle)$, but the key distinction lies in the fact that the stagnation point area also exhibits significant values.

To gain a deeper understanding, the components of $\nabla \cdot (\langle \Omega\rangle \times \langle U\rangle)$ in equation 5.3 are plotted along lines A and B in figure 5.4. Interestingly, $\langle S\rangle : \langle S\rangle$ and $\frac{1}{2}(\langle \Omega\rangle \cdot \langle \Omega\rangle)$ show a nearly similar distribution. Based on this finding we can approximate equation 5.3 as follows:

$$\nabla \cdot (\langle \Omega\rangle \times \langle U\rangle) \approx -\frac{1}{2}\nabla^2(\langle U\rangle \cdot \langle U\rangle) . \tag{5.4}$$

Along line A, a striking characteristic is that $-\frac{1}{2}\nabla^2(\langle U\rangle \cdot \langle U\rangle)$ has two peaks of equal size but opposite sign; this is explained by the curvature of the velocity profile. The steepest change of $\frac{1}{2}\langle \Omega\rangle \cdot \langle \Omega\rangle$ occurs between $y/C \approx 0.3$ and 0.35 when it goes from zero to ≈ 140 (observed in figure 5.4(a) from left to right). As this occurs, $-\frac{1}{2}\nabla^2(\langle U\rangle \cdot \langle U\rangle)$ turns super-harmonic, i.e. $-\frac{1}{2}\nabla^2(\langle U\rangle \cdot \langle U\rangle) \geq 0$. Prior to $\frac{1}{2}\langle \Omega\rangle \cdot \langle \Omega\rangle$ reaching its maximum value at $y/C \approx 0.28$, $-\frac{1}{2}\nabla^2(\langle U\rangle \cdot \langle U\rangle)$ switches rapidly to sub-harmonic $-\frac{1}{2}\nabla^2(\langle U\rangle \cdot \langle U\rangle) \leq 0$. Eventually, as the flow enters the recirculation bubble, $-\frac{1}{2}\nabla^2(\langle U\rangle \cdot \langle U\rangle)$ reaches a quasi-harmonic state where it is approximately equal to 0. A similar pattern is noticed in the region of the shear layer

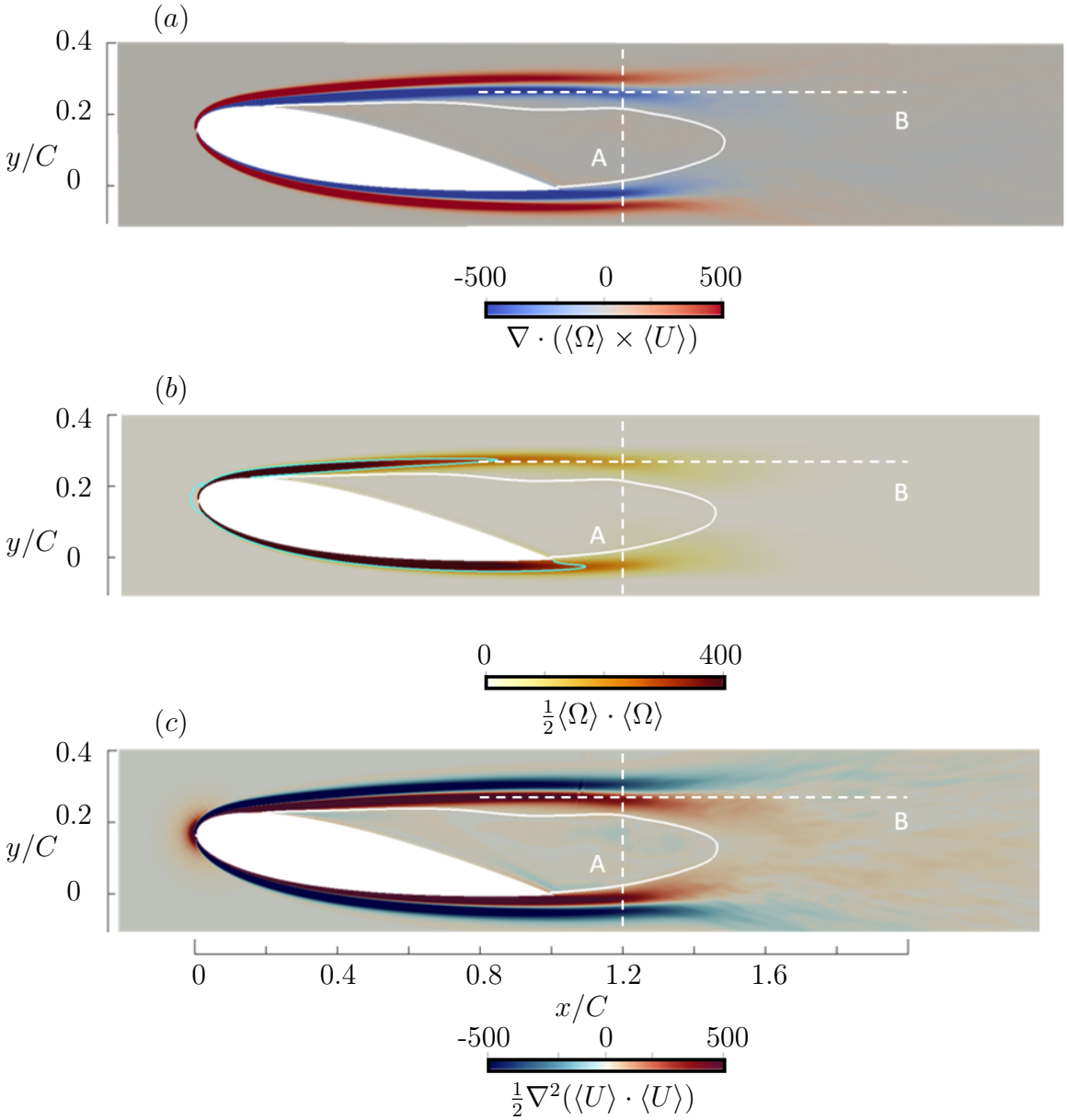


Figure 5.3: Contours of (a) $\nabla \cdot (\langle\Omega\rangle \times \langle U\rangle)$ and its components (b) $\frac{1}{2}\langle\Omega\rangle \cdot \langle\Omega\rangle$ and (c) $\frac{1}{2}\nabla^2(\langle U\rangle \cdot \langle U\rangle)$ in the $x-y$ plane at $z/C = -0.2$. The light blue isoline represents $\langle S\rangle : \langle S\rangle = 250$.

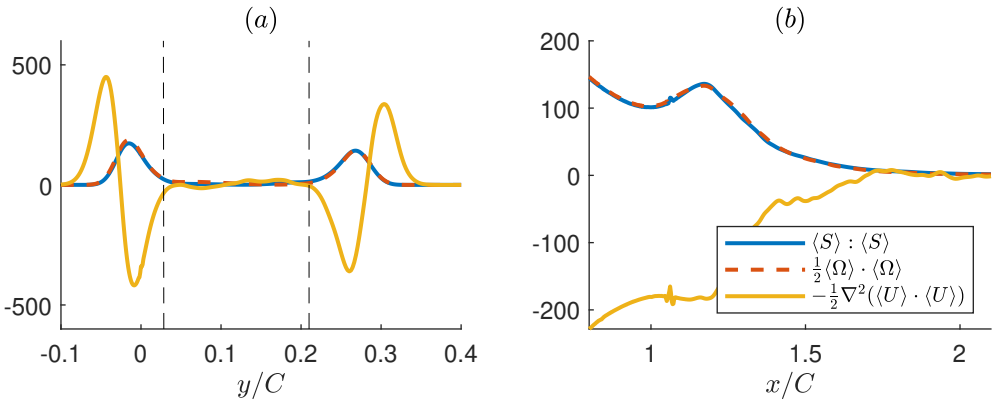


Figure 5.4: The components of $\nabla \cdot (\langle\Omega\rangle \times \langle U\rangle)$ (a) along line A and (b) along line B.

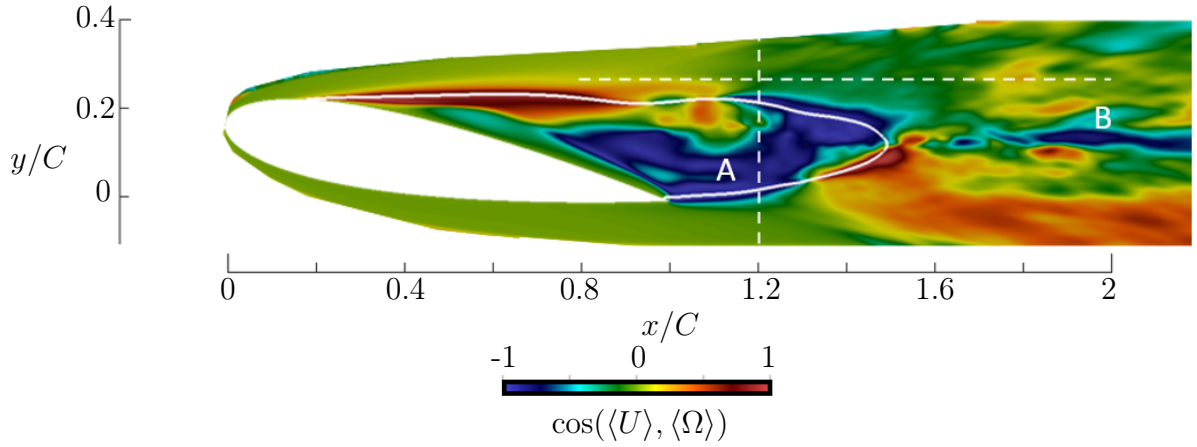


Figure 5.5: Contours of $\cos(\langle U\rangle, \langle\Omega\rangle)$ in the $x-y$ plane at $z/C = -0.2$.

originating from the pressure side, specifically between $y/C \approx -0.1$ and 0.1. Along line B, fixed at $y/C = 0.26$, large concentrations of $\frac{1}{2}\langle\Omega\rangle \cdot \langle\Omega\rangle$ are present. This coincides with the areas of the domain where $-\frac{1}{2}\nabla^2(\langle U\rangle \cdot \langle U\rangle)$ remains negative. Downstream of $x/C \approx 1.2$, there is an abrupt decay of all the terms and negligible values after $x/C \approx 1.6$ are found.

A deeper look into the properties of $\langle U\rangle$ and $\langle\Omega\rangle$ in relation to the three-dimensionality of the flow can be taken by analyzing their alignment. Figure 5.5 show the contours of the $\cos(\langle U\rangle, \langle\Omega\rangle)$ and figure 5.6 shows the spatial variation along lines A and B. Lower values close to -1 of $\cos(\langle U\rangle, \langle\Omega\rangle)$ are a sign of helical behaviour which can be observed inside the recirculating bubble, as depicted in figure 5.5. The three-dimensionality of the flow is due to the penetration of the spanwise flow stemming from the tip region into the recirculating bubble. Inside the recirculating bubble, the spanwise flow and reversed flow form a complex spiral-like but low-magnitude vortical motion. This enables the flow to show spots of helical motions with the $\cos(\langle U\rangle, \langle\Omega\rangle) \approx -1$ (upper side of the bubble) and ≈ 1 (lower side of the bubble). This is a very different scenario from two-dimensional flow, where vorticity is perpendicular to the velocity field, thus $\cos(\langle U\rangle, \langle\Omega\rangle) = 0$. Along line B (figure 5.6 (b)), however, $\langle U\rangle$ seems to be fixed almost perpendicular to $\langle\Omega\rangle$ as turbulence production peaks and mean enstrophy is at its maximum.

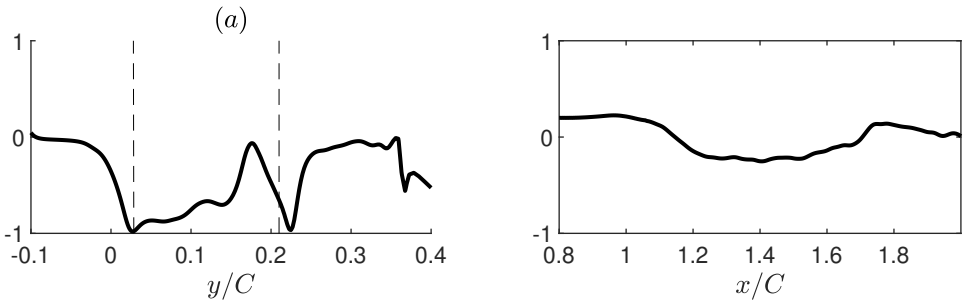


Figure 5.6: Variation of $\cos(\langle U\rangle, \langle\Omega\rangle)$ (a) along line A and (b) along line B.

5.2 The Lamb vector of the turbulent fluctuations

Attention now turns to the Lamb vector of the fluctuating velocity. We are interested in quantifying the values of the divergence of Lamb vector for small-scales and understanding how it differs qualitatively from the large-scale. Using the fluctuating velocity field, equation 5.3 becomes,

$$\nabla \cdot \langle \omega \times u \rangle = \langle s : s \rangle - \frac{1}{2}\langle \omega \cdot \omega \rangle - \frac{1}{2}\nabla^2 \langle u \cdot u \rangle \,. \tag{5.5}$$

In figures 5.7(a) and (b), we plot $\nabla\cdot\langle\omega\times u\rangle$, $\langle s : s\rangle - \frac{1}{2}\langle\omega\cdot\omega\rangle$ and $-\nabla^2\langle u\cdot u\rangle$ respectively along lines A and B. We can observe two distinct characteristics. Firstly, the quantity $\langle s : s\rangle - \frac{1}{2}\langle\omega\cdot\omega\rangle$ is non-zero and tends to cluster at specific positions. Secondly, the quantity $-\frac{1}{2}\nabla^2\langle u \cdot u\rangle$ has negligible value. Starting with the first observation, $\langle s : s\rangle - \frac{1}{2}\langle\omega \cdot \omega\rangle$ can be considered as an indicator of inhomogeneity; this term is zero for HIT. In Panel (a), it is observed that there are positive values within the bubble, which means that there is an excess of strain in that region. Based on the analysis of chapter 4, it is suggested that the QR region 6, characterized by strain, is the dominant one within the bubble in terms of occupancy. This suggests that the high occupancy of strain in QR region 6 might be the reason behind the presence of positive values within the bubble. As we move towards the border of the bubble and its vicinity, the dominant region shifts to QR region 3, characterized by rotation. Further outside the bubble, where enstrophy values are negligible, QR region 6 dominates again. These changes in the fraction of occupancy determine how the surplus or deficit of quantities cluster in specific regions. In panel (b), it is important to note that $\omega = 0$ before transition begins. QR region 2 is dominant until reaching $x/C \approx 1.3$, at which point QR region 6 takes over. This takeover

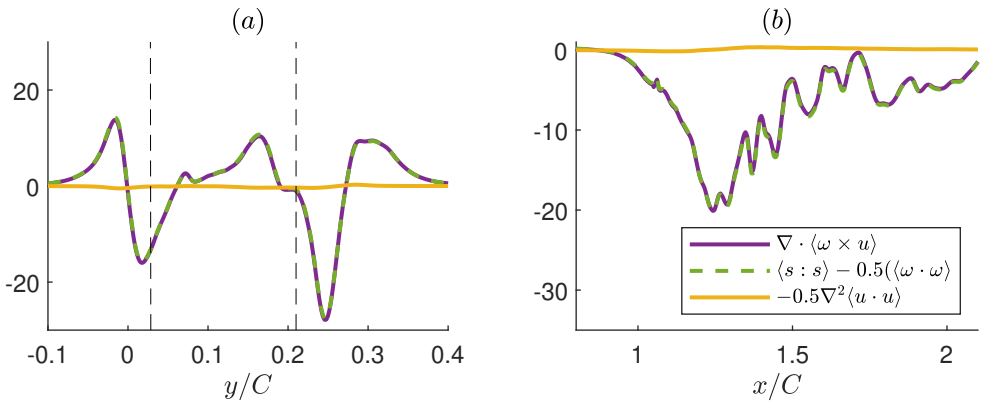


Figure 5.7: Plot of components of $\nabla \cdot \langle \omega \times u \rangle$ (equation 5.5) (a) along line A and (b) along line B.

may contribute to the gradual decrease of $-\frac{1}{2}\nabla^2\langle u \cdot u \rangle$ after it reaches its peak. The maximum values for $\nabla \cdot \langle \omega \times u \rangle$ are approximately ten times smaller compared to the peak values observed in the mean flow shown in figure 5.3. The negligible values of $-\nabla^2\langle u \cdot u \rangle$ might be linked to the small curvature of k as it decays. Based on this observation, the following approximation is valid,

$$\nabla \cdot \langle \omega \times u \rangle \approx \langle s : s \rangle - \frac{1}{2}\langle \omega \cdot \omega \rangle \,. \tag{5.6}$$

The left column of figure 5.8 (a),(c),(e) shows contours of $\nabla \cdot \langle \omega \times u \rangle$, $\langle s : s \rangle - \frac{1}{2}\langle \omega \cdot \omega \rangle$ and $-\nabla^2\langle u \cdot u \rangle$ respectively. The separation between positive and negative contours is less structured for the fluctuating quantities compared to the mean flow. In figure 5.8 (a), around $x/C \approx 1.15 - 1.4$, however the light red and blue contours (positive and negative values respectively) above and below the recirculation bubble form a similar pattern that closely resembles the footprints of $\nabla \cdot (\langle \Omega \rangle \times \langle U \rangle)$. Inside the bubble, positive finite values arise. Figure 5.8 (c) shows the deficit or surplus of $\langle s : s \rangle$ with respect to $\frac{1}{2}\langle \omega \cdot \omega \rangle$. Overall a very similar distribution in form and magnitude is found when compared to $\nabla \cdot \langle \omega \times u \rangle$ in panel (a) as expected from our approximation 5.6. In figure 5.8 (e), we plot $-\nabla^2\langle u \cdot u \rangle$ and the values are an order of magnitude lower than $s : s - \frac{1}{2}\langle \omega \cdot \omega \rangle$.

In order to provide more information about the organization and structure of the flow, as well as to demonstrate how the flow evolves qualitatively, we plot the instantaneous values of the same terms in the right-column panels (b), (d) and (f). In figure 5.8 (b), the contours of

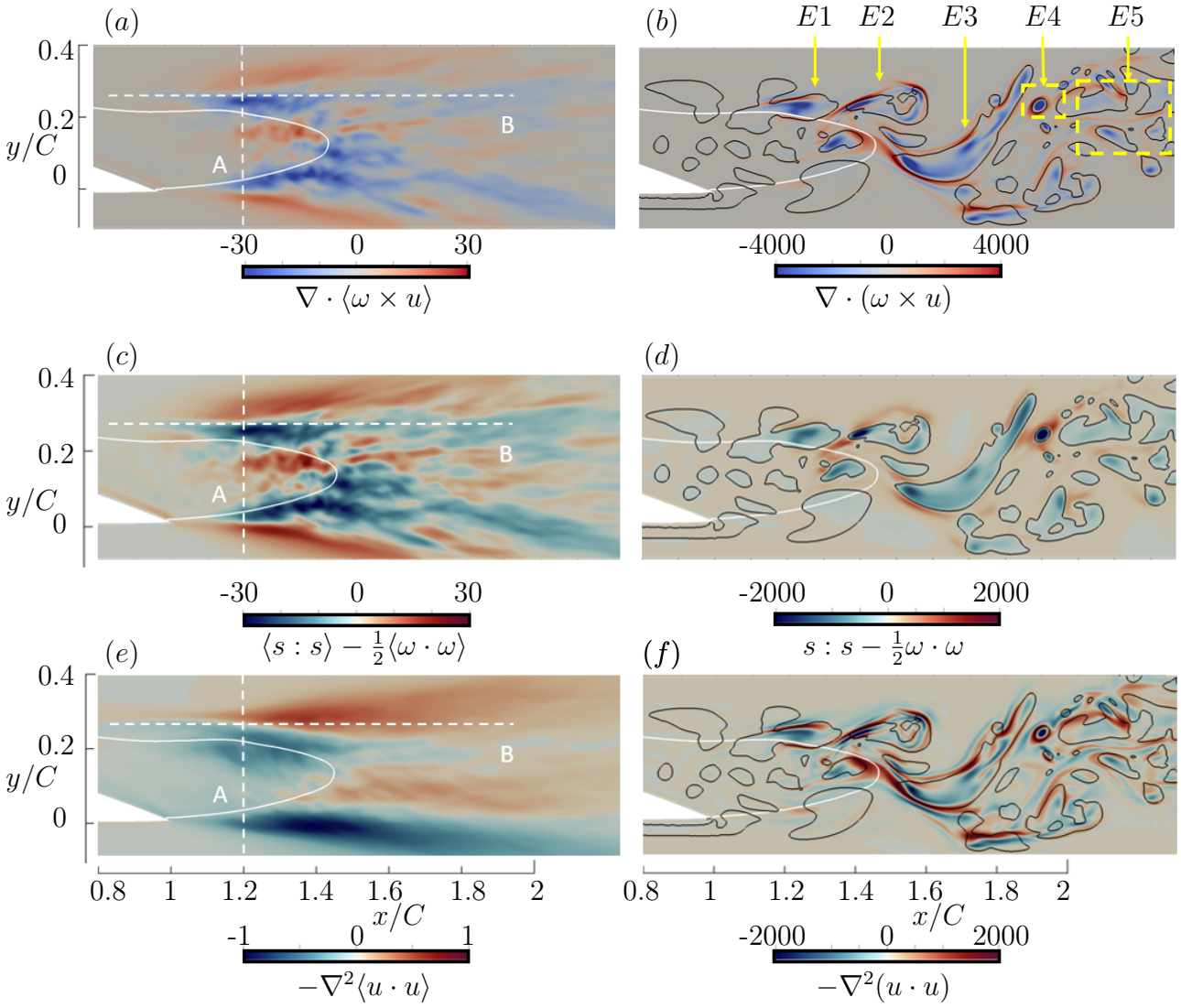


Figure 5.8: Contours of $\nabla \cdot \langle \omega \times u \rangle$ and its components in the $x - y$ plane (left column); instantaneous snapshots are shown in the right column. Vortical structures are represented by the Q-criterion value of 2.

$\nabla \cdot (\omega \times u)$ are superimposed with $Q = 2$ values which enable us to capture multiple eddies of different sizes. Hereby, $E1$ and $E2$ are structures formed as a consequence of the KH waves that form at the early stages of transition. $E3$ is a large eddy stemming from the suction side. $E4$ has the form of a fine-scale eddy with a high concentration of vorticity and $E5$ represents a group of eddies when turbulence breakdown has completed.

In panel (b), we can see that the upper portion of the structures $E1$ and $E2$, exhibit a distinct transition from positive to negative values of $\nabla \cdot (\omega \times u)$ across the Q isoline contours. These structures maintain a consistent formation and shape that can be traced back to the Kelvin-Helmholtz instabilities. This consistency in the shape of the structures might explain why the contours of $\nabla \cdot \langle \omega \times u \rangle$ are similar to the contours of the mean flow. In figure 5.8 (d), there is excess of $\frac{1}{2}\omega \cdot \omega$ inside while strain is found outside the Q isolines as expected by the definition of Q. The presence of a recirculating bubble prevents structures such as $E1$ and $E2$ from prematurely mixing with the eddies from the pressure side. Moreover, as we move further downstream, the closure of the unsteady bubble enhances the effectiveness of mixing between the structures from the suction and pressure side, like $E3$. This is consistent with the blurred contours of $\nabla \cdot \langle \omega \times u \rangle$ and $-\nabla^2 \langle u \cdot u \rangle$ (panel (a) and (b) respectively) after $x/C \approx 1.5$, indicating the enhanced mixing effectiveness. Interestingly, figure 5.8 (f) shows that $-\nabla^2(u \cdot u)$ can be of the same order of magnitude as $s : s$ or $\frac{1}{2}\omega \cdot \omega$. The Laplacian operator $-\nabla^2(u \cdot u)$ represents the curvature of the instantaneous kinetic energy u^2. It can be seen that multiple layers of positive and negative values of $-\nabla^2 u \cdot u$ are arranged next to each other and tend to accumulate in the borders of the Q isolines which shows that these regions have the highest energy curvature.

It is important to note the relationship between $\nabla \cdot \langle \omega \times u \rangle$ and the Reynolds stresses. According to Chacin and Cantwell [2000], the most significant Reynolds stress events are associated with the extremes of the discriminant Δ, concentrated within areas characterized by high spatial gradients. The Eulerian viewpoint (refer to figure 4.22) reveals that instantaneously the highest concentration of Δ occurring in the nearby spatial regions of 2 and 6, deviating from the Lagrangian anti-clockwise sequence (2-1-5-6) (see section 4.6). This pattern aligns with the peaks identified in panel (d) related to $\langle s : s \rangle - \frac{1}{2}\langle \omega \cdot \omega \rangle$. In panel (f), the expression $-\nabla^2(u \cdot u)$

indicates that the regions following the Lagrangian path, as well as other areas where Δ is not notably significant, demonstrate negligible time-averaged values, as discussed earlier (see panel (e)). This suggests that the Reynolds stress and its trace k may be more closely linked to sudden changes from region 2 to 6, with only specific parts of the eddies holding dynamical significance in terms of the time-averaged Lamb vector dilatation. Therefore, the relatively strong and evenly distribution of enstrophy in an eddy (for example, $E1$ and $E2$, see figure 4.13) is not equally correlated with its dynamic significance. This offers an alternative perspective for evaluating importance of vorticity in a time-averaged sense, bridging the gap and reinforcing previous statements by Tsinober [1998], Carbone and Bragg [2020].

5.3 Lamb vector and mean flow enstrophy

To gain further insight, we analyze the transport equation of $\langle\Omega_i\rangle\langle\Omega_i\rangle$ from the perspective of the Lamb vector. Taking the dot product of the equation of vorticity with Ω, we obtain

$$\frac{1}{2}\frac{\partial\Omega\cdot\Omega}{\partial t} + \nabla\times(\Omega\times U)\cdot\Omega = \nu\nabla^2\Omega\cdot\Omega\,. \tag{5.7}$$

The curl of the Lamb vector $\nabla\times(\Omega\times U)$ influences the stretching and tilting of vorticity lines, thereby driving the shearing process of coherent vortical structures [Hamman et al., 2008]. Moreover, the expression $\nabla\times(\Omega\times U)$ is used in the definition of generalised Beltrami flows which allows exact analytical solutions of vortex flows [Wu et al., 2015]. In a generalised Beltrami flow, $\nabla\times(\Omega\times U)=0$, thus $(\Omega\times U)=\nabla\alpha$ where a is α scalar. We will return to these points in the next sections.

The transport equation for enstrophy of the mean flow $\langle\Omega_i\rangle\langle\Omega_i\rangle$ can be derived by applying Reynolds decomposition and time-averaging to Equation 5.7. This equation effectively captures the interaction between the mean and fluctuating vorticities [Tennekes et al., 1972],

$$\frac{1}{2}\frac{\partial\langle\Omega_i\rangle\langle\Omega_i\rangle}{\partial t} = \underbrace{-0.5\langle U_j\rangle\frac{\partial\langle\Omega_i\rangle\langle\Omega_i\rangle}{\partial x_j}}_{\mathcal{CM}_\Omega}\underbrace{-\frac{\partial\langle\omega_i u_j\rangle}{\partial x_j}\langle\Omega_i\rangle}_{\mathcal{PM}_\Omega} + \underbrace{\langle\Omega_j\rangle\langle\Omega_i\rangle\langle S_{ij}\rangle}_{\mathcal{EM}_\Omega} \\ \underbrace{+\langle\Omega_j\rangle\langle\omega_i s_{ij}\rangle}_{\mathcal{EF}_\Omega} + \underbrace{\nu\frac{\partial^2 0.5\langle\Omega_i\rangle\langle\Omega_i\rangle}{\partial x_j^2}}_{\mathcal{DM}_\Omega} - \underbrace{\nu\frac{\partial\langle\Omega_i\rangle}{\partial x_j}\frac{\partial\langle\Omega_i\rangle}{\partial x_j}}_{\epsilon\mathcal{M}_\Omega}, \tag{5.8}$$

where $\mathcal{CM}_\Omega$ is the convection of $\langle\Omega_i\rangle\langle\Omega_i\rangle$ by mean flow, $\mathcal{PM}_\Omega$ the production or destruction by velocity-vorticity fluctuations, $\mathcal{EM}_\Omega$ is generation or destruction via large-scale vortex stretching or compression, $\mathcal{EF}_\Omega$ is the enstrophy production or destruction via small-scale vortex stretching or compression, $\mathcal{DM}_\Omega$ and $\epsilon\mathcal{M}_\Omega$ are the viscous diffusion and dissipation of $\langle\Omega_i\rangle\langle\Omega_i\rangle$ respectively.

Figure 5.9 and 5.10 show the main sources and sinks terms respectively in the $x-z$ planes. We can divide the process of turbulence development in the present three-dimensional shear flow into three distinct phases: Phase I represents the convection-driven region, Phase II corresponds to the region where inviscid break-up of vortical structure occurs and Phase III where fully developed turbulence is reached.

Phase I is the convection-driven region as vorticity produced at the wing surface (no-slip condition) is carried away by the mean flow over the suction side of the wing. The viscous diffusion term $\mathcal{DM}_\Omega$ is the main sink term. Figure 5.9(a) shows $\mathcal{CM}_\Omega$ highest values can be found until $x/C \approx 0.4$. On the other hand $\mathcal{DM}_\Omega$ (5.10(b)) is concentrated more towards the midspan section of the wing. In figure 5.9(b) the vortex stretching of the mean flow field $\mathcal{EM}_\Omega$ exhibits a mark of a singular focal point of lower values in the midspan region where the flow is known to be distorted due to finite aspect ratio. This observation aligns with the discoveries made by Zhang et al. [2020b], who showed that unswept wings (NACA 0015 at $Re_c = 400$) experiencing midspan separation exhibited a surface foci. Neal and Amitay [2023] reported similarly the formation of surface foci on the suction surface on the borders of the midspan reverse flow at $15° - 22°$ and $Re_c = 3.3 \times 10^5$. Note in figure 5.11(a) from $x/C = 0.2$ to 0.5, the value of peaks of $\mathcal{CM}_\Omega$ have decreased by $\approx 91\%$ and the rest of the terms have accordingly smaller values however the signature of the budget is similar.

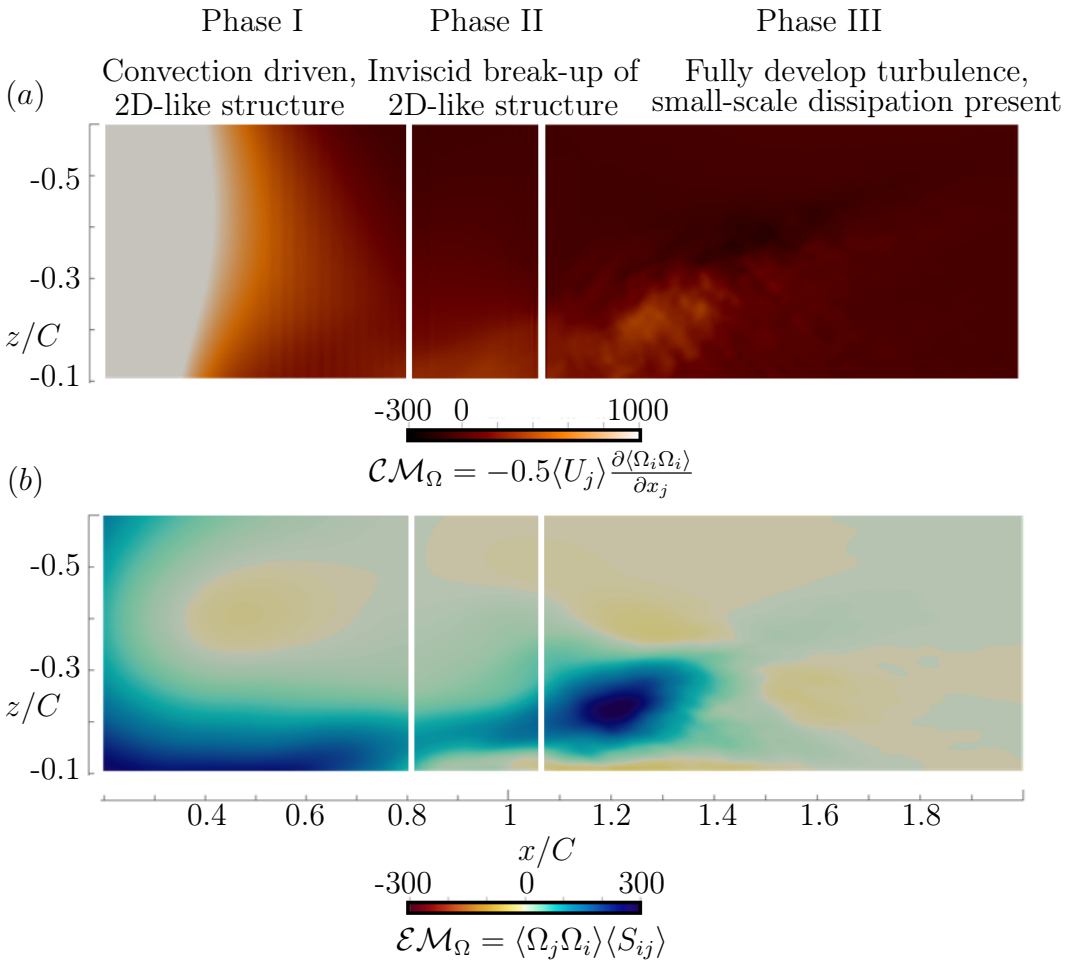


Figure 5.9: Contours of (a) $\mathcal{CM}_\Omega$ and (b) $\mathcal{EM}_\Omega$ in the $x-z$ at $y/C = 0.26$ (vertical position of line B).

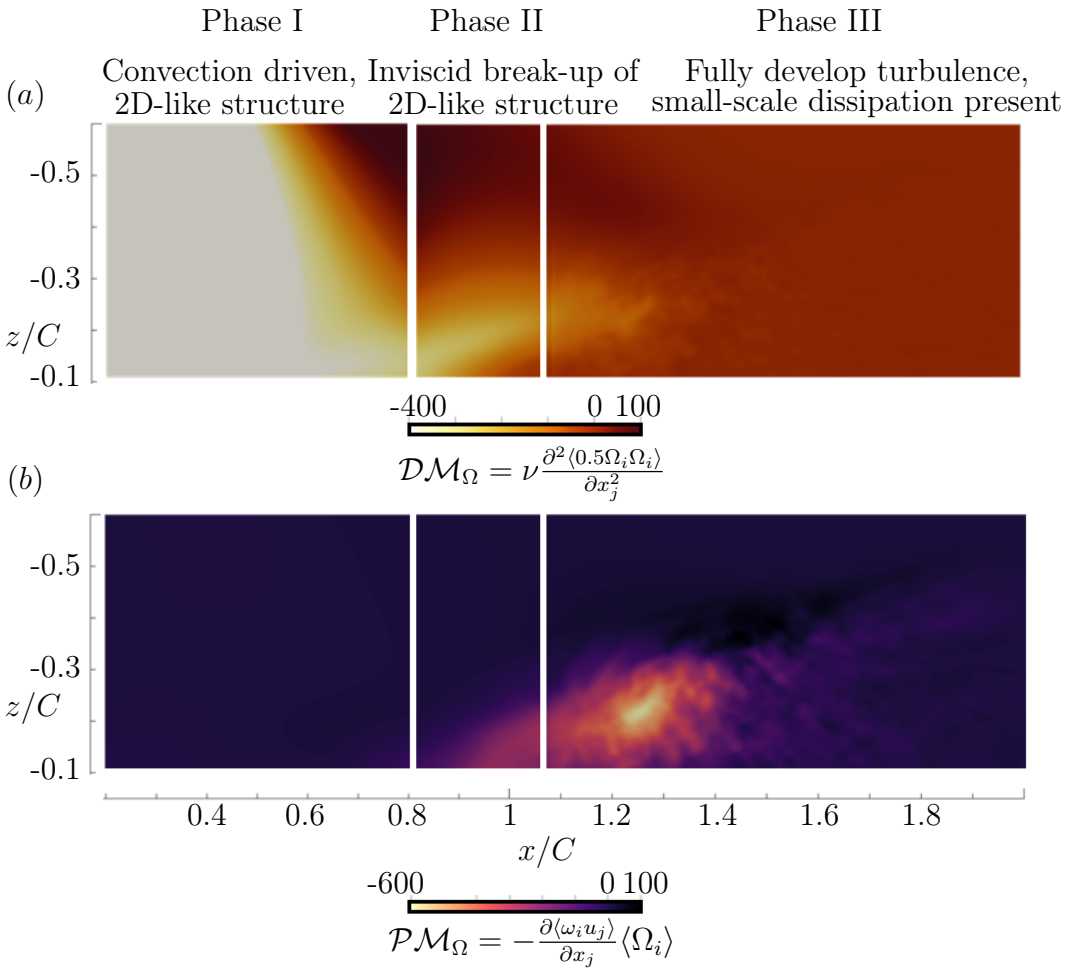


Figure 5.10: Contours of(a) $\mathcal{DM}_\Omega$ and (b) $\mathcal{PM}_\Omega$ in the $x - z$ plane at $y/C = 0.26$ (vertical position of line B).

Moving to Phase II, based on Q-criterion contours (refer to figure 4.13), this is the location where the shear layer disintegrates inviscidly and forms KH rolls. The distribution of the terms in figure 5.11(c) at $x/C = 0.9$ confirms that the source and sink terms have further diminished. Figure 5.9(b) shows us $\mathcal{EM}_\Omega$ is approximately half the magnitude of $\mathcal{CM}_\Omega$. The maximum values of these two terms are balanced out by $\mathcal{DM}_\Omega$. This allows us to observe that the KH rolls process is largely driven by convention, although a significant portion is also influenced by the large-scale stretching term $\mathcal{EM}_\Omega$, which could accelerate the transition to turbulence. It is also noteworthy that $\mathcal{PM}\Omega$, although negligible in 5.11(c), shows early traces in 5.9(b), where it is observed to develop diagonally rather than uniformly across the domain, following the patterns of $\mathcal{EM}_\Omega$ which suggest that the disintegration of the KH-rolls is not uniform.

Phase III is the region where fully developed turbulence is reached however many complex processes happen simultaneously. From $x/C = 1.1$ to 1.2 (figure 5.12(a) and (b)), it can be observed that $\mathcal{CM}_\Omega$ is overtaken by $\mathcal{EM}_\Omega$. The contours of the latter term extends diagonally across the wake, connecting it with the tip-vortex area. We computed the nine terms that comprise $\mathcal{EM}_\Omega$ and determined the one with the maximum contribution. This term was found to be the spanwise stretching $\langle\Omega_3\rangle\langle\Omega_3\rangle\langle S_{zz}\rangle$. The origins of this term can be traced back to the mixture of inboard and outboard mean velocities, as a product of the influx of tip flow, which induce levels of spanwise elongation $\langle S_{zz}\rangle$. The spanwise stretching term $\langle\Omega_3\rangle\langle\Omega_3\rangle\langle S_{zz}\rangle$, aids in the generation of $\langle\Omega_i\rangle\langle\Omega_i\rangle$ which peaks at $x/C \approx 1.2$ (figure 5.9(b)). At this location, the flow is already unstable and this term further incites the fragmentation of vortical structures. In a nominal two-dimensional case i.e. infinite wing, the following condition holds $\langle\Omega_3\rangle\langle\Omega_3\rangle\langle S_{zz}\rangle = 0$ (because $\langle S_{zz}\rangle = 0$). This condition implies that the resultant fluctuating sink or source terms are primarily balanced by $\mathcal{CM}_\Omega$. In terms of the sink terms, viscous diffusion term $\mathcal{DM}_\Omega$ continues to decrease, while the vorticity-velocity correlation term $\mathcal{PM}_\Omega$ takes the lead as the primary sink term. By analysing the contours in figure 5.9(b) and 5.10(b), $\mathcal{EM}_\Omega$ reaches its maximum slightly earlier than $\mathcal{PM}_\Omega$. This observation implies that mean flow vortex stretching $\mathcal{EM}_\Omega$ apart from generating $\langle\Omega_i\rangle\langle\Omega_i\rangle$, it also acts disruptively accelerating the disintegration of larger structures within the flow at this location. The fact that $\mathcal{CM}_\Omega$ is approximately constant while $\mathcal{EM}_\Omega$ and $\mathcal{PM}_\Omega$ grow and the other terms oscillate around zero supports this claim.

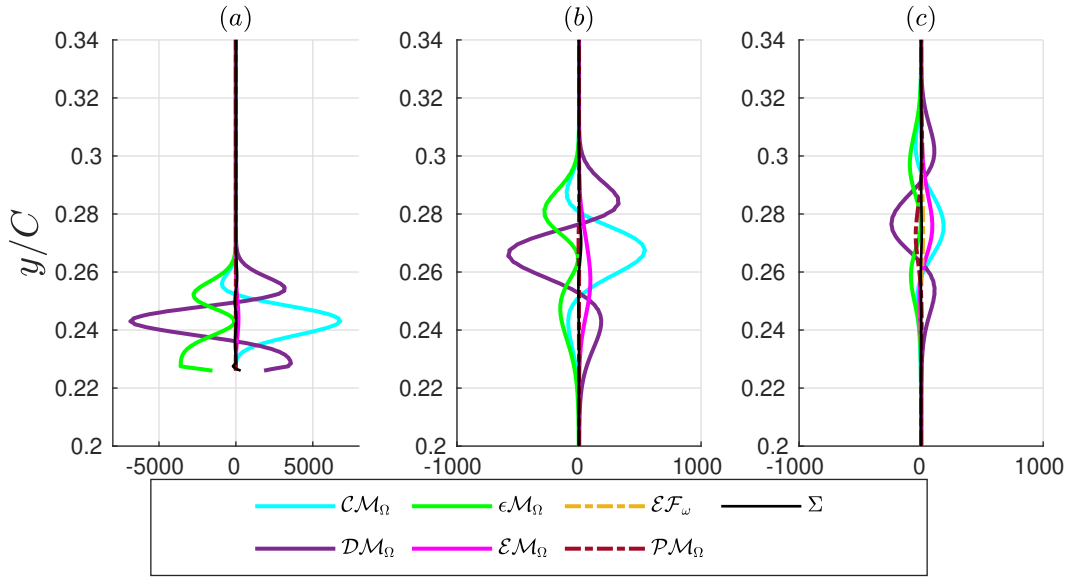


Figure 5.11: Vertical evolution ($y/C = 0.2 - 0.34$) of the budgets of the transport equation of $0.5\langle\Omega_i\rangle\langle\Omega_i\rangle$ measured at (a) $x/C = 0.2$, (b) $x/C = 0.5$ and (c) $x/C = 0.9$. Dashed lines correspond to components containing fluctuations.

From $x/C = 1.2$ to 1.3 (figure 5.12(b) and (c)), it can be observed that $\mathcal{CM}_\Omega$ regains its dominance overtaking $\mathcal{EM}_\Omega$. As previously mentioned, at $x/C \approx 1.2$, the streamwise flow rapidly increases due to the reduction of the recirculating bubble. At these locations, the effects of the ring-like structure of the spanwise stretching term $\langle\Omega_3\rangle\langle\Omega_3\rangle\langle S_{zz}\rangle$ start to diminish. $\mathcal{DM}_\Omega$ values are close to zero which indicates that the diffusion caused by kinematic viscosity is relatively less effective when compared to the non-viscous terms in controlling the growth of mean flow enstrophy. The production term based on fluctuating vortex stretching $\mathcal{EF}_\Omega$ maintains finite values in these stages, however notably lower than the large scale vortex stretching $\mathcal{EM}_\Omega$. This difference can be attributed to the scale size at which $\mathcal{EF}_\Omega$ operates. The impact of the latter term on the large-scale flow is less influential compared to the velocity-vorticity counterpart such as $\mathcal{PM}_\Omega$, which plays a more prominent role in counteracting against $\mathcal{CM}_\Omega$.

5.4 Alignments between velocity and vorticity

In this section, we will explore the alignments between velocity and vorticity vectors. These alignments play a crucial role in determining the values of the individual terms of the Lamb vector and its potential component, which we will explore in the following subsection.

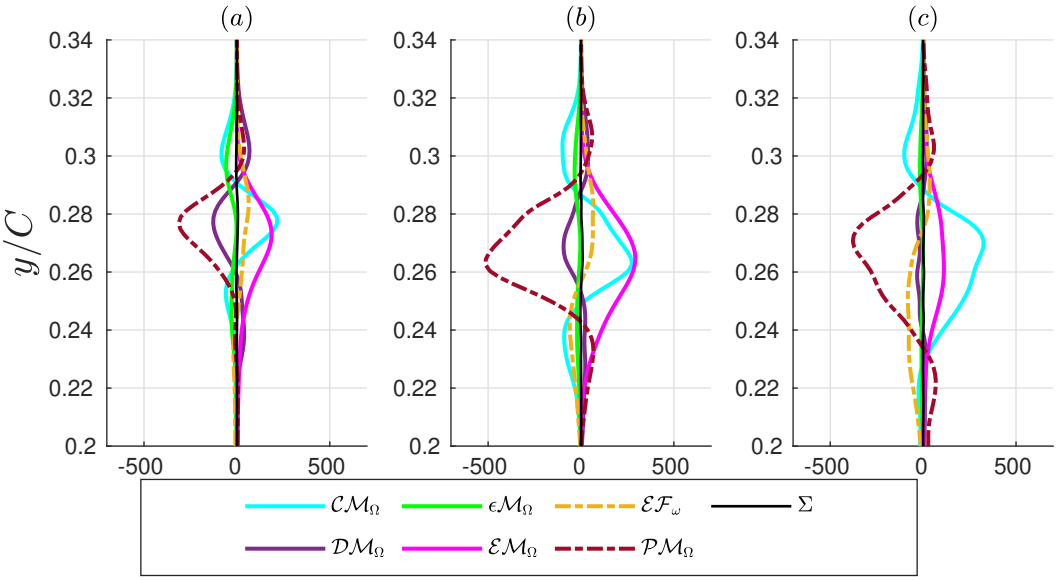


Figure 5.12: Vertical evolution ($y/C = 0.2 - 0.34$) of the budgets of the transport equation of $0.5\langle\Omega_i\rangle\langle\Omega_i\rangle$ measured at (a) $x/C = 1.1$, (b) $x/C = 1.2$ and (c) $x/C = 1.3$. Dashed lines correspond to components containing fluctuations.

Figure 5.13(a) shows instantaneous contours of $|u \times \omega|$ where significant values are shown inside the Q contours as expected, between $x/C \approx 1.2$ and 2. The contours of $|\cos(u, \omega)|$ are found in panel (b). High concentrations of nearly parallel alignment are observed inside the bubble and further downstream in $E5$. The remaining structures align perpendicularly creating a favourable condition for high levels of $|\omega \times u|$.

Figure 5.13(c) shows instantaneous contours of $|\langle U\rangle \times \omega|$. The areas above and below the recirculating bubble show significant values, for example, such as the case of $E4$ where its entire structure is affected by this linkage. Also, it is interesting to note that $|\langle U\rangle \times \omega|$ is active in certain parts of $E2$ and $E3$ where $|\cos(u, \omega)|$ is not, showing a clear example of how a vortical structure can be affected simultaneously by the interplay of multiple length scales. Figure 5.13(d) shows that in specific parts of $E2$ and $E3$, where the magnitude of $|\langle U\rangle \times \omega|$ is high, there is a noticeable increase in perpendicular alignment. On the other hand, the other vortical structures with negligible values of $|\langle U\rangle \times \omega|$ exhibits a random distribution of alignments.

Contours of $|u \times \langle\Omega\rangle|$ (panel (e)) can only be observed between $x/C \approx 1.2$ and 1.8 and these are at least an order of magnitude lower than the first two which indicates the minimal impact of the velocity fluctuations on the mean vorticity. It is worth noting that values of this term are not limited to being within the Q contour. $|\cos(u, \langle\Omega\rangle)|$ in panel (f) shows larger areas of

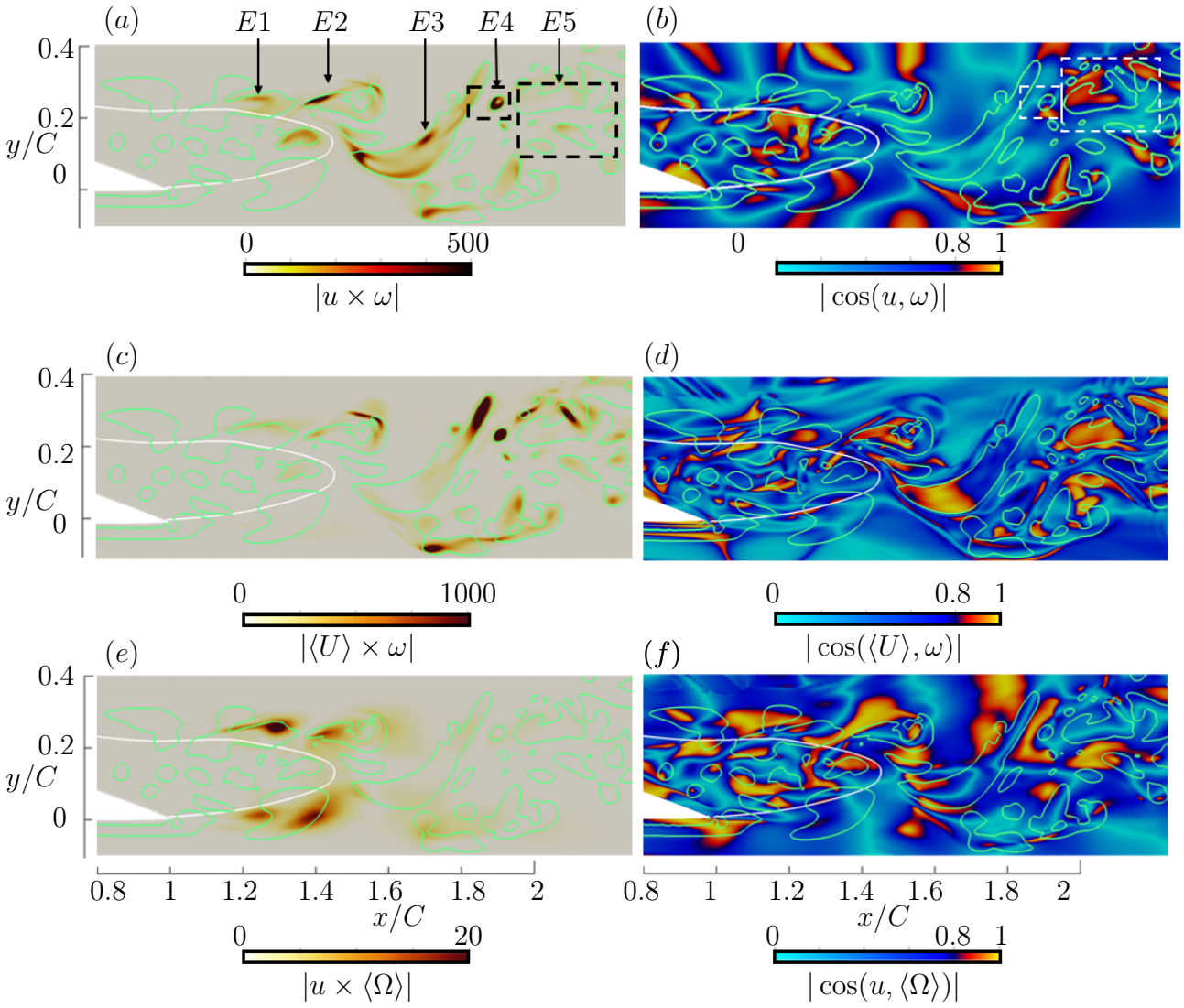


Figure 5.13: Contours of instantaneous absolute values of (a) $|u \times \omega|$, (b) $|\langle U \rangle \times \omega|$, and (c) $|u \times \langle \Omega \rangle|$ are shown, along with their alignments (b) $|\cos(u, \omega)|$, (d) $|\cos(\langle U \rangle, \omega)|$, and (f) $|\cos(u, \langle \Omega \rangle)|$.

parallel alignment.

Lastly, high values of $u \cdot \langle U \rangle$ in figure 5.14 are found as expected in the peripheries of the recirculating bubble. $|\cos(u, \langle U \rangle)|$ in panel (b), shows that parallel alignment is present above and inside the recirculating flow and in the $E5$.

5.5 Interaction of the fluctuating, mixed and mean flow quantities in the Lamb vector and its potential component

In generalised Beltrami flows $\nabla \times (\Omega \times U) = 0$, thus $\Omega \times U = -\nabla \alpha$ where the Bernoulli

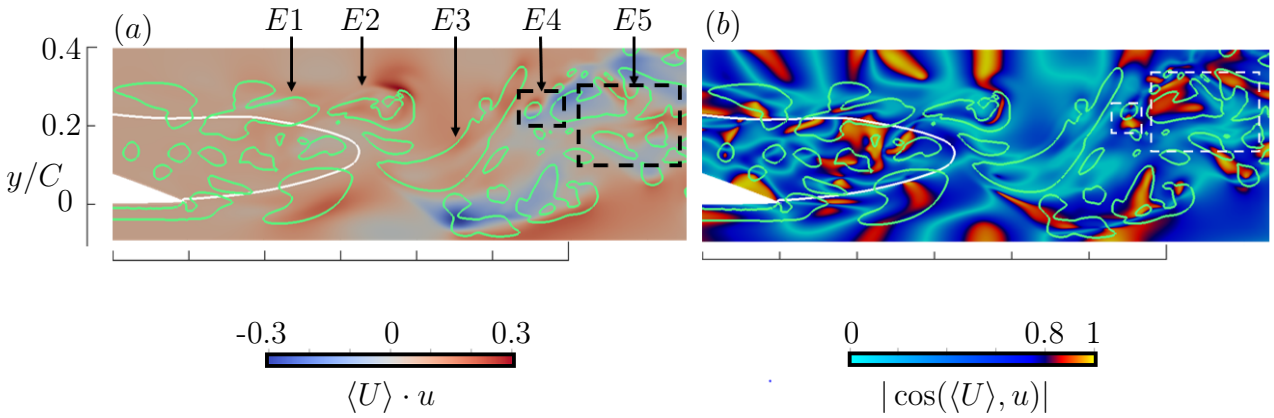


Figure 5.14: Contours of (a) $\langle U\rangle \cdot u$ and (b)$|\cos(\langle U\rangle, u)|$.

function α is a scalar. If $\nabla \times (\Omega \times U) \neq 0$, where $\nabla \times \nabla\alpha = 0$, then the Lamb vector possesses a non-zero, divergence-free component. In such cases, the flow cannot be classified as a generalized Beltrami flow.

In figure 5.15, we show the contours of $|\nabla \times (\langle\Omega\rangle \times \langle U\rangle)|$ which indicate that the present flow departs from a generalized Beltrami flow and the divergence-free part is present. The following vector identity can be used directly for the mean flow

$$|\nabla \times (\langle\Omega\rangle \times \langle U\rangle)| = |\underbrace{\langle U\rangle \cdot \nabla\langle\Omega\rangle}_{\text{convective term}} - \underbrace{\langle\Omega\rangle \cdot \nabla\langle U\rangle}_{\text{vortex stretching}}|. \tag{5.9}$$

The contour stripes observed along the leading edge separated shear are related to values of convection $\langle U\rangle \cdot \nabla\langle\Omega\rangle$ and stretching of vorticity $\langle\Omega\rangle \cdot \nabla\langle U\rangle$ in the mean flow, which is associated with the absolute values of $\mathcal{CM}\Omega$ and $\mathcal{EM}\Omega$ respectively (refer to figure 5.11 and 5.12). These stripes exhibit significant deterioration after the bubble closes at $x/C \approx 1.6$.

We now evaluate the norm of the Lamb vector, $L \cdot L$. As will be seen, this captures the interaction between the mean, fluctuating and mixed terms. By employing Reynolds decomposition on $L = (\langle\Omega\rangle + \omega) \times (\langle U\rangle + u)$ and $\nabla\alpha = \frac{1}{\rho}\nabla(\langle P\rangle + p) + \frac{1}{2}\nabla(\langle U\rangle + u)(\langle U\rangle + u)$ and by expanding $\langle L \cdot L\rangle$ and $\langle\nabla\alpha \cdot \nabla\alpha\rangle$, we obtain, three types of pairs: all-mean, mixed, all-fluctuating pairs (see section G for further details)

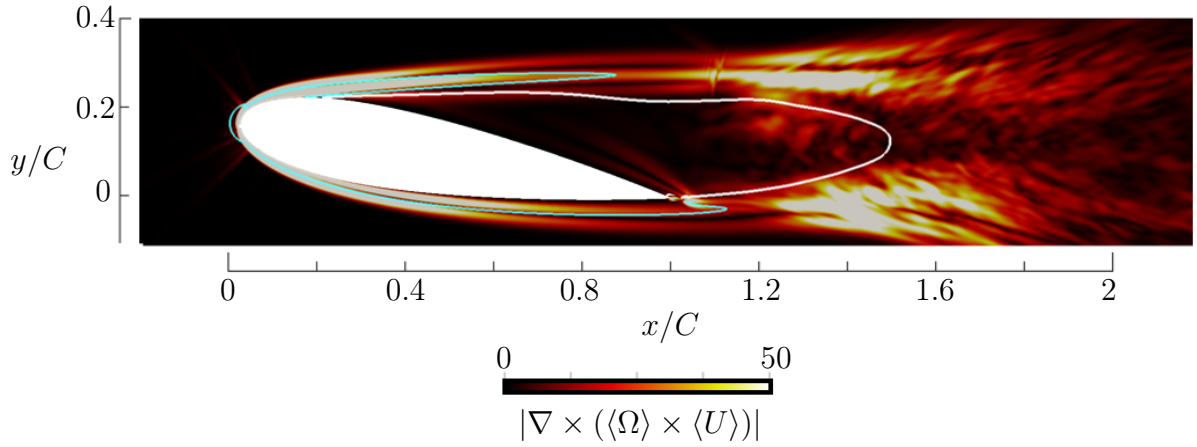


Figure 5.15: Contours of $|\nabla \times (\langle\Omega\rangle \times \langle U\rangle)|$. The light blue isoline in (b) represents $\frac{1}{2}\langle\Omega\rangle \cdot \langle\Omega\rangle = 250$.

$$\langle L \cdot L\rangle = (\langle\Omega\rangle \times \langle U\rangle)^2 + \langle(\langle\Omega\rangle \times u)^2\rangle + \langle(\omega \times \langle U\rangle)^2\rangle + \langle(\omega \times u)^2\rangle + 2(\langle\Omega\rangle \times \langle U\rangle) \cdot \langle\omega \times u\rangle + 2\langle(\langle\Omega\rangle \times u) \cdot (\omega \times u)\rangle + 2\langle(\omega \times \langle U\rangle) \cdot (\omega \times u)\rangle + 2\langle(\omega \times \langle U\rangle) \cdot (\langle\Omega\rangle \times u)\rangle \quad (5.10)$$

and

$$\langle \nabla\alpha \cdot \nabla\alpha\rangle = \nabla\langle P\rangle \cdot \nabla\langle P\rangle + \langle\nabla p \cdot \nabla p\rangle + \nabla\langle P\rangle \cdot \nabla\langle U\rangle^2 + \nabla\langle P\rangle \cdot \nabla\langle u^2\rangle + \langle\nabla p \cdot \nabla\left(u\langle U\rangle\right)\rangle + 2\langle\nabla p \cdot \nabla u^2\rangle + \frac{1}{4}\nabla\langle U\rangle^2 \cdot \nabla\langle U\rangle^2 + \frac{1}{2}\nabla\langle U\rangle^2 \cdot \nabla\langle u^2\rangle + \langle\nabla\left(\langle U\rangle u\right) \cdot \nabla u^2\rangle + \langle(\nabla\langle U\rangle u)^2\rangle + \frac{1}{4}\langle\nabla u^2 \cdot \nabla u^2\rangle\,. \quad (5.11)$$

For HIT we obtain,

$$\langle L \cdot L\rangle_{HIT} = \langle(\omega \times u) \cdot (\omega \times u)\rangle\,, \quad (5.12)$$

and

$$\langle \nabla\alpha \cdot \nabla\alpha\rangle_{HIT} = \langle\nabla p \cdot \nabla p\rangle + 2\langle\nabla p \cdot \nabla u^2\rangle + \frac{1}{4}\langle\nabla u^2 \cdot \nabla u^2\rangle\,. \quad (5.13)$$

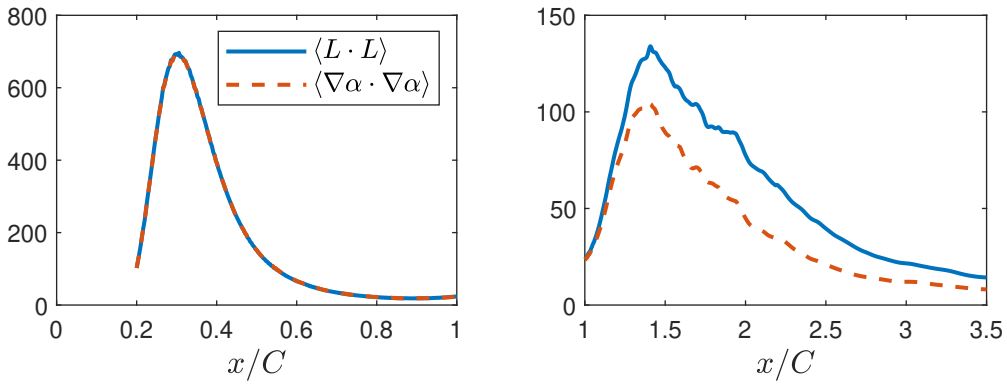


Figure 5.16: Streamwise evolution of $\langle L \cdot L \rangle$ and $\langle \nabla\alpha \cdot \nabla\alpha \rangle$ along line B.

In HIT, the mean of the norm of the Lamb vector $\langle L \cdot L \rangle$ can be expressed using the Helmholtz decomposition in the following form [Shtilman, 1992, Iyer et al., 2022],

$$\langle L \cdot L \rangle = \langle \nabla\alpha \cdot \nabla\alpha \rangle + \langle \nabla \times \beta \cdot \nabla \times \beta \rangle \,, \tag{5.14}$$

where $\nabla \times \beta$ is the solenoidal part and $\langle \nabla\alpha \cdot \nabla \times \beta \rangle = 0$ [Tsinober, 1990, Iyer et al., 2022].

Figure 5.16 shows the distribution of $\langle L \cdot L \rangle$ and $\langle \nabla\alpha \cdot \nabla\alpha \rangle$ along line B. It can be seen that for $x/C < 1$, the values $\langle L \cdot L \rangle$ are equal to $\langle \nabla\alpha \cdot \nabla\alpha \rangle$ and they peak at $x/C \approx 0.3$ as the line intersects the separated shear layer. For $x/C > 1$, $\langle L \cdot L \rangle$ starts to diverge from $\langle \nabla\alpha \cdot \nabla\alpha \rangle$. Both $\langle L \cdot L \rangle$ and $\langle \nabla\alpha \cdot \nabla\alpha \rangle$ peak at $x/C \approx 1.5$.

Figure 5.17 shows the distribution of $\langle \nabla\alpha \cdot \nabla\alpha \rangle / \langle L \cdot L \rangle$ as transition occurs. The ratio exhibits a quasi-linear decay (growth) until $x/C \approx 2$. At approximately $x/C \approx 2.6$, it reaches its minimum value of around $\approx$ 0.52. Afterward, the ratio grows slightly and appears to stagnate at approximately 0.60. Tsinober [1990] showed that the following relation is valid: $\langle \nabla\alpha \cdot \nabla\alpha \rangle / \langle L \cdot L \rangle = 0.5$, when considering the Lamb vector $\omega \times U$, with ω as an isotropic solenoidal vector field and U as a constant vector.

Figure 5.18(a) shows the contours of $\langle \nabla\alpha \cdot \nabla\alpha \rangle / \langle L \cdot L \rangle$ in the plane $x - y$. The separated laminar shear layer (between $x/C \approx 0.2$ and 0.8) contains predominantly the potential term. The light blue isoline representing $\frac{1}{2}\langle \Omega \rangle \cdot \langle \Omega \rangle = 250$ covers a specific area where the values are close to 1. Between $x/C \approx 1.3$ and 1.5, as the flow undergoes transition, $\langle L \cdot L \rangle - \langle \nabla\alpha \cdot \nabla\alpha \rangle$ becomes noticeable, turning the ratio into a more uniform distribution in the cross-stream direction. Note that inside the recirculating zone, the presence of $\langle L \cdot L \rangle - \langle \nabla\alpha \cdot \nabla\alpha \rangle$ is significant.

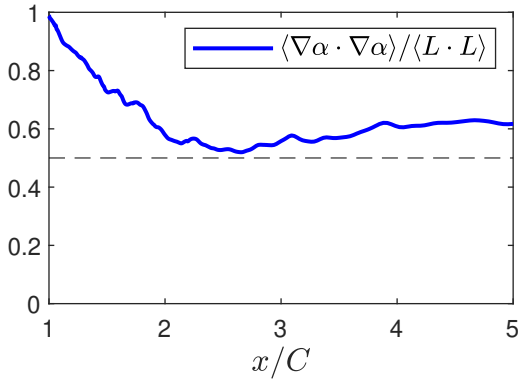


Figure 5.17: Streamwise evolution of $\langle\nabla\alpha\cdot\nabla\alpha\rangle/\langle L\cdot L\rangle$ along line B.

Further downstream, the values of the ratio turn even more homogeneous, converging towards ≈ 0.5. Figure 5.18(b) shows the contours of $\langle\nabla\alpha\cdot\nabla\alpha\rangle$ where higher values are found in the laminar shear layer detaching from the leading edge. Downstream $x/C \approx 1.2$, the contours become more diffuse because of mixing caused by the developing turbulence. Figure 5.18(c) shows contours of $\langle L\cdot L\rangle - \langle\nabla\alpha\cdot\nabla\alpha\rangle$. It can be observed that there are significant values in the proximity of the leading edge, although the contour is thinner compared to $\langle\nabla\alpha\cdot\nabla\alpha\rangle$. These high values decrease rapidly as the flow separates from the surface at $x/C \approx 0.2$. Some finite values following the footprint of the shear layers can be found between $x/C \approx 0.2$ and 0.8, however, they are very small. The highest concentration of $\langle L\cdot L\rangle - \langle\nabla\alpha\cdot\nabla\alpha\rangle$ is found above and below the recirculating bubble and in the section of fully developed turbulence downstream of $x/C \approx 1.5$.

We proceed with the analysis of the individual terms of $\langle L\cdot L\rangle$ in figure 5.19. In figure 5.19(a), the absence of fluctuations for $x/C < 1$ makes $(\langle\Omega\rangle\times\langle U\rangle)^2$ the only term active in this section. In figure 5.16(b), the slight gain of $(\langle\Omega\rangle\times\langle U\rangle)^2$ could be primarily attributed to the closure of the recirculating bubble, which causes acceleration of the streamwise velocity and the associated three-dimensional effects of the flow as discussed in the previous subsections. As transition to turbulence starts, the mixed term $\langle(\omega\times U)\cdot(\omega\times U)\rangle$ increases rapidly peaking at $x/C \approx 1.4$. The $\langle(\omega\times u)(\omega\times u)\rangle$ also reaches its peak at $x/C \approx 1.4$, but it only reaches half of the value of $\langle(\omega\times U)(\omega\times U)\rangle$. Term $\langle(\Omega\times u)(\Omega\times u)\rangle$ peaks slightly earlier at $x/C \approx 1.3$ (close to the location of the peak $(\langle\Omega\rangle\times\langle U\rangle)^2$). The only relevant negative term is $2\langle(\omega\times U)(\omega\times u)\rangle$.

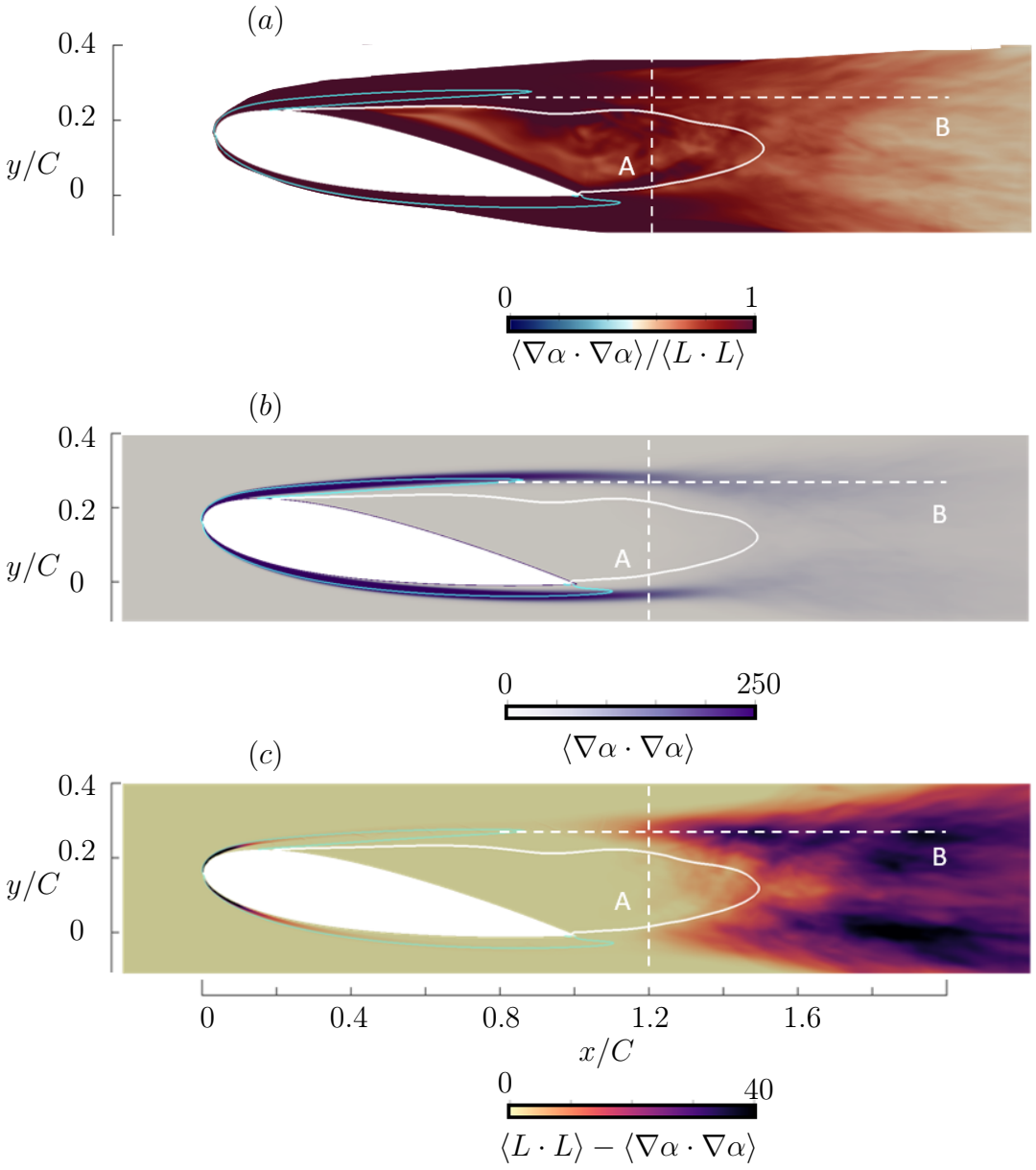


Figure 5.18: Contours of (a) $\langle \nabla\alpha \cdot \nabla\alpha \rangle / \langle L \cdot L \rangle$, (b) $\langle \nabla\alpha \cdot \nabla\alpha \rangle$ and (c) $\langle L \cdot L \rangle - \langle \nabla\alpha \cdot \nabla\alpha \rangle$ in the $x - y$ plane at $z/C = -0.2$. The light blue isoline represents $\frac{1}{2}\langle \Omega \cdot \Omega \rangle = 250$.

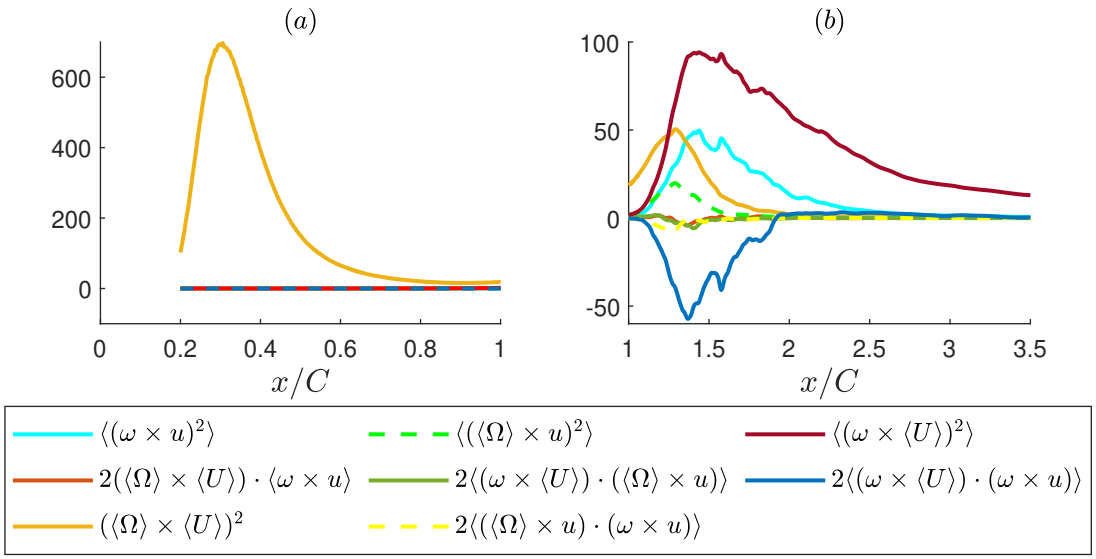


Figure 5.19: Streamwise evolution (along line B) of components of $\langle L \cdot L \rangle$.

The rest of the cross-correlation terms have negligible values.

The terms comprising $\langle \nabla\alpha \cdot \nabla\alpha \rangle$ are displayed in figure 5.20. In the laminar section, $\frac{1}{4}\nabla\langle U\rangle^2 \cdot \nabla\langle U\rangle^2$ is the dominant term. The small values of $\langle P \rangle$ also impact the values of $\nabla\langle P\rangle \cdot \nabla\langle P\rangle$ and $\nabla\langle P\rangle \cdot \nabla\langle U\rangle^2$, both of which have negligible values. The following approximation holds for the sections between $x/C \approx 0.2$ and 1,

$$(\langle\Omega\rangle \times \langle U\rangle)^2 \approx \frac{1}{4}\nabla\langle U\rangle^2 \cdot \nabla\langle U\rangle^2 \,. \tag{5.15}$$

For $x/C > 1$, the term $\frac{1}{4}\nabla\langle U\rangle^2 \cdot \nabla\langle U\rangle^2$ experiences an increase, eventually reaching values similar to $(\langle\Omega\rangle \times \langle U\rangle)^2$ at $x/C \approx 1.3$. The mixed term $\langle(\nabla\langle U\rangle u)^2\rangle$ peaks at $x/C \approx 1.4$, achieving $\approx 50\%$ of the value of $\langle(\omega \times \langle U\rangle)^2\rangle$. For the section $x/C \approx 1.4 - 2$ the following approximation can be made

$$\langle(\nabla\langle U\rangle u)^2\rangle \approx 0.5\langle(\omega \times \langle U\rangle)^2\rangle \,. \tag{5.16}$$

The fluctuating terms $\frac{1}{4}\langle\nabla u^2 \cdot \nabla u^2\rangle$ and $\langle\nabla p \cdot \nabla p\rangle$ have a similar distribution with the former having slightly higher values than the latter. After $x/C \approx 2$, $\langle(\nabla\langle U\rangle u)^2\rangle$ is the primary term contributing to the potential term. This shows that along line B, the influence of the mean flow persists. At this point, the quantity $\langle(\nabla\langle U\rangle u)^2\rangle$ has experienced a reduction of $\approx 65\%$

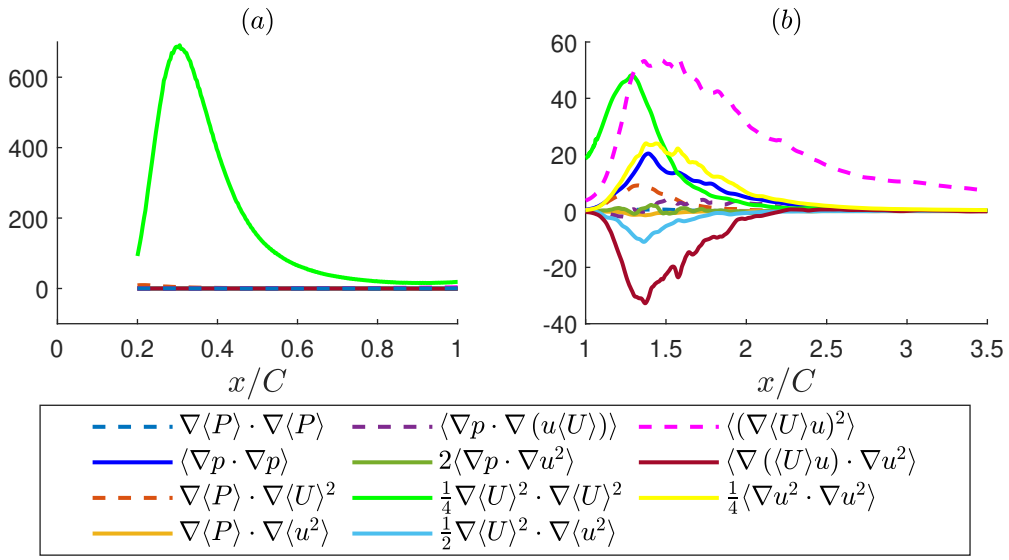


Figure 5.20: Streamwise evolution (along line B) of components of $\langle\nabla\alpha\cdot\nabla\alpha\rangle$.

compared to its peak value. The end of the quasi-linear decay and beginning of stagnation in the ratio (at $x/C\approx 2$) in figure 5.17 coincides with this section of the flow where the ratios start to depend only on $\langle(\omega\times\langle U\rangle)^2\rangle$ and $\langle(\nabla\langle U\rangle u)^2\rangle$. Also in this section, the respective alignments of these two terms tend to exhibit a more randomized distribution as discussed earlier. $\langle\nabla(\langle U\rangle u)\cdot\nabla u^2\rangle$ is the main sink term along with $\frac{1}{2}\nabla\langle U\rangle^2\cdot\nabla\langle u^2\rangle$ which accounts for 25% the value of the former term. The peak value of $\nabla\langle P\rangle\cdot\nabla\langle U\rangle^2$ is approximately $\approx 20\%$ of $\frac{1}{4}\nabla\langle U\rangle^2\cdot\nabla\langle U\rangle^2$. This suggests that the mean pressure plays a significant role in the separated shear flow in this section. The rest terms are negligible in magnitude.

Moving now to the recirculating section along line A, the vertical evolution of terms comprising $\langle L\cdot L\rangle$ and Potential term $\langle\nabla\alpha\cdot\nabla\alpha\rangle$ is plotted in figure 5.21. The figure shows a noticeable decline in the potential term that persists along the entire line. Figure 5.22(a-d) shows the variations at different locations along the streamwise direction of the recirculation bubble until its closure. In all observed cases, the potential term has consistently accounted for more than half of the value of $\langle L\cdot L\rangle$ i.e $\langle\nabla\alpha\cdot\nabla\alpha\rangle/\langle L\cdot L\rangle > 0.5$. The values obtained in the middle section are the following (a)≈ 0.76, (b)≈ 0.73, (c)≈ 0.77 and (d) ≈ 0.71. The ratios approach the value of ≈ 0.78 obtained by Iyer et al. [2022] in HIT for $Re_{\zeta_i}=38$.

In figure 5.23, as the flow evolves downstream from panel (a) to (d) terms consisting of mean-mean values are overtaken by mixed terms. In the middle panels, specifically, at $x/C=1.4$ and $x/C=1.5$, $\langle(\omega\times u)^2\rangle$ is the single component representing $\langle L\cdot L\rangle$. In figure 5.24, as the

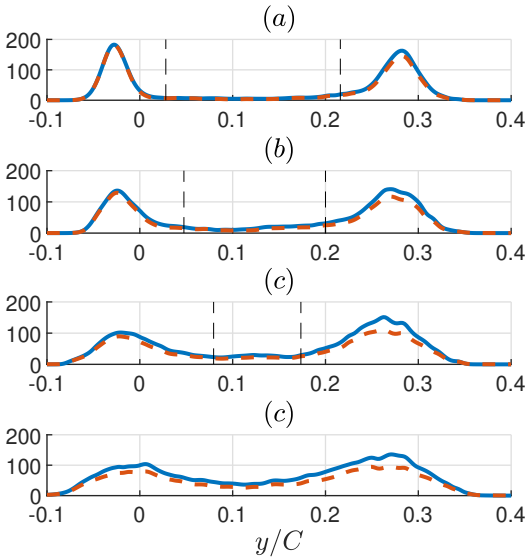


Figure 5.21: Vertical evolution of terms comprising the Lamb vector $\langle L \cdot L \rangle$ and Potential term $\langle \nabla\alpha \cdot \nabla\alpha \rangle$ measured at different downstream locations: (a) $x/C = 1.2$, (b) $x/C = 1.3$, (c) $x/C = 1.4$ and (d) $x/C = 1.5$.

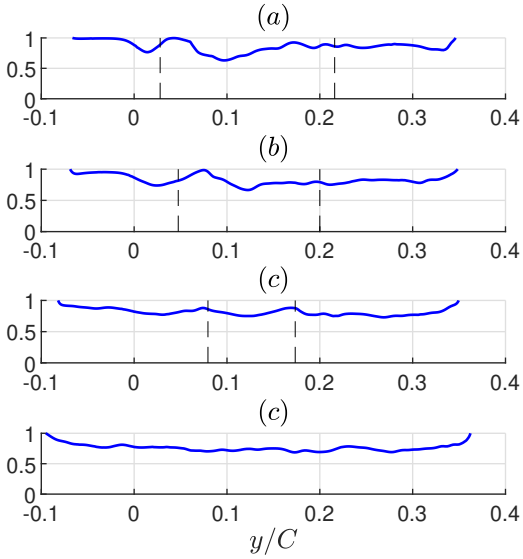


Figure 5.22: Vertical evolution of $\langle \nabla\alpha \cdot \nabla\alpha \rangle / \langle L \cdot L \rangle$ measured at different locations: (a) $x/C = 1.2$, (b) $x/C = 1.3$, (c) $x/C = 1.4$ and (d) $x/C = 1.5$.

flow evolves downstream from panel (a) to (d) similar trend is observed where the all-mean terms are overtaken by mixed terms. In the middle panels, mixed terms vanish leaving only the all-fluctuating terms. At $x/C \approx 1.5$, the following approximation can be made

$$\frac{1}{4}\langle \nabla u^2 \cdot \nabla u^2 \rangle \approx 2\langle \nabla p \cdot \nabla p \rangle \,. \tag{5.17}$$

Pearson and Antonia [2001] presented various approximations, including a DNS in HIT, to investigate the influence of Reynolds number on the pressure-gradients mean square $\langle \nabla p \cdot \nabla p \rangle$. The results indicated that $\langle \nabla p \cdot \nabla p \rangle$ changes with increasing Reynolds number, however remains constant once the Reynolds number exceeds 300. The Reynolds number within the bubble exhibits a gradual increase as we move further downstream, ranging approximately between 20 and 40. Although the data suggests that the quantity $\frac{1}{4}\langle \nabla u^2 \cdot \nabla u^2 \rangle$ increases at a faster rate than $\langle \nabla p \cdot \nabla p \rangle$ downstream (refer to middle panels in figure 5.24), it is still uncertain how these two quantities will evolve under the present flow settings at higher Reynolds numbers.

5.6 Summary

We investigated the physical characteristics and spatial development of the Lamb vector and its divergence in a separated three-dimensional turbulent shear flow around a finite wing. The flow field was obtained from the DNS that was used in chapter 4. The y-component of the Lamb vector (where $|\langle \Omega_3 \rangle \langle U_1 \rangle| \gg |\langle \Omega_1 \rangle \langle U_3 \rangle|$) was found to be by far the largest term with two clear peaks of opposite sign outside of the recirculation zone along line A. The recirculation bubble exhibited strong three-dimensionality in the form of a concentration of helical spots, in comparison to the shear layer, which maintained the orthogonality between velocity and vorticity vectors, $\cos(\langle U \rangle, \langle \Omega \rangle) \approx 0$.

We further examined the sequence of events from the leading edge to the fully developed turbulent flow in the wake. In this analysis, we analyzed the transport equation of $\langle \Omega_i \rangle \langle \Omega_i \rangle$ from the perspective of the Lamb vector. We categorized the process of turbulence development in the current three-dimensional shear flow into three distinct stages: Phase I represents the convection-driven region, Phase II corresponds to the region where inviscid break-up of vortical structure occurs and Phase III where fully developed turbulence is reached. By analyzing the

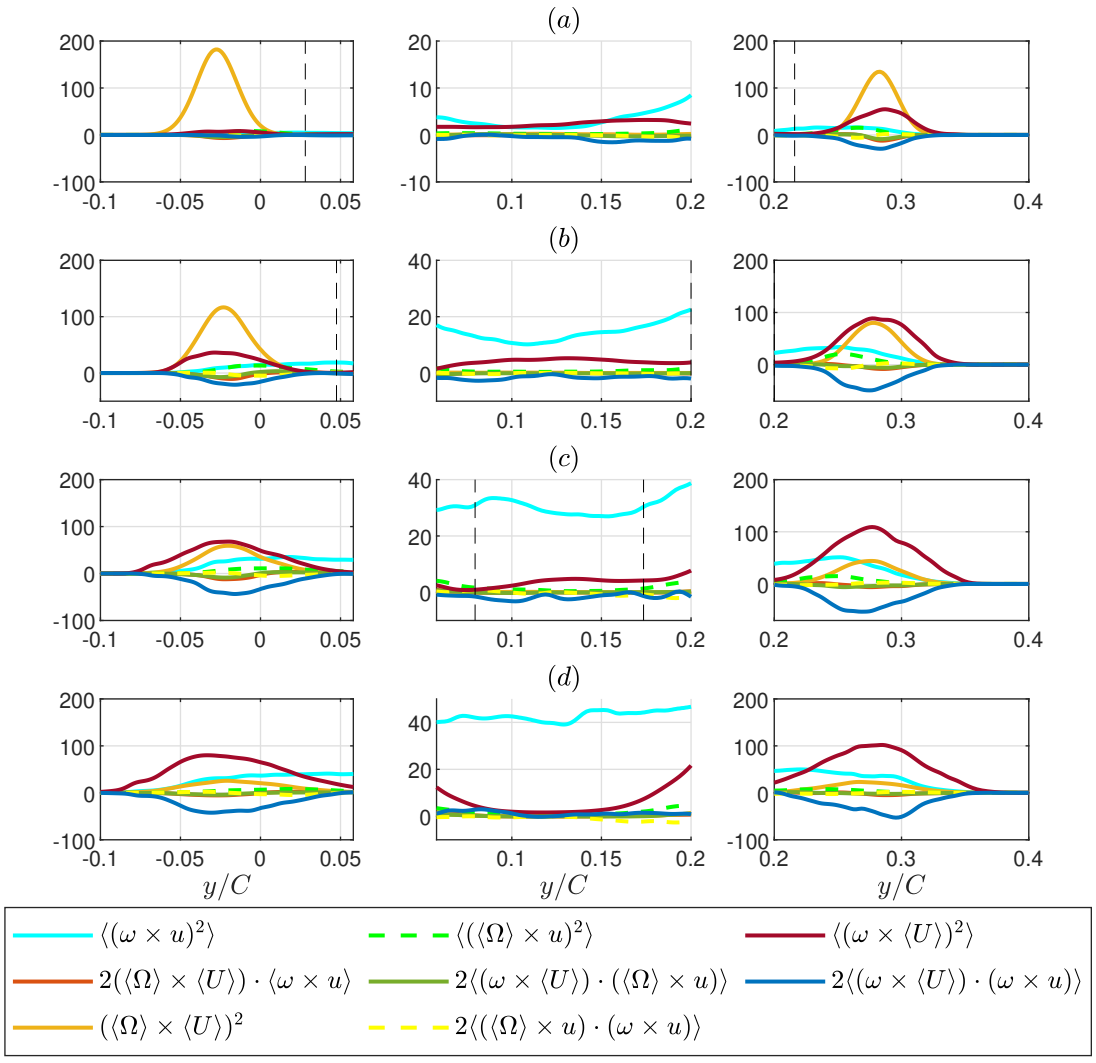


Figure 5.23: Vertical evolution of components of $\langle L \cdot L \rangle$ measured at different locations: (a) $x/C = 1.2$, (b) $x/C = 1.3$, (c) $x/C = 1.4$ and (d) $x/C = 1.5$.

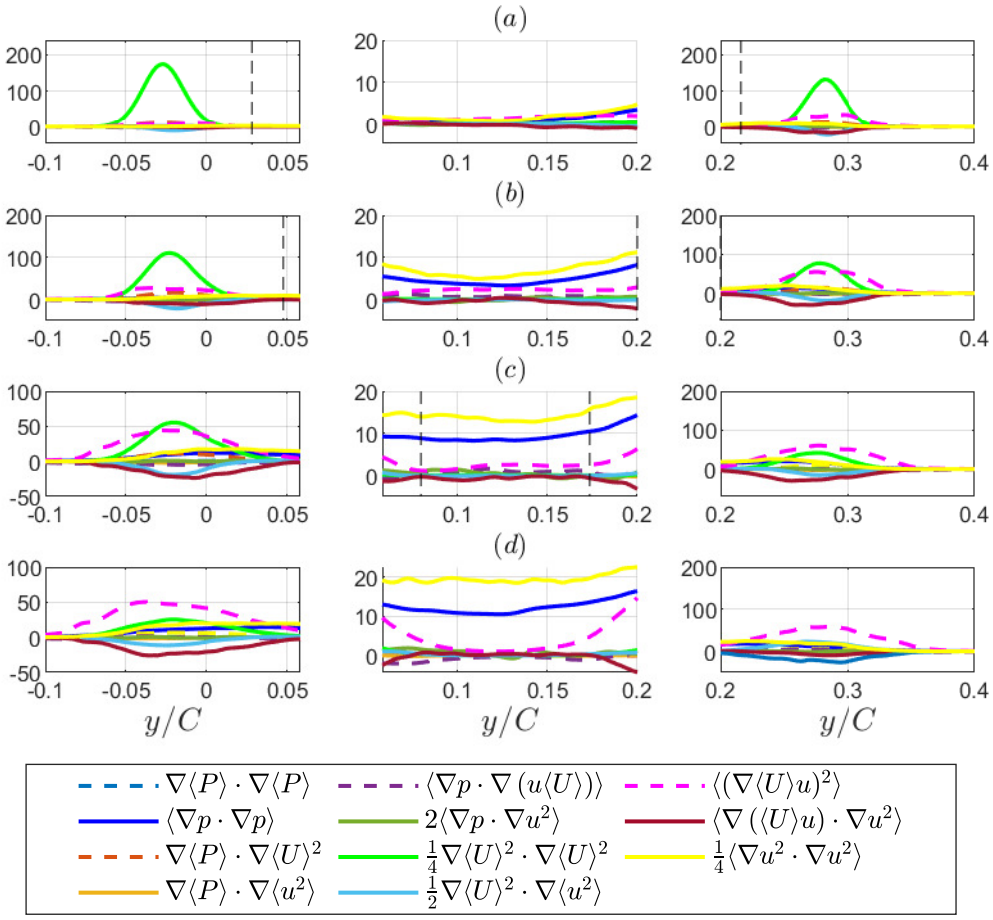


Figure 5.24: Vertical evolution of components of $\langle \nabla\alpha \cdot \nabla\alpha \rangle$ measured at different locations: (a) $x/C = 1.2$, (b) $x/C = 1.3$, (c) $x/C = 1.4$ and (d) $x/C = 1.5$.

transport equation of the enstrophy of the mean flow, we were able to identify the main source terms and sinks. It was discovered that the vortex stretching of the mean flow, $\mathcal{EM}_\Omega$, is the second most significant source term after the convection term $\mathcal{CM}_\Omega$ (dominant source term in a two-dimensional shear flow) in the region of fully developed turbulence (Phase III), specifically between $x/C \approx 1.1$ and ≈ 1.4. As we computed the full term $\mathcal{EM}_\Omega$, we were able to determine that the spanwise stretching $\langle\Omega_3\rangle\langle\Omega_3\rangle\langle S_{zz}\rangle$ has the highest value among all 9 terms. In a nominal two-dimensional case i.e. infinite wing, this term vanishes. Both $\mathcal{EM}_\Omega$ and $\mathcal{CM}_\Omega$ are directly associated with the curl of the Lamb vector $\nabla \times (\Omega \times U)$.

The ratio $\langle\nabla\alpha \cdot \nabla\alpha\rangle/\langle L \cdot L\rangle$ was used to quantify the importance of the potential component of the Lamb vector. In the separated laminar flow, even though contours show that the divergence-free values were present, the magnitudes were significantly smaller when compared to the potential terms. As the flow transitioned, the presence of the potential part decreased steadily however the ratio stagnated after the flow became fully turbulent, still maintaining a value of approximately 0.5. This indicates that the potential part becomes less crucial as the flow is less dependent on the mean shear. The ratios obtained inside the recirculating bubble indicated that in all observed cases the potential term has consistently accounted for more than half of the value and closely aligned with the value obtained by Iyer et al. [2022] in HIT for $Re_{\zeta_i} = 38$.

Chapter 6

Conclusions and future work

In this chapter, the main conclusions of the thesis are summarised and some suggestions for future work are made.

6.1 Summary of main findings

Structure of vorticity and turbulence fields in a separated flow around a finite wing

(i) We thoroughly examined and elucidated the initial formation and subsequent development of the vortices on the wing surface at a high angle of attack. It was found that the LV vortex is mainly sustained by vortex stretching. As the flow develops, vorticity intensification becomes weaker, and the core of LV is lifted up, emerging on the suction side of the wing. In this region, it is amalgamated with the arch-shaped shear layer which is found above the trailing edge recirculation pocket. The counterclockwise rotating vortex RV is suspended at a higher wall-normal distance and is sustained by stretching. RV eventually disintegrates further downstream once it has left the trailing edge. The vortical structure of V0 consists of a separating shear layer emanating from the sharp top edge of the tip. Axial vorticity is intensified in the shear layer and subsequently feeds the core via convection. In the core region, however, a region of vorticity suppression is identified, leading to the eventual decay further downstream. The wake tip vortex V1 experiences increased intensity through vortex stretching. This intensification is caused by the high strain rate resulting from the recovery of streamwise velocity downstream of the recirculation bubble that forms around the tip of the trailing edge.

(ii) We also analysed the production terms of the individual Reynolds stresses. With respect to the tip vortex V1, the term $-2\langle u_1u_2\rangle\frac{\partial\langle U_1\rangle}{\partial x_2}$ was identified as the dominant term responsible for sustaining high levels of $\langle u_1u_1\rangle$, this is the standard production term for wall-bounded flows. Additionally, the wall-normal stress source term $-2\langle u_2u_2\rangle\frac{\partial\langle U_2\rangle}{\partial x_2}$ was responsible for maintaining $\langle u_2u_2\rangle$ primarily in the spiral wakes in the near field. In relation to vortex V0, the levels of $\langle u_1u_1\rangle$ that encircle the vortex, can be traced back to $-2\langle u_1u_1\rangle\frac{\partial\langle U_1\rangle}{\partial x_1}$.

Non-normality and small-scale statistics in a separated shear flow

(iii) The generation of enstrophy caused by mean strain rate fields $\mathcal{EM}\omega$, and the amplification of strain by mean strain rate $\mathcal{SM}s$ are the important production terms for enstrophy and total strain, respectively. The maximum values of the $\mathcal{EM}\omega$ occur in the separated shear layer originating from the leading edge, where $\mathcal{EM}\omega$ reaches values approximately $\approx 25\%$ higher than the maximum values of $\mathcal{EF}\omega$. The presence of $\mathcal{EM}\omega$ activates the turbulent transport terms around its peak. The levels of $\mathcal{EM}\omega$ inside the recirculating bubble are negligible and thus $\mathcal{EF}\omega$ is balanced solely by the dissipation of enstrophy ϵ_ω as in the case of HIT. The transport equation of enstrophy in the transitional region (line B) revealed that the primary contributor to the rapid increase in enstrophy during the flow transition ("growth" section) was the generation term $\mathcal{EM}\omega$. This term reached its maximum before the peak of enstrophy, while the enstrophy production term $\mathcal{EF}\omega$ continued to grow at a much slower pace. Here also, the highest values of $\mathcal{EM}\omega$ are $\approx 30\%$ higher than the ones of $\mathcal{EF}\omega$. With respect to the total strain transport equation, similar findings were observed concerning the role of $\mathcal{SM}s$ and the regions where HIT behaviour is found. However, it is important to note that in the transitional section, the strain self-amplification $\mathcal{SF}_s$ peak values are $\approx 60\%$ higher than $\mathcal{SM}s$.

(iv) We computed fractions of occupancy of QR regions along lines A and B and compared them to HIT. The alignments of fluctuating vorticity and the principal directions of the fluctuating strain rate tensor also from HIT have been used as references. No point along lines A and B was found to exactly match the HIT parameters at the given $Re_{\zeta i}$. However,

when considering the fractions of occupied QR regions and alignments, it was observed that areas that approximate HIT were found in the middle section of the recirculating bubble. Similarly, in the turbulent shear flow along line B, to some degree, there was good approximation to HIT towards the end of the region. In the recirculating flow, the areas that deviate the most from HIT were observed at the furthest ends of the domain (as expected), where the enstrophy is zero (indicating an irrotational flow). As a result, regions 4 and 6 dominate the total occupancy. Outside the bubble, region 6 is notably diminished and the fraction of the occupancy of region 2 reaches a maximum value of $\approx 30\%$. It has been observed that a growth (decay) in enstrophy is accompanied by an immediate increase (decrease) in the occupancy of region 2. Along line B, as enstrophy levels increase in the "growth" section, the proportion of region 2 occupancy also increases. It reaches a maximum of $\approx 40\%$ before the enstrophy reaches its peak. Downstream of this point, as enstrophy decays, there is a sharp decline in the fraction of occupancy of region 2 while region 6 increases notably leading to the occupancy for half of the "decay" section. Instantaneous visualization of the topology of the flow indicates that the higher presence of region 6 might be due to the less dense packed vortical structures (where region 2 tends to concentrate). These less dense packed vortical structures are facilitated by the closure of the bubble, which provides additional space. At the end of the domain, there is a significant reduction in the size of the structures, which are more homogeneously distributed, closely resembling the values of HIT. The most "efficient" regions of production and reduction of enstrophy were regions 2 and 1 respectively. In the case of the production of strain, it was region 6.

(v) The probability of occurrence of large events (defined as 10 times greater than the time-average value) is below 5% for both. However, the contribution of the large events to the mean value of enstrophy is $\approx 60\%$ whereas for strain-self amplification is $\approx 40\%$. In the recirculating flow, the contributions of these events reach a peak in the middle of the bubble reaching $\approx 50\%$ and $\approx 70\%$ respectively. In the "decay" section of the transitional flow, the contributions from large events gradually diminish.

(vi) The value for the non-normality index, k_{BC}, for HIT is ≈ 0 but along line A, during the

second half of the "decay" section, there was a significant deviation where values of ≈ 0.15 were obtained. On the other hand, along line B, in the sections in the proximity outside of the recirculating bubble, the values reached ≈ -0.13. The leading term of enstrophy production around these two peaks is the mixed term $\langle \mathrm{Tr}(\Omega_C \Omega_C S_B) \rangle$. In the case of the strain self-amplification the leading term is also the mixed term $\langle \mathrm{Tr}(\Omega_C \Omega_C S_B) \rangle$ followed closely by the normal term $-\langle \det(S_B) \rangle$.

In the transitional flow along line B, one of the areas that deviate largely from the HIT estimation is the first half of the "decay" section, where a value of approximately 0.1 was obtained. This value indicates a dominance of normality. These results can be traced back to the high occupancy of region 6 in this section. In the "peak" section, the value of k_{BC} changes from positive to negative whereas the "growth" section is largely non-normal.

(vii) The Schur decomposition has been applied to the enstrophy production by mean strain rate fields $\mathrm{Tr}\left(\langle \Omega_A^2 \rangle S_A^M\right)$. The use of this decomposition has led to the emergence of nine new terms. When it comes to the topological organization, our results showed us that the highest values of the normal term $\|S_B^M\|^2$ which represents the total product of the normal mean strain rate is concentrated near the front of the leading edge. $\|S_C^M\|^2$ represents the total product of the non-normal mean strain rate and is found in the separated shear layers at the suction side and the attached boundary layer at the pressure side.

The structure of the Lamb vector in a separated three-dimensional turbulent flow

(viii) The y-component of the Lamb vector (where $|\langle \Omega_3 \rangle \langle U_1 \rangle| \gg |\langle \Omega_1 \rangle \langle U_3 \rangle|$) is by far the largest term with two clear peaks of opposite sign outside of the recirculation zone along line A. Despite the fact that the wing causes an asymmetric disturbance of the flow, the lower shear peaks only slightly higher than the leading edge separated flow. The recirculation bubble exhibited strong three-dimensionality in the form of a concentration of helical spots, in comparison to the shear layer, which maintained its orthogonality $\cos(\langle U \rangle, \langle \Omega \rangle) \approx 0$.

(ix) The ratio $\langle \nabla\alpha \cdot \nabla\alpha \rangle / \langle L \cdot L \rangle$ was used to measure the importance of the potential component

of the Lamb vector. In the separated laminar flow, the following approximation can be made: $\langle \nabla\alpha \cdot \nabla\alpha \rangle \approx \langle L \cdot L \rangle$. However as the flow starts transitioning from $x/C \approx 1.1$ onwards, $\langle \nabla\alpha \cdot \nabla\alpha \rangle$ starts to diverge from $\langle L \cdot L \rangle$. $\langle \nabla\alpha \cdot \nabla\alpha \rangle / \langle L \cdot L \rangle$ exhibit a quasi-linear decay until $x/C \approx 2$. Around $x/C \approx 2.6$, the ratio achieved is lowest value, which are approximately 0.52. Following this, the ratio recovered slowly and stabilized at approximately 0.60. Measurements were taken at different locations along the streamwise direction of the recirculation bubble until its closure. In all observed cases the potential term has consistently accounted for more than half of the value of $\langle L \cdot L \rangle$ i.e $\langle \nabla\alpha \cdot \nabla\alpha \rangle / \langle L \cdot L \rangle > 0.5$.

6.1.1 A further discussion on the physical and technical findings

A key observation in this study is the identification of specific features related to the active influence of the mean shear on the flow. The results demonstrate how the mean strain can shape the fluctuating velocity field differently compared to its effect on the fluctuating vorticity field. The pdf of the fluctuating velocity field (with a zero mean) exhibits a quasi-Gaussian distribution. Its departure from a Gaussian distribution, where a Gaussian distribution is a common assumption in various turbulence theories (i.e, Millionshtchikov's quasi-normal (QN) theory, see Monin and Yaglom [2013]), can be attributed to the influence of vortical structures randomly positioned around the measurement point where the signal is sampled. This close to Gaussian distribution is a product of the central limit theorem [Davidson, 2015]. The Biot-Savart law establishes the relationship between the velocity field and a multitude of randomly oriented adjacent vortices. In this study, within regions of active turbulence production, the distinct shapes of the vortical structures (refer to $E1$ and $E2$ in figure 4.11) and the peak of the correlation term $\langle u_1 u_2 \rangle$ (refer to figure 4.3) indicate the fragmentation of the KH-rolls. This is influenced by the mean strain rate, displaying a vortex sheet configuration based on its eigenvalues (see section 4.2). This configuration suggests that the velocity field is likely to deviate from a Gaussian distribution and exhibit increased organization or coherence. This is reflected in the distinctive pdf observed in figure 4.8, where the alignment production is notably non-random.

In the context of a vortex sheet model, a visible similarity can be observed in the behaviour of the leading edge separated layer. This is manifested through the order of the eigenvalues computed in section 4.2. In this context, a vortex sheet is represented by one compressive and two stretching eigenvalues. As mentioned earlier, one of the notable characteristics of the vortex sheet model is its potential to exhibit KH instabilities, leading to the development of vortical structures and the roll-up of the sheet. In this study, following the transition, the form of the separated shear layer indicates that the compressing eigenvalue Λ_3^M (refer to section 4.2) is directing in the vertical direction. This indication suggests that the traces attributed to the compressive eigenvalue are reflected in the production term of $\langle u_2 u_2 \rangle$, as depicted in figure 3.22(a) in chapter 3. On the other hand $\langle u_1 u_2 \rangle$ as well as $\langle u_1 u_1 \rangle$ are linked to the instability patterns induced by the KH-rolls as the turbulence production peaks.

A small-scale perspective on the divergence of the time-averaged Lamb vector $\nabla \cdot \langle \omega \times u \rangle$ reveals that the majority of the values are dependent on the component $\langle s : s \rangle - \frac{1}{2}\langle \omega \cdot \omega \rangle$, while the component $-\nabla^2 \langle u \cdot u \rangle$ are neglible when it is time averaged. Another observation is that, when strictly considering the small-scale Lamb vector and its connection with the Reynolds stresses in a time-averaged context, only specific parts of the eddies appear to be dynamically significant (see section 5.8). This is in contrast to the contours of enstrophy, which to some extent exhibit a more uniform spread across the entire body (see section 4.11). This could have implications for the efficiencies of certain regions within vortical structures in generating k particularly as the turbulent flow is developing. In this context, it is important to note the distinction between "vortex stretching" and "vorticity stretching". This is particularly visible during the transition and breaking up of $E1$, $E2$, and $E3$, whereas further downstream, as the flow becomes fully developed, $E4$ and $E5$ are single vortical structures. An additional interesting feature is clearly captured in figure 5.13, where identified vortical structures are influenced by multiple cross-scale components, each impacting specific regions of the eddies. This perspective reveals additional intricacies beyond the traditional depiction of an eddy as a uniform structure that breaks down into smaller, similar structures. It introduces new insights into cross-scale interactions occurring within a real flow scenario and the significance of concentrated vorticity in a time-averaged context.

6.2 Discussion and future work

In this section, we propose possible directions for future research that can build upon the findings and insights presented in the preceding chapters.

On active flow control

At subsonic speeds, drag is primarily caused by two factors: the effect of viscosity, mainly through skin friction, and pressure drag, which encompasses form drag (resulting from flow separation) and induced drag associated with the inefficiencies in lift generation [Gad-el Hak et al., 2003]. In an incompressible and adiabatic flow with a three-dimensional configuration, the induced drag D_i generated by a wing can be characterized as $D_i = \iint_{S_z} \frac{1}{2}\rho(\langle U_2\rangle^2 + \langle U_3\rangle^2)\, d_{S_z}$ [Birch et al., 2004]. This representation illustrates that induced drag is directly related to the magnitudes of the vertical and spanwise mean velocities, which are intricately connected to both the vorticity distribution, strength and persistence. It is worth noting that induced drag is an inherent characteristic of lifting wings. Additionally, the rapid diffusion of the trailing vortices contributes to the improved operational capability of aircraft. The following points can provide new pathways for future applications

- By analyzing V0 in terms of the Q and R, as well as its axial stretching capabilities (refer to section 3.2.1), we have been able to observe its relative resemblance to the Burgers vortex [Burgers, 1948] in a real flow scenario. The Burgers vortex has served as a fundamental component of some vortex models for fine-scale turbulent structures particularly the elongated tubes that characterizes structures with high-amplitude vorticity [Wu et al., 2015, Davidson, 2015]. The core radius is scaled solely based on the viscosity and stretching rate and its total dissipation per unit axial length is finite but independent of ν. However, some interesting differences can be found. While V0 is to a certain degree axisymmetrically compressed (see figure 3.9), the input from convection in the presented results only connects with the core through a limited section via the feeding shear (see figure 3.6), rather than in a fully axisymmetric manner as in the Burgers model. The exact spatial measurements and levels of limited connection between V0 and its feeding shear, as well as the levels of stretching or compression obtained in this work, provide a

pathway to better capture the complexities of real flow scenarios in a new vortex model. This can be used to assess the spatially varying strength of the vortex. The core of V0 remains relatively undisturbed until its decay, suggesting that the unbounded flow domain assumption, treating it as an isolated entity in the vortex model, could be applicable to some degree.

- The current study has identified the location of the bubble on the wingtip and the section with the highest circulation of the wake tip vortex (see figure 3.24). It would be beneficial to conduct a parametric study to assess how the placement and frequency of control mechanisms can disrupt the recirculating bubble, a key contributor to the intensification of V1, and use its circulation strength as a responsive parameter. A good example is the work of Zhang and Samtaney [2015], where synthetic jet actuators were employed to disrupt large leading edge recirculating bubbles. It would be interesting to investigate whether V1 could diffuse more rapidly and exhibit significant variations in strength as a result of the fragmentation of the bubble.

- Our study has investigated the feeding shear layer (refer to figure 3.8) which has been identified as the primary source of vorticity for V0. This findings are especially significant for wings operating at lower angles of attack, where V0 may exhibit greater strength and endurance. The reminiscent of this feeding shear layer intensifies after the bubble is closed and forms V1. It would be important to explore the positioning of actuating devices between $x/C = 0.7 - 0.8$ once the LV has merged into the feeding shear. Specifically, investigating methods to more rapidly diffuse the strength of the feeding shear, instead of displacing the LV which is already weak in these locations or V0, which depends on that layer.

On LES and hybrid methods

The dynamic Smagorinsky model, introduced by Germano et al. [1991], aims to address the limitations of using a constant Smagorinsky coefficient C_s across the domain of interest in flows of industrial relevance. This model computes the required value of C_s as a function of space and time, based on the scale-similarity assumption, relating turbulent stresses at different scales.

Notably, this approach has been successfully implemented by Yu and Lu [2020], Yu et al. [2021], who improved the model by incorporating non-local effects in boundary and mixing layers. In this context, the following points offer additional avenues for exploring and enhancing its adaptability.

- The dynamic Smagorinsky model relies on the scale-similarity assumption, which involves establishing a relationship between the turbulent stresses at a particular scale and those at a larger scale. By employing the scale-similarity assumption, the goal is to determine a value of C_s that is applicable to both scales at each point and time. This is supported by the coexistence of both scales in the inertial range of turbulence, which makes valid the scale-similarity [Hanjalić and Launder, 2022]. The method for determining the coefficient is established using a test filter with a filtered width Δ'_{SGS} that greater than Δ_{SGS}. In the case of Yu and Lu [2020], Yu et al. [2021], Δ'_{SGS} is set to be equal to $2\Delta_{SGS}$, as it is reported to be common practice. In the present work, it was observed that non-local strain $\langle|S_C|^2\rangle$ is notably more sensitive in regions characterized by high shear, the presence of mean shear, and transient flow sections where it tends to be generated in greater proportion compared to its normal part. This is in contrast to regions exhibiting behavior similar to HIT conditions, where $\langle|S_C|^2\rangle \approx \langle|S_B|^2\rangle$ (see figure 4.36). If the aim is to enhance the economic viability of LES where the implementation of a non-uniform mesh grid with varying levels of refinement is required, it is crucial to establish new thresholds for filter length, test filter length, and mesh resolution. This is essential for evaluating the accuracy of simulations, particularly focusing on the input of $\langle|S_C|^2\rangle$ and assessing its response. Of particular interest are flows such as the current one, featuring separated flow with recirculation. It is well-documented that abrupt transient effects in separated shear flow have presented a consistent challenge in turbulence modeling for many years [Leschziner, 2006]. This stands in contrast to flows such as boundary and mixing layer, where for instance, in log-law regions, various models have demonstrated relative success [Durbin and Reif, 2011].

- The present work has investigated sections where the early formation and development of V0 and V1 take place, which are highly externally intermittent (turbulent and non-

turbulent regions) and spatially confined. It is reported that the scale-similarity assumption may not hold true in areas where Δ_{SGS} approaches the integral length scale and where either transition or laminarization occurs (for laminar regions, the corresponding value of C_s is 0) [Hanjalić and Launder, 2022]. The grid size should effectively capture the inertial range, while the cut-off filter ideally needs to be positioned within the inertial cascade. In the work of Yu et al. [2021], the mesh is evenly distributed in both the streamwise and spanwise directions, which is characteristic of a boundary layer setup. The ratios of the filtered lengths in each direction are determined by the typical geometric shape of eddies near the wall within the logarithmic layer. This was the single determining sizing factor for the whole domain. Considering differences between boundary layers and vortical flows such as the one of the present work, it is essential to conduct a comprehensive parametric study to determine the appropriate filter length and the implementation of an adaptable test filter width in accordance with the grid resolution and pre-existing information. Special attention should be directed towards the turbulence in the spiral wakes identified in this study, where the regions of their maximum intensity and their evolution were analysed and documented in this work. An effective method that could be used for assessing the accuracy levels, while considering rotational effects in the presence of turbulence, is the alignment of mean strain rate and Reynolds stresses [Garmann and Visbal, 2017].

- Within the Hybrid RANS-LES (HRL) methods, the seamless methods enables users to intentionally designate specific areas to be handled in either RANS or LES mode by adjusting the mesh to be coarser or finer as required. Conversely, the zonal methods uses prescribed sections where the modeling strategy is implemented [Hanjalić and Launder, 2022]. In this thesis, the sections of laminar flow characterized by high three-dimensional complexity, including areas where LV develop on the tip side, the separated leading edge flow, and the early development of vortices V0, RV, and LV at sharp edges where identified. The considerable influence of resolution level near the wall on the evolution of vortices and the three-dimensionality of flow structures, particularly in relation to sharp edge separation, emphasize the importance of investigating and understanding the ben-

efits and limitations of these approaches in terms of grid resolution refinement and the quality of results. This is important in regions characterized by complex vortical motion and laminar flow, as the knowledge obtained here could form the basis for applications in transitional and fully turbulent domains.

Further topics and applications

- The Lamb vector is relatively unexplored in turbulent flows, and more concerted effort is needed in the analysis of the potential and solenoidal components in turbulent recirculating and related flows. Particularly, it is still uncertain whether the ratios can drastically change by modifying solely the boundary conditions and settings of the flow while keeping the same Reynolds number. We observed stagnation of the ratio at the end of the domain, however it is still uncertain whether this state will eventually be reached in other mean flow-dominated, inhomogeneous, and anisotropic turbulent flows.

- The incorporation of mean flow into the Schur decomposition has opened the application to inhomogeneous flows. Levels of mean normal strain rate norm $\|S_B^M\|^2$ were found clustered in the leading edge of the wing where the flow is laminar. It would be interesting to further explore the role of S_B^M in other types of flow where this term plays a major role as well as where fully developed turbulence and stagnation are present. These types of flows could be impinging jets, or turbulent flows over converging-diverging nozzles and forward-facing steps.

Bibliography

J. D. Anderson. Fundamentals of aerodynamics. *McGraw-Hill, New York*, 1991.

ARCHER2. Archer2 uk national supercomputing service. `https://www.archer2.ac.uk`, 2024. Accessed: 2024.

W. T. Ashurst, A. Kerstein, R. Kerr, and C. Gibson. Alignment of vorticity and scalar gradient with strain rate in simulated Navier–Stokes turbulence. *The Physics of fluids*, 30(8):2343–2353, 1987.

Z.-Z. Bai and J.-Y. Pan. *Matrix analysis and computations*. SIAM, 2021.

S. Bailey, S. Tavoularis, and B. Lee. Effects of free-stream turbulence on wing-tip vortex formation and near field. *Journal of Aircraft*, 43(5):1282–1291, 2006.

S. Balay, W. D. Gropp, L. C. McInnes, and B. F. Smith. Efficient management of parallelism in object oriented numerical software libraries. In E. Arge, A. M. Bruaset, and H. P. Langtangen, editors, *Modern Software Tools in Scientific Computing*, pages 163–202. Birkhäuser Press, 1997.

S. Balay, S. Abhyankar, M. Adams, J. Brown, P. Brune, K. Buschelman, L. Dalcin, A. Dener, V. Eijkhout, W. Gropp, et al. Petsc users manual: Revision 3.10. Technical report, Office of Scientific and Technical Information (OSTI), 2018.

S. Barbarino, O. Bilgen, R. M. Ajaj, M. I. Friswell, and D. J. Inman. A review of morphing aircraft. *Journal of intelligent material systems and structures*, 22(9):823–877, 2011.

G. K. Batchelor. *An introduction to fluid dynamics*. Cambridge university press, 1967.

P. Beaumard, O. Buxton, and C. Keylock. The importance of non-normal contributions to velocity gradient tensor dynamics for spatially developing, inhomogeneous, turbulent flows. *Journal of Turbulence*, 20(9):577–598, 2019.

P. Bechlars and R. Sandberg. Evolution of the velocity gradient tensor invariant dynamics in a turbulent boundary layer. *Journal of Fluid Mechanics*, 815:223–242, 2017a.

P. Bechlars and R. Sandberg. Variation of enstrophy production and strain rotation relation in a turbulent boundary layer. *Journal of Fluid Mechanics*, 812:321–348, 2017b.

R. Betchov. An inequality concerning the production of vorticity in isotropic turbulence. *Journal of Fluid Mechanics*, 1(5):497–504, 1956.

R. Betchov. On the non-gaussian aspects of turbulence. *Archiwum Mechaniki Stosowanej*, 28 (5):837–845, 1976.

J. C. Bilbao-Ludena and G. Papadakis. Structure of vorticity and turbulence fields in a separated flow around a finite wing: Analysis using direct numerical simulation. *Phys. Rev. Fluids*, 8:014704, Jan 2023. doi: 10.1103/PhysRevFluids.8.014704.

D. Birch, T. Lee, F. Mokhtarian, and F. Kafyeke. Rollup and near-field behavior of a tip vortex. *Journal of Aircraft*, 40(3):603–607, 2003.

D. Birch, T. Lee, F. Mokhtarian, and F. Kafyeke. Structure and induced drag of a tip vortex. *Journal of Aircraft*, 41(5):1138–1145, 2004.

J. M. Burgers. A mathematical model illustrating the theory of turbulence. *Advances in applied mechanics*, 1:171–199, 1948.

O. Buxton and B. Ganapathisubramani. Amplification of enstrophy in the far field of an axisymmetric turbulent jet. *Journal of Fluid Mechanics*, 651:483–502, 2010.

B. J. Cantwell. On the behavior of velocity gradient tensor invariants in direct numerical simulations of turbulence. *Physics of Fluids A: Fluid Dynamics*, 5(8):2008–2013, 1993.

M. Carbone and A. D. Bragg. Is vortex stretching the main cause of the turbulent energy cascade? *Journal of Fluid Mechanics*, 883, 2020.

J. M. Chacin and B. J. Cantwell. Dynamics of a low Reynolds number turbulent boundary layer. *Journal of Fluid Mechanics*, 404:87–115, 2000.

B. Chen, X. Yang, G. Chen, X. Tang, J. Ding, and P. Weng. Numerical study on the flow and noise control mechanism of wavy cylinder. *Physics of Fluids*, 34(3), 2022.

T. Chen and T. Liu. Near-wall Lamb vector and its temporal–spatial evolution in the viscous sublayer of wall-bounded flows. *AIP Advances*, 12(3), 2022.

Z.-P. Cheng, S.-Y. Qiu, Y. Xiang, and H. Liu. Quantitative features of wingtip vortex wandering based on the linear stability analysis. *AIAA Journal*, 57(7):2694–2709, 2019.

L. Chevillard and C. Meneveau. Lagrangian dynamics and statistical geometric structure of turbulence. *Physical review letters*, 97(17):174501, 2006.

M. S. Chong, A. E. Perry, and B. J. Cantwell. A general classification of three-dimensional flow fields. *Physics of Fluids A: Fluid Dynamics*, 2(5):765–777, 1990.

J. S. Chow, G. G. Zilliac, and P. Bradshaw. Mean and turbulence measurements in the near field of a wingtip vortex. *AIAA Journal*, 35(10):1561–1567, 1997.

Y. Chu, L. Wang, and X. Lu. Interaction between strain and vorticity in compressible turbulent boundary layer. *Science China Physics, Mechanics & Astronomy*, 57:2316–2329, 2014.

M. J. Churchfield and G. A. Blaisdell. Numerical simulations of a wingtip vortex in the near field. *Journal of Aircraft*, 46(1):230–243, 2009.

T. Craft, A. Gerasimov, B. Launder, and C. Robinson. A computational study of the near-field generation and decay of wingtip vortices. *International Journal of Heat and Fluid Flow*, 27 (4):684–695, 2006.

A. Crivellini and V. D'Alessandro. Spalart-Allmaras model apparent transition and rans simulations of laminar separation bubbles on airfoils. *International Journal of Heat and Fluid Flow*, 47:70–83, 2014.

P. A. Davidson. *Turbulence: an introduction for scientists and engineers*. Oxford university press, 2015.

P. A. Davidson, Y. Kaneda, K. Moffatt, and K. R. Sreenivasan. *A voyage through turbulence*. Cambridge University Press, 2011.

J. Délery. *Three-dimensional separated flow topology: critical points, separation lines and vortical structures*. John Wiley & Sons, 2013.

J. M. Délery. Robert legendre and henri werlé: toward the elucidation of three-dimensional separation. *Annual review of fluid mechanics*, 33(1):129–154, 2001.

W. J. Devenport, M. C. Rife, S. I. Liapis, and G. J. Follin. The structure and development of a wing-tip vortex. *Journal of Fluid Mechanics*, 312:67–106, 1996. doi: 10.1017/S0022112096001929.

M. Dghim, M. Ferchichi, and H. Fellouah. On the effect of active flow control on the meandering of a wing-tip vortex. *Journal of Fluid Mechanics*, 896, 2020.

K. R. Dinesh, K. Jenkins, A. Savill, and M. Kirkpatrick. Swirl effects on external intermittency in turbulent jets. *International journal of heat and fluid flow*, 33(1):193–206, 2012.

D. Dritschel and D. Waugh. Quantification of the inelastic interaction of unequal vortices in two-dimensional vortex dynamics. *Physics of Fluids A: Fluid Dynamics*, 4(8):1737–1744, 1992.

H. L. Dryden, G. Schubauer, W. Mock, and H. Skramstad. Measurements of intensity and scale of wind-tunnel turbulence and their relation to the critical Reynolds number of spheres. Technical report, US Government Printing Office, 1937.

P. A. Durbin and B. P. Reif. *Statistical theory and modeling for turbulent flows*. John Wiley & Sons, 2011.

M. Eckert. *The Turbulence Problem: A Persistent Riddle in Historical Perspective*. Springer Nature, 2019.

R. D. Falgout and U. M. Yang. hypre: A library of high performance preconditioners. In *International Conference on computational science*, pages 632–641. Springer, 2002.

J. Friedrich. *Non-perturbative methods in statistical descriptions of turbulence*. Springer, 2021.

M. Gad-el Hak, A. Pollard, and J.-P. Bonnet. *Flow control: fundamentals and practices*, volume 53. Springer Science & Business Media, 2003.

B. Galanti and A. Tsinober. Is turbulence ergodic? *Physics Letters A*, 330(3-4):173–180, 2004.

D. J. Garmann and M. R. Visbal. Interactions of a streamwise-oriented vortex with a finite wing. *Journal of Fluid Mechanics*, 767:782–810, 2015.

D. J. Garmann and M. R. Visbal. Investigation of the unsteady tip vortex structure on a NACA0012 wing at fixed incidence. In *AIAA Paper 2017-1002*, 2017.

M. Gaster. *The structure and behaviour of laminar separation bubbles*. Citeseer, 1967.

M. Gauding, M. Bode, Y. Brahami, É. Varea, and L. Danaila. Self-similarity of turbulent jet flows with internal and external intermittency. *Journal of Fluid Mechanics*, 919:A41, 2021.

M. Germano, U. Piomelli, P. Moin, and W. H. Cabot. A dynamic subgrid-scale eddy viscosity model. *Physics of Fluids A: Fluid Dynamics*, 3(7):1760–1765, 1991.

J. D. Gibbon and D. D. Holm. solutions of the three-dimensional euler and Navier Stokes equations. *Mathematical aspects of fluid mechanics*, 402:201, 2012.

M. Giuni. *Formation and early development of wingtip vortices*. PhD thesis, University of Glasgow, 2013.

G. H. Golub and C. F. Van Loan. *Matrix computations*. JHU press, 2013.

S. Green. *Fluid vortices*, volume 30. Springer, 2012.

J.-L. Guermond, P. Minev, and J. Shen. An overview of projection methods for incompressible flows. *Computer methods in applied mechanics and engineering*, 195(44-47):6011–6045, 2006.

R. Gurka, G. Hetsroni, A. Liberzon, N. Nikitin, and A. Tsinober. On turbulent energy production in wall bounded flows. *Physics of Fluids*, 16(7):2704–2707, 2004.

P. E. Hamlington, J. Schumacher, and W. J. Dahm. Direct assessment of vorticity alignment with local and nonlocal strain rates in turbulent flows. *Physics of Fluids*, 20(11):111703, 2008.

C. W. Hamman, J. C. Klewicki, and R. M. Kirby. On the Lamb vector divergence in Navier–Stokes flows. *Journal of Fluid Mechanics*, 610:261–284, 2008.

K. Hanjalić and B. Launder. *Modelling Turbulence in Engineering and the Environment: Rational Alternative Routes to Closure*. Cambridge University Press, 2022.

K. Hao, A. Tian, and Y. Zhou. Characteristics of small-scale motions in a dual-plane jet flow. *International Journal of Heat and Fluid Flow*, 91:108851, 2021.

W. He, R. d. S. Gioria, J. M. Pérez, and V. Theofilis. Linear instability of low Reynolds number massively separated flow around three NACA airfoils. *Journal of Fluid Mechanics*, 811:701–741, 2017.

E. H. Hirschel, A. Rizzi, C. Breitsamter, and W. Staudacher. *Separated and Vortical Flow in Aircraft Wing Aerodynamics: Basic Principles and Unit Problems*. Springer Nature, 2020.

I. Hosokawa and K. Yamamoto. Intermittency of dissipation in a directly simulated fully-developed turbulence. *Journal of the Physical Society of Japan*, 59(2):401–404, 1990.

J. C. Hunt, O. M. Phillips, and D. Williams. *Turbulence and stochastic processes: Kolmogorov's ideas 50 years on*. Royal Society London, 1991.

K. P. Iyer, K. R. Sreenivasan, and P. Yeung. Nonlinear amplification in hydrodynamic turbulence. *Journal of Fluid Mechanics*, 930:R2, 2022.

L. Jacquin and C. Pantano. On the persistence of trailing vortices. *Journal of Fluid Mechanics*, 471:159–168, 2002.

J. Jeong and F. Hussain. On the identification of a vortex. *Journal of Fluid Mechanics*, 285: 69–94, 1995.

L. Jiang and C. Liu. Parallel DNS for flow separation and transition around airfoil. In *Parallel Computational Fluid Dynamics 2003*, pages 205–212. Elsevier, 2004.

L. Jiang, J. Cai, and C. Liu. Large-eddy simulation of wing tip vortex in the near field. *International Journal of Computational Fluid Dynamics*, 22(5):289–330, 2008.

J. Jiménez, A. A. Wray, P. G. Saffman, and R. S. Rogallo. The structure of intense vorticity in isotropic turbulence. *Journal of Fluid Mechanics*, 255:65–90, 1993.

J. Katz and J. B. Galdo. Effect of roughness on rollup of tip vortices on a rectangular hydrofoil. *Journal of Aircraft*, 26(3):247–253, 1989.

R. M. Kerr. Higher-order derivative correlations and the alignment of small-scale structures in isotropic numerical turbulence. *Journal of Fluid Mechanics*, 153:31–58, 1985.

C. J. Keylock. The schur decomposition of the velocity gradient tensor for turbulent flows. *Journal of Fluid Mechanics*, 848:876–905, 2018. doi: 10.1017/jfm.2018.344.

C. J. Keylock. Studying turbulence structure near the wall in hydrodynamic flows: An approach based on the schur decomposition of the velocity gradient tensor. *Journal of Hydrodynamics*, 34(5):806–825, 2022.

M. Kholmyansky, A. Tsinober, and S. Yorish. Velocity derivatives in the atmospheric surface layer at re {*Lambda*= 10 4. *Physics of Fluids*, 13(1):311–314, 2001.

W. Kollmann. *Navier-Stokes Turbulence*. Springer, 2019.

A. N. Kolmogorov. On the degeneration of isotropic turbulence in an incompressible viscous fluid. In *Dokl. Akad. Nauk SSSR*, volume 31, pages 319–323, 1941a.

A. N. Kolmogorov. The local structure of turbulence in incompressible viscous fluid for very large Reynolds. *Numbers. In Dokl. Akad. Nauk SSSR*, 30:301, 1941b.

A. N. Kolmogorov. A refinement of previous hypotheses concerning the local structure of turbulence in a viscous incompressible fluid at high Reynolds number. *Journal of Fluid Mechanics*, 13(1):82–85, 1962.

A. N. Kolmogorov. Dissipation of energy in the locally isotropic turbulence. *Proceedings of the Royal Society of London. Series A: Mathematical and Physical Sciences*, 434(1890):15–17, 1991a.

A. N. Kolmogorov. The local structure of turbulence in incompressible viscous fluid for very large Reynolds numbers. *Proceedings of the Royal Society of London. Series A: Mathematical and Physical Sciences*, 434(1890):9–13, 1991b.

W. M. Lai, D. Rubin, and E. Krempl. *Introduction to continuum mechanics*. Butterworth-Heinemann, 2009.

S. Laizet, J. Vassilicos, and C. Cambon. Interscale energy transfer in decaying turbulence and vorticity–strain-rate dynamics in grid-generated turbulence. *Fluid Dynamics Research*, 45 (6):061408, 2013.

S. Laizet, J. Nedić, and C. Vassilicos. Influence of the spatial resolution on fine-scale features in dns of turbulence generated by a single square grid. *International Journal of Computational Fluid Dynamics*, 29(3-5):286–302, 2015.

M. Leschziner. Modelling turbulent separated flow in the context of aerodynamic applications. *Fluid dynamics research*, 38(2-3):174–210, 2006.

T. Leung, N. Swaminathan, and P. Davidson. Geometry and interaction of structures in homogeneous isotropic turbulence. *Journal of Fluid Mechanics*, 710:453–481, 2012.

E. Levich. Certain problems in the theory of developed hydrodynamical turbulence. *Physics Reports*, 151(3-4):129–238, 1987.

T. Leweke, S. Le Dizes, and C. H. Williamson. Dynamics and instabilities of vortex pairs. *Annual Review of Fluid Mechanics*, 48:507–541, 2016.

Y. Li, E. Perlman, M. Wan, Y. Yang, C. Meneveau, R. Burns, S. Chen, A. Szalay, and G. Eyink. A public turbulence database cluster and applications to study lagrangian evolution of velocity increments in turbulence. *Journal of Turbulence*, (9):N31, 2008.

A. Liberzon, B. Lüthi, M. Guala, W. Kinzelbach, and A. Tsinober. Experimental study of the structure of flow regions with negative turbulent kinetic energy production in confined three-dimensional shear flows with and without buoyancy. *Physics of Fluids*, 17(9):095110, 2005.

J.-E. W. Lombard, D. Moxey, S. J. Sherwin, J. F. Hoessler, S. Dhandapani, and M. J. Taylor. Implicit Large Eddy Simulation of a wingtip vortex. *AIAA Journal*, 54(2):506–518, 2016.

T. S. Lund and E. Novikov. Parameterization of subgrid-scale stress by the velocity gradient tensor. *Annual Research Briefs, 1992*, 1993.

C. R. Maliska. *Fundamentals of Computational Fluid Dynamics: The Finite Volume Method*, volume 135. Springer Nature, 2023.

H. Marmanis. Analogy between the Navier–Stokes equations and maxwell's equations: Application to turbulence. *Physics of fluids*, 10(6):1428–1437, 1998.

C. Marongiu and R. Tognaccini. Far-field analysis of the aerodynamic force by Lamb vector integrals. *AIAA journal*, 48(11):2543–2555, 2010.

C. Marongiu, R. Tognaccini, and M. Ueno. Lift and lift-induced drag computation by Lamb vector integration. *AIAA journal*, 51(6):1420–1430, 2013.

J. Martın, A. Ooi, M. S. Chong, and J. Soria. Dynamics of the velocity gradient tensor invariants in isotropic turbulence. *Physics of Fluids*, 10(9):2336–2346, 1998.

R. McKeown, R. Ostilla-Mónico, A. Pumir, M. P. Brenner, and S. M. Rubinstein. Cascade leading to the emergence of small structures in vortex ring collisions. *Physical Review Fluids*, 3(12):124702, 2018.

B. Mele and R. Tognaccini. Aerodynamic force by Lamb vector integrals in compressible flow. *Physics of Fluids*, 26(5), 2014.

C. Meneveau. Lagrangian dynamics and models of the velocity gradient tensor in turbulent flows. *Annual Review of Fluid Mechanics*, 43(1):219–245, 2011.

METIS. Metis - serial graph partitioning and fill-reducing matrix ordering. `https://http://glaros.dtc.umn.edu/gkhome/metis/metis/overview`, 2024. Accessed: 2024.

P. Meunier, S. Le Dizes, and T. Leweke. Physics of vortex merging. *Comptes Rendus Physique*, 6(4-5):431–450, 2005.

K. Mikhaylov, S. Rigopoulos, and G. Papadakis. Reconstruction of large-scale flow structures in a stirred tank from limited sensor data. *AIChE Journal*, page e17348, 2021.

L. M. Milne-Thomson. *Theoretical Arodynamics*. Dover Publications, New York, US, 1958.

H. Moffatt. Fixed points of turbulent dynamical systems and suppression of nonlinearity comment 1. In *Whither Turbulence? Turbulence at the Crossroads: Proceedings of a Workshop Held at Cornell University, Ithaca, NY, March 22–24, 1989*, pages 250–257. Springer, 2005.

O. S. Mohamed, A. A. Ibrahim, A. K. Etman, A. A. Abdelfatah, and A. M. Elbaz. Numerical investigation of Darrieus wind turbine with slotted airfoil blades. *Energy Conversion and Management: X*, 5:100026, 2020.

S. Monin, Andrei and A. M. Yaglom. *Statistical fluid mechanics, volume II: mechanics of turbulence*, volume 2. Courier Corporation, 2013.

J. A. Mullin and W. J. Dahm. Dual-plane stereo particle image velocimetry measurements of velocity gradient tensor fields in turbulent shear flow. i. accuracy assessments. *Physics of Fluids*, 18(3), 2006.

NASA. ARMD urban air mobility grand challenge uam grand challenge scenarios. `https://evtol.news/__media/PDFs/eVTOL-NASA-Revised_UAM_Grand_Challenge_Scenarios.pdf`, 2018. Accessed: 2024.

J. M. Neal and M. Amitay. Three-dimensional separation over unswept cantilevered wings at a moderate Reynolds number. *Physical Review Fluids*, 8(1):014703, 2023.

R. Ni, N. T. Ouellette, and G. A. Voth. Alignment of vorticity and rods with lagrangian fluid stretching in turbulence. *Journal of Fluid Mechanics*, 743:R3, 2014.

F. Nicoud and F. Ducros. Subgrid-scale stress modelling based on the square of the velocity gradient tensor. *Flow, turbulence and Combustion*, 62(3):183–200, 1999.

F. Novak and T. Sarpkaya. Turbulent vortex breakdown at high Reynolds numbers. *AIAA Journal*, 38(5):825–834, 2000.

K. Ohkitani and S. Kishiba. Nonlocal nature of vortex stretching in an inviscid fluid. *Physics of Fluids*, 7(2):411–421, 1995.

M. O'Meara and T. J. Mueller. Laminar separation bubble characteristics on an airfoil at low Reynolds numbers. *AIAA journal*, 25(8):1033–1041, 1987.

A. Ooi, J. Martin, J. Soria, and M. S. Chong. A study of the evolution and characteristics of the invariants of the velocity-gradient tensor in isotropic turbulence. *Journal of Fluid Mechanics*, 381:141–174, 1999.

G. Papadakis. Implementation of fractional step method in code pantarhei. Technical report, Imperial College London, 2019.

I. Paul. *Evolution of velocity and scalar gradients in a spatially developing turbulence*. PhD thesis, Imperial College London, 2017.

I. Paul, G. Papadakis, and J. Vassilicos. Genesis and evolution of velocity gradients in near-field spatially developing turbulence. *Journal of Fluid Mechanics*, 815:295–332, 2017.

B. Pearson and R. Antonia. Reynolds-number dependence of turbulent velocity and pressure increments. *Journal of Fluid Mechanics*, 444:343–382, 2001.

A. Perry and M. Chong. Topology of flow patterns in vortex motions and turbulence. *Applied Scientific Research*, 53:357–374, 1994.

A. E. Perry and M. S. Chong. A description of eddying motions and flow patterns using critical-point concepts. *Annual review of fluid mechanics*, 19(1):125–155, 1987.

W. Phillips. The turbulent trailing vortex during roll-up. *Journal of Fluid Mechanics*, 105 (451), 1981.

U. Piomelli and E. Balaras. Wall-layer models for large-eddy simulations. *Annual Review of Fluid Mechanics*, 34(1):349–374, 2002.

S. B. Pope. *Turbulent flows*. Cambridge university press, 2000.

F. A. Portela. *Turbulence Cascade in an Inhomogeneous Turbulent Flow.* PhD thesis, Imperial College London, 2017.

C. M. Rhie and W.-L. Chow. Numerical study of the turbulent flow past an airfoil with trailing edge separation. *AIAA journal*, 21(11):1525–1532, 1983.

L. F. Richardson. *Weather prediction by numerical process.* University Press, 1922.

V. J. Rossow. Lift-generated vortex wakes of subsonic transport aircraft. *Progress in Aerospace Sciences*, 35(6):507–660, 1999.

M. E. Rosti, M. Omidyeganeh, and A. Pinelli. Direct numerical simulation of the flow around an aerofoil in ramp-up motion. *Physics of Fluids*, 28(2):025106, 2016.

J. Rotta. Turbulent boundary layers in incompressible flow. *Progress in aerospace sciences*, 2 (1):1–95, 1962.

G. Rousseaux, S. Seifer, V. Steinberg, and A. Wiebel. On the Lamb vector and the hydrodynamic charge. *Experiments in fluids*, 42:291–299, 2007.

G. Ruetsch and M. Maxey. Small-scale features of vorticity and passive scalar fields in homogeneous isotropic turbulence. *Physics of Fluids A: Fluid Dynamics*, 3(6):1587–1597, 1991.

S. G. Saddoughi and S. V. Veeravalli. Local isotropy in turbulent boundary layers at high Reynolds number. *Journal of Fluid Mechanics*, 268:333–372, 1994.

P. Sagaut and C. Cambon. *Homogeneous turbulence dynamics*, volume 10. Springer, 2008.

N. Sandham. Transitional separation bubbles and unsteady aspects of aerofoil stall. *The Aeronautical Journal*, 112(1133):395–404, 2008.

R. K. Schlander. *Study of turbulent pipe flows laden with low-inertia particles using proper orthogonal decomposition and resolvent analysis.* PhD thesis, Imperial College London, 2023.

R. K. Schlander, S. Rigopoulos, and G. Papadakis. Analysis of wall mass transfer in turbulent pipe flow combining extended proper orthogonal decomposition and Fukugata-Iwamoto-Kasagi identity. *Phys. Rev. Fluids*, 7:024603, Feb 2022.

J. R. Schott. *Matrix analysis for statistics.* John Wiley & Sons, 2016.

J. Schumacher, K. R. Sreenivasan, and V. Yakhot. Asymptotic exponents from low-Reynolds-number flows. *New Journal of Physics*, 9(4):89, 2007.

H. Shan, L. Jiang, and C. Liu. Direct numerical simulation of flow separation around a NACA 0012 airfoil. *Computers & Fluids*, 34(9):1096–1114, 2005.

Z.-S. She, E. Jackson, and S. A. Orszag. Structure and dynamics of homogeneous turbulence: models and simulations. *Proceedings of the Royal Society of London. Series A: Mathematical and Physical Sciences*, 434(1890):101–124, 1991.

L. Shtilman. On the solenoidality of the Lamb vector. *Physics of Fluids A: Fluid Dynamics*, 4 (1):197–199, 1992.

E. D. Siggia. Numerical study of small-scale intermittency in three-dimensional turbulence. *Journal of Fluid Mechanics*, 107:375–406, 1981.

T. Smith and Y. Ventikos. Wing-tip vortex dynamics at moderate Reynolds numbers. *Physics of Fluids*, 33(3):035111, 2021.

J. Soria, R. Sondergaard, B. Cantwell, M. Chong, and A. Perry. A study of the fine-scale motions of incompressible time-developing mixing layers. *Physics of Fluids*, 6(2):871–884, 1994.

P. R. Spalart. Airplane trailing vortices. *Annual Review of Fluid Mechanics*, 30(1):107–138, 1998.

C. G. Speziale. Icase report no. 87-69. 1987.

K. R. Sreenivasan and R. Antonia. The phenomenology of small-scale turbulence. *Annual review of fluid mechanics*, 29(1):435–472, 1997.

M. Stanisic. *The mathematical theory of turbulence*. Springer Science & Business Media, 2012.

G. W. Stewart. *Matrix Algorithms: Volume II: Eigensystems*. SIAM, 2001.

K. Taira and T. Colonius. Effect of tip vortices in low-Reynolds-number poststall flow control. *AIAA Journal*, 47(3):749–756, 2009a.

K. Taira and T. Colonius. Three-dimensional flows around low-aspect-ratio flat-plate wings at low Reynolds numbers. *Journal of Fluid Mechanics*, 623:187–207, 2009b.

G. Taylor. The statistical theory of isotropic turbulence. *Journal of the Aeronautical Sciences*, 4(8):311–315, 1937.

G. I. Taylor. Statistical theory of turbulenc. *Proceedings of the Royal Society of London. Series A-Mathematical and Physical Sciences*, 151(873):421–444, 1935.

H. Tennekes and J. L. Lumley. *A first course in turbulence*. MIT press, 2018.

H. Tennekes, J. L. Lumley, J. L. Lumley, et al. *A first course in turbulence*. MIT press, 1972.

N. Thomareis and G. Papadakis. Effect of trailing edge shape on the separated flow characteristics around an airfoil at low Reynolds number: A numerical study. *Physics of Fluids*, 29 (1), 2017.

N. Thomareis and G. Papadakis. Resolvent analysis of separated and attached flows around an airfoil at transitional Reynolds number. *Phys. Rev. Fluids*, 3:073901, Jul 2018.

W. Timmer. Two-dimensional low-Reynolds number wind tunnel results for airfoil NACA 0018. *Wind engineering*, 32(6):525–537, 2008.

M. Tobak and D. J. Peake. Topology of three-dimensional separated flows. *Annual review of fluid mechanics*, 14(1):61–85, 1982.

W. Tollmien, H. Schlichting, H. Görtler, W. Tollmien, H. Schlichting, H. Görtler, and F. Riegels. Applications of modern hydrodynamics to aeronautics. *Ludwig Prandtl Gesammelte Abhandlungen: zur angewandten Mechanik, Hydro-und Aerodynamik*, pages 433–515, 1961.

F. Tong, Z. Tang, C. Yu, X. Zhu, and X. Li. Numerical analysis of shock wave and supersonic turbulent boundary interaction between adiabatic and cold walls. *Journal of Turbulence*, 18 (6):569–588, 2017.

TOP500. Top500. `https://https://www.top500.org/system/180036/`, 2024. Accessed: 2024.

A. Townsend. The fully developed wake of a circular cylinder. *Australian Journal of Chemistry*, 2(4):451–468, 1949.

C. Truesdell. *The kinematics of vorticity*. Indiana University Press, 1954.

M. Tsagkaridis. *Population Balance Modelling of Nanoparticle Formation in Laminar and Turbulent Flows*. PhD thesis, Imperial College London, 2022.

A. Tsinober. On one property of Lamb vector in isotropic turbulent flow. *Physics of Fluids A: Fluid Dynamics*, 2(4):484–486, 1990.

A. Tsinober. Is concentrated vorticity that important? *European Journal of Mechanics-B/Fluids*, 17(4):421–449, 1998.

A. Tsinober. Vortex stretching versus production of strain/dissipation. *Turbulence structure and vortex dynamics*, 164:191, 2000.

A. Tsinober. *An informal conceptual introduction to turbulence*. Springer, 2009.

A. Tsinober, E. Kit, and T. Dracos. Experimental investigation of the field of velocity gradients in turbulent flows. *Journal of Fluid Mechanics*, 242:169–192, 1992.

P. Tucker. Computation of unsteady turbomachinery flows: Part 1—progress and challenges. *Progress in Aerospace Sciences*, 47(7):522–545, 2011.

USCG. United states coast guard. `https://theaviationist.com/2012/06/20/uscg-c130/`, 2012. Accessed: 2024.

A. Uzun and M. Y. Hussaini. Simulations of vortex formation around a blunt wing tip. *AIAA Journal*, 48(6):1221–1234, 2010.

P. Vieillefosse. Internal motion of a small element of fluid in an inviscid flow. *Physica A: Statistical Mechanics and its Applications*, 125(1):150–162, 1984.

A. Vincent and M. Meneguzzi. The spatial structure and statistical properties of homogeneous turbulence. *Journal of Fluid Mechanics*, 225:1–20, 1991.

M. R. Visbal. Unsteady flow structure and loading of a pitching low-aspect-ratio wing. *Physical Review Fluids*, 2(2):024703, 2017.

C. Vourtsis, V. C. Rochel, N. S. Müller, W. Stewart, and D. Floreano. Wind defiant morphing drones. *Advanced Intelligent Systems*, 5(3):2200297, 2023.

A. Vulpiani and R. Livi. *The Kolmogorov legacy in physics*, volume 636. Springer, 2003.

C. Wang. Exact solutions of the steady-state Navier-Stokes equations. *Annual Review of Fluid Mechanics*, 23(1):159–177, 1991.

D. C. Wilcox et al. *Turbulence modeling for CFD*, volume 2. DCW industries La Canada, CA, 1998.

M. Wilczek and C. Meneveau. Pressure Hessian and viscous contributions to velocity gradient statistics based on gaussian random fields. *Journal of Fluid Mechanics*, 756:191–225, 2014.

E. Wood-Bowyer, A. West, J. Ho Mun Onn, and C. Cantwell. Large eddy simulation of wingtip vortex evolution in an adverse pressure gradient. In *AIAA Scitech 2021 Forum*, page 1940, 2021.

J. Wu, L. Liu, and T. Liu. Fundamental theories of aerodynamic force in viscous and compressible complex flows. *Progress in Aerospace Sciences*, 99:27–63, 2018.

J.-Z. Wu, Y. Zhou, X.-Y. Lu, and M. Fan. Turbulent force as a diffusive field with vortical sources. *Physics of Fluids*, 11(3):627–635, 1999.

J.-Z. Wu, H.-Y. Ma, and M.-D. Zhou. *Vortical flows*, volume 28. Springer, 2015.

Z. Wu and Y. Zhang. Integrated network design and demand forecast for on-demand urban air mobility. *Engineering*, 7(4):473–487, 2021.

D. Xiao. *Nonlinear optimal control of bypass transition in a flat plate boundary layer*. PhD thesis, Imperial College London, 2017.

D. Xiao and G. Papadakis. Nonlinear optimal control of transition due to a pair of vortical perturbations using a receding horizon approach. *Journal of Fluid Mechanics*, 861:524–555, 2019.

C.-Y. Xu, B. Wang, H. Liu, Y. Men, and J.-H. Sun. Large-eddy simulation of the compressible flows around a wavy-axis square cylinder. *Physics of Fluids*, 34(8), 2022.

D. Xu, J. Wang, M. Wan, C. Yu, X. Li, and S. Chen. Effect of wall temperature on the kinetic energy transfer in a hypersonic turbulent boundary layer. *Journal of Fluid Mechanics*, 929: A33, 2021.

P.-F. Yang, Z. Zhou, H. Xu, and G. He. Strain self-amplification is larger than vortex stretching due to an invariant relation of filtered velocity gradients. *Journal of Fluid Mechanics*, 955: A15, 2023.

V. E. Yanitskii. Transport equation for the deformation-rate tensor and description of an ideal incompressible liquid by a system of equations of the dynamical type. *Doklady Akademii Nauk*, 266(2):305–308, 1982.

H. Yao, J.-P. Mollicone, and G. Papadakis. Analysis of interscale energy transfer in a boundary layer undergoing bypass transition. *Journal of Fluid Mechanics*, 941:A14, 2022. doi: 10.1017/jfm.2022.285.

P. Yeung, X. Zhai, and K. R. Sreenivasan. Extreme events in computational turbulence. *Proceedings of the National Academy of Sciences*, 112(41):12633–12638, 2015.

P.-K. Yeung and S. B. Pope. Lagrangian statistics from direct numerical simulations of isotropic turbulence. *Journal of Fluid Mechanics*, 207:531–586, 1989.

S. Young, E. Ancel, A. Moore, E. Dill, C. Quach, J. Foster, K. Darafsheh, K. Smalling, S. Vazquez, E. T. Evans, et al. Architecture and information requirements to assess and predict flight safety risks during highly autonomous urban flight operations. 2020.

A. Yu, L. Li, D. Zhou, and J. Ji. Large eddy simulation of the pulsation characteristics in the cavitating flow around a NACA 0015 hydrofoil. *Ocean Engineering*, 267:113289, 2023.

J.-L. Yu and X.-Y. Lu. Subgrid effects on the filtered velocity gradient dynamics in compressible turbulence. *Journal of Fluid Mechanics*, 892, 2020.

J.-L. Yu, Z. Zhao, and X.-Y. Lu. Non-normal effect of the velocity gradient tensor and the relevant subgrid-scale model in compressible turbulent boundary layer. *Physics of Fluids*, 33 (2):025103, 2021.

O. Zeman. The persistence of trailing vortices: a modeling study. *Physics of Fluids*, 7(1): 135–143, 1995.

K. Zhang, S. Hayostek, M. Amitay, A. Burtsev, V. Theofilis, and K. Taira. Laminar separated flows over finite-aspect-ratio swept wings. *Journal of Fluid Mechanics*, 905, 2020a.

K. Zhang, S. Hayostek, M. Amitay, W. He, V. Theofilis, and K. Taira. On the formation of three-dimensional separated flows over wings under tip effects. *Journal of Fluid Mechanics*, 895, 2020b.

Q. Zhang, C. Gao, F. Zhou, D. Yang, and W. Zhang. Study on flow noise characteristic of transonic deep buffeting over an airfoil. *Physics of Fluids*, 35(4), 2023a.

Q. Zhang, H. Ma, Z. Xie, and Z. Wang. Manipulating near-wall flow instability and transport characteristics by the airfoil probe: Investigation on a transonic compressor cascade. *Physics of Fluids*, 35(8), 2023b.

W. Zhang and R. Samtaney. A direct numerical simulation investigation of the synthetic jet frequency effects on separation control of low-re flow past an airfoil. *Physics of Fluids*, 27 (5):055101, 2015.

W. Zhang, W. Cheng, W. Gao, A. Qamar, and R. Samtaney. Geometrical effects on the airfoil flow separation and transition. *Computers & Fluids*, 116:60–73, 2015.

Y. Zhou, K. Nagata, Y. Sakai, H. Suzuki, Y. Ito, O. Terashima, and T. Hayase. Development of turbulence behind the single square grid. *Physics of Fluids*, 26(4):045102, 2014a.

Y. Zhou, K. Nagata, Y. Sakai, H. Suzuki, Y. Ito, O. Terashima, and T. Hayase. Relevance of turbulence behind the single square grid to turbulence generated by regular-and multiscale-grids. *Physics of Fluids*, 26(7):075105, 2014b.

Y. Zhou, K. Nagata, Y. Sakai, Y. Ito, and T. Hayase. On the evolution of the invariants of the velocity gradient tensor in single-square-grid-generated turbulence. *Physics of Fluids*, 27(7): 075107, 2015.

Y. Zhou, K. Nagata, Y. Sakai, Y. Ito, and T. Hayase. Enstrophy production and dissipation in developing grid-generated turbulence. *Physics of Fluids*, 28(2):025113, 2016a.

Y. Zhou, K. Nagata, Y. Sakai, Y. Ito, and T. Hayase. Spatial evolution of the helical behavior and the 2/3 power-law in single-square-grid-generated turbulence. *Fluid Dynamics Research*, 48(2):021404, 2016b.

Z. Zhou, G. He, S. Wang, and G. Jin. Subgrid-scale model for large-eddy simulation of isotropic turbulent flows using an artificial neural network. *Computers & Fluids*, 195:104319, 2019.

Appendix A

Derivation of transport equation of $\langle s_{ij}s_{ij}\rangle$ from the NSE

The mean total strain of turbulent fluctuations $\frac{1}{2}\frac{\partial\langle s_{ij}s_{ij}\rangle}{\partial t}$ has been presented in its full form in the books of [Tsinober, 2009] and in some recent papers involving the study of VGT [Paul et al., 2017]. Besides the introduction of strain evolution equation by [Yanitskii, 1982] in a paper only available in Russian, there are no available derivations available in the literature related to the fluctuating mean total strain of turbulent fluctuations. Understanding the impact of terms in the transport equation can be facilitated by tracing their origins back to the NSE. The NSE for incompressible flows ($\nabla \cdot Ui = 0$ and $\rho = const.$) is given as follows

$$\frac{DU_i}{Dt} = \frac{\partial U_i}{\partial t} + U_k\frac{\partial(U_i)}{\partial x_k} = -\frac{1}{\rho}\frac{\partial P}{\partial x_i} + \nu\frac{\partial^2 U_i}{\partial x_k^2}\,, \tag{A.1}$$

by taking the partial derivative ∂x_j of equation A.1 and incorporating $\frac{\partial U_i}{\partial x_j} = S_{ij} + \Omega_{ij}$, we obtain the following equation by selecting the symmetric parts of the equation

$$\frac{DS_{ij}}{Dt} = -S_{ik}S_{kj} - \Omega_{ik}\Omega_{ik} - \frac{\partial^2 P}{\partial x_i \partial x_j} + \nu\frac{\partial^2 S_{ij}}{\partial x_j^2}\,, \tag{A.2}$$

where $\Omega_{ik} = -\frac{1}{2}\epsilon_{ijk}\omega_k$. Following the general identity $\epsilon_{ijm}\epsilon_{klm} = \delta_{ik}\delta_{jl} - \delta_{il}\delta_{jk}$ [Lai et al., 2009] we can get $\Omega_{ik}\Omega_{kj} = \frac{1}{4}(\omega_i\omega_j - \omega^2\delta_{ij})$, obtaining

$$\frac{DS_{ij}}{Dt} = -S_{ik}S_{kj} - \frac{1}{4}(\omega_i\omega_j - \omega^2\delta_{ij}) - \frac{\partial^2 P}{\partial x_i \partial x_j} + \nu\frac{\partial^2 S_{ij}}{\partial x_j^2}\,. \tag{A.3}$$

Considering the material derivative components $\frac{DS_{ij}}{Dt} = \frac{\partial S_{ij}}{\partial t} + \frac{\partial(U_k S_{ij})}{\partial x_k}$. It is important to note

that when the term $\omega^2\delta_{ij}$ gets multiplied by S_{ij}, the resulting expression will vanish as a result of $\delta_{ij}S_{ij} = 0$. For this reason we will omit the term $\omega^2\delta_{ij}$ in the next steps.

Once we reach this stage, we will proceed by subtracting the terms of the mean strain equation in Reynolds decomposed form $\frac{D\langle\langle S\rangle+s\rangle}{Dt}$, from the non-averaged Reynolds decomposed equation $\frac{D(\langle S\rangle+s)}{Dt}$ (see A.4). By performing this subtraction, we will be able to obtain the transport equation for the fluctuating strain $\frac{Ds}{Dt}$. The resulting expression will be then multiplied by s and averaged to achieve the mean total strain product of the turbulent fluctuations $\frac{1}{2}\frac{D\langle s^2\rangle}{Dt}$. To illustrate the aforementioned derivation process we will begin by employing substantial derivatives as follows

$$\left\langle \left(\frac{D(\langle S\rangle + s)}{Dt} - \frac{D\langle\langle S\rangle + s\rangle}{Dt} \right) \cdot s \right\rangle = 0 \tag{A.4}$$

$$\left\langle \left(\frac{D\langle S\rangle}{Dt} + \frac{Ds}{Dt} - \frac{D\langle S\rangle}{Dt} + \underbrace{\frac{D\langle s\rangle}{Dt}}_{0} \right) \cdot s \right\rangle = 0\,, \tag{A.5}$$

where $\frac{D\langle s\rangle}{Dt} = 0$ and the mean terms cancel each other out leaving

$$\left\langle \frac{Ds}{Dt} \cdot s \right\rangle = \frac{1}{2}\frac{D\left\langle s^2\right\rangle}{Dt}\,. \tag{A.6}$$

Keeping this in consideration in analogy with (A.4), we proceed first with the Reynolds decomposition of (A.3) in the form of $S = \langle S\rangle + s$ resulting in

$$\begin{aligned} \frac{D\langle S_{ij}\rangle}{Dt} + \frac{Ds_{ij}}{Dt} = \frac{\partial\langle S_{ij}\rangle}{\partial t} + \frac{\partial s_{ij}}{\partial t} + \frac{\partial}{\partial x_k}(\langle U_k\rangle + u_k)(\langle S_{ij}\rangle + s_{ij}) \\ \frac{\partial\langle S_{ij}\rangle + s_{ij}}{\partial t} + \frac{\partial(\langle U_k\rangle\langle S_{ij}\rangle)}{\partial x_k} + \frac{\partial(\langle U_k\rangle s_{ij})}{\partial x_k} + \frac{\partial(u_k\langle S_{ij}\rangle)}{\partial x_k} + \frac{\partial(u_k s_{ij})}{\partial x_k}\,. \end{aligned} \tag{A.7}$$

This expression is analogous to the following expression that includes now the RH terms of

equation (A.3).

$$\begin{aligned}\frac{\partial\langle S_{ij}\rangle}{\partial t}+\frac{\partial s_{ij}}{\partial t}+\frac{\partial}{\partial x_k}(\langle U_k\rangle+u_k)(\langle S_{ij}\rangle+s_{ij}) = & -(\langle S_{ik}\rangle+s_{ik})(\langle S_{kj}\rangle+s_{kj}) \\ & -\frac{1}{4}\{(\langle\Omega_i\rangle+\omega_i)(\langle\Omega_j\rangle+\omega_j)\} \\ & -\left(\frac{\partial^2\langle P\rangle}{\partial x_i\partial x_j}+\frac{\partial^2 p}{\partial x_i\partial x_j}\right)+\left(\nu\frac{\partial^2\langle S_{ij}\rangle}{\partial x_k^2}+\nu\frac{\partial^2 s_{ij}}{\partial x_k^2}\right),\end{aligned} \tag{A.8}$$

expanding the equation

$$\begin{aligned}\frac{\partial\langle S_{ij}\rangle}{\partial t}+\frac{\partial s_{ij}}{\partial t}+\frac{\partial}{\partial x_k}(\langle U_k\rangle+u_k)(\langle S_{ij}\rangle+s_{ij}) = & -(\langle S_{ik}\rangle\langle S_{ik}\rangle+\langle S_{ik}\rangle s_{kj}+s_{ik}\langle S_{kj}\rangle+s_{ik}s_{kj}) \\ & -\frac{1}{4}\{(\langle\Omega_i\rangle\langle\Omega_j\rangle+\langle\Omega_i\rangle\omega_j+\omega_i\langle\Omega_j\rangle+\omega_i\omega_j)\} \\ & -\left(\frac{\partial^2\langle P\rangle}{\partial x_i\partial x_j}+\frac{\partial^2 p}{\partial x_i\partial x_j}\right)+\left(\nu\frac{\partial^2\langle S_{ij}\rangle}{\partial x_k^2}+\nu\frac{\partial^2 s_{ij}}{\partial x_k^2}\right),\end{aligned} \tag{A.9}$$

we take the mean of equation (A.9) using $\langle s_{ij}\rangle = 0$ resulting in the mean strain equation $\frac{D\langle S\rangle}{Dt}$,

$$\begin{aligned}\frac{\partial\langle S_{ij}\rangle}{\partial t}+\frac{\partial(\langle U_k\rangle\langle S_{ij}\rangle)}{\partial x_k}+\frac{\partial\langle u_k s_{ij}\rangle}{\partial x_k} = & -\langle S_{jk}\rangle\langle S_{ki}\rangle-\langle s_{ik}s_{kj}\rangle-\frac{1}{4}\{\langle\omega_i\omega_j\rangle+(\Omega_i\Omega_j)\} \\ & -\frac{\partial^2\langle P\rangle}{\partial x_i\partial x_j}+\nu\frac{\partial^2\langle S_{ij}\rangle}{\partial x_k^2}.\end{aligned} \tag{A.10}$$

We now substract the terms of the mean strain equation $\frac{D\langle S\rangle}{Dt}$ from the strain equation (A.10) in Reynolds decomposed form $\frac{D(\langle S\rangle+s)}{Dt}$ (A.9). Considering $S-\langle S\rangle = s$ and the symmetric properties of $s_{ij} = s_{ji}$. We rest the respective material derivatives and perform Reynolds decomposition $\frac{\partial}{\partial x_k}[(U_k S_{ij})-\langle U_k S_{ij}\rangle]$

$$
\begin{aligned}
\frac{\partial}{\partial x_k}[(U_k S_{ij}) - \langle U_k S_{ij}\rangle] &= \frac{\partial}{\partial x_k}((\langle U_k\rangle + u_k)(\langle S_{ij}\rangle + s_{ij}) - \langle(\langle U_k\rangle + u_k)(\langle S_{ij}\rangle + s_{ij})\rangle) \\
&= \frac{\partial(\langle U_k\rangle\langle S_{ij}\rangle)}{\partial x_k} + \frac{\partial(\langle U_k\rangle s_{ij})}{\partial x_k} + \frac{\partial(u_k\langle S_{ij}\rangle)}{\partial x_k} + \frac{\partial(u_k s_{ij})}{\partial x_k} \\
&\quad - \frac{\partial(\langle U_k\rangle\langle S_{ij}\rangle)}{\partial x_k} - \frac{\partial\langle u_k s_{ij}\rangle}{\partial x_k} \\
&= \frac{\partial(\langle U_{kij})}{\partial x_k} + \frac{\partial(u_k\langle S_{ij}\rangle)}{\partial x_k} + \frac{\partial(u_k s_{ij})}{\partial x_k} - \frac{\partial\langle u_k s_{ij}\rangle}{\partial x_k}\,.
\end{aligned}
\tag{A.11}
$$

We obtain the following expression

$$
\begin{aligned}
\frac{\partial s_{ij}}{\partial t} = &- \frac{\partial(\langle U_k\rangle s_{ij})}{\partial x_k} - \frac{\partial(u_k\langle S_{ij}\rangle)}{\partial x_k} - \frac{\partial(u_k s_{ij})}{\partial x_k} + \frac{\partial\langle u_k s_{ij}\rangle}{\partial x_k} \\
&- 2s_{ik}\langle S_{kj}\rangle - s_{ik}s_{kj} + \langle s_{ik}s_{kj}\rangle - \frac{1}{4}\omega_i\omega_j + \frac{1}{4}\langle\omega_i\omega_j\rangle \\
&+ \frac{1}{2}\omega_i\langle\Omega_j\rangle - \frac{\partial^2 p}{\partial x_i\partial x_j} + \nu\nabla^2 s_{ij}\,,
\end{aligned}
\tag{A.12}
$$

we then multiply by s_{ij}

$$
\begin{aligned}
\frac{\partial s_{ij}}{\partial t}s_{ij} = &- \frac{\partial(\langle U_k\rangle s_{ij})}{\partial x_k}s_{ij} - \frac{\partial(u_k\langle S_{ij}\rangle)}{\partial x_k}s_{ij} - \frac{\partial(u_k s_{ij})}{\partial x_k}s_{ij} + \frac{\partial\langle u_k s_{ij}\rangle}{\partial x_k}s_{ij} \\
&- 2s_{ij}s_{ik}\langle S_{kj}\rangle - s_{ij}s_{ik}s_{kj} + s_{ij}\langle s_{ik}s_{kj}\rangle - \frac{1}{4}\omega_i\omega_j s_{ij} + \frac{1}{4}\langle\omega_i\omega_j\rangle s_{ij} \\
&+ \frac{1}{2}\omega_i s_{ij}\langle\Omega_j\rangle - s_{ij}\frac{\partial^2 p}{\partial x_i\partial x_j} + \nu s_{ij}\nabla^2 s_{ij}\,,
\end{aligned}
\tag{A.13}
$$

we take the mean of equation A.13 and eliminate the terms of type $\langle s_{ij}\langle s_{ik}s_{kj}\rangle\rangle = 0$, obtaining

$$
\begin{aligned}
\langle\frac{\partial s_{ij}}{\partial t}s_{ij}\rangle = &- \left\langle\frac{\partial(\langle U_k\rangle s_{ij})}{\partial x_k}s_{ij}\right\rangle - \left\langle\frac{\partial(u_k\langle S_{ij}\rangle)}{\partial x_k}s_{ij}\right\rangle - \left\langle\frac{\partial(u_k s_{ij})}{\partial x_k}s_{ij}\right\rangle \\
&- \langle 2s_{ij}s_{ik}\langle S_{kj}\rangle - \langle s_{ij}s_{ik}s_{kj}\rangle - \frac{1}{4}\langle\omega_i\omega_j s_{ij}\rangle \\
&+ \frac{1}{2}\langle\omega_i s_{ij}\langle\Omega_j\rangle\rangle - \left\langle s_{ij}\frac{\partial^2 p}{\partial x_i\partial x_j}\right\rangle + \nu\langle s_{ij}\nabla^2 s_{ij}\rangle\,.
\end{aligned}
\tag{A.14}
$$

By rearranging the terms considering the following identities $\left\langle\frac{\partial(\langle U_k\rangle s_{ij})}{\partial x_k}s_{ij}\right\rangle = \langle U_k\rangle\frac{\partial}{\partial x_k}\frac{1}{2}\langle s_{ij}s_{ij}\rangle$, $\left\langle\frac{\partial(u_k s_{ij})}{\partial x_k}s_{ij}\right\rangle = \frac{1}{2}\frac{\partial}{\partial x_k}\{\langle u_k s_{ij}s_{ij}\rangle\}$, we can finally simplify the expression to obtain the familiar

form,

$$\begin{aligned}\frac{1}{2}\frac{\partial\langle s_{ij}s_{ij}\rangle}{\partial t} = & -\langle U_k\rangle\frac{\partial}{\partial x_k}\frac{1}{2}\langle s_{ij}s_{ij}\rangle - \langle u_k s_{ij}\rangle\frac{\partial\langle S_{ij}\rangle}{\partial x_k} - \frac{1}{2}\frac{\partial}{\partial x_k}\{\langle u_k s_{ij}s_{ij}\rangle\} \\ & - 2\langle s_{ij}s_{ik}\rangle\langle S_{kj}\rangle + \frac{1}{2}\langle\omega_i s_{ij}\rangle\langle\Omega_j\rangle - \langle s_{ij}s_{jk}s_{ki}\rangle - \frac{1}{4}\langle\omega_i\omega_j s_{ij}\rangle \\ & - \left\langle s_{ij}\frac{\partial^2 p}{\partial x_i\partial x_j}\right\rangle + \nu\langle s_{ij}\nabla^2 s_{ij}\rangle\,.\end{aligned} \tag{A.15}$$

The transport equation of $\frac{1}{2}\frac{\partial\langle\omega_i\omega_i\rangle}{\partial t}$ can be obtained by applying ∂x_j to equation A.1 but instead of selecting the symmetric parts as in the case of S_{ij}, we select the skew symmetric parts. The rest of the derivation follows in a similar manner.

Appendix B

Schur decomposition in complex form

The Schur triangularization theorem states that for any n-square matrix A, there exists an n-square unitary matrix U such that U^*AU is upper-triangular. The following unitary similarity transformation holds,

$$U^*AU = T = L + N\,, \tag{B.1}$$

where D is a diagonal matrix and N is scrictly upper-triangular. A unitary matrix U is a square matrix whose conjugate transpose (denoted by an asterisk) is equal to its inverse, i.e., $U^*U = UU^* = I$, where I is the identity matrix.

We will show that this decomposition exists through a matrix proof (see [Golub and Van Loan, 2013, Stewart, 2001, Schott, 2016] for further details). Let the eigenvalues of A be defined as $\lambda(A) = \{\lambda_1, ..., \lambda_n\}$ where e_i is an eigenvector corresponding to λ_n. For $n = 1$, we have

$$Ae_1 = \lambda_1 e_1\,, \tag{B.2}$$

where $e_1 \neq 0$ and ${e_1}^*e_1 = 1$. For $n > 1$, we can extend e_1 from a vector to a unitary matrix X with $X = \begin{bmatrix} e_1 & X_2 \end{bmatrix}$ where the following expression is valid

$$X^*AX = \begin{bmatrix} {e_1}^* \\ {X_2}^* \end{bmatrix} A \begin{bmatrix} e_1 & X_2 \end{bmatrix} = \begin{bmatrix} {e_1}^*Ae_1 & {e_1}^*AX_2 \\ {X_2}^*Ae_1 & {X_2}^*AX_2 \end{bmatrix}\,. \tag{B.3}$$

Here, ${e_1}^*Ae_1 = {e_1}^*\lambda_1 e_1 = \lambda_1$ holds true because ${e_1}^*e_1 = 1$. Likewise, $X_2{e_1}^* = 0$, allows

${X_2}^* A e_1 = \lambda {X_2}^* e_1 = 0$. This simplifies our formulation to

$$X^* A X = \begin{bmatrix} \lambda_1 & {e_1}^* A X_2 \\ 0 & {X_2}^* A X_2 \end{bmatrix} = \begin{bmatrix} \lambda_1 & r^* \\ 0 & B \end{bmatrix}, \tag{B.4}$$

here, $r^* = {e_1}^* A X_2$ is a n-row vector not necessarily zero. Considering that B is a block triangular matrix, $\lambda(A) = \lambda_1 \cup \lambda(B)$ with $\lambda(B) = \{\lambda_2, ..., \lambda_n\}$. Our main objective is now to generalize matrix B by induction. Let now F be a set of unitary matrices such that $F^* B F = T_{22}$, T_{22} and is an upper triangular matrix with $\lambda_2, ..., \lambda_n$ on the diagonal. Assume P be a unitary matrix, given that matrix F is unitary

$$P = \begin{bmatrix} 1 & 0 \\ 0 & F \end{bmatrix}. \tag{B.5}$$

If we assign $U = XP$, then U is also unitary,

$$U^* A U = X^* P^* A X P = \begin{bmatrix} 1 & 0 \\ 0 & F^* \end{bmatrix} \begin{bmatrix} \lambda_1 & r^* \\ 0 & B \end{bmatrix} \begin{bmatrix} 1 & 0 \\ 0 & F \end{bmatrix} = \begin{bmatrix} \lambda_1 & r^* F \\ 0 & F^* B F \end{bmatrix} = \begin{bmatrix} \lambda_1 & r^* F \\ 0 & T_{22} \end{bmatrix}. \tag{B.6}$$

Then we have the general form, where the resulting matrix is in upper triangular form, with $T = U^* A U = L + N$ and $L = \lambda_1, ..., \lambda_n$ on the diagonal.

The eigenvalues of Hermitian matrices (defined as $A^* = A$) are real whereas the eigenvalues of a skew Hermitian matrix (defined as $A^* = -A$) can only be either zero or have purely imaginary values and the eigenvectors in both cases orthonormal (orthogonal to each other and have unit norms) [Stewart, 2001, Bai and Pan, 2021].

Non-normality can be measured with $\|N\|^2$ [Golub and Van Loan, 2013]

$$\|N\|^2 = \|A\|^2 - \|L\|^2 = \|A\|^2 - \Sigma_{i=1}^{n} |\lambda i|^2 . \tag{B.7}$$

S_{ij} and Ω_{ij} are examples of symmetric and skew-symmetric tensors respectively for which the departure from normality would be zero.

If the real form of the Schur decomposition is implemented, we obtain [Golub and Van Loan,

2013]

$$U^*AU = \begin{bmatrix} R_{11} & R_{12} & \cdots & R_{1m} \\ 0 & R_{22} & \cdots & R_{2m} \\ \vdots & \vdots & \ddots & \vdots \\ 0 & 0 & \cdots & R_{mm} \end{bmatrix}, \tag{B.8}$$

where each R_{ii} is either a 1×1 matrix for a real eigenvalues or a 2×2 matrix having complex conjugate eigenvalues. In case we encounter complex eigenvalues, this form prevents matrix A from being partitioned in the same manner (with a diagonal and strictly upper triangular part) as the previous complex implementation. For this reason, the complex implementation is chosen to address this limitation.

Appendix C

Proof that $\|S_C\|^2 = \|\Omega_C\|^2$

We demonstrate that the non-normal components are evenly distributed, i.e. the norm of matrix S_C is equal to the norm of matrix Ω_C. We have,

$$\begin{aligned} S_C S_C^* &= \frac{1}{2}(C + C^*)\frac{1}{2}(C^* + C) \\ &= \frac{1}{4}(CC^* + CC + C^*C^* + C^*C) \\ &= \frac{1}{4}(UNN^*U^* + UNNU^* + UN^*N^*U^* + UN^*NU^*)\,. \end{aligned} \tag{C.1}$$

The products of two strictly upper (lower) triangular matrices, denoted as NN and N^*N^*, have zero entries on their main diagonal. In contrast, the products NN^* and N^*N have a non-zero trace. Therefore, the Frobenius norm of the decomposition shown in equation C.1 is equivalent to

$$\|S_C\| = \sqrt{\mathrm{Tr}(S_C S_C^*)} = \frac{1}{4}\sqrt{\mathrm{Tr}(UNN^*U^* + UN^*NU^*)}\,, \tag{C.2}$$

Ω_C is a skew-Hermitian tensor that obeys $-\Omega_C = \Omega_C^*$. The rotational component is expressed as follows

$$\begin{aligned} \Omega_C \Omega_C^* &= \frac{1}{2}(C - C^*)(-\frac{1}{2}(C - C^*)) \\ &= \frac{1}{4}(-CC + CC^* + C^*C - C^*C^*) \\ &= \frac{1}{4}(-UNNU^* + UNN^*U^* + UN^*NU^* - UN^*N^*U^*)\,, \end{aligned} \tag{C.3}$$

where the traces of negative terms are zero as in the previous step. The Frobenius norm of C.3

is equal to

$$\|\Omega_C\| = \sqrt{\mathrm{Tr}(\Omega_C \Omega_C^*)} = \frac{1}{4}\sqrt{\mathrm{Tr}(UNN^*U^* + UN^*NU^*)}\,. \tag{C.4}$$

By squaring C.2 and C.4 we get $\|S_C\|^2 = \|\Omega_C\|^2$.

Appendix D

Proof that the traces of matrices involving triple products of the form of $S_B S_B S_C$ and $\Omega_B \Omega_B S_C$ are zero

The trace of matrices involving triple products with two identical normal terms, for example $S_B S_B$ and one non-normal term i.e. S_C, is zero. As an example we consider $\mathrm{Tr}(S_B S_B S_C)$. We use $B^* = (ULU^*)^* = (U^*)^*(UL)^* = UL^*U^*$ to decompose $S_B S_B$ as follows

$$\begin{aligned} S_B S_B &= \frac{1}{2}(B + B^*)\frac{1}{2}(B + B^*) \\ &= \frac{1}{4}(BB + BB^* + B^*B + B^*B^*) \\ &= \frac{1}{4}(ULLU^* + ULL^*U^* + UL^*LU^* + UL^*L^*U^*) \\ &= \frac{1}{4}UDU^*\,, \end{aligned} \tag{D.1}$$

where $D = LL + LL^* + L^*L + L^*L^*$ is a diagonal matrix. S_C can be decomposed as follows

$$S_C = \frac{1}{2}(C + C^*) = \frac{1}{2}(UNU^* + UN^*U^*)\,. \tag{D.2}$$

Multiplying D.1 with D.2, we obtain

$$\begin{aligned} S_B S_B S_C &= \frac{1}{4}(UDU^*)\frac{1}{2}(UNU^* + UN^*U^*) \\ &= \frac{1}{8}U(DN + DN^*)U^*\,. \end{aligned} \tag{D.3}$$

Here, DN and DN^* take the form of a strictly upper and lower triangular matrix respectively with zero diagonal entries. For this reason, $\mathrm{Tr}(DN) = \mathrm{Tr}(DN^*) = 0$, and since the trace

remains invariant under a similarity transformation, $\mathrm{Tr}(S_B S_B S_C) = 0$. The same proof also applies to $\mathrm{Tr}(S_B S_B S_C) = \mathrm{Tr}(S_C S_B S_B) = \mathrm{Tr}(S_B S_C S_B) = 0$ taking into account cyclical permutation. The same proof this proof can be extended to the terms of type $\mathrm{Tr}(\Omega_B \Omega_B S_C) = \mathrm{Tr}(S_C \Omega_B \Omega_B) = \mathrm{Tr}(\Omega_B S_C \Omega_B) = 0$.

Appendix E

Derivation of the Schur decomposition of enstrophy production by mean strain-rate fields

We derive the Schur decomposition of $\mathrm{Tr}\left(\langle\Omega_A^2\rangle S_A^M\right)$. By considering the identity $\Omega_{ik}\Omega_{kj} = \frac{1}{4}(\omega_i\omega_j - \omega^2\delta_{ij})$ where $\delta_{ij}S_A^M = 0$ (see Appendix A for more details), we have the following equivalence

$$\frac{1}{4}\langle\omega_i\omega_j\rangle\langle S_{ij}\rangle = \mathrm{Tr}\left(\langle\Omega_A^2\rangle S_A^M\right) . \tag{E.1}$$

Furthermore, if we write $\langle S_{ij}\rangle = \langle S_{ij}^B\rangle + \langle S_{ij}^C\rangle$, $\omega_j = \omega_j^B + \omega_j^C$ and use $\omega_j\langle S_{ij}\rangle\omega_i = \omega_i\omega_j\langle S_{ij}\rangle$ we obtain

$$\begin{aligned}
\langle\omega_i\omega_j\rangle\langle S_{ij}\rangle &= \langle(\omega_i^B + \omega_i^C)(\omega_j^B + \omega_j^C)\rangle(\langle S_{ij}^B\rangle + \langle S_{ij}^C\rangle) \\
&= \langle\omega_i^B\omega_j^B + 2\omega_i^B\omega_j^C + \omega_j^C\omega_j^C\rangle(\langle S_{ij}^B\rangle + \langle S_{ij}^C\rangle) \\
&= \langle\omega_i^B\omega_j^B\rangle\langle S_{ij}^B\rangle + 2\langle\omega_i^C\omega_j^B\rangle\langle S_{ij}^B\rangle + \langle\omega_j^C\omega_j^C\rangle\langle S_{ij}^B\rangle \\
&\langle\omega_i^B\omega_j^B\rangle\langle S_{ij}^C\rangle + 2\langle\omega_i^C\omega_j^B\rangle\langle S_{ij}^C\rangle + \langle\omega_j^C\omega_j^C\rangle\langle S_{ij}^C\rangle ,
\end{aligned} \tag{E.2}$$

which is equivalent in matrix notation to

$$\begin{aligned}
\mathrm{Tr}\left(\langle\Omega_A^2\rangle S_A^M\right) = \mathrm{Tr}\left(\langle\Omega_B\Omega_B\rangle S_B^M\right) + 2\mathrm{Tr}\left(\langle\Omega_C\Omega_B\rangle S_B^M\right) + \mathrm{Tr}\left(\langle\Omega_C\Omega_C\rangle S_B^M\right) \\
+ \mathrm{Tr}\left(\langle\Omega_B\Omega_B\rangle S_C^M\right) + 2\mathrm{Tr}\left(\langle\Omega_C\Omega_B\rangle S_C^M\right) + \mathrm{Tr}\left(\langle\Omega_C\Omega_C\rangle S_C^M\right) .
\end{aligned} \tag{E.3}$$

All terms in E.3 are are finite (see Appendix F for details) compared to the simpler all-fluctuating term version in equation 1.50.

Appendix F

Proof that all the terms of the fluctuating-mean combination are not identically zero

We show that trace of components consisting of fluctuating-mean parts are not identically zero. We take the term $\mathrm{Tr}\left(\Omega_B\Omega_B S_C^M\right)$ as an example where its all-fluctuating variant is unconditionally zero ($\mathrm{Tr}\left(\Omega_B\Omega_B S_C\right) = 0$) as seen in Appendix D. Starting with the fluctuating part

$$\begin{aligned}\Omega_B\Omega_B &= \frac{1}{2}\left(B - B^*\right)\frac{1}{2}\left(B - B^*\right)\\ &= \frac{1}{4}\left(BB - BB^* + B^*B - B^*B^*\right)\\ &= \frac{1}{4}\left(ULLU^* - ULL^*U^* + UL^*LU^* - UL^*L^*U^*\right)\\ &= \frac{1}{4}\left(UEU^*\right),\end{aligned} \tag{F.1}$$

where $E = LL - LL^* + L^*L - L^*L^*$ is a diagonal matrix. S_C^M is

$$S_C^M = \frac{1}{2}\left(C^M + C^{M^*}\right) = \frac{1}{2}\left(U^M N^M U^{M^*} + U^M N^{M^*} U^{M^*}\right), \tag{F.2}$$

where N^M and N^{M^*} are the strictly upper and lower triangular matrix corresponding to the mean term, likewise U^M is the unitary of the mean term. Multiplying (F.1) with (F.2) we obtain

$$\begin{aligned}\Omega_B\Omega_B S_C^M &= \frac{1}{8}UEU^*\left(U^M N U^{M^*} + U^M N^{M^*} U^{M^*}\right)\\ &= \frac{1}{8}\left(UEU^*U^M N U^{M^*} + UEU^*U^M N^{M^*} U^{M^*}\right).\end{aligned} \tag{F.3}$$

The unitary matrices of the fluctuating and mean part are different $U \neq U^M$ and this does not allow the formation of the identity matrix I. For this reason, $U^* U^M$ prevents the trace to become zero. This also applies for any possible permutation thus these terms are not identically zero.

Appendix G

Norm of the Lamb vector and its potential term including mean, fluctuating and mixed terms

We are interested in the mean of $\langle \nabla\alpha \cdot \nabla\alpha \rangle$ and $\langle L \cdot L \rangle$ where $L = \Omega \times U$, and of $\nabla\alpha = \nabla(\frac{P}{\rho} + \frac{1}{2}U^2)$ [Hamman et al., 2008, Rousseaux et al., 2007]. The variables Ω, P and U can be Reynolds-decomposed as $\Omega = \langle\Omega\rangle + \omega$, $P = \langle P \rangle + p$ and $U = \langle U \rangle + u$ respectively. The Reynolds decomposition of the Lamb vector is

$$L = (\langle\Omega\rangle + \omega) \times (\langle U \rangle + u) \tag{G.1}$$

$$L = \langle\Omega\rangle \times \langle U \rangle + \langle\Omega\rangle \times u + \omega \times \langle U \rangle + \omega \times u \,, \tag{G.2}$$

and for the potential term:

$$\nabla\alpha = \frac{1}{\rho}\nabla\left(\langle P \rangle + p\right) + \frac{1}{2}\nabla(\langle U \rangle + u)(\langle U \rangle + u) \tag{G.3}$$

$$\nabla\alpha = \frac{1}{\rho}\nabla(\langle P \rangle + p) + \frac{1}{2}\nabla(\langle U \rangle^2 + 2\langle U \rangle u + u^2) \,. \tag{G.4}$$

To obtain $\langle L \cdot L \rangle$, we proceed by taking the dot product of equation G.2 with itself and we obtain

$$L \cdot L = (\langle\Omega\rangle \times U + \langle\Omega\rangle \times u + \omega \times U + \omega \times u) \cdot (\langle\Omega\rangle \times U + \langle\Omega\rangle \times u + \omega \times U + \omega \times u) \,. \tag{G.5}$$

We expand G.5, and take the average to obtain

$$\langle L \cdot L \rangle = (\langle \Omega \rangle \times \langle U \rangle)^2 + \langle (\langle \Omega \rangle \times u)^2 \rangle + \langle (\omega \times \langle U \rangle)^2 \rangle + \langle (\omega \times u)^2 \rangle + 2(\langle \Omega \rangle \times \langle U \rangle) \cdot \langle \omega \times u \rangle + 2\langle (\langle \Omega \rangle \times u) \cdot (\omega \times u) \rangle + 2\langle (\omega \times \langle U \rangle) \cdot (\omega \times u) \rangle + 2\langle (\omega \times \langle U \rangle) \cdot (\langle \Omega \rangle \times u) \rangle \,, \quad \text{(G.6)}$$

Similarly to obtain $\langle \nabla\alpha \cdot \nabla\alpha \rangle$, we take the dot product of equation G.4 with itself and we obtain

$$\nabla\alpha \cdot \nabla\alpha = \left(\frac{1}{\rho} \nabla \left(\langle P \rangle + p \right) + \frac{1}{2} \nabla (\langle U \rangle + u)(\langle U \rangle + u) \right) \cdot \left(\frac{1}{\rho} \nabla \left(\langle P \rangle + p \right) + \frac{1}{2} \nabla (\langle U \rangle + u)(\langle U \rangle + u) \right) , \quad \text{(G.7)}$$

and expanding we get,

$$\langle \nabla\alpha \cdot \nabla\alpha \rangle = \nabla\langle P \rangle \cdot \nabla\langle P \rangle + \langle \nabla p \cdot \nabla p \rangle + \nabla\langle P \rangle \cdot \nabla\langle U \rangle^2 + \nabla\langle P \rangle \cdot \nabla\langle u^2 \rangle + \langle \nabla p \cdot \nabla \left(u\langle U \rangle \right) \rangle + 2\langle \nabla p \cdot \nabla u^2 \rangle + \frac{1}{4} \nabla\langle U \rangle^2 \cdot \nabla\langle U \rangle^2 + \frac{1}{2} \nabla\langle U \rangle^2 \cdot \nabla\langle u^2 \rangle + \langle \nabla \left(\langle U \rangle u \right) \cdot \nabla u^2 \rangle + \langle (\nabla\langle U \rangle u)^2 \rangle + \frac{1}{4} \langle \nabla u^2 \cdot \nabla u^2 \rangle \,. \quad \text{(G.8)}$$